ABSTRACT

MULTI-WAVELENGTH INVESTIGATION OF ENERGY RELEASE AND CHROMOSPHERIC EVAPORATION IN SOLAR FLARES

by

Viacheslav M. Sadykov

For a comprehensive understanding of the energy release and chromospheric evaporation processes in solar flares it is necessary to perform a combined multi-wavelength analysis using observations from space-based and ground-based observatories, and compare the results with predictions of the radiative hydrodynamic (RHD) flare models. Initially, the case study of spatially-resolved chromospheric evaporation properties for an M 1.0-class solar flare (SOL2014-06-12T21:12) using data form IRIS (Interface Region Imaging Spectrograph), HMI/SDO (Helioseismic and Magnetic Imager onboard Solar Dynamics Observatory), and VIS/GST (Visible Imaging Spectrometer at Goode Solar Telescope), demonstrate a complicated nature of evaporation and its connection to the magnetic field topology. Following this study, the Interactive Multi-Instrument Database of Solar Flares (IMIDSF) is designed for efficient search, integration, and representation of solar flares for statistical studies. Comparison of the energy release and chromospheric evaporation properties for seven solar flares simultaneously observed by IRIS and RHESSI (Reuven Ramaty High Energy Solar Spectroscopic Imager) with predictions of the RHD electron beam-heating flare models reveals weak correlations between deposited energy fluxes and Doppler shifts of IRIS lines for observations and strong fore models, together with other quantitative discrepancies. Statistical analysis of properties of Soft X-Ray (SXR) emission, plasma temperature (T), and emission measure (EM), derived from GOES (Geostationary Operational Environmental Satellite) observations demonstrate that flares form two groups, “T-controlled” and “EM-controlled”, distinguished by different contribution of T and EM to the SXR peak formation and presumably evolving in loops of different lengths. Also, the modeling of the SDO/HMI line-of-sight observables for RHD flare models highlights that for relatively high deposited energy fluxes ($\geq 5.0 \times 10^{10}\ \mathrm{erg\,cm^{-2}\,s^{-1}}$) the sharp magnetic transients and Doppler velocities observed during the solar flares by HMI/SDO should be interpreted with caution. Finally, problems of the solar flare prediction and the role of the magnetic field Polarity Inversion Lines (PIL) in the initiation and development of flares are considered. In particular, the possibility to enhance the daily operational forecasts of M-class flares by considering jointly PIL and other magnetic field and SXR characteristics is demonstrated, with corresponding Brier Skill Scores ($BSS = 0.29 \pm 0.04$) higher than for the SWPC NOAA operational probabilities ($BSS = 0.09 \pm 0.04$).

MULTI-WAVELENGTH INVESTIGATION OF ENERGY RELEASE AND CHROMOSPHERIC EVAPORATION IN SOLAR FLARES

by
Viacheslav M. Sadykov

A Dissertation
Submitted to the Faculty of
New Jersey Institute of Technology and
Rutgers, The State University of New Jersey – Newark
in Partial Fulfillment of the Requirements for the Degree of
Doctor of Philosophy in Applied Physics

Department of Physics

May 2019

APPROVAL PAGE

MULTI-WAVELENGTH INVESTIGATION OF ENERGY RELEASE AND CHROMOSPHERIC EVAPORATION IN SOLAR FLARES

Viacheslav M. Sadykov

Dr. Alexander G. Kosovichev, Dissertation Advisor Date
Professor of Physics, NJIT

Dr. Haimin Wang, Committee Member Date
Distinguished Professor of Physics, NJIT

Dr. Bin Chen, Committee Member Date
Assistant Professor of Physics, NJIT

Dr. Zhen Wu, Committee Member Date
Professor of Physics, Rutgers Newark

Dr. Gelu M. Nita, Committee Member Date
Research Professor of Physics, NJIT

Dr. Vincent Oria, Committee Member Date
Professor of Computer Science, NJIT

BIOGRAPHICAL SKETCH

Author: Viacheslav M. Sadykov

Degree: Doctor of Philosophy

Date: May 2019

Undergraduate and Graduate Education:

- Doctor of Philosophy in Applied Physics,
  New Jersey Institute of Technology, Newark, NJ, 2019
- Master of Science in Applied Mathematics and Physics,
  Moscow Institute of Physics and Technology, Dolgoprudny, Moscow Region, Russia, 2015
- Bachelor of Science in Applied Mathematics and Physics,
  Moscow Institute of Physics and Technology, Dolgoprudny, Moscow Region, Russia, 2013

Major: Applied Physics

Publications:

V. Sadykov, A. Kosovichev and I. Kitiashvili, "Testing Enhancement of Binary and Probabilistic SWPC NOAA Flare Forecast by Using Machine Learning Algorithms," in preparation, 2019.

V. Sadykov, A. Kosovichev, I. Kitiashvili and G. Kerr, "Behavior of SDO/HMI Observables for Solar Atmosphere Heated by Precipitating High-energy Electrons," in preparation, 2019.

N. Huang, Y. Xu, V. Sadykov, J. Jing and H. Wang, "Spectral Diagnosis of Mg II and Hα Lines during the Initial Stage of an M6.5 Flare," *The Astrophysical Journal Letters*, under review, 2019.

V. Sadykov, A. Kosovichev, I. Kitiashvili and A. Frolov, "Statistical Properties of Soft X-ray Emission of Solar Flares," *The Astrophysical Journal*, vol. 874, article id 19, 11 pp, 2019.

V. Sadykov, A. Kosovichev, I. Sharykin and G. Kerr, "Statistical Study of Chromospheric Evaporation in Impulsive Phase of Solar Flares," *The Astrophysical Journal*, vol. 871, article id 2, 13 pp, 2019.

V. Sadykov and A. Kosovichev, "Relationships between Characteristics of the Line-of-sight Magnetic Field and Solar Flare Forecasts," *The Astrophysical Journal*, vol. 849, article id 148, 9 pp, 2017.

V. Sadykov, A. Kosovichev, V. Oria and G. Nita, "An Interactive Multi-instrument Database of Solar Flares", *The Astrophysical Journal Supplement Series*, vol. 231, article id 6, 8 pp, 2017.

I. Sharykin, A. Kosovichev, V. Sadykov, I. Zimovets and I. Myshyakov, "Investigation of Relationship between High-energy X-Ray Sources and Photospheric and Helioseismic Impacts of X1.8 Solar Flare of 2012 October 23," *The Astrophysical Journal*, vol. 843, article id 67, 8 pp, 2017.

I. Sharykin, V. Sadykov, A. Kosovichev, S. Vargas-Dominguez and I. Zimovets, "Flare Energy Release in the Lower Solar Atmosphere near the Magnetic Field Polarity Inversion Line," *The Astrophysical Journal*, vol. 840, article id 84, 13 pp, 2017.

V. Sadykov, A. Kosovichev, I. Sharykin, I. Zimovets and S. Vargas-Dominguez, "Relationship Between Chromospheric Evaporation and Magnetic Field Topology in an M-Class Solar Flare," *The Astrophysical Journal*, vol. 828, article id 4, 9 pp, 2016.

I. Zimovets and V. Sadykov, "Spatially Resolved Observations of a Coronal Type II Radio Burst with Multiple Lanes," *Advances in Space Research*, vol. 56, pp 2811-2832, 2015.

V. Eselevich, M. Eselevich, V. Sadykov and I. Zimovets, "Evidence of a Blast Shock Wave Formation in a CME-streamer Interaction," *Advances in Space Research*, vol. 56, pp 2793-2803, 2015.

V. Sadykov, S. Vargas-Dominguez, A. Kosovichev, I. Sharykin, A. Struminsky and I. Zimovets, "Properties of Chromospheric Evaporation and Plasma Dynamics of a Solar Flare from IRIS Observations," *The Astrophysical Journal*, vol. 828, article id 4, 9 pp, 2015.

V. Sadykov and A. Kosovichev, "Using MHD Simulations to Model H-alpha and UV Spectral Lines for Interpretation of IRIS and NST Data," *E-print ArXiv*, 1412.0288, 2014.

V. Sadykov and I. Zimovets, "A Green's Function Method for Calculating the Potential Magnetic Field in Solar Active Regions in a Spherical Geometry," *Astronomy Reports*, vol. 58, pp 345-352, 2014.

Presentations:

V. Sadykov, A. Kosovichev and I. Kitiashvili, “Using Machine Learning Methods and Expert Prediction Probabilities to Forecast Solar Flares,” *Poster presentation*, AGU Fall meeting, Washington, DC, 2018.

V. Sadykov, “Using Intelligent Flare Database for Statistical Analysis and Machine Learning Predictions,” *Oral Presentation*, EarthCube RCN Workshop, NJIT, Newark, NJ, 2018.

V. Sadykov, “Intelligent Databases and Machine Learning Forecast of Solar Flares,” *Seminar talk*, HelioAnalytics Seminar, NASA Goddard Space Flight Center, Greenbelt, MD, 2018

V. Sadykov, “Intelligent Databases and Machine Learning Forecast of Solar Flares,” *Seminar talk*, AMS Seminar Series, NASA Ames Research Center, Moffett Field, CA, 2018.

V. Sadykov, “Statistical Study of Chromospheric Evaporation in Impulsive Phase of Solar Flares,” *Seminar talk*, Lockheed Martin Solar & Astrophysics Laboratory Seminar, Lockheed Martin, Palo Alto, CA, 2018.

V. Sadykov, A. Kosovichev, A. Frolov, “Testing a Standard Picture of Chromospheric Evaporation through a Statistical Study of Soft X-ray Emission Properties from GOES observations,” *Oral presentation*, Triennial Earth-Sun Summit, Leesburg, VA, 2018.

V. Sadykov, A. Kosovichev, G. Nita, V. Oria, “An Intelligent Database of Solar Events and Active Regions (IDSEAR),” *Poster presentation*, Triennial Earth-Sun Summit, Leesburg, VA, 2018.

V. Sadykov, “An Interactive Multi-Instrument Database of Solar Flares,” *Oral presentation*, The 9th Community Coordinated Modeling Center Workshop, University of Maryland, College Park, MD, 2018

V. Sadykov, A. Kosovichev, “Characteristics of the Polarity Inversion Line and Solar Flare Forecasts,” *Oral presentation*, Solar Physics Division Meeting, Portland, OR, 2017

V. Sadykov, A. Kosovichev, “Analysis of Chromospheric Evaporations in Solar Flares,” *Oral presentation*, Joint Hinode-11/IRIS-8 Science Meeting, Seattle, WA, 2017

V. Sadykov, R. Gupta, G. Nita, V. Oria, A. Kosovichev, “Interactive Multi-Instrument Database for Studying Solar Flares,” *Poster presentation*, Space Weather Workshop, Bloomfield, CO, 2016

To my wife Liliia and my son Tagir. You are the brightest Suns that surround me every day.

To my parents, Oksana and Marat. I would never be who I am now if it were not for you.

In the memory of my grandfather Farit, the strongest and the kindest person in my life.

ACKNOWLEDGMENT

First and foremost, I would like to express my deepest appreciation to my dissertation advisor, Dr. Alexander Kosovichev. I would like to thank him for his great mentoring, brilliant research ideas and suggestions, timely advice during the PhD program, insightful feedback and direction. He always helped me with the financial support and travel opportunities, so that I can focus on our research and promote it to the scientific community.

I would like to acknowledge the support and help of Dr. Haimin Wang, Dr. Bin Chen, Dr. Zhen Wu, Dr. Gelu Nita and Dr. Vincent Oria for being in dissertation committee. I am very thankful for their valuable suggestions and careful review of the dissertation.

I am very grateful to Dr. Andrei Sirenko and Dr. Haimin Wang for their valuable advice and help during the entire PhD program, as well as for the financial support from the Department of Physics. I also thank Christine Oertel, Leslie Williams, Cindy Montalvo-Harden, and Jessica Witte-Dyer, for the timely solutions and help with any questions and concerns during the PhD program.

A special thanks goes to our Center of Computational Heliophysics (CCH) lead by Dr. Alexander Kosovichev. It is a pleasure to work with Dr. Vincent Oria and Dr. Gelu Nita, to discuss and implement into life the interdisciplinary ideas and gain knowledge especially important nowadays. I am very thankful to my colleagues and friends at CCH, Andrey Stejko and John Stefan, for the great time and support at NJIT and possibility to share with them thoughts, worries and ideas. I also thank my colleagues Rishabh Gupta, Nalinaksh Gaur, Sheetal Rajgure and Wei Wang for their help with the development and implementation of the Interactive Multi-Instrument Database of Solar Flares.

I would like to thank NASA Ames Heliophysics Modeling and Simulation team, Dr. Nagi Mansour, Dr. Irina Kitiashvili and Dr. Alan Wray, for extremely valuable discussions during the entire four years of PhD. I especially thankful to Dr. Irina Kitiashvili for the great internship opportunity during the Summer 2018 resulting in a very productive work and future research options. I also thank the team of NASA Advanced Supercomputing, especially Dr. Shubha Ranjan, for implementing our IMIDSF database at NASA side.

I would like to separately thank my collaborators, Dr. Ivan Sharykin, Dr. Graham Kerr, Dr. Ivan Zimovets, Dr. Santiago Vargas Dominguez, Dr. Yan Xu, Dr. Ju Jing, Nengyi Huang, and Alexander Frolov, for the great time of working together with them on research projects and papers. I am also thankful for the Center for Solar-Terrestrial Research (CSTR) at NJIT and for the scientist and personnel working in the center, for the opportunity to discuss scientific and routine problems and ideas. I also thank Dr. Dmitri Laptev for valuable discussions of the magnetogram segmentation algorithm.

I am very grateful to the following organizations for their financial support: the National Aeronautics and Space Administration for the NASA Earth and Space Science Fellowship Award, which was the primary source of the financial support of my PhD program; the Solar Heliospheric and Interplanetary Environment (SHINE) workshop steering committee for the travel support at SHINE 2018 workshop; the Solar Physics Division (SPD) of the American Astronomical Society for the financial support to attend SPD 2017 meeting; the steering committee of the Joint Hinode-11/IRIS-8 Science Meeting for the travel support to attend the meeting in 2017; the steering committee of the Space Weather Workshop for the travel support to attend the meetings at 2016 and 2019; and the Graduate Student Association of New Jersey Institute of Technology for the travel award to attend Triennial Earth-Sun Summit in 2018.

I thank teams of the GOES, RHESSI, SDO/HMI, SDO/AIA, SDO/EVE, IRIS, Fermi and Hinode space missions, and also teams of the BBSO, EOVSA and Nobeyama ground-based observatories for the availability of the high-quality scientific data. Thanks also to the teams managing the catalogs of the flare and flare-related events (GOES, RHESSI, Hinode, Fermi GBM, Konus-WIND, OVSA flare catalogs, Filament eruption catalog, CACTus CME catalog and Heliophysics Event Knowledgebase) for the possibility to work with their data. I thank also researchers and developers of the F-CHROMA project (`http://www.fchroma.org/`) for bringing the open access to the cutting-edge simulation results, and deeply acknowledge the Stanford Solar Observatories Group and NASA Ames Research Center for the possibility to use the computational resources.

The research presented in this dissertation was supported by the NASA Grants NNX11AO736, NNX12AD05A, NNX14AB68G, NNX14AB70G and NESSF fellowship NNX16AP05H, NSF grants AGS-1250818 and 1639683, and by the NJIT Faculty Seed Grant (FSG).

TABLE OF CONTENTS

TABLE OF CONTENTS
(Continued)

Chapter **Page**

TABLE OF CONTENTS
(Continued)

TABLE OF CONTENTS
(Continued)

Chapter **Page**

LIST OF TABLES

LIST OF TABLES
(Continued)

Table **Page**

LIST OF FIGURES

LIST OF FIGURES
(Continued)

LIST OF FIGURES
(Continued)

LIST OF FIGURES
(Continued)

LIST OF FIGURES
(Continued)

LIST OF FIGURES
(Continued)

LIST OF FIGURES
(Continued)

Figure **Page**

CHAPTER 1

INTRODUCTION

1.1 Multi-wavelength Nature of Solar Flares

Solar flares are a very complex phenomenon and the most energetic process occurring in the Heliosphere. Usually lasting from several minutes to several hours, a solar flare releases about 10^{30}-10^{32} erg of energy [56]. The flare energy stored in magnetic fields and electric currents rapidly transforms into the kinetic energy of the Solar Energetic Particles (SEPs), fast-moving Coronal Mass Ejections (CMEs), and impulsive radiation from radio waves to X-rays and gamma-rays. The high-energy particles and photons can damage equipment onboard satellites, and are dangerous for astronauts working in open space. CMEs with embedded magnetic field can disturb the Earth's magnetosphere and cause geomagnetic storms leading to communication problems, and ground return currents destroying electric transformers and initiating corrosion in pipelines. One can claim that the solar flares are among the primary drivers of the Space Weather. Correspondingly, the understanding of the underlying physical processes and development of the reliable solar flare forecasts are among the primary problems of Heliophysics.

Solar flares are observable in a broad range of the electromagnetic spectrum, from radiowaves to γ-rays. For better understanding of solar flares and their prediction, it is crucially important to analyze multi-wavelength observations, as different physical processes are reflected at different energies. For example, in the Standard flare model [38, 218, 83, 114, 108, 169, 212], the hard X-ray radiation is assumed to be bremsstrahlung emission of accelerated particles, and carries information about acceleration processes associated with magnetic energy release. At the same time, observations of visible and ultraviolet spectral lines allow us to understand photospheric and chromospheric responses to the energy release. The opportunity to diagnose different physical processes from radiation at different wavelength ranges is one of the reasons why the solar flares are observed by numerous satellites and ground-based observatories generating tremendous amounts of scientific data and metadata.

Many problems of flare physics require performing analyses using data from a particular set of instruments, or/and for a sample of flares with particular characteristics. However, usually, flare lists are created for specific routinely-observing instruments, and poorly communicate with each other. Addressing problems of communication between various flare catalogs, integration of the flare records, and organization of a convenient search and quicklook tools can save a significant time for preparation of lists of events for the statistical studies. This is one of the points which we plan to address in this Dissertation.

1.2 Chromospheric Evaporation in Solar Flares

The most successful model of solar flares is called the Standard Flare Model, or the CSHKP model [38, 218, 83, 114, 108, 169, 212]. In this model, the primary energy release occurs high in the corona, where a quasi-vertical current sheet is formed. Electrons and protons accelerated in this region precipitate along magnetic field lines into the chromosphere, lose their energy and create an overpressure region. The hot chromospheric plasma heated in this region expands up to the corona and fills coronal magnetic loops. This process is called "chromospheric evaporation". From this model, it follows that properties of the chromospheric evaporation, such as velocity, temperature, and amounts of evaporated plasma, depend on the heating rates, and thus on the mechanism of the energy release and transport, as well as on the plasma radiative losses and dynamics. This is why the process of chromospheric evaporation is a key to understanding of how the flare energy is released, deposited and transported in the solar atmosphere.

Eruptions of the chromospheric plasma caused by flares can be seen from imaging observations. However, to determine physical characteristics of chromospheric evaporations, analysis and modeling of multiline spectroscopic observations are necessary [68, 147]. Different spectral lines are formed at different heights of the solar atmosphere: some lines reflect the thermodynamic properties and dynamics of the hot coronal plasma, while some other correspond to the relatively cold chromospheric layers. The currently operating NASA's Interface Region Imaging Spectrograph [50, IRIS] observes the chromosphere and chromosphere-corona transition region with high spatial ($0.33''$) and spectral resolutions(26-53 mÅ) in a variety of observing modes. The IRIS spectral coverage includes several strong lines formed in the upper chromosphere: Mg II h&k 2796 Å and 2803 Å ($T = 8-10\times10^3 K$) and in the lower transition region: C II 1334/1335 Å ($T = 1-2\times10^4 K$) and Si IV 1403 Å ($T = 5-10\times10^4 K$). In the hot plasma of solar flares IRIS can observe the Fe XXI 1354.1 Å line which corresponds to a magnetic dipole transition and is formed at 1.1×10^7 K. This line appears during flares in the IRIS O I spectral window. The observed spectral lines are summarized in Table 1.1.

Analysis of these lines allows us to understand simultaneous plasma motions in the upper chromosphere, lower transition region and hot corona, and trace all stages of the chromospheric evaporation process. Also, simultaneous data from hard X-ray observations from the Reuven Ramaty High Energy Solar Spectroscopic Imager [131, RHESSI] reveals the properties of the energy release in the form of the deposit of high-energy accelerated electrons, and allows us to test the validity of the standard CSHKP model and chromospheric evaporation modeling approaches. In this aspect, a systematic statistical study of events jointly observed by IRIS and RHESSI becomes of particular interest.

Table 1.1 Spectral Lines Observed by IRIS

Spectral line	Atomic transition	Average formation temperature
Mg II k 2796 Å	$2p^63p, J = 3/2 \rightarrow 2p^63s, J = 1/2$	$T = 8 - 10 \times 10^3 K$ (UChr)
Mg II h 2803 Å	$2p^63p, J = 1/2 \rightarrow 2p^63s, J = 1/2$	$T = 8 - 10 \times 10^3 K$ (UChr)
C II 1334 Å	$2s2p^2, J = 3/2 \rightarrow 2s^22p, J = 1/2$	$T = 1 - 2 \times 10^4 K$ (TR)
C II 1335 Å	$2s2p^2, J = 5/2 \rightarrow 2s^22p, J = 3/2$	$T = 1 - 2 \times 10^4 K$ (TR)
Si IV 1394 Å	$2p^63p, J = 3/2 \rightarrow 2p^63s, J = 1/2$	$T = 5 - 10 \times 10^4 K$ (TR)
Si IV 1403 Å	$2p^63p, J = 1/2 \rightarrow 2p^63s, J = 1/2$	$T = 5 - 10 \times 10^4 K$ (TR)
Fe XXI 1354.1 Å	$2s^22p^2, J = 1 \rightarrow 2s^22p^2, J = 0$	$T = 1.1 \times 10^7 K$ (Cor)

Note: Notations used in the table: UChr — upper chromosphere, TR — transition region, Cor — coronal plasma.

The spectral lines and their behavior contain information about physical parameters of the atmosphere and its dynamics. To correctly interpret the observed line profiles a radiative transfer modeling based on first physical principles is needed. The radiative transfer problem is not easy to solve because it is essentially non-local and non-linear in nature, and the conditions of line formation are often far from the Local Thermodynamic Equilibrium (LTE). The typical system of equations for the radiative transfer problem can be written as follows:

$$\frac{dI_{s,\nu}}{ds} = -\chi_{s,\nu} I_{s,\nu} + \eta_{s,\nu} \tag{1.1}$$

$$n_l \sum_{l'} (R_{ll'} + C_{ll'}) - \sum_{l'} n_{l'} (R_{l'l} + C_{l'l}) = \frac{dn_l}{dt} \tag{1.2}$$

Here $I_{s,\nu}$ is the intensity along the ray direction s and at frequency ν, $\chi_{s,\nu}$ and $\eta_{s,\nu}$ are the opacity and emissivity coefficients, n_l is number of atoms (of the considered element) with level l populated, $R_{ll'}$ and $C_{ll'}$ are the radiative and collisional rate coefficients for the transition from level l to level l'. Several non-LTE computational methods and codes have been developed to solve this system of equations, including RH radiative transfer code [189, 190, 227, 164], which allow us to calculate the line profiles observed by IRIS and other instruments under the statistical equilibrium assumption ($dn_l/dt = 0$). These methods in combination with realistic radiative hydrodynamic simulations of the chromospheric evaporation [2, 5, 6, 7] are a very powerful technique for physical diagnostics of the flare processes.

In general, the studies of the energy release and chromospheric evaporation processes are not limited by the spectroscopic observations in UV and visible light lines. For example, the X-ray Sensor [23, XRS] onboard the Geostationary Operational Environmental Satellite (GOES) series measures the Soft X-ray (SXR) flux in two channels, 1-8 Å and 0.5-4 Å, where the strongest contribution comes from thermal emission of evaporated plasma. Studying properties of the XRS/GOES measurements during the solar flares is very useful for understanding general behavior of the chromospheric evaporation process.

In addition, several studies [209, 207] found that impulsive variations observed in filtergrams of the Helioseismic and Magnetic Imager onboard the Solar Dynamics Observatory [200, 44, SDO/HMI] are highly correlated with the Hard X-ray signals. This demonstrates that high-energy particles can disturb the photospheric Fe 6173 Å line properties measured by SDO/HMI, i.e., that the properties of the energy release can be potentially reflected in and diagnosed from photospheric observations in some cases.

1.3 Development of the Solar Flare Forecasts

Reliable operational forecast of solar flares remains one of the most challenging and not completely solved tasks in the Heliophysics. The interest to this task increased significantly during the last decade because of the exponential growth of the machine learning methodology and accessibility of the computational resources, as well as availability of the high-quality routine observational data.

It has long been known that understanding the relationships between solar flares and the properties of magnetic field in active regions is extremely important for developing flare forecasts. The strongly non-potential magnetic field of active regions is the only reservoir able to store amounts of energy typically released in a solar flare. The availability of the high-quality SDO/HMI data starting from 2010 with almost no interruptions significantly increased the number of forecasting attempts, including employment of the state-of-art deep learning techniques [86, 155]. It is also realized that properties of the magnetic field Polarity Inversion Line (PIL) in regions of strong field plays an important role in the flare activity [231, 61, 113, 203]. The flare development process is very often closely connected to the dynamics in the

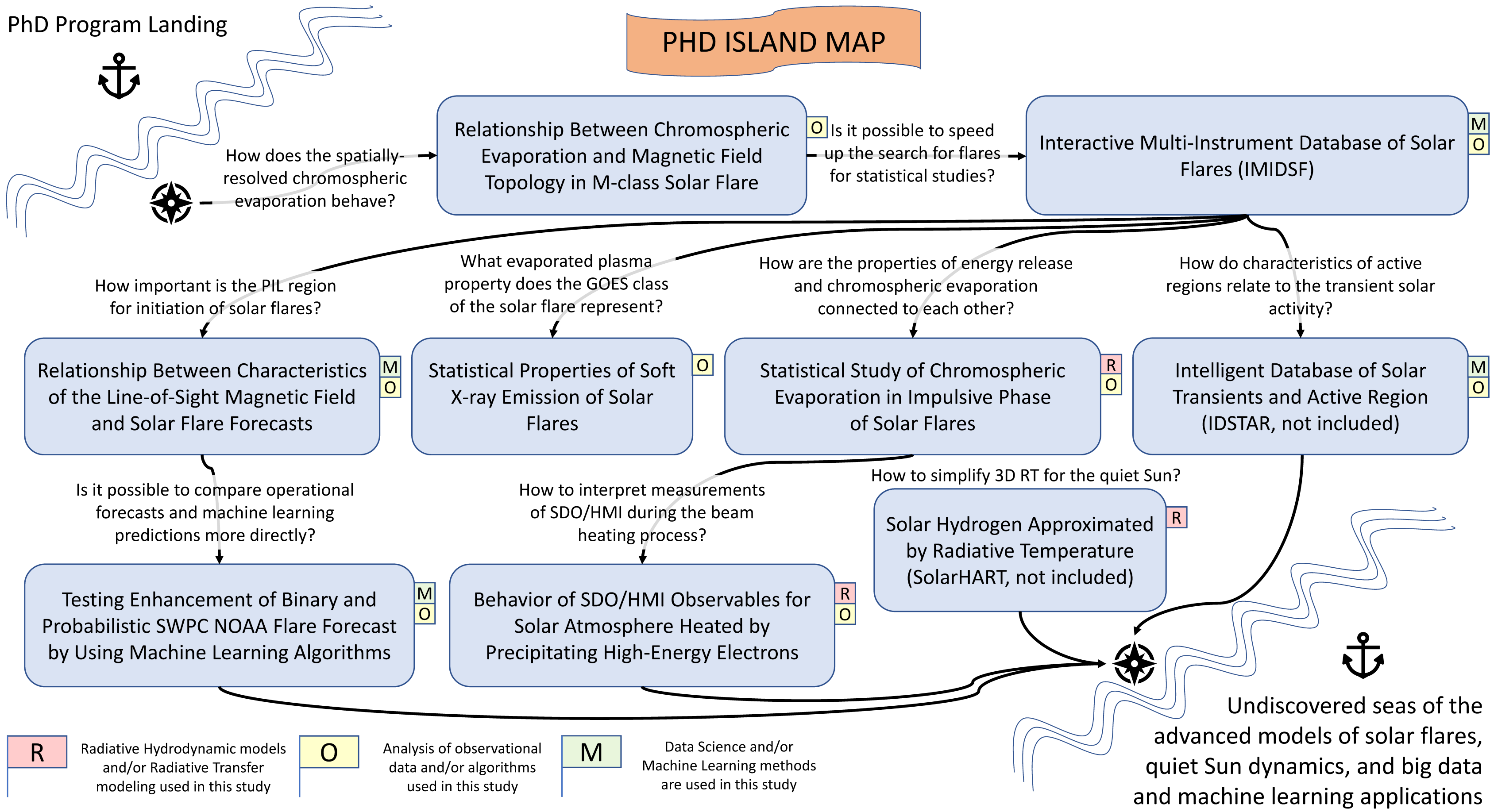

Figure 1.1 Schematic representation of studies competed/conducted during my PhD program, and relations between them.

vicinity of the PIL. The characteristics of the PIL and the magnetic field structure nearby represent a valuable information for the forecasting attempts.

1.4 Structure of the Dissertation

The research projects conducted during the PhD program are schematically illustrated in Figure 1.1. Each rectangle in this Figure represents a separate study. The key questions which motivated us to begin each study are also presented in the Figure. Among nine works described, two are not included in the Dissertation (and designated by words "not included" in the end of the project title). Also, the Dissertation (as well as Figure 1.1) does not include several collaboration projects done together with my colleagues during the time of PhD [209, 208, 85].

The other seven works presented in Figure 1.1 are represented by seven separate chapters in this Dissertation. Chapter 2 describes the case study of the relationship between the chromospheric evaporation and magnetic field topology in an M-class solar flare observed on June 12th 2014 at 21:01 UT. Chapter 3 presents an Interactive Multi-Instrument Database of Solar Flares created for more convenient and efficient search among solar flares based on their physical characteristics. Chapter 4 presents a statistical study of chromospheric evaporation in impulsive phase of solar flares from both, observational and modeling, points of view. Chapter 5 describes an analysis of statistical properties of soft X-ray emission of solar flares, one of the most widely-used types of measurements. Chapter 6 is dedicated to modeling of SDO/HMI observables for solar atmosphere heated by precipitating high-energy electrons.

We also discuss the questions of prediction of strong solar flares from the characteristics of solar magnetic field and soft X-ray radiation. Chapter 7 illustrates relationship between characteristics of the line-of-sight magnetic field and solar flare forecasts, with particular focus on the Polarity Inversion Line (PIL) properties. We extend this study in Chapter 8 where we test an enhancement of the binary and probabilistic forecasts of solar flares done by Space Weather Prediction Center of the National Oceanic and Atmospheric Administration (SWPC NOAA) by using machine learning algorithms.

Finally, Chapter 9 briefly summarizes the studies presented in the dissertation and highlights the main results, and presents concluding remarks.

CHAPTER 2

RELATIONSHIP BETWEEN CHROMOSPHERIC EVAPORATION AND MAGNETIC FIELD TOPOLOGY IN M-CLASS SOLAR FLARE

2.1 Introduction and Motivation

Spectroscopic observations provide a very powerful tool to study atmospheric properties and dynamics of solar flares. The long history of these studies includes observations from numerous satellites and rocket missions [68, 147]. The currently operating NASA's Interface Region Imaging Spectrograph [50, IRIS] observes the chromosphere and chromosphere-corona transition region with high spatial, temporal and spectral resolutions. The IRIS spectral coverage includes several strong lines formed in the upper chromosphere: Mg II h&k 2796 Å and 2803 Å ($T = 8-10\times10^3 K$) and in the lower transition region: C II 1334/1335 Å ($T = 1 - 2 \times 10^4 K$) and Si IV 1403 Å ($T = 5 - 10 \times 10^4 K$). In the hot plasma of solar flares IRIS can observe the Fe XXI 1354.1 Å line which corresponds to a forbidden transition and is formed at 1.1×10^7 K. This line appears during flares in the IRIS O I spectral window.

IRIS provides a unique opportunity for the chromospheric evaporation studies [17, 30, 76, 128, 129, 168, 220, 221, 239, 198]. In particular, the Fe XXI line appearing only during flares detects the hot upward-moving plasma flows as a Fe XXI blueshift. The chromospheric evaporation is also observed in the IRIS UV chromospheric and transition region lines. However, interpretation of the Doppler shift is less straightforward and depends on the energy transfer mechanism and heating rates resulting in “gentle” and “explosive” types of evaporation [9, 240, 67, 66, 65].

The chromospheric evaporation process is still not well understood. Despite many numerical simulations [114, 67, 112, 134, 184, 185, 178], some details of the process could not be reproduced. One of the most disputed effects is a time delay of the coronal evaporation flow relative to the chromospheric response observed as redshift of relatively cold UV lines corresponding to the downward motions of plasma. Graham and Cauzzi [76], Battaglia et al. [17], Young et al. [239] found the delays of about 60 s using IRIS spectroscopic data. The simulations of Rubio da Costa et al. [185] are the most successful in reproducing this effect. The delays between the maximum of the upflow plasma velocity and the maximum of the downflow velocity can reach ≈45 s for a low heating model with the maximum temperature less than 10^7 K. However, most of the numerical simulations of the standard "thick-target" flare model predict that both phenomena should occur almost simultaneously.

There are some attempts to explain this discrepancy. Emission of the Fe XXI line might be very weak at the initial and supposedly blueshifted stages of the evaporation, and then became stronger but less blueshifted. This situation is clearly illustrated in the paper of Graham and Cauzzi [76]. The weak Fe XXI emission may happen due to non-equilibrium ionization effects [17]. In particular, Figures 6-8 of Bradshaw [26] demonstrate that for the number density of $10^8 - 10^9$ cm^{-3} the characteristic ionization time can reach ≈60 s for Fe XIX and higher ionization degree ions, which may cause the blueshift delays for about one minute. However, the theory cannot explain the observed delays for a couple of minutes or longer.

In this chapter we focus on a detailed spatio-temporal analysis of the chromospheric evaporation during an M 1.0 class flare occurred on 12 June, 2014 from 21:01 UT to 21:19 UT in active region NOAA 12087. At this time the active region was located south-east (heliocentric coordinates S22E49) on the solar disc, and the flare event was well-covered by the IRIS observations in the coarse-raster mode (the IRIS observational set started long before the flare beginning and continued long after the flare decay). The eight slit positions run in a cyclic order with a high cadence (≈ 20 s for the full cycle) allowed us to study the flare spectra in most of the flare region. Some general properties of the chromospheric evaporation during this flare have already been studied in our previous paper [198]. Dynamical and magnetic processes in the vicinity of the magnetic polarity inversion line (PIL) have been studied by Kumar et al. [116] and Sharykin et al. [209]. This study highlights the process of chromospheric evaporation and its relations to the flare magnetic geometry in more detail.

In addition to the spectroscopic data, the knowledge of the magnetic field topology is very important for understanding of the flare dynamics. The magnetic field and corresponding electric current systems are the primary energy sources of solar flares. They can store the magnetic energy and convert about 10^{30}-10^{32} erg [56] into the kinetic energy of moving plasma and accelerated particles via magnetic reconnection, Joule heating and other mechanisms. Thus, it is especially important to know the magnetic field configuration. Nowadays it is possible to obtain photospheric vector magnetograms from the SDO/HMI telescope [200] and reconstruct magnetic field in the solar atmosphere under certain assumptions. One of the key characteristics of the magnetic field structure is the Quasi-Separatrix Layer [52, 51]. From the physical point of view, the QSL is a relatively thin surface where the magnetic field connectivity exhibits strong gradients [14], which can work as a channel of magnetic energy dissipation.

Nowadays, it is also possible to analyze flares with high-resolution using observations with large ground-based telescopes. One of the most breakthrough ground-based facilities is the Goode Solar Telescope [75, GST] at Big Bear Solar Observatory. The 1.6 m primary mirror and implemented adaptive optics provide diffraction-limited images and resolve features that are smaller than $0.1''$. The studied flare was observed by the GST, and in this work we utilize the GST observations obtained in the Hα line core.

2.2 Methodology

The IRIS observation covered temporarily the entire event for more than one hour from appearance of the first signs of flaring activity until the end of the decay phase. The instrument obtained spectra in several wavelength windows in each point of the region with ≈20 s temporal and $0.33'' \times 2''$ spatial resolution. To analyze the large amount of spectroscopic data, we implemented the following techniques of the line profile analysis.

For each IRIS line formed in the chromosphere and chromosphere-corona transition region, the center-of-gravity approach used in the previous paper [198] can be implemented. We decided to use the C II 1334.5 Å line as a representative of the colder chromospheric layer response to the flare heating. The C II line is formed at $T = 1 - 2 \times 10^4 K$. It is not overexposed in this flare unlike the Si IV line, and its shape is simpler than that of the Mg II lines. For each C II line profile the following characteristics are calculated: 1) the line peak intensity and 2) the Doppler shift defined as a difference between the center of gravity of the line and the reference wavelength for this line $\langle\lambda\rangle - \lambda_{ref} = \int \lambda I d\lambda / \int I d\lambda - \lambda_{ref}$. The reference wavelength of the C II line was calibrated using observations of several quiet-Sun areas before the flare and was chosen to be equal to 1334.56 Å. Obviously, the implemented technique cannot be applied to blended spectral lines. An example of such kind of lines is, in fact, the IRIS Fe XXI 1354.1 Å line that is formed in the 1.1×10^7 K hot plasma, and is very important for our study. The blends of this line are discussed by Tian et al. [220, Figure 2] and Young et al. [239, Appendix A]. We decided to take into account only the strongest blend, the C I 1354.3 Å line. Our previous study [198] did not reveal significant Doppler shifts of this line during the flare. Thus, for the Fe XXI line we performed a double-Gaussian fitting with a fixed peak wavelength of the second Gaussian profile corresponding to reference wavelength of the C I line ($\lambda_{ref} = 1354.34$ Å). This reference wavelength was also determined from observations of several quiet-Sun regions before the flare. We kept the wavelength difference between Fe XXI and C I lines the same as in Vilhu et al. [230], and obtained the Fe XXI reference wavelength equal to 1354.146 Å. Parameters of the Fe XXI line obtained by Gaussian fitting are used to estimate its intensity (as the amplitude of the Gaussian) and its Doppler shift (difference between the wavelength corresponding to the peak of the Gaussian, and the reference wavelength). Using the procedures described above, we determined the temporal and spatial behavior of the Doppler shift of lower transition region C II 1334.5 Å and coronal Fe XXI 1354.1 Å lines that are essential for studying the chromospheric evaporation.

As mentioned before, it is especially important to study the delay of the evaporated hot plasma flow observed as blueshift of the hot coronal lines relative to the chromospheric response (observed as redshift or blueshift of the cooler chromospheric or transition region lines). The IRIS raster scans provide an opportunity to study the spatial configuration of the delays across the flare region. For this analysis the following procedure was performed. First, the Doppler shift of the C II 1334.5 Å line was estimated at every point for each time moment of the IRIS scans in the region, and the same was done for the Fe XXI 1354.1 Å line. After this, the temporal evolutions of the redshift and blueshift in each point were plotted and smoothed with a 50 s running window for better estimation of their peak times. The peak times of the redshift and blueshift maxima were determined visually from the plotted curves. In places where the redshifts or blueshifts did not show any peak we set the delay to zero. Also, the delay was determined only in the flare "bright points", where the averaged over time magnitude of the C II 1334.5 line was greater than the one eighth of the mean magnitude of this line across the flare region. The uncertainties of the measured delays are ≈20 s because of the time needed for the IRIS to scan the 8 spatial positions.

To reconstruct the magnetic field for the studied event, we followed the approach of Wheatland et al. [236] implemented in the NLFFF package of the Solar Software (SSW) for Interactive Data Language (IDL). The algorithm finds the solution for the Nonlinear Force-Free Field (NLFFF) approximation assuming that all electric currents flow along the field lines. For the boundary conditions, the 12-minute full-Sun vector magnetograms obtained by the HMI/SDO instrument [200] were used. We reconstructed the magnetic field for eight time moments covering the flare period from 20:22:25 UT to 21:46:25 UT with 12 min cadence. For the magnetic force line tracing, a tri-linear interpolation technique implemented in the SSW NLFFF package was used. To estimate topological peculiarities of the magnetic field in the flare region we applied a method of quasi-separatrix layer (QSL) calculation [51]. The QSLs mark areas in the extrapolated field with sharp variations of magnetic field connectivity. To make a quantitative estimate of the connectivity changes at a point $P(x, y, z)$ we use parameter called Squashing factor $N(x, y, z)$ calculated as:

$$N(x, y, z) = \sqrt{\sum_{i=1}^{2} \left(\frac{\partial X_i}{\partial x}\right)^2 + \left(\frac{\partial X_i}{\partial y}\right)^2 + \left(\frac{\partial X_i}{\partial z}\right)^2}. \tag{2.1}$$

Here X_1 and X_2 are components of the vector connecting the point where the field line crossing point $P(x, y, z)$ is directed outward from the photosphere with the point where the same line is directed down into the photosphere. The coordinate derivatives ∂_x, ∂_y and ∂_z characterize variations of magnetic connectivity from point to point.

In addition, we analyzed the flare X-ray data from the Reuven Ramaty High-Energy Solar Spectroscopic Imager [131, RHESSI] and compared the 12-25 keV X-ray sources reconstructed by using the CLEAN algorithm with the magnetic field topology. Data from the detectors 1F-7F are used for the reconstruction. RHESSI observations covered the entire flare event, from ≈ 21:40 UT till ≈ 21:35 UT. The X-ray flux above 25 keV was very weak and insufficient for the source reconstruction.

2.3 Results

2.3.1 Behavior of the Integrated Redshifts

The integrated (averaged over the flare region) intensities and Doppler shifts of the C II 1334.5 Å and Fe XXI 1354.1 Å lines are displayed in Figure 2.1. For the C II line, the intensity is measured at its peak, and the Doppler shift is estimated using the Center-of-Gravity approach discussed in Sec. 2. For the Fe XXI line, the intensity and the Doppler shift correspond to the amplitude and the mean shift of the corresponding Gaussian (see Sec. 2 for the details). The mean intensities and Doppler shifts are plotted with different colors (see caption of Figure 2.1 for the color code).

The panel a) of Figure 2.1 represents the Fe XXI 1354.1 Å line intensity and Doppler shift integrated over the flare region. A delay of the Fe XXI line intensity relative to its Doppler shift is very obvious, and, probably, occurs because of the gradual filling the magnetic loops by the hot evaporated plasma. The panel b) of Figure 2.1 displays the mean intensity and Doppler shift of the C II line. The delay between the high-temperature Fe XXI line and low-temperature C II emission of about 6 min is not a surprising result: the same types of delays were observed in several works [33, 31]. One can notice an increase of the C II redshift during the flare, and its correlations with the X-ray 12-25 keV light curve from RHESSI. Previously (see [198] for details), it was found that the slowly varying redshifts mainly represent some background activity in the region. Figure 2.1 shows that we observe a superposition of the relatively steady downflows and fast varying downflows due to the flare energy release.

The panel c) in Figure 2.1 displays the C II and Fe XXI normalized Doppler shifts fitted with cubic splines. The tension of splines was chosen to smoothly fit all the significant features of the time curves. Additionally, the normalized derivatives of these splines are plotted in Figure 2.1c. Despite the first peaks of the C II line redshift and Fe XXI line blueshift, marked as two dotted vertical lines in

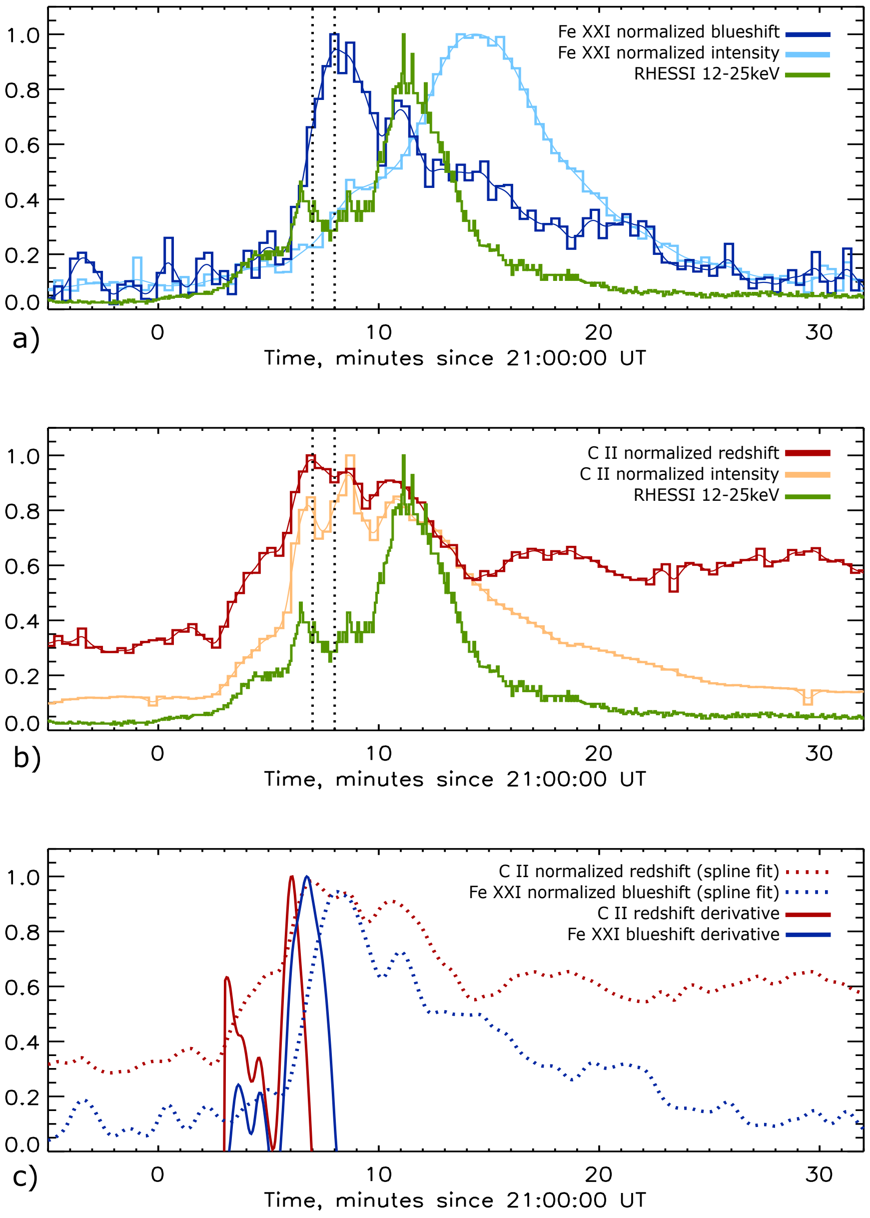

Figure 2.1 a) the time dependence of the integrated Fe XXI 1354.1Å line blueshift (dark blue) and its peak intensity (light blue), calculated from the line profile observed by IRIS and averaged over the flare region. Additionally, the RHESSI X-ray 12-25 keV flux (green) is shown. b) the time curves for the integrated C II 1334.5 Å line redshift (red) and its peak intensity (orange). The corresponding spline fits have the same color code and are shown by thin solid lines. Two vertical dotted lines indicate the strongest peaks of the Fe XXI and C II Doppler shifts. c) spline fits of the Fe XXI 1354.1Å line blueshift (blue dotted) and the C II 1334.5 Å line redshift (red dotted line). The normalized derivatives of splines are shown by solid curves of the same colors.

Source: [197].

Figure 2.1ab, are separated in time by about a minute, these curves started to rise almost simultaneously as one can see from the derivatives in Figure 2.1c. This is in a good correspondence with the expectations of the "thick-target" model, in which the chromosphere is heated by a beam of accelerated electrons. Two dotted vertical lines in Figures 2.1a,b correspond to the first peaks of the C II line redshift and Fe XXI line blueshift. One can see that the peak of the Fe XXI blueshift is delayed with respect to the C II line redshift for about one minute.

The typical values of the C II line redshifts are ∼30-50 km/s, and the typical blueshifts of the Fe XXI line are ∼50 km/s. In the previous paper [198] we mentioned that the evaporation process in this flare can be characterized as of the "gentle" type because of the subsonic velocities of the evaporated plasma [9]. However, the integrated redshift of the C II line (Figure 2.1) starts increasing at the beginning of the flare activity, which may be a sign of the explosive evaporation [67]. Figure 2.1 also reveals significant background steady plasma downflows obvious before and after the flare. Possibly, the evaporation in this region is very complex structured, and cannot be classified as a pure explosive or gentle type, according to the models.

2.3.2 Spatial Structure of Chromospheric Evaporation

The distribution of the Fe XXI 1354.1Å blueshift maximum delay relative to the C II 1334.5 Å redshift maximum across the flare region is demonstrated in Figure 2.2. The procedure which we have performed to measure the delays is described in Sec. 2. The result is presented in the form of the contour lines corresponding to the delays of 30 s, 60 s, 120 s and 240 s. The underlying IRIS 1330 Å slit-jaw (SJ) image is shown for better representation of the chromospheric activity.

As one can see, the delays distributed across the flare region can be longer than two minutes that is longer than the previously reported 1-minute delays [76, 17, 239]. The delays are distributed along the flare ribbon visible in the background IRIS 1330 Å

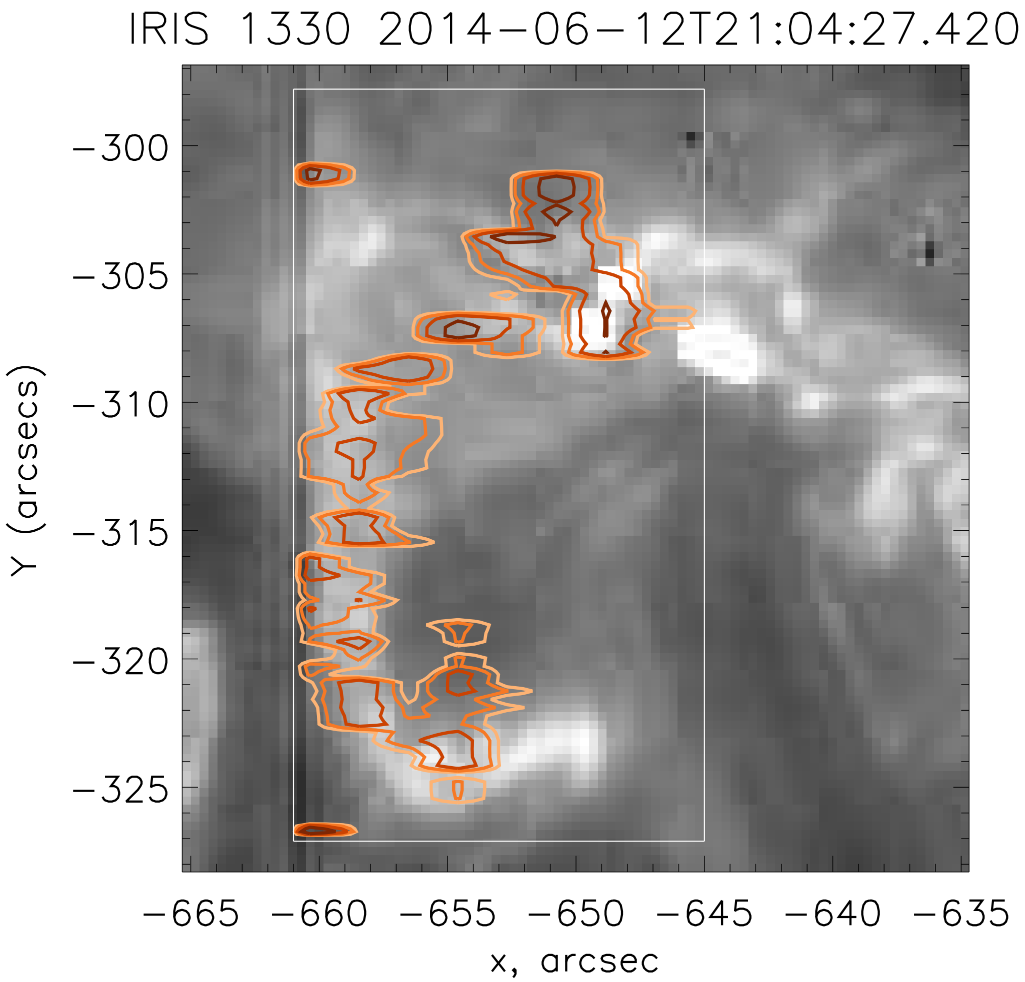

Figure 2.2 Distribution of the Fe XXI blueshift delays relative to the C II redshift maxima. The contour lines correspond to 30 s, 60 s, 120 s and 240 s delays (from light orange to dark red). Background is the corresponding IRIS 1330 Å SJ image. White rectangle marks the region covered by the IRIS spectral observations.

Source: [197].

SJ image, and are not uniform. Flare ribbons are thought to be closely connected to the magnetic field configuration in the region. In the standard flare model it is assumed that because of the deposit of energy of accelerated particles and heat flux along the flare loops, the plasma emission becomes stronger near the loop footpoints that becomes visible as the flare ribbons. Thus, we have decided to study the magnetic field properties in the region in order to better understand their relationship to the observed delay distribution.

2.3.3 Flare Process and Field Topology

For the magnetic field reconstruction, we use the NLFFF method [236] and vector magnetograms from HMI/SDO as the boundary conditions. Figure 2.3 represents the reconstructed magnetic field structure. In panel (a) this structure resembles the flux-rope which was observed in the GST images and reported by Sharykin et al. [209] and Kumar et al. [116]. The underlying grey-scale image represents the radial magnetic field (white for the positive and black for the negative polarity regions). As one can see, the field lines of the flux rope are twisted, reflecting a nonpotential nature of the magnetic field in the studied region with the currents embedded. This configuration is located exactly at the polarity inversion line (PIL). The detailed structure and dynamics of this region, which is likely to be the primary energy source for the flare, is discussed in a separate paper by Sharykin et al. [209].

Panels (b) and (c) of Figure 2.3 illustrate the reconstructed magnetic field structure and the flare ribbons observed in the IRIS SJ 1330 Å image. For better understanding the structure, only the magnetic field lines reaching a certain range of heights ($2''$-$6''$, or 1.5-4.5 Mm) are presented. The higher magnetic field lines have their footpoints far away from the flare ribbons, and thus do not participate in the energy transfer during the flare. The underlying image is the IRIS 1330 Å slit-jaw image for 21:04:43 UT. The field lines corresponding to the flux rope mentioned above

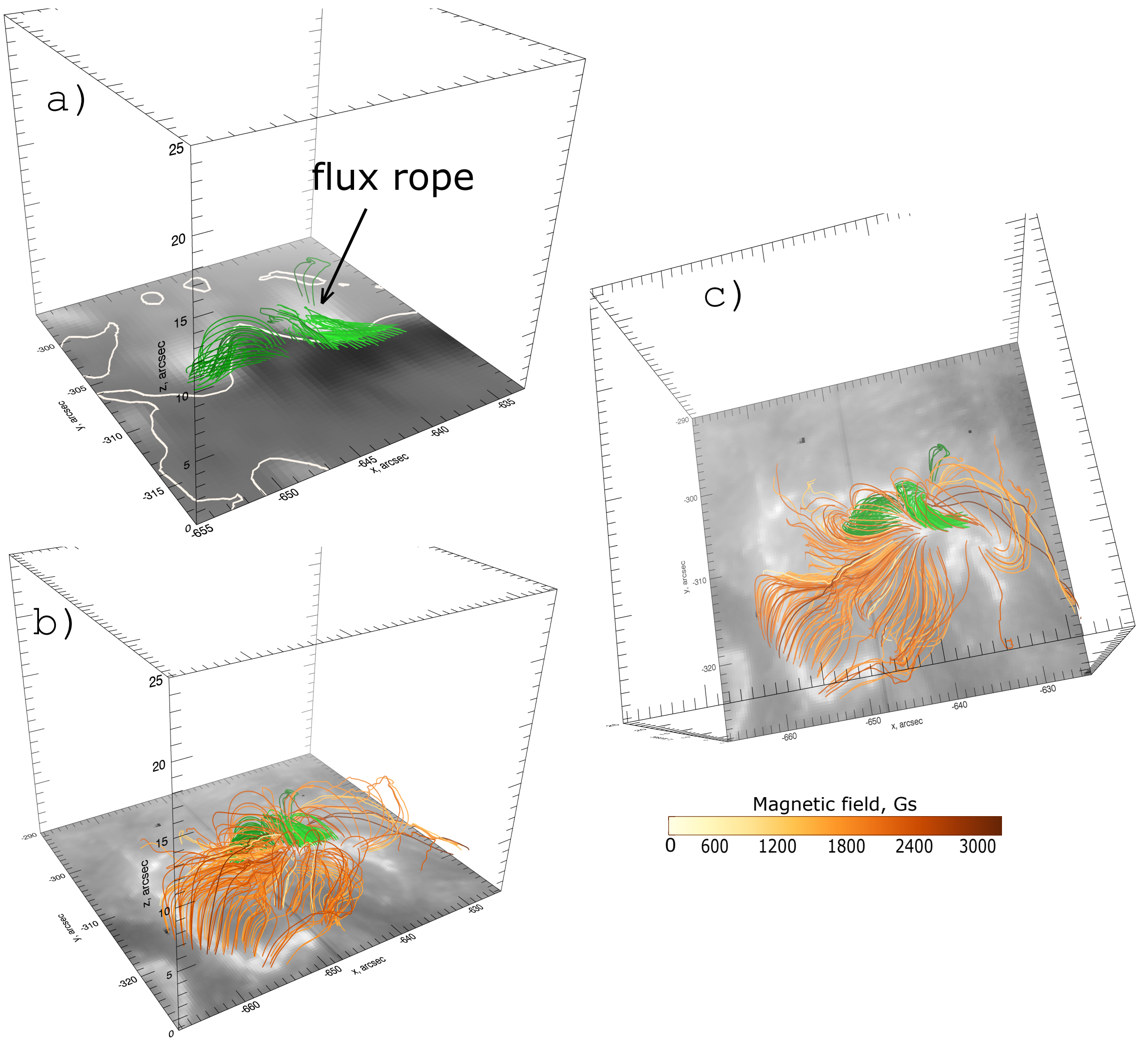

Figure 2.3 Reconstruction of the Nonlinear Force-Free magnetic field lines from the SDO/HMI vector magnetogram obtained at 20:58:25 UT. Panel a) shows the field lines (green) corresponding to the flux rope structure observed by GST [209]. The radial magnetic field map is shown in the background in the range [-2000,3200] G. The white line is the polarity inversion line (PIL). Panels b) and c) show two different projections of the field lines connecting the flare ribbons (orange) and the flux rope (green). The orange palette corresponds to the magnetic field strength in the start point (see the scale below the panel c)). The background is the IRIS 1330 Å SJ image (21:04:43 UT). Notice that the height of all displayed magnetic field lines is 2″-6″ (1.5-4.5 Mm).

Source: [197].

are shown in green in this figure. One can see that almost all the lines starting from the flare ribbons have their other footpoint near the flux rope region at the PIL.

One of the possibilities to understand changes of the magnetic field topology and its connection with the observed delays is to reconstruct the so-called Quasi-Separatrix Layer [52, 51, QSL]. We have already described the computational procedure in Sec. 2. It was found that the QSL evolves with height very smoothly. Thus, we decided to utilize the QSL at height of $\approx 1000\,\mathrm{km}$ above the photosphere, and calculated the squashing factor for the comparison.

The QSL structure presented in Figure 2.4 is mostly stable before (from 20:22:25 UT to 20:58:25 UT) and after (from 21:22:25 UT to 21:46:25 UT) the flare. However, during the flare impulsive phase the QSL undergoes significant changes in the region marked by the red dashed ellipse. The magnetic field neutral line also undergoes significant changes restricted to the marked region. Because of the 12 min integration time of the SDO/HMI vector magnetogram data, we cannot determine when exactly during the period from 21:04:25 UT to 21:16:25 UT the QSL evolved.

We compare the QSL chromospheric structure with the flare ribbons visible in the IRIS 1330 Å SJ images and the GST Hα line core images. The result is presented in Figure 2.5. The observing times are shown for each panel. One can notice a correspondence between the flare ribbons and the QSL cross-section. Also, the evolution of both the QSL and the flare ribbons (for both GST and IRIS observations) demonstrates similar patterns, confirming the idea that the flare energy transport along the QSL forms the flare ribbons [201, 140, 41].

To understand when exactly the evolution of the flare ribbons occurred, we studied the behavior of the Hα flare ribbon in more details. We found that the motions of the flare ribbon occurred during the period from 21:12 UT to 21:15 UT, i.e after the impulsive phase of the flare. This time interval is within the uncertainty interval determined for the QSL change (from 21:04:25 UT to 21:16:25 UT). Also, only

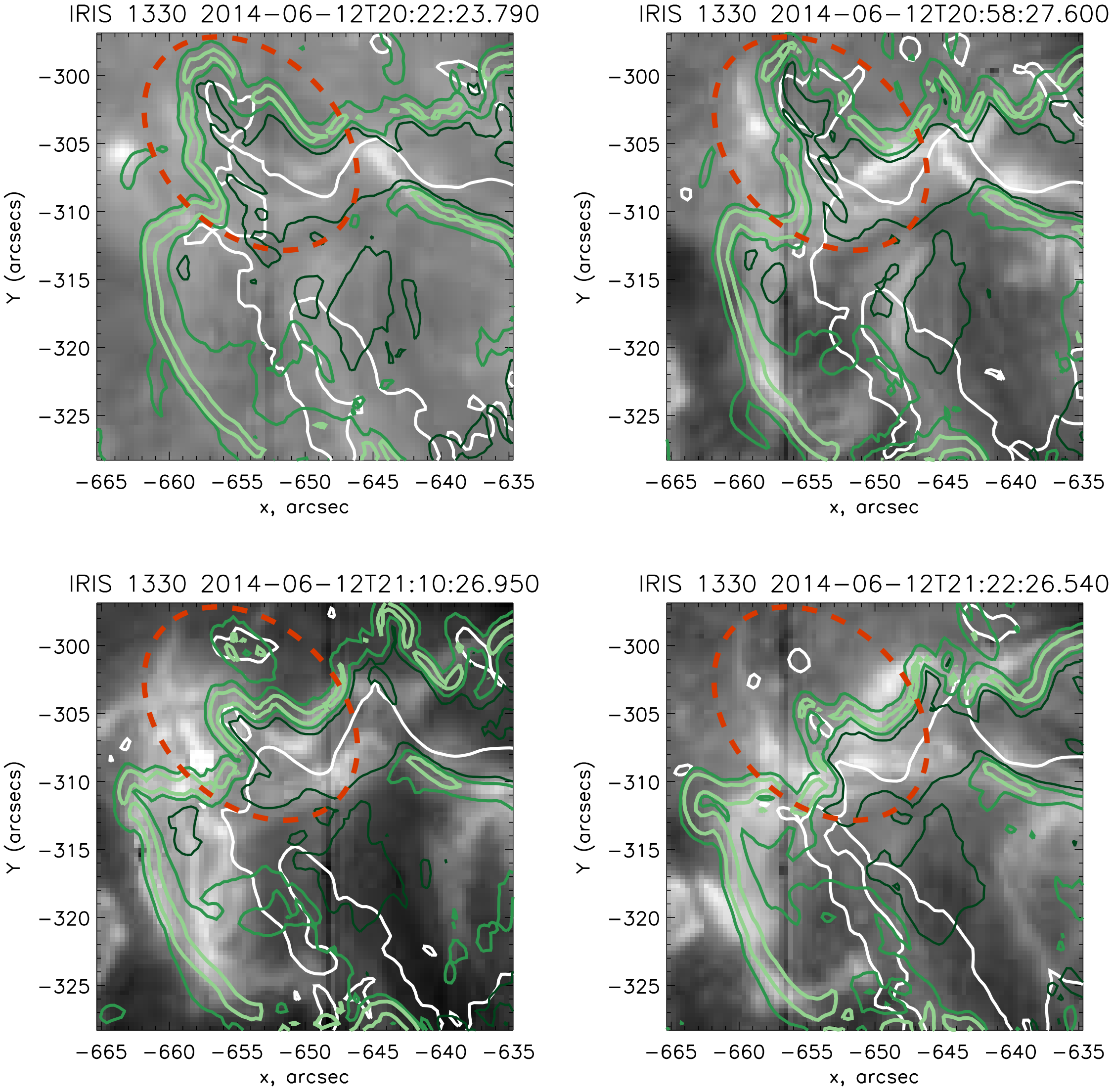

Figure 2.4 Evolution of the Quasi-Separatrix Layer (Squashing factor N, Eq. 2.1) at the chromospheric level. The panels represent the IRIS SJ 1330 Å images for four moments of time indicated in the panel titles with the overplotted contours of the Squashing factor corresponding to the 60%, 40% and 20% of its maximum value of ≈25 (from light to dark green). The magnetic filed is reconstructed from the HMI vector magnetograms for the same moments of time with a 12 min integration time. The white curve is the magnetic polarity inversion line (PIL). The dashed red ellipse marks the region where the changes of the QSL are the most significant.

Source: [197].

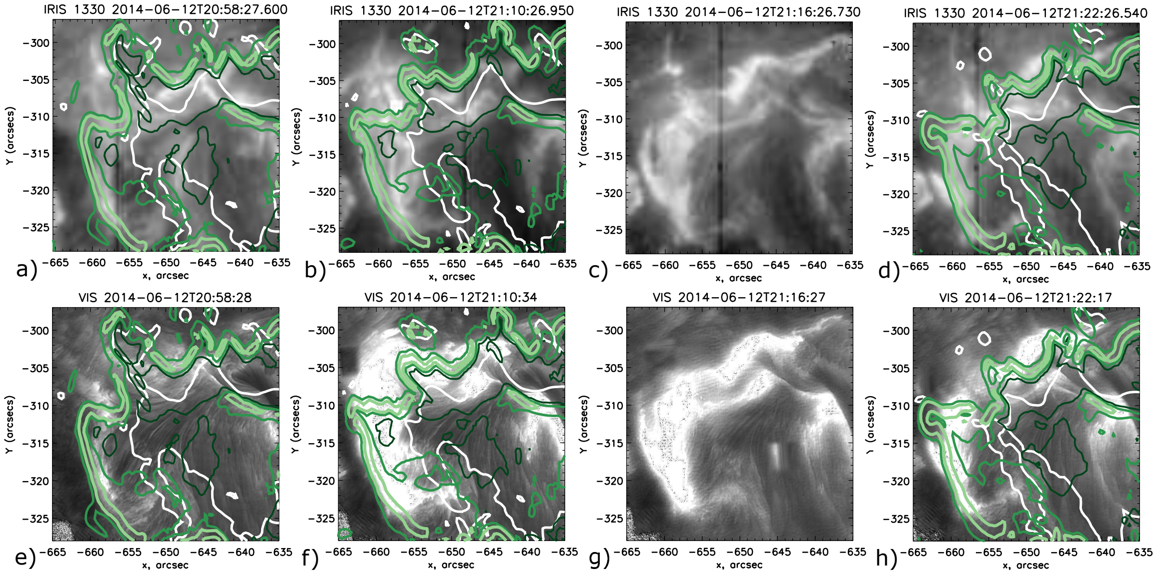

Figure 2.5 Comparison of the evolution of the QSL structure, UV flare ribbons observed by IRIS (top panels) and Hα ribbons observed by GST (bottom panels): before the flare at ≈20:58:30 UT (panels a and e); during the maximum phase at ≈21:10:30 UT (b and f), and at ≈21:16:30 UT (c and g); after the flare at ≈21:22:30 UT (d and h). The QSL chromospheric cross-section (Squashing factor N, Eq. 2.1) computed for the corresponding times is shown by green contours (the contour levels are the same as in Figure 2.4). The white curve is the magnetic polarity inversion line.

Source: [197].

the north-eastern part of the ribbon changed, the other parts were mostly stable (see Figure 2.5 g-h).

Figure 2.6 demonstrates the distribution of the delays across the flare region with the QSL chromospheric cross-section and the magnetic field lines originated from the delay regions. For convenience, only the field lines corresponding to the main arcade are plotted. The GST Hα-line core image is displayed in the background. Additionally, we plot the RHESSI 12-25 keV contours for different integration times in the same Figure. Similarly to Figure 2.3, the height of most of the field lines does not exceed 4.5 Mm (or $6''$). So, the lines connecting the flux rope site and the delay regions do not extend high into the solar corona. The RHESSI 12-25 keV sources evolve along the reconstructed arcade with time as illustrated in Figure 2.6b,c. For 21:04:00 UT - 21:05:40 UT the primary source is located near the flux rope region (solid contours in Figure 2.6b), while at 21:05:40 UT - 21:06:16 UT it appears closer to the southeastern part of the flare ribbon (dashed contours). The X-ray sources do not match the flare ribbons and arcade footpoints. During the further periods, shown in Figure 2.6c, the X-ray source is slightly moving towards the top of the arcade, and becomes more diffuse. Perhaps, it represents the emission of the hot evaporated plasma. Thus, from the observations, we cannot confirm that the chromospheric evaporation observed in the flare ribbons is caused by the accelerated electrons, as predicted by the standard model. Unfortunately, the flux above 25 keV does not allow us to analyze higher energy sources.

2.4 Discussion and Conclusion

In this project we studied the chromospheric evaporation event during the M 1.0 GOES class flare occurred on June 12, 2014 from 21:01 UT till 21:19 UT. The evaporated plasma flows were detected in the hot Fe XXI 1354.1 Å line, and the response of the "colder" layers was studied with the help of the lower transition

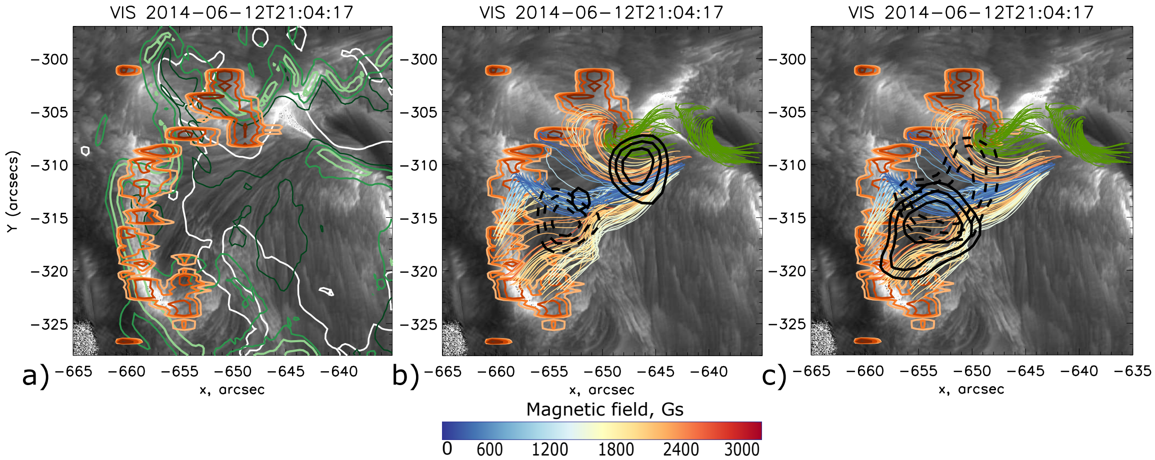

Figure 2.6 (a) The Fe XXI blueshift delays relative to the C II redshift maxima shown by contour lines for 30 s, 60 s, 120 s and 240 s (from light orange to dark red), and the QSL chromospheric Squashing factor before the flare (for 20:58:25 UT) shown by green contours (the contour levels are the same as in Figure 2.4). The GST Hα line core image is shown in the background in all panels. The white curve represents the PIL. (b) The reconstructed magnetic field lines with the starting footpoints in the delay regions. The line colors correspond to the magnetic field magnitude at the starting point (see the scale below the panels). The field lines corresponding to the flux rope (see Figure 2.3) are plotted in green. Additionally, the RHESSI 12-25 keV X-ray sources for the 21:04:00 UT - 21:05:40 UT (solid) and 21:05:40 UT - 21:06:16 UT (dashed) time periods are plotted by level contours corresponding to the 90%, 80% and 70% of their maxima. (c) the same as b) for RHESSI 12-25 kev 21:06:24 UT - 21:07:48 UT (solid) and 21:07:48 UT - 21:09:12 UT (dashed) time periods.

Source: [197].

region C II 1334.5 Å line. The main focus was on the distribution of the chromospheric evaporation delay time between the C II Doppler shift maximum and the Fe XXI blueshift maximum. In addition, the magnetic field lines were reconstructed from the photospheric vector magnetograms, and the QSL was computed and compared with the flare ribbons. Let us summarize the main observational findings mentioned in this study:

1. The averaged over the region C II redshift presented in Figure 2.1 is correlated with the flare activity observed in the X-ray 12-25 keV energy range. The onsets of the Fe XXI blueshift and the C II redshift are almost simultaneous. The Fe XXI blueshift maximum is delayed relative to the C II redshift maximum for about 1 min.
2. The detailed spatially-resolved study demonstrates that the delays are presented in many points along the flare ribbon, and in some places can be longer than 2 min (see Figure 2.2). The distribution of the delays across the initially-observed flare ribbon (in both IRIS 1330 Å and GST Hα line core observations) is not uniform.
3. The reconstructed magnetic field lines originating from the delay regions mostly connect the flare ribbon with the flux rope structure. The height of the magnetic arcades rarely exceeds 4.5 Mm, revealing their low-lying nature.
4. The X-ray 12-25 keV sources demonstrate a dynamic behavior along the main bundle of the reconstructed field lines. Initially located near the flux rope region, the sources later appear closer to the southeast flare ribbons, and then move towards the top of the reconstructed arcade (Figure 2.6b,c).
5. The evolution of the QSL and flare ribbons detected in the 1330 Å and Hα line core images demonstrate the same patterns: a mostly stable configuration with a rapid change in the North-East part of the region. This region is the only one along the initial QSL where the delays were not detected due to the weak Fe XXI signal.

The spatio-temporal properties of the chromospheric evaporation reveal very strong delays of the blueshift of the hot evaporating plasma relative to the redshifts of the cold chromospheric plasma across the flare region. While the averaged over the region blueshift of the Fe XXI line (see Figure 2.1) demonstrates the delay for about 1 min, the spatially-resolved delays are found to be even more than 2 min in several zones along the flare ribbon. Thus, the delay averaged over the region represents itself the superposition of many spatially-distributed delays occurred in different zones and caused by the excitation of the chromospheric evaporation process in different loops. In this sense, the observed situation corresponds to the "multi-thread" model [233] proposing a sequence of independently heated threads occurred in different loops. As it is clearly seen from our previous work [198], the chromospheric excitation took place in different points across the region at different times. And thus it is not surprising that we have found the same kind of behavior for the delays. A "multi-thread" model was considered for the chromospheric evaporation studies in the work of Rubio da Costa et al. [183], where the authors used the RADYN code and superposition of evaporation events occurred in several loops at different times to adequately model the observed signals.

The reconstructed magnetic field geometry also corresponds to the multi-thread model but reveals an interesting complex configuration. As was observed from Figure 2.3, the magnetic configuration of the region represents twisted small-scale system of loops constructing a magnetic flux rope located at the polarity inversion line, and a bundle of more large-scale magnetic field lines with one footpoint located near the flux rope and the other footpoint located in the flare ribbons, i.e., connecting the flare ribbons and evaporating regions with the flux rope. This magnetic flux rope was studied in more details in the paper of Sharykin et al. [209]. One of the conclusions was that the dissipation processes in this region can be the primary energy source for this flare. It is obvious from the reconstructed magnetic field configuration that accelerated particles and heat flux can spread from the flux rope region to the observed flare ribbons along the field lines. Injections of the particles and heat flux into different loops produce the chromospheric evaporation in different spatial zones as we find in the observations. Thus, the flux rope region at the polarity inversion line may play a role of the "energy source" for the event.

It was found that almost all the magnetic field lines connecting the blueshift delay regions with the flux rope are low-lying (see Figure 2.6). Their height rarely exceeds 4.5 Mm, thus, these loops mainly do not expand high into the corona. This means that all the delays were observed in the low-lying loops. The delays are non-uniformly distributed along the flare ribbon (upper panel of Figure 2.6), but without any obvious patterns. One of the possible explanations of the delays based on the non-equilibrium ionization of the highly-ionized Fe atoms [17, 26, 76] was discussed in the introduction. The results presented in Figures 6-8 of Bradshaw [26] show that the Fe XIX ion population reaches equilibrium for the considered durations of the heating phase (up to 60 s), but the Fe XXIV ions are out of equilibrium with a low population. There are no results presented for Fe XXI, and it is hard to understand how the Fe XXI ion population behaves during the heating phase. However, the highly ionized Fe fractions (including Fe XIX and Fe XXIV) are in the equilibrium conditions during the thermal conductive cooling phase. The non-equilibrium ionization explanation of delays becomes suitable only in the case of very long continuous heating (for more than 2 min). This may contradict to the impulsive nature of solar flares. The strong growth of the C II intensity light curve in Figure 2.1, and results presented in Figure 7 of Sadykov et al. [198] support the idea that the chromosphere heating was impulsive. Thus, the non-equilibrium ionization mechanism may be partly, but not fully responsible for the observed delays.

The only region where the delays are not present or not possible to calculate is a part of the flare ribbon located in the upper left corner of Figure 2.6. Figures 2.4 and 2.5 clearly show that this region is the only one where a rapid motion of the flare ribbon and the QSL chromospheric cross-section was observed. We looked at the spectra of this region in detail and revealed the following: the C II redshift was significant, but the weak signal in the Fe XXI line made it impossible to measure the delay. As shown in panels a, d, e and h of Figure 2.5, the computed QSL cross-section fits the observed flare ribbons quite accurately before and after the impulsive phase of the flare. Thus, one can assume that the QSL evolved at the same time as the flare ribbons — i.e., from 21:12 UT to 21:16 UT. The first 12-25 keV X-ray pulse occurred at ∼21:06 UT (the first 12-25 keV peak corresponds to the first peak in the C II integrated light curve in Figure 2.1). However, at the time when the flare ribbon motion was observed, the 12-25 keV curve, as well as the C II integrated light curves, shows the decay phase. It could be that the motion of the flare ribbons corresponds to the process called "slipping magnetic reconnection" [90, 13]. This model is quite new but already found observational evidences [128, 89]. On the other hand, it seems that the studied flare was not driven by the slipping magnetic reconnection mechanism. Despite that the ribbon motion was observed, it occurred definitely after the impulsive phase of the flare. Even if the slipping mechanism was responsible for this motion, it happened after the impulsive phase and could not support the idea that the flare energy was released by this mechanism.

Of course, the found relationship between the chromospheric evaporation delays and the magnetic field configuration is based only on one studied event. Further statistical study is needed to confirm the proposed dependences.

CHAPTER 3

INTERACTIVE MULTI-INSTRUMENT DATABASE OF SOLAR FLARES

3.1 Introduction

Flare events are observed by a variety of space- and ground-based instruments in different wavelengths. Usually, flare lists are created for specific routinely-observing instruments. Currently, the primary flare catalog is based on soft X-ray emission peaks (so-called X-ray flare classes) observed by the Geostationary Operational Environmental Satellites [23, GOES]. The GOES X-ray instruments have observed the solar activity for several decades, and created the largest database of solar flares. Another example of flare-observing instruments is the Reuven Ramaty High Energy Solar Spectroscopic Imager [131, RHESSI], launched in 2002. RHESSI observes the X-ray radiation of flares in a wide range of energies, from $6\,\mathrm{keV}$ to $>300\,\mathrm{keV}$. The satellite detects the events and has its own flare list separate from the GOES flare list. Two instruments onboard the Solar Dynamics Observatory (SDO) observe solar flares in EUV bands: the Extreme Ultraviolet Variability Experiment instrument [238, EVE] observes the EUV spectra of the integrated solar emission, and the Atmospheric Imaging Assembly [125, AIA] instrument observes high-resolution images in several EUV bands. The flare data from both of these instruments are stored in independent data catalogs. In the EVE data, the flares are detected as enhancement of the EUV emission, and in the AIA data, the flare events are detected using image processing algorithms [138] and are summarized in the Heliophysics Event Knowledgebase [88]. Some of these events are linked to the GOES database.

The Virtual Solar Observatory (VSO, `http://sdac.virtualsolar.org/cgi/search`, accessed on 04/08/2019) collects and accesses metadata from many space missions and ground-based observatories, allowing the user to search for available data for a particular time range. It also contains several flare and flare-related event catalogs (SOHO/LASCO CME catalog, GOES X-ray Catalog, RHESSI Flare list etc.) The user can search the events having particular properties within each catalog, and request the corresponding data. However, VSO does not allow a detailed search based on flare parameters. The RHESSI browser (`http://sprg.ssl.berkeley.edu/~tohban/browser/`, accessed on 04/08/2019) allows users to look at RHESSI and Fermi data products, and to check the observational coverage of the detected flare events by the Hinode and IRIS satellites. On the other hand, this browser does not provide the ability to search for flares having particular properties.

Many problems of flare physics require performing analyses using data from a particular set of instruments, or/and for a sample of flares with particular characteristics. For example, find all events having GOES class $\geq$ C5.0 that were observed by RHESSI, or find the flares observed by the IRIS satellite in the EUV range, and by the Nobeyama radio telescope, in the microwave range. To address this type of problems, we developed a new interactive multi-instrument database of solar flares.

This is not the first attempt to provide flare lists or event catalogs. For example, the Owens Valley Solar Array [87, 73, OVSA] legacy radio bursts database [157] allows for the searching of events based on their physical parameter ranges, and the Solar Flare Finder tool [150, `http://hesperia.gsfc.nasa.gov/sff/`, accessed on 04/08/2019], recently developed as a part of Solar SoftWare package for Interactive Data Language [69, SSW IDL], allows selecting flaring events simultaneously observed by GOES, RHESSI, SDO/AIA, Hinode, SDO/EVE and IRIS, and to see their data summaries. However there is still room for a comprehensive solution that could include features such as implementing user-interactive filters, providing more convenient representation of the output set of events and improving the accessibility of the data by providing a search tool with minimum software requirements. We provide these and other new features in our newly developed database.

Figure 3.1 represents the basic structure of the database, and each block of this Figure is explained in the following sections of this study. In Sec. 3.2, we describe the flare and flare-related event lists, as well as actual data, which serve as daily input for our database. In Sec. 3.3, we explain the daily processing of the event lists and data: integration of the flares from different lists, calculation of additional event descriptors, preparation (smoothing) of the light curves. The processed data are stored in a MySQL database allowing convenient and fast interaction. In Sec. 3.4, we describe the web interface, the structure and logic of queries for our database, and the structure of the output data available to the user. A query example is also presented in this section. We present our conclusions in Sec. 3.5.

3.2 Data Collection and Storage

In this Section, we describe the catalogs of events used as inputs. The complete and up-to-date list of the integrated event sources can be found via the link `https://solarflare.njit.edu/datasources.html` (accessed on 04/08/2019), and the current list is summarized in Table 3.1.

3.2.1 Primary Event Lists

The event lists are divided in “primary” and “secondary”. The primary event lists represent daily-updated lists of flares independently detected by GOES, RHESSI and SDO/AIA instruments. The secondary lists include partial flare lists, representing subsets of the primary lists, and catalogs of flare-related phenomena (such as Filament eruptions or CMEs).

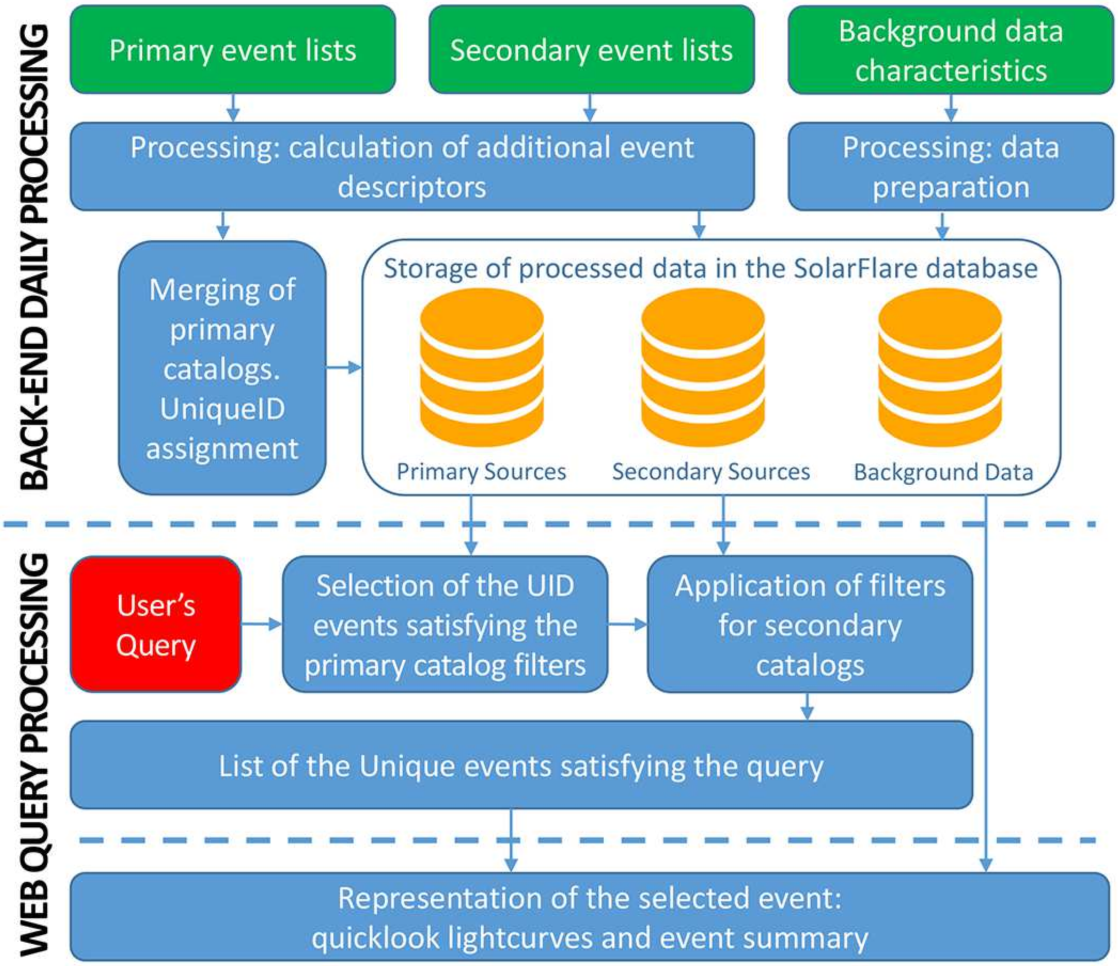

Figure 3.1 Schematic representation of the Interactive Multi-Instrument Database of Solar Flares (IMIDSF). The database stores the metadata from GOES, RHESSI, SDO, SOHO, Hinode, IRIS, Fermi and other space- and ground-based instruments, as well as some instrument-specific light curves.

Source: [194].

Table 3.1 Event Catalogs Implemented in the Interactive Multi-Instrument Database of Solar Flares (https://solarflare.njit.edu/)

Source Name	Dates presented	Source web link
Primary flare lists		
GOES flare list	Jan, 2002 — current time	`ftp://ftp.swpc.noaa.gov/pub/warehouse/`
RHESSI flare list	Feb, 2002 — current time	`http://hesperia.gsfc.nasa.gov/hessidata/dbase/`
HEK flare list	Feb, 2010 — current time	`https://www.lmsal.com/isolsearch`
Secondary event catalogs		
IRIS observing logs	Jul, 2013 — current time	`http://iris.lmsal.com/search/`
Hinode flare catalog	Nov, 2006 — July, 2016	`http://st4a.stelab.nagoya-u.ac.jp/hinode_flare/`
Fermi GBM flare catalog	Nov, 2008 — current time	`https://hesperia.gsfc.nasa.gov/fermi/gbm/qlook/`
Nobeyama coverage check	Jan, 2010 — current time	`ftp://solar-pub.nao.ac.jp/pub/nsro/norp/xdr/`
OVSA flare catalog	Jan, 2002 — Dec, 2003	`http://www.ovsa.njit.edu/data/`
CACTus CME catalog	Jan, 2002 — current time	`http://sidc.oma.be/cactus/`
Filament eruption catalog	Apr, 2010 — Oct, 2014	`http://aia.cfa.harvard.edu/filament/`
Konus-Wind flare catalog	Jan, 2002 — Jul, 2016	`http://www.ioffe.ru/LEA/Solar/index.html`

Source: [194]

Each event in the primary lists is characterized by start, peak, and end times. In most cases, the event coordinates and the associated active region number are also reported. We use three primary event catalogs:

- *GOES flare list.* The daily lists of events observed by the GOES satellites in the 1-8 Å channel are available from June 2002 to present. The reported characteristics include the GOES class, the X-ray peak flux during the event, and the information about the active region and coordinates of the event (not for all events). The daily lists are available at the NOAA website.
- *RHESSI flare list.* The list of the flares observed by the RHESSI X-ray telescope from February 2002 to present. Besides the usual descriptors (the flare times and position), the catalog contains the highest energy band in which the flares were observed, the number of counts during the flares, and a variety of observational quality flags.
- *HEK SDO/AIA event list.* The events detected in the EUV images from the AIA/SDO instrument from February 2010 to present. The events reported in this catalog are characterized by a variety of different parameters (besides the common ones): the wavelength in which the event was detected, the coordinates in a variety of coordinate systems, peak fluxes, web links to quick-look images and movies, etc.

These three primary event lists are integrated into a single database, and Unique Identifiers (UniqueID) are prescribed for each event, as discussed in Sec. 3.3.

3.2.2 Secondary Event Sources.

In addition to the primary event lists, the following secondary data sources are integrated in our catalog:

- *The Interface Region Imaging Spectrograph data* [50, IRIS]. IRIS obtains the slit-jaw UV images, as well as spectra of the Sun. The flare events are associated with IRIS observations based on the time and pointing stored in the form of instrument observing logs. The quicklook data web links allow the users to select the events of interest.
- *Hinode flare catalog* [235]. The original catalog includes the events from the GOES flare list observed by the Hinode spacecraft. This catalog includes the

availability of observations for each Hinode instrument, and quicklook data links.

- *Fermi Gamma-ray Burst Monitor [146, GBM] solar flare catalog.* The list of the flares observed by the Fermi GBM in the 8 keV-40 MeV energy range from November 2008 to present. This catalog includes duration of the observed flares and number of counts during the flares.
- *Nobeyama Radio-polarimeter light curves [153].* The polarimetric measurements from Nobeyama Radio Observatory are available for almost every day, usually approximately 8 hours per day.
- *OVSA legacy flare catalog* [157], which includes short-time summaries of events observed by the Ovens Valley Solar Array in the 1-18 GHz microwave range, from 2001 to 2003 only.
- *Computer Aided CME Tracking (CACTus) catalog* [179, 180]. This catalog collects records of CMEs detected by the LASCO/SOHO coronograph, and contains a variety of CME properties, including the onset time, principal angle, velocity, etc. The CME-flare event matching algorithm currently implemented in our database is based on the following rule: the recorded CME onset time must lie in an predefined time interval relative to the flare start and end times, which can be interactively adjusted by the user by means of a “Search time interval” filter.
- *Filament eruption catalog* [142]. The filament-flare event matching is based on the time and position of the eruptions. A variety of filament parameters are available. The catalog production was stopped on Oct, 19, 2014.
- *Konus-Wind flare catalog* [10, 159]. The original catalog includes the events from the GOES flare list observed by the Konus-Wind spacecraft.

Our database is designed in such a way that it can support a continuously expanding number of input sources of different types. These include flare and flare-related event catalogs, and information about the observational coverage by different instruments.

3.2.3 Background Data Characteristics

The aim of the developed database is not only to collect and integrate the flare records from different sources, but also to provide users with an overview of the events they potentially want to study. The flare catalogs themselves already contain many useful quicklook links. For example, each HEK flare record contains the links to the quicklook movies and images obtained by AIA/SDO. Our approach is to contribute to the flare overview, and present additional data for each selected event.

Here is the summary of the time plots we provide for each event (if covered by the instrument):

- *GOES X-ray light curves* (two channels 0.5-4 Å and 1-8 Å).
- *Temperature and Emission Measure determined from the GOES X-ray data in a one-temperature approximation.*
- *SDO/EVE ESP light curves* (four diode channels: 18 nm, 26 nm, 30 nm, 36 nm).
- *Nobeyama Polarimeter data* (six frequency bands, two polarizations: 1 GHz, 2 GHz, 3.75 GHz, 9.4 GHz, 17 GHz, 35 GHz, I and V polarizations for each frequency).

Each of the described sources is updated daily. The Temperature (T) and Emission Measure (EM) for the events are computed using the Temperature and Emission measure-Based Background Subtraction Algorithm [187, TEBBS] described in Section 3.3. For the SDO/EVE ESP light curves, we apply 10-second averaging in order to obtain smoother profiles. The same approach is used for the Nobeyama Polarimeter data. These characteristics which help describe the flare evolution, may provide useful information for selecting particular events for further detailed studies.

3.2.4 Data Storage and Queries

For quick access to the flare catalog information and other metadata derived from the observational data, we store the information in a MySQL database. Each catalog is created as a separate relation, and proper indexes are created to speed up the search. A web interface allows the user to query and visualize the results. A query can take from several seconds (for a typical one-month time period) to several minutes (for the entire time period and no active filters).

3.3 Data Enrichment and Processing

Besides the routine daily updates of the event lists, we perform additional processing to enrich the original data. First, we calculate physical descriptors of the events (coordinates, Temperature and Emission Measure peaks and their times for GOES events) which are in addition to the descriptors already stored in the original lists. Second, we match each event from each primary list with its counterparts in other primary lists, and assign a unique identifier (UniqueID) for each uniquely-matched case. These procedures are described in this section.

3.3.1 Determination of Coordinates for the GOES Events

The GOES flare list reports the events detected from the integrated X-ray light curves and includes coordinates only for some events. However, in most cases, the NOAA active region number where the flare occurred is known and reported in the list, but without its coordinates. To estimate the coordinates of the event based on the active region number, we utilize the Solar Region Summary (SRS) files. Such files are formed every day half-an-hour after midnight and report the current active regions, and their locations at 00:00 UT. Using these angular coordinates, we compute the position of the active region at the flare start time, assuming the Carrington rotation period $T \approx 27.3$ days, and taking into account the variations of the solar radius with time as a function of the Earth's position in its orbit.

3.3.2 Temperature and Emission Measure for GOES Events

Important physical properties derived from the GOES X-ray observations are Temperature (T) and Emission Measure (EM) [219, 237]. These parameters can be defined for each moment of time, and provide T and EM profiles for every flare. In our database, we characterize flares by the peak values of these parameters (T_{max} and EM_{max}), as well as by the times when these peak values are reached. To remove the background (non-flare) X-ray flux, we use the Temperature and Emission measure Based Background Subtraction (TEBBS) algorithm, initially proposed by Bornmann [22] and improved by Ryan et al. [187] based on the assumption that T and EM must grow during the flare impulsive phase. We have implemented in our database the algorithm proposed by Ryan et al. [187]. The corresponding GitHub repository is available for public access: `https://github.com/vsadykov/TEBBS.git` (accessed on 04/08/2019)

As mentioned above, the algorithm receives all the physically-possible combinations of the background level, which provide growing T and EM curves after the flare start time. For each of these curves, we calculate the T and EM maximum values during the flare. The range of these values defines the physical interval for T_{max} and EM_{max}. To obtain "the best" curve representing the T and EM dynamics, we simultaneously minimize the deviation from the T_{max} and EM_{max} median values for all curves, and choose the one corresponding to the minimum mean deviation. For the best estimate curve, we compute T_{max} and EM_{max}, and the corresponding time moments, and store them in our database, together with the possible physical intervals of T_{max} and EM_{max}. An example of the TEBBS calculations for a C3.9 class flare is presented in Figure 3.2.

3.3.3 UniqueID Assignment and Relation to the SOL ID

The three "primary" catalogs (GOES, RHESSI and HEK flare lists) of the database are updated on daily basis. For every new flare event, we assign the Unique Identifiers (UniqueIDs) by integrating the information from these three different sources.

Each of the "primary" catalogs reports the events with the known start, peak, and end times. Also, the information about the event coordinates is provided or calculated as described above. This information is used to determine if the entries in

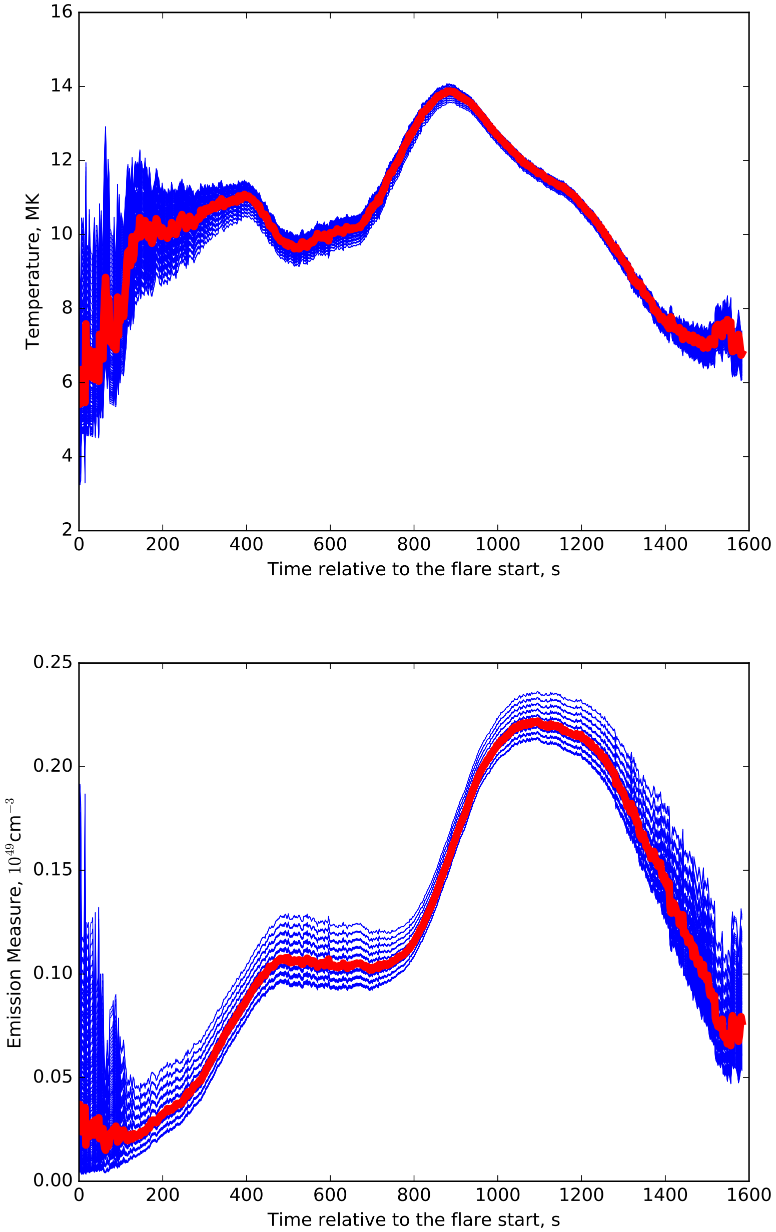

Figure 3.2 Example of the Temperature (top panel) and Emission Measure (bottom panel) calculations using the TEBBS algorithm for the SOL2016-02-15T04:02:00 event (C3.9 class flare). The blue curves represent the physically possible Temperature and Emission Measure solutions. The red lightcurves represent the best-estimate solution. *Source:* [194].

these catalogs represent the same physical phenomenon, i.e., they happened at the same time in the same place, or they belong to different events.

For assigning the UniqueID, we introduce the following hierarchy order: NOAA GOES, RHESSI, and the HEK flare list. This order means the following: if a flare event is reported by GOES, then it labeled as a GOES event ("gev"). If an event is not in the GOES catalog, but reported by RHESSI, this event is labeled as a RHESSI event ("rhessi"). If an event is not reported by GOES and RHESSI, but recorded as a flare in the HEK database, this is labeled as a HEK event ("hek"). The UniqueID consists of two parts: the name of the primary instrument that observed the flare, and its start time. For example, the GOES event observed at "yyyy-mm-dd hh:mm" gets the UniqueID "gev_yyyymmdd_hhmm00", while the RHESSI or HEK events are labeled "rhessi_yyyymmdd_hhmmss" and "hek_yyyymmdd_hhmmss" respectively (we add "00" to the GOES event UniqueIDs for compatibility with the UniqueIDs from other catalogs). In the case of events with the same start time but different locations (which was found for some HEK event only), we assign the UniqueID "hek_yyyymmdd_hhmmss_i", where "i" is an increasing integer, starting from 1 for each such case. The advantage of the event ID assignment procedure we adopted is that this classification can be easily extended for any number of flare-reporting instruments.

The procedure of the UniqueID assignment is the following:

1. Query GOES flare list events for their coordinates and active region numbers. Then, sort the events according to their GOES X-ray class in the descending order. For each event (hereafter parental event) assign "gev_yyyymmdd_hhmmss" UniqueID according to the event. Then,

   a) For each "gev" event, find all events in the RHESSI and HEK flare catalogs overlapping in time, from the start to end times, and obtain their coordinates and active regions. This is a list of candidate events corresponding to the parental event.

b) For each candidate event compare the coordinates and active regions with the parent event. The events are assigned the same UniqueID as the parent event if they have the same active regions and their location differs by no more than $\delta = 250''$. This value was chosen experimentally, and it is approximately equal to the size of a large active region. If one of the compared events (parental or candidate) has coordinate or/and active region information missing, the corresponding condition is assumed to be satisfied.

2. Repeat the procedure for the events for which the UniqueID is still not assigned, using the RHESSI flare catalog. These events are sorted according to their energy range and their UniqueIDs are assigned ("rhessi_yyyymmdd_hhmmss").
3. Repeat the procedure for the remaining set of events for which the UniqueID is still not assigned, using the HEK register. The HEK register contains events overlapping in time (for example, reported for different SDO/AIA channels, or from different locations), thus the matching procedure is still needed. For the matched events, assign UniqueIDs "hek_yyyymmdd_hhmmss_i", where "i" represents a discriminatory index assigned only to those events characterized by the same start time but different locations.

The procedure of the UniqueID assignment for new events is repeated on a daily basis. Nevertheless, a complication may happen if one of the events is reported with a delay of one day or more. If this is the case, the UniqueIDs of the events overlapping with such delayed events are deleted, and the UniqueID assignment starts for all the events with empty UniqueIDs.

The same UniqueID may be defined for several GOES, HEK and RHESSI events. For all such overlapping, we keep the maximum and minimum values for each of the coordinates among all the matched events.

The last thing needed to be mentioned is how our UniqueIDs correspond to other event IDs. The Solar Object Locator (SOL), which in its simplest form contains only the event time, is one of the widely-used identifiers. Because it is not documented whether the event time should correspond to the start, peak or end time, although, for display purposes, we use the flare start time as a default reference time, but we also assign and maintain in the database the correspondence between our UniqueID and these three possible versions of the SOL IDs.

3.4 Query Structure and Processing

In this chapter, we discuss the structure of the query engine. This engine is the most important software component for the construction of the Web Application, because it should be efficient, fast, and user-friendly. The current implementation retrieves and displays the final list of events in a convenient form, works fast, and it is constructed in such a way that adding new catalogs does not require changing the code structure.

To perform a query, the user needs to fill the request form in the Web Application site: a web request form available at `https://solarflare.njit.edu/webapp.html` (accessed on 04/08/2019). In the request form, the user selects the desired time interval (including the ability to select the whole time range, starting from January 1st, 2002), select the position of the event on the solar disk, apply instrument-specific filters such as event availability of the uniquely-matched events in different catalogs, as well as ranges of various physical parameters, and executes the query by pressing the submit button. Alternatively, the user can load previously saved query result.

3.4.1 Primary Catalogs, Filters and Appearance of the Additional Fields

The "primary" flare catalogs (GOES, RHESSI and HEK flare records) are updated on a daily basis and have the flare records detected by their own algorithms. The descriptors of the primary catalogs are displayed independent of the user's selection of filters. For example, if the user is searching for all events listed in the RHESSI flare catalog, the output may have empty GOES or HEK fields. All fields will be populated only if the data availability filters in "primary" catalogs are selected.

The on-the-fly generation of additional search fields corresponding to specific event descriptors for the other catalogs depends upon user selection. For example, let us consider the case of a user looking for the events listed in the Hinode catalog. In such cases, the descriptor fields related to the Hinode catalog (number of observed frames, corresponding quicklook link etc.) will appear in the final table, as additional columns. This strategy allows us to make the tables as short and informative as possible based on the user's query. Almost each of the parameter fields may be tuned during the query: the filters allow not only the ability to check the appearance of the event in a certain catalog, but also to select events having particular physical characteristics.

The initially-constructed table (based on the primary catalogs) is the backbone for the query: we simply discard from this table the event records which do not pass additionally selected filters. This allows us to check the selected filters one by one, without pulling them into one large query. This structure has one more advantage: we can add the filters for new-uploaded catalogs/lists without disturbing the working system. Adding of a new event table would just require a new independent block in the query engine.

The final result of a query is presented in the form of a web table with moving headers. One can simply drag the table to the right to see various characteristics of the events. For better performance, we currently restrict the number of events appearing in the table to 1000. However, the full lists of events are available for downloading in the output file, which can be saved locally and reloaded anytime. We also added the possibility to sort the output table according to the flare characteristics. The sorting procedure represents another query to the server and includes all events, even if the number of events exceeds 1000. The user has the option to download the output table. In order to simplify the processing of the output file, we created a Python parser which reads the table and creates the structure corresponding to the events.

3.4.2 Detailed Visualization of a Selected Event

The main purpose of the created database is to integrate the entries from different catalogs, and to present a complete list of events satisfying a set of conditions specified by the user. However, from a practical perspective, it is very important to have a brief look at the event data, and decide whether a particular event is interesting for a case study or not. For this purpose, we created the ability to look at the event light curves derived from different instruments. To proceed into the event page, one needs to select the event of interest from the summary table retrieved in the previous stage, and click the "Plot Data" button.

The main elements of this event page are the two dynamic graphs reflecting the behavior of several event light curves: X-ray fluxes, Temperature and Emission Measure calculated for the GOES data using the TEBBS algorithm, light curves from the SDO/EVE/ESP instrument, and the Nobeyama Radio Polarimeter fluxes. The user can select which plot to display, and scale it accordingly. For visualization, we are currently using the Google Charts tool.

The interactive web interface also allows the user to download all the displayed light curves. The downloaded file contains the GOES data with 2s resolution, and the 10s averaged Nobeyama and SDO/EVE/ESP data. Besides the graphs, we also provide the user with an image of the flare generated from SDO/AIA 1600 Å data, and a detailed description of all overlapping events from the primary GOES, RHESSI and HEK lists corresponding to the same UniqueID, as well as from the secondary event sources. Besides the usual flare descriptors, the HEK database contains links to the flare quicklook images: we keep these links in our event summary page, which also can be downloaded.

In addition, the users are provided with the option of a similarity search mechanism (currently beta version) that allows automatic selection of similar events from the initial query table, based on some predefined and user-defined characteristics. Each such event characteristic is normalized, and, if the associated fields are absent from the table for some of the events, they are replaced by the median values of the corresponding characteristic. The nearest neighbors of the selected event are determined based on the selected (predefined) characteristics using the Euclidean distance.

3.4.3 Example of a Query

To demonstrate the capabilities of our Multi-Instrument Database of Solar Flares, we provide here an example of a multi-instrument query. Suppose that the user wants to study the chromospheric evaporation processes occurred during strong solar flares ($\geq$M1.0) in 2015 using the spatially-resolved high-cadence multiline spectroscopic observations performed by the IRIS satellite, and simultaneously analyze the energy released by precipitating accelerated electrons using RHESSI observations. Selecting the corresponding GOES filter: GOES class $\geq$M1.0; the IRIS filter: expansion of the field-of-view by $100''$, $\geq$4 slit positions, $\geq 5''$ covered perpendicular to the slits with cadence of $\leq$60s; the availability of RHESSI observations, and selecting the non-limb events (located not farther than $750''$ from the disc center to avoid strong projection effects), the query would return six records. Some descriptors of these flares are presented in Table 3.2. After such a query, the user can check the events manually: see the lightcurves for each event, proceed to the IRIS quick look images and movies, and check how well the events were covered by the IRIS slit positions, etc.

3.5 Conclusion and Future Plans

We have created an Interactive Multi-Instrument Database of the Solar Flares available to the community at `https://solarflare.njit.edu/`. This database integrates a set of available solar flare lists and data in a convenient way, and includes the following main features:

- The integration of the flare events from different flare catalogs (GOES, RHESSI, HEK, Hinode, Fermi GBM, Konus-Wind, OVSA flare catalogs). The match of events from GOES, RHESSI and HEK primary flare lists, and assignment of Unique Identifiers (UniqueIDs) for flares. The queries provide "one flare — one

Table 3.2 Results of the Sample Query

SOL ID	Flare Class	RHESSI highest energy	IRIS raster mode and number of slits
SOL2015-03-10T23:46:00	M2.9	12-25 keV	coarse, 4-step
SOL2015-03-11T16:11:00	X2.1	25-50 keV	coarse, 4-step
SOL2015-03-11T18:37:00	M1.0	25-50 keV	coarse, 4-step
SOL2015-06-22T17:39:00	M6.5	100-300 keV	sparse, 16-step
SOL2015-08-27T04:48:00	M2.9	12-25 keV	coarse, 8-step
SOL2015-11-04T13:31:00	M3.7	50-100 keV	coarse, 16-step

Note: see text for the query details.

Source: [194].

result." After the UniqueID assignment, the flare reports are integrated with secondary flare catalogs (Hinode, Fermi GBM, Konus-Wind, OVSA) and flare-related events (Filament Eruption catalog, CACTus CME catalog), depending on the user's query;

- The search of the flare events based on their physical descriptors (both stored in the catalogs and calculated by our efforts) and availability of observations (currently IRIS and Nobeyama observational filters are available). The search allows the users to select the events of interest based on the specified filters, get the integrated properties of the events in one table, download the results of the query, and visualize the processed light curves for each event;
- The detailed look at the data (GOES, ESP/EVE and Nobeyama light curves, and temperature and emission measure derived from GOES data) for a particular event, and to its summary containing quicklook links stored in the primary catalogs, allows the user to form an initial opinion about the selected event, and to decide whether the event would be interesting for a case study.

The integrated catalog results generated by our database provide a tool to assist researches who study solar flares using large data archives. Firstly, the tool we have created allows the user to search for events having the parameters of interest for various statistical studies, handling all the catalog-creation tasks, or at least providing a catalog to start from. Secondly, it provides a summary for each event, allowing the researchers to understand if the particular event satisfies the criteria for particular case studies. Our web application allows a platform- and software-independent access to the data.

As far as we know, there are almost no examples of such kinds of query engines for solar flares. In this case, our database really provides a unique overlook of the flare data. Currently, there are many filters, catalogs and data processing modules already implemented in our database. However, the design allows further addition of the instrumental logs and sources without distortion of the current schema. Further expansion of the sources is definitely in our plans. We also plan to increase the flexibility of the project by developing a true Web API which will allow the user to receive the flare lists, apply different integration schema, and contribute to the database by adding his own records and data. We also plan to integrate the VSO API and generate data links for the stored flare events.

CHAPTER 4

STATISTICAL STUDY OF CHROMOSPHERIC EVAPORATION DURING IMPULSIVE PHASE OF SOLAR FLARES

4.1 Introduction

Depending on the deposited energy flux, the chromospheric evaporation during the solar flares can be of two types: "gentle" (with subsonic velocities of the evaporated plasma and timescales of several minutes) driven by low-energy flux electron beams or heat conduction, and "explosive" (characterized by supersonic upflows on shorter timescales) driven by high-intensity electron beams [9, 240]. Interestingly, the response of the chromospheric and lower transition region layers differs in these regimes. For the "explosive" type, the model predicts downward expansion accompanied by formation of a radiative shock and a relatively low-temperature ($\sim 10^4\,$K) dense layer formed in the shock relaxation zone [112], which is called the "chromospheric condensation". For the "gentle" type, the downward expansion is weak, so that upward motions dominate. Numerical simulations by Fisher et al. [67, 66, 65] confirmed the existence of such evaporation regimes, and showed that the critical energy flux for transition from the "gentle" to "explosive" is $\sim 10^{10}$ erg cm^{-2} s^{-1} for electron beams with a 20 keV low-energy cutoff. It is obvious that evaporation properties are closely connected to the energy release and transport mechanisms.

Multiwavelength spectroscopy is of special interest for studying chromospheric evaporation because different spectral lines are formed at different heights and can represent local properties of the plasma at these heights. An overview of multiwavelength spectroscopic studies of solar flares was presented by Milligan [147]. Previous observational studies [148, 173, 29, 55, 74, etc.] have confirmed the existence of the "gentle" [149, 198] and "explosive" [33, 30, 127, 32] chromospheric evaporation regimes which was concluded from the observations of the Doppler shifts of the chromospheric and transition region lines of different signs. In addition, transition between these regimes had been observed during some flares [173, 129].

Observations by the Interface Region Imaging Spectrograph [50, IRIS] provide a unique opportunity for detailed spectroscopic studies of dynamics of the solar atmosphere associated with chromospheric evaporation. IRIS observes several lines formed in the chromosphere and lower transition region (Mg II h & k 2796 Å and 2803 Å lines, C II 1334 Å and 1335 Å lines and Si IV 1394 Å and 1403 Å lines), and, in addition, the Fe XXI 1354.1 Å line which corresponds to a forbidden magneto-dipole transition and is formed in a very hot $\sim 10^7$ K plasma. There have been many works on analysis of the chromospheric evaporation process using the high spatial, spectroscopic and temporal resolution observations from IRIS [220, 30, 76, 100, 129, 168, 198, 221, 239, 167, 197, 241, 32, 121, 126, 130, etc]. A wide range of velocities of the hot evaporated plasma and various dynamical responses of colder chromospheric layers have been reported.

Radiative hydrodynamic flare simulations developed in recent years allow us to understand a complicated physics behind the observed phenomena. Many numerical simulations of the chromospheric evaporation process have been performed, both for general studies of the flare dynamics and applications to specific flare events, considering various heating mechanisms and energy release rates [114, 135, 67, 66, 65, 112, 134, 27, 96, 175, 184, 185, 99, 176, 178, 183, 92, 93]. In the simulations, it is possible to test a variety of initial conditions and heating mechanisms, understand how the atmosphere responds from the physical point of view, and derive relations between the observed characteristics of the chromospheric evaporation and the deposited energy flux and other parameters. Currently one of the most advanced code for the modeling is the RADYN radiative hydrodynamic code [37, 1, 2, 5, 6, 134, 7]. A grid of RADYN models is available online from the F-CHROMA project website (`http://www.fchroma.org/`, accessed on 04/08/2019), allowing us to investigate various regimes of flare energy release in the form of non-thermal electrons, and to compare the atmospheric response to observations.

The goal of this project is to perform a statistical analysis of chromospheric evaporation in flares simultaneously observed by RHESSI and IRIS, and compare the derived relations with those obtained from the RADYN models. In particular, we focus on analysis of the C II 1334.5 Å and Fe XXI 1354.1 Å lines observed by IRIS in the fast scanning regimes. The synthetic line profiles are calculated using the RH 1.5D radiative transfer program [189, 190, 227, 164] and the Chianti atomic line database [119]. Section 4.2 explains details of the spectroscopic data analysis and calculation of the synthetic line profiles. The analysis results are described in Section 4.3. A discussion is presented in Section 4.4, followed by a summary and conclusion in Section 4.5.

4.2 Data Selection and Analysis

4.2.1 Selection of Events

Using the Interactive Multi-Instrument Database of Solar Flares [191, IMIDSF, `https://helioportal.nas.nasa.gov/`, accessed on 04/08/2019], we select flares the impulsive phase of which was simultaneously observed by RHESSI and IRIS. Our initial selection is restricted to the flare events from the GOES and RHESSI flare lists, which have the GOES X-ray class of C5.0 or greater, located not farther than $750''$ from the solar disk center (to avoid strong projection effects), and observed by IRIS in one of the fast scanning regimes (with ≥ 4 slit positions across the flare region covering $\geq 6''$ in the direction perpendicular to the slit, with ≤ 90 s cadence per cycle). The events with HXR sources not covered by the IRIS slit or with no prominent non-thermal component in HXR spectra are excluded from the analysis. Also, the events, for which the emission of Fe XXI 1354.1 Å line is non-detectable by

Table 4.1 Characteristics of the Analyzed Flares from Spectroscopic Analysis of UV and X-ray Radiation

	SOL1 2014-02-13 01:32	SOL2 2014-02-13 02:41	SOL3 2014-03-29 17:35	SOL4 2014-06-12 18:03	SOL5 2014-06-13 00:30	SOL6 2015-03-11 11:21	SOL7 2015-08-27 04:48
GOES class	M1.8	M1.0	X1.0	M1.3	C8.5	C5.8	M2.9
RHESSI analysis times	01:34:35-01:36:05	02:47:35-02:48:35	17:44:55-17:45:55	18:07:30-18:08:30	00:33:30-00:34:30	11:26:00-11:28:00	05:36:20-05:37:20
RHESSI detectors	1, 3, 4, 5, 7-9	1, 3, 4, 5, 7-9	2, 4, 5, 7-9	2, 4, 5, 7-9	1, 2, 4, 5, 7	1, 3, 5, 7-9	1, 5-9
Fitting energy range [keV]	6-40	6-40	6-100	6-49	6-70	6-40	6-58
F_{nonth}[erg/cm^{2}s]	$(9.6\pm1.4)\cdot10^9$	$(3.9\pm1.1)\cdot10^8$	$(2.2\pm1.1)\cdot10^{10}$	$(9.0\pm2.6)\cdot10^8$	$(2.6\pm1.1)\cdot10^9$	$(3.1\pm0.8)\cdot10^8$	$(4.8\pm0.3)\cdot10^{10}$
E_c[keV]	19.4±0.1	18.8±0.3	17.0±0.3	19.0±0.4	17.2±0.1	22.2±0.9	19.8±0.1
δ	8.93±0.25	9.09±0.13	4.65±0.15	6.69±0.47	6.50±0.29	9.81±0.56	8.35±0.11
C II mean Doppler shift [km/s]	-21±27	-14±17	-24±33	-32±30	-54±48	-10±13	-40±48
C II mean Doppler shift time	01:36:18-01:36:56	02:47:34-02:48:12	17:45:36-17:46:41	18:08:21-18:08:39	00:34:10-00:34:28	11:27:04-11:28:09	05:37:25-05:37:46
C II strongest redshifts [km/s]	-85±3	-40±3	-84±4	-90±5	-156±5	-31±4	-169±19
C II strongest redshifts time	01:37:01-01:37:39	02:47:34-02:48:12	17:45:36-17:46:41	18:08:21-18:08:39	00:33:49-00:34:07	11:25:48-11:26:54	05:38:14-05:38:35
Fe XXI mean Doppler shift [km/s]	43±27	17±18	42±34	142±42	27±24	42±25	53±47S
Fe XXI mean Doppler shift time	01:36:18-01:36:56	02:48:17-02:48:55	17:45:36-17:46:41	18:07:59-18:08:18	00:33:49-00:34:07	11:25:48-11:26:54	05:37:25-05:37:46
Fe XXI strongest blueshifts [km/s]	112±6	54±6	181±52	217±9	70±9	88±8	146±7
Fe XXI strongest blueshifts time	01:36:18-01:36:56	02:48:17-02:48:55	17:44:21-17:45:27	18:08:21-18:08:39	00:33:49-00:34:07	11:27:04-11:28:09	05:37:25-05:37:46

Note: Parameters from the RHESSI X-ray data are obtained using thick-target spectral fitting and images reconstructed using “vis_cs” algorithm. The spectral line Doppler shift characteristics are deduced from the IRIS UV data.

Source: [196].

our methods, are also eliminated from the analysis. The final selection includes 7 flare events (see Table 4.1) that satisfy all the criteria.

4.2.2 RHESSI Data Analysis

The X-ray spectroscopic data obtained by RHESSI [131] allow us to estimate the deposited energy rates as well as the size and location of the hard X-ray (HXR) source and therefore derive the energy flux, one of the key parameters for the flare hydrodynamic simulations.

To estimate the deposited energy rate we fit the thermal plus non-thermal thick-target model [34, 114] to the X-ray spectra calculated for five 12 sec intervals (or 18-24 s for the flares with low count rates) covering the emission peaks in the 25-50 keV energy range. The pileup correction and isotropic albedo component are applied to the spectra. The total time intervals, fitting energy intervals, and the RHESSI detectors used for our spectral analysis are listed in Table 4.1. In the case of several HXR peaks we select the one preceding the enhancement of UV line characteristics observed by the IRIS satellite.

The fitting is performed using a least-squares procedure available from the OSPEX Solar SoftWare [69, SSW] package. The fit functions include three components: "vth", isotropic "albedo", and "thick2". The deposited energy rate for each time interval is calculated using the formula $P_{\mathrm{nonth}} = \frac{\delta - 1}{\delta - 2} F(E > E_{\mathrm{c}}) E_{\mathrm{c}}$, where E_{c} is the low-energy cutoff derived from the spectra, $F(E > E_{\mathrm{c}})$ is the number of deposited electrons per second, δ is the spectral index. From the five time intervals for each flare we select two intervals with prominent non-thermal components, the highest deposited energy rates, and the smallest relative errors of the fitting parameters. In addition to the deposited energy rates, for each event we derive the averaged parameters of the energy spectra, δ and E_{c}. We note here that E_{c} is notoriously hard to measure, and consider a maximum value that is consistent with the data, meaning that the derived power carried by non-thermal electrons is a lower limit.

To determine the energy flux, we reconstruct the RHESSI images using the recently developed "vis_cs" algorithm [63] applied with the standard $\lambda = 0.5$ sparseness parameter to the entire time intervals of the RHESSI analysis. The data from detectors 2-8 are used for image reconstruction. The source size, S, is determined as the area within 50% contours of the reconstructed images of the HXR flux in the energy range of 25-50 keV. The reconstructed HXR sources areas are likely overestimated, meaning that the stated energy fluxes are lower limits. Finally, we derive the flux rate of non-thermal electrons for each flare event as $F_{\mathrm{nonth}} = P_{\mathrm{nonth}}/S$ (projection effects are taken into account in the source size calculation) and use this value as the deposited energy flux. Along with the low-energy cutoff, E_{c}, and the power-law index, δ, it is used for identifying the closest RADYN model for the analyzed flares. In addition, we calculate the mean 25-50 keV photon fluxes emitted from the HXR sources by dividing the integrated flux by the source area.

4.2.3 IRIS Data Analysis

The spatially-resolved measurements of ultraviolet (UV) spectra obtained by IRIS [50] allow us to understand the properties of the evaporated plasma, as well as the dynamical response of the lower layers of the solar atmosphere. In this study, we focus on analysis of the C II 1334.5 Å ($1-2\cdot10^4$ K) and Fe XXI 1354.1 Å ($\approx 10^7$ K) lines which reflect the dynamics of the relatively cold chromospheric and lower transition region layers (including the chromospheric condensation) and the hot evaporating plasma respectively. We choose the C II line because it has a less complex profile than the Mg II lines, and it is rarely overexposed during the flares. However, the C II line is still optically-thick [174] which can make any interpretation of C II Doppler shifts ambiguous [117].

For analysis of the C II line, we calculate the center-of-gravity parameters: (1) the line peak intensity, and (2) the Doppler shift defined as the difference between the center of gravity of the line and the reference wavelength for this line $\langle\lambda\rangle - \lambda_{ref} = \int \lambda I d\lambda / \int I d\lambda - \lambda_{ref}$. This approach was tested in our previous works [198, 197]. We calculate these characteristics for every spatial point and every available time moment, and reconstruct time-dependent maps of the line intensity and Doppler shift. Examples of such maps and the line profiles are presented in Figure 4.1 for SOL2014-06-12T18:03:00 event. The reference wavelength for the C II line, λ_{ref}, is estimated for each flare separately from the spectra in the areas not affected by the flares.

The Center-of-Gravity estimates cannot be directly applied to the Fe XXI line, because it is blended with other lines. The strongest blend of the Fe XXI line is the C I 1354.334 Å line. These two lines are dominant in the corresponding IRIS spectral window during the flares. Thus, we fit the spectra using the double-Gaussian fitting, the applicability of which was demonstrated by Battaglia et al. [17]. From the fitting parameters, we estimate the peak intensity of the Fe XXI line (as the amplitude of the corresponding Gaussian) and its Doppler shift (as a mean shift of the corresponding Gaussian from the reference wavelength). The spectra where the fitting results are unreliable (the intensity in the channel does not exceed preflare activity level, the standard deviation of the Gaussian corresponding to C I line exceeds 0.15 Å, and the standard deviation of the Gaussian corresponding to the Fe XXI line is outside the 0.15 Å-0.30 Å range) are not considered in the analysis. The reference wavelength of the Fe XXI line is kept equal to 1354.14 Å as in our previous work [198]. This estimate deviates from the value of 1354.106 Å derived by Young et al. [239] by $\sim$ 0.03 Å (or $\sim$6 km/s). However, the difference does not affect analysis of chromospheric evaporation flows with velocities of $\sim$100 km/s or greater. An example of Fe XXI

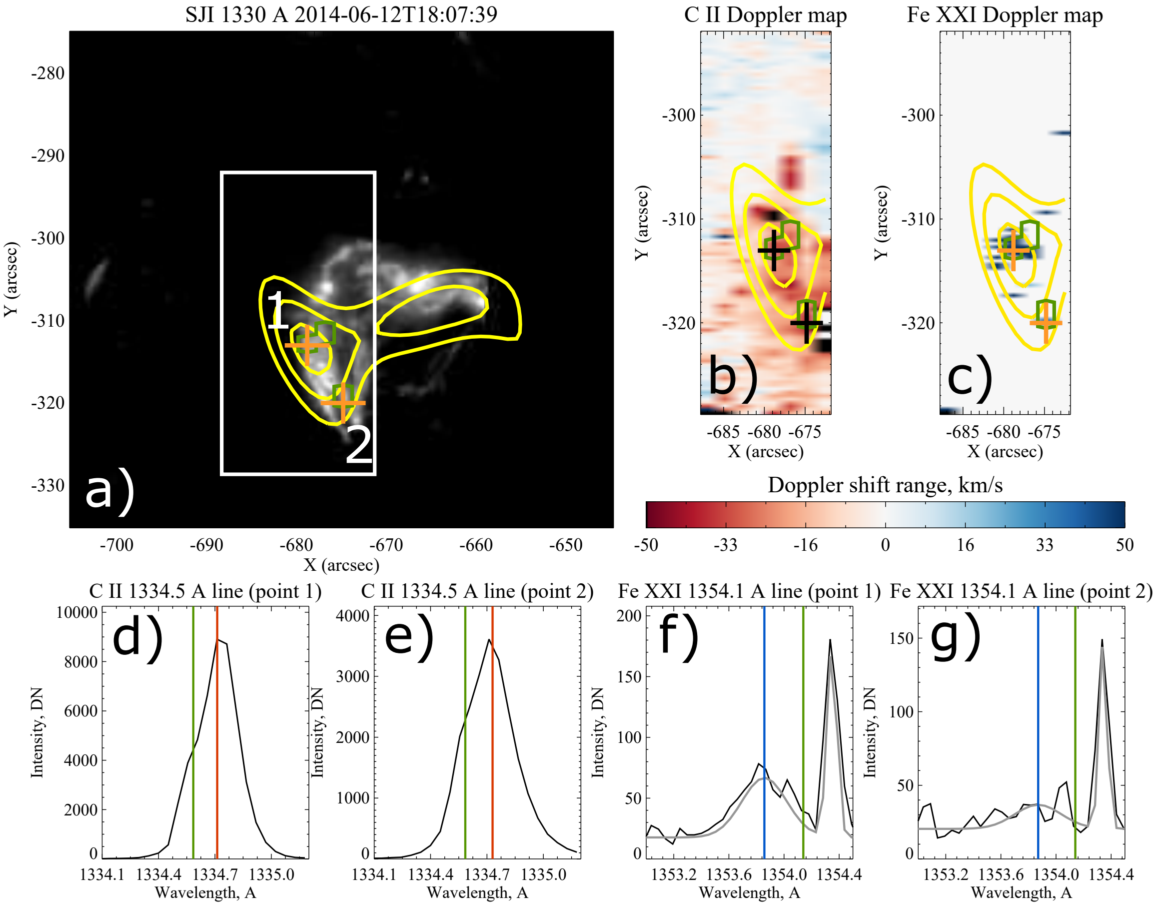

Figure 4.1 An example of joint IRIS and RHESSI observations of the SOL2014-06-12T18:03:00 flare event. a) IRIS 1330 Å slit-jaw image. White rectangle corresponds to the region scanned by the spectrograph slit. b) Map of C II 1334.5 Å line Doppler shifts. c) Map of Fe XXI 1354.1 Å line Doppler shifts. Yellow contours in panels a)-c) correspond to the 50%, 70%, and 90% of the maximum of the HXR 25-50 keV source reconstructed from RHESSI data for 18:07:30-18:08:30 time period. Green contours correspond to the mask of points for which the Doppler estimates (mean and strongest) are obtained. d,e) C II line profiles obtained for points 1 and 2 (orange and black crosses in panels a-c). Red vertical line corresponds to the centroid of the line, green vertical line — to its reference wavelength. f,g) Fe XXI and C II line profiles obtained for points 1 and 2 (black and grey crosses in panels a-c). Grey profiles show the corresponding double-Gaussian fitting. Blue vertical lines indicate the center of the Gaussian corresponding to the Fe XXI line, green vertical lines — its reference wavelength.

Source: [196]

Doppler shift map together with examples of Fe XXI and C I line profiles and double-Gaussian fitting are also presented in Figure 4.1.

After calculating the line intensities and Doppler shifts for the entire flare region, we determine a time-dependent mask of points involved in the flare heating. First, we find the maximum of the averaged C II line intensities (integrated across the scanned region) for each scan during the flare and define it as a threshold, and then for each scan, construct the mask of points where the C II intensity is greater than the threshold. The derived masks capture the flare dynamics and are independent from the RHESSI data. A comparison of the mask derived for SOL2014-06-12T18:03:00 with the HXR sources is presented in Figure 4.1a-c. Basically, for each considered flare event the derived IRIS masks intersect the previously obtained regions of the 25-50 keV HXR sources.

To quantify the response of the solar atmosphere, we calculate the mean values of the C II and Fe XXI Doppler shifts within the derived masks, and record the time and value of their maxima. We calculate the standard deviation for the mean Doppler shift values to estimate their uncertainties. An example of the evolution of C II and Fe XXI mean Doppler shifts during the SOL2014-03-29T17:35:00 X1.0 class flare is presented in Figure 4.2. The mean Doppler shift peaks are very prominent, and correspond to the first pulse of HXR 25-50 keV flux. In addition, we quantify the Doppler shifts in the areas that responded most strongly to the heating. The following procedure is applied: 1) for each IRIS slit scan, derive the Doppler shift level above which 95% of detected C II Doppler shifts are located (i.e., separating the 5% strongest C II redshifts across the flare region); 2) find the minimum among the derived Doppler shift levels. We repeat the same procedure for the Fe XXI blueshifts (hereafter referred as "Fe XXI strongest blueshifts"). Their values and times are summarized in Table 4.1 for each flare. To estimate errors in the determination of the C II strongest redshifts and Fe XXI strongest blueshifts, we decreased the IRIS raster field-of-view by 25%

and repeated the procedure. The standard deviations for the mean Doppler shifts are comparable with the Doppler shifts themselves, but the uncertainties for the strongest Doppler shift values are usually lower than the IRIS spectral resolution value, $\approx$3 km/s, for the C II line, and the uncertainty in the reference wavelength of the Fe XXI line.

4.2.4 Calculation of Synthetic Line Profiles

The F-CHROMA database provides the 1D radiative hydrodynamic (RADYN) models of solar flares for a variety of the electron beam parameters (averaged energy fluxes from 1.5×10^{9} to $5.0\times10^{10}\,\mathrm{erg\,cm^{-2}s^{-1}}$, low-energy cutoff values of 15 keV, 20 keV, or 25 keV, and spectral indexes ranging from 3 to 8). The RADYN code solves the coupled, non-linear, equations of hydrodynamics, radiation transport, and non-equilibrium atomic level populations, on an adaptive 1D vertical grid. The elements that are important for the chromospheric energy balance are treated in the non-LTE formulation, and the other species are included in the radiative loss function in the LTE approximation. The atomic level population and radiation transport equations are solved for a 6-level-with-continuum hydrogen atom, a 9-level-with-continuum helium atom, and a 6-level-with-continuum Ca II atom. For a detailed description see Allred et al. [7] and references therein. In the F-CHROMA database, the 1D flare models are calculated with 300 height grid points and 201 frequency points. To avoid overestimating radiative losses from the Ly-α line partial redistribution (PRD) effects were mimicked by modeling these lines as Doppler profiles. The initial atmosphere is described using the VAL3C model [229]. The temporal profile of the deposited energy flux rate is a triangle; the electron beam heating lasts for 20 s with the peak at 10 s. In this work, we analyze 20 RADYN models. Although there are models which are close to the analyzed flares in terms of the averaged energy flux, averaged low-energy cutoff and spectral index, we do

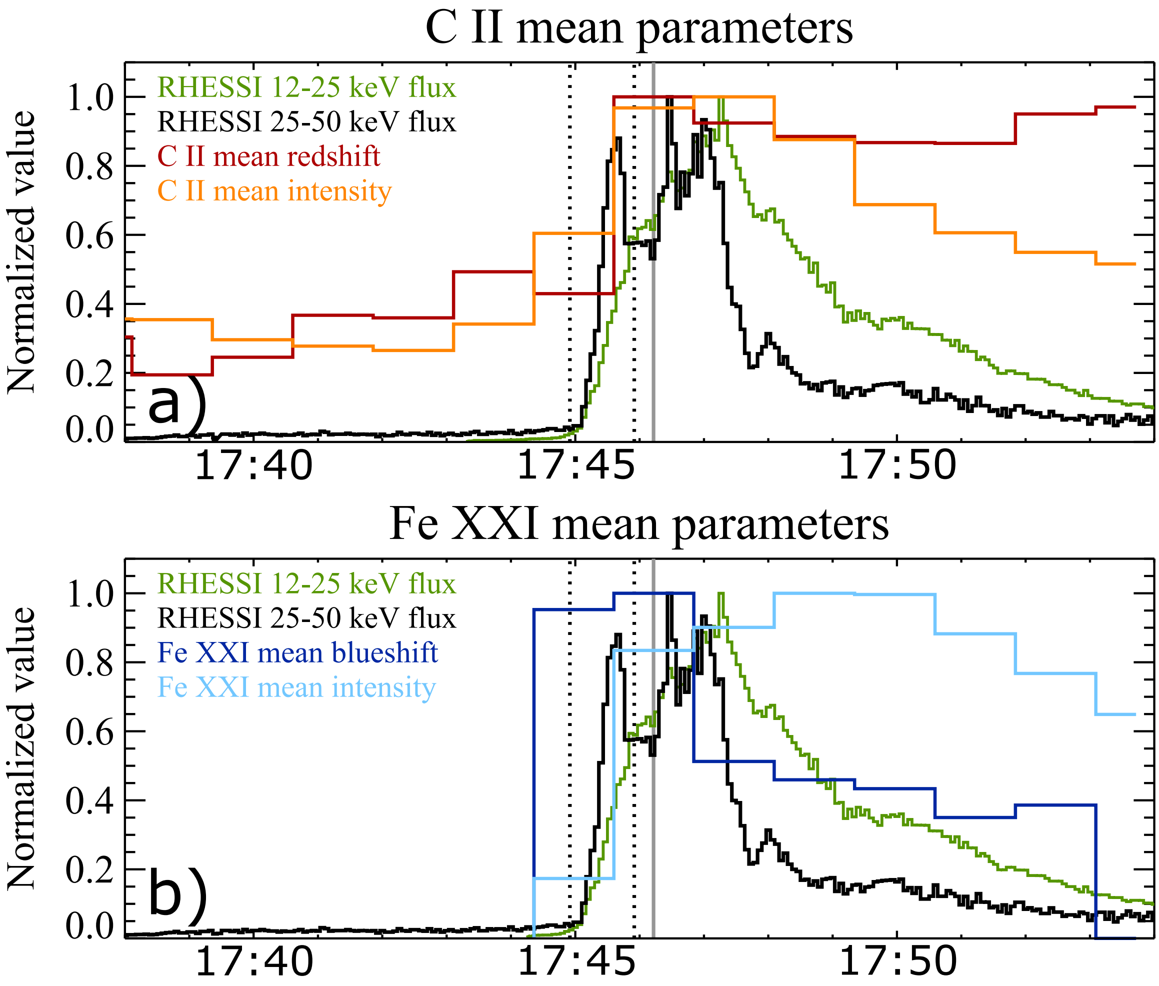

Figure 4.2 An example of the normalized integrated light curves and variations of the spectral line parameters for the SOL2014-03-29T17:35:00 flare event. a) normalized HXR 12-25 keV (green), 25-50 keV (black) light curves and normalized C II 1334.5 Å intensity (orange) and Doppler shift (red). b) normalized HXR 12-25 keV (green), 25-50 keV (black) light curves and normalized Fe XXI 1354.1 Å intensity (light blue) and Doppler shift (dark blue). Black dotted vertical lines mark the time interval where the deposited energy flux was estimated from RHESSI data. Grey vertical line represents the middle of the time interval where the peaks of the Doppler shifts means occur.

Source: [196]

not explicitly compare them to each other because of ambiguities (and possible overestimations) in HXR source areas derived from RHESSI data. The selection results are summarized in Table 4.2.

To calculate the C II 1334.5 Å line we use the height scale, density, temperature, electron density, plasma vertical velocity, and hydrogen populations from the RADYN snapshots as an input for the RH radiative transfer code [189, 190, 227, 164]. The latest version of the RH 1.5D massively-parallel code (`https://github.com/ITA-Solar/rh`, accessed on 04/08/2019) has been adopted for the calculations. Notice that the code assumes that the populations of atomic levels are in the statistical equilibrium, but the non-equilibrium electron density distribution is taken from the RADYN models. The inclusion of the non-LTE hydrogen, carbon, and silicon [174, 97, an important source of background opacity for C II lines] populations provides results accurate enough for the C II line profile calculations, other species are assumed to be in LTE. Also, the calculations are done under the complete frequency redistribution assumption (CRD) that has been proven to be adequate for the C II line [174]. The C II line profiles are calculated with 1 s time cadence for the selected RADYN models.

To calculate the Fe XXI 1354.1 Å line, we use Chianti atomic line database [119]. It allows us to simulate the optically-thin emission of the Fe XXI line under the ionization equilibrium assumption for a single temperature plasma. Using the Chianti software we simulate the Fe XXI emission at each grid point of the RADYN model (assuming thermal line broadening only), calculate the emission Doppler shift according to the local plasma velocities, and sum up the results for each snapshot.

Finally, the Doppler shift is calculated using the Center-of-Gravity method for both C II and Fe XXI lines. An example of the Doppler shift behavior and the simulated C II and Fe XXI line profiles is presented in Figure 4.3, which illustrates the "explosive" chromospheric evaporation (with strong redshifts of the C II line). For each run, we record the peak C II Doppler shifts during or within five seconds

Table 4.2 Characteristics of Spectral Lines Calculated from the RADYN Models

F-CHROMA ID	F_{nonth}[erg/cm^{2}s]	E_c[keV]	δ	C II Doppler shift maximum, km/s	Fe XXI Doppler shift maximum, km/s
d4_3.0e10_t20s_15keV	$1.5\cdot10^{9}$	15	4	38.2	99.0
d7_3.0e10_t20s_15keV	$1.5\cdot10^{9}$	15	7	44.7	71.0
d8_3.0e10_t20s_15keV	$1.5\cdot10^{9}$	15	8	39.7	54.0
d7_3.0e10_t20s_20keV	$1.5\cdot10^{9}$	20	7	17.2	—
d8_3.0e10_t20s_20keV	$1.5\cdot10^{9}$	20	8	12.6	—
d4_3.0e10_t20s_25keV	$1.5\cdot10^{9}$	25	4	8.4	—
d7_1.0e11_t20s_15keV	$5.0\cdot10^{9}$	15	7	-4.6	400.0
d8_1.0e11_t20s_15keV	$5.0\cdot10^{9}$	15	8	-11.4	422.0
d4_1.0e11_t20s_20keV	$5.0\cdot10^{9}$	20	4	28.9	148.0
d7_1.0e11_t20s_20keV	$5.0\cdot10^{9}$	20	7	27.0	94.0
d8_1.0e11_t20s_20keV	$5.0\cdot10^{9}$	20	8	39.7	73.0
d8_1.0e11_t20s_25keV	$5.0\cdot10^{9}$	25	8	17.4	—
d8_3.0e11_t20s_15keV	$1.5\cdot10^{10}$	15	8	-44.7	510.0
d4_3.0e11_t20s_20keV	$1.5\cdot10^{10}$	20	4	8.3	436.0
d8_3.0e11_t20s_20keV	$1.5\cdot10^{10}$	20	8	-17.8	559.0
d6_3.0e11_t20s_25keV	$1.5\cdot10^{10}$	25	6	11.4	242.0
d8_3.0e11_t20s_25keV	$1.5\cdot10^{10}$	25	8	10.9	184.0
d4_1.0e12_t20s_20keV	$5.0\cdot10^{10}$	20	4	-30.5	614.0
d5_1.0e12_t20s_20keV	$5.0\cdot10^{10}$	20	5	-36.9	705.0
d5_1.0e12_t20s_25keV	$5.0\cdot10^{10}$	25	5	-15.7	706.0

Source: [196].

after the heating phase, and the peak Fe XXI Doppler shifts during the entire run, and use them as a measure of the atmospheric response to the heating. The peak values of the Doppler shifts for each model are shown in Table 4.2. The missing Fe XXI values correspond to the RADYN models for which the plasma temperature does not exceed 10^6 K or the Fe XXI Doppler shift was still increasing in the end of the model. We do not apply any instrumental effects to our synthetic spectra (resolution, point-spread-function). Also, we assume that the emergent synthetic spectra are at disk center, originating from a vertical flux tube. While this is an adequate assumption for C II line which forms over in a narrow region deep in the flare loop, Fe XXI line likely forms over an extended region. Therefore when we sum up the emission from Fe XXI we are not separating footpoint emission from looptop emission. Our observations originate from various locations on the disk, and so geometric effects in some events may account for some differences between our model-data comparison.

4.3 Results

In this section, we analyze correlations among the observed flare parameters and compare them with the correlations found for the RADYN RHD flare models. Relationships between the energy fluxes and Doppler shifts are of particular interest. Such relations can provide a possibility to diagnose the properties of the energy release from the observed UV spectroscopic data. To analyze presence of correlations for each considered pair of parameters we calculate non-parametric Kendall's τ coefficient (Kendall's rank correlation coefficient) defined as:

$$\tau = \frac{2}{n(n-1)} \sum_{i<j} sgn(x_i - x_j) sgn(y_i - y_j) \qquad (4.1)$$

Here $\{x_i\}$ and $\{y_i\}$ are the values of the considered pair of parameter; sgn is a sign operator; n is a number of elements in each data set. Kendall's τ ranges between

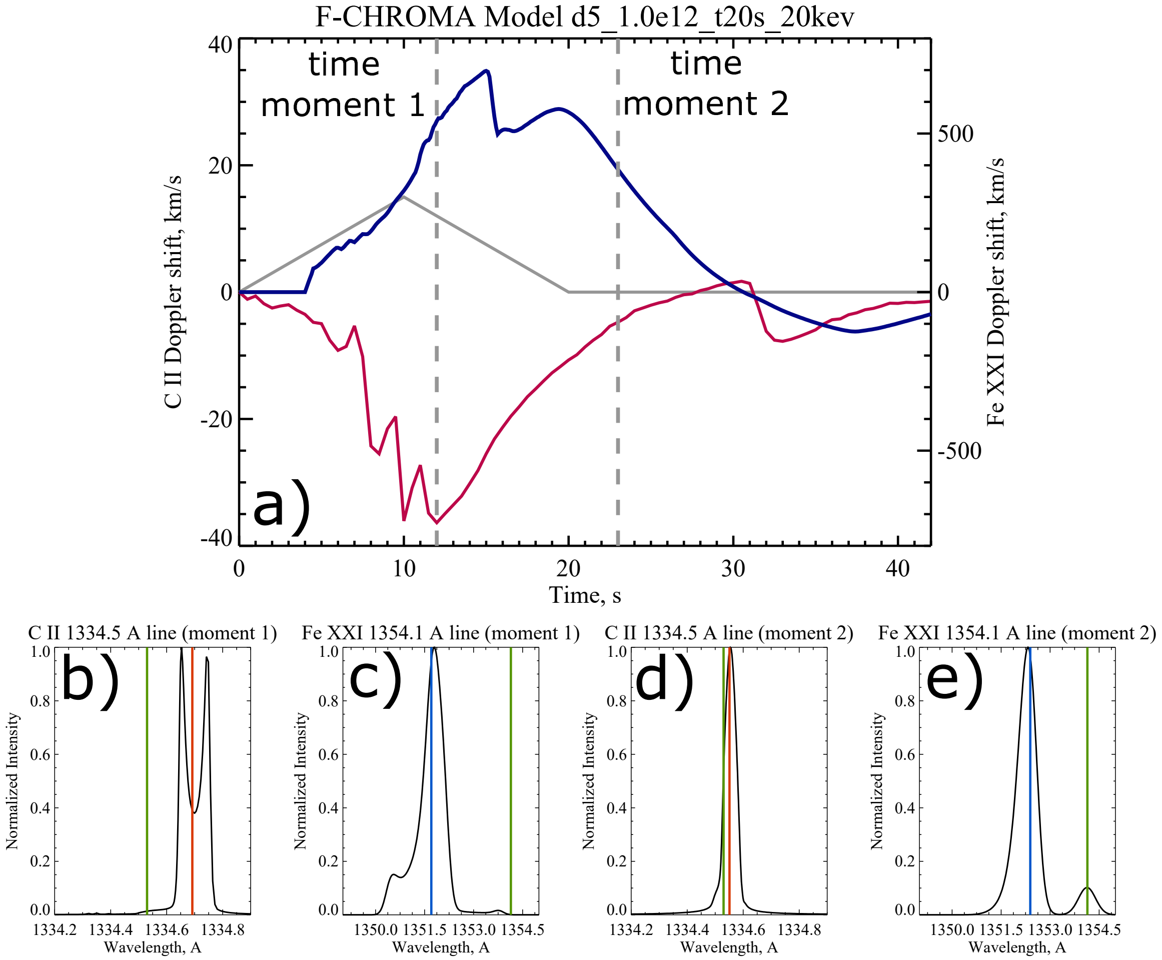

Figure 4.3 a) An example of the C II 1334.5 Å and Fe XXI 1354.1 Å line Doppler shift calculations for the RADYN run d5_1.0e12_t20s_20keV. In this simulation, a non-thermal electron distribution with a slope of $\delta = 5$, low energy cutoff $E_c = 20$ keV was injected for 20s, according to the triangle-shaped profile (gray), delivering a total time-integrated flux of 1.0 $\times 10^{12}$ erg cm^{-2}. The corresponding C II (red, left scale) and Fe XXI (blue, right scale) Doppler shift evolutions are presented. Gray dashed lines mark the time moments for which the simulated C II and Fe XXI line profiles in panels b)-e) are presented. Red and blue vertical lines in panels b)-e) correspond to the centroids of the lines, green vertical lines — to their reference wavelengths.

Source: [196]

-1 and 1, and its value is expected to be 0 for independent data sets. We calculate a p-value for a hypothesis test whose null hypothesis is an absence of association ($\tau = 0$). Low p-value (< 0.05) indicates that the difference of the presented τ values from zero is statistically significant. We also calculate linear regression correlation coefficients (CC) and the corresponding p-values (for a hypothesis test whose null hypothesis is that the slope is zero), with a weighted least squares procedure applied for the regression. Results of the statistical analysis, together with the empirical dependences for parameters, are summarized in Table 4.3.

Figure 4.4 presents the relationship between the 25-50 keV averaged photon flux and the estimated electron energy flux for the analyzed flare events. The correlation between these parameters in the log-log scale is significant (τ=0.90, p-value 0.0043), with the linear correlation coefficient (CC) of 0.88. The observed correlation confirms the applicability of the thick-target flare model which assumes that the observed HXR emission is a bremsstrahlung radiation of high-energy electrons.

Figure 4.5 shows the observed relationships between (a) the C II 1334.5 Å line mean Doppler shift and the deposited energy flux, and (b) the C II line strongest redshifts and the deposited energy flux. Panel (c) shows the C II Doppler shift vs the energy flux for the RADYN models. Although all panels demonstrate correlations between the deposited energy flux and the C II Doppler shift parameters (with τ of -0.52, -0.52, and -0.58, and with linear CCs of -0.42, -0.67, and -0.73 for panels a-c), the correlations are statistically significant only for models (p-values for observational relationships are high). However, the correlation between the C II strongest redshifts and the deposited energy flux also has a trend toward significance: the corresponding p-value for Kendall's τ is ~ 0.1. The strongest difference between the models and observations (panels a and b) is that no positive C II mean Doppler shifts (blueshifts) are found in the observations, although according to the RADYN models these are expected for some of the observed flare events.

Table 4.3 Correlation Coefficients and Relationships for the Observed and Modeling Parameters

Pair of parameters	Kendall's τ	Kendall's τ p-value*	Linear fit CC	Linear fit p-value$^+$	Linear fit equation
Observational parameters					
F_{ph} and F_{nonth}	0.90	0.0043	0.88	0.0083	$log_{10}F_{\mathrm{nonth}} = (11.6 \pm 0.5) + (0.87 \pm 0.20) \cdot log_{10}F_{\mathrm{ph}}$ (2)
F_{nonth} and $v^{\mathrm{C\,II}}_{\mathrm{mean}}$	-0.52	0.10	-0.42	0.34	—
F_{nonth} and $v^{\mathrm{C\,II}}_{5\%red}$	-0.52	0.10	-0.68	0.093	$v^{\mathrm{C\,II}}_{5\%\ \mathrm{red}} = (302 \pm 195) - (42 \pm 21) \cdot log_{10}F_{\mathrm{nonth}}$ (3)
F_{nonth} and $v^{\mathrm{Fe\,XXI}}_{\mathrm{mean}}$	0.29	0.36	-0.08	0.87	—
F_{nonth} and $v^{\mathrm{Fe\,XXI}}_{5\%\ \mathrm{blue}}$	0.33	0.29	0.39	0.38	$v^{\mathrm{Fe\,XXI}}_{5\%\ \mathrm{blue}} = (-138 \pm 274) + (28 \pm 29) \cdot log_{10}F_{\mathrm{nonth}}$ (4)
$v^{\mathrm{C\,II}}_{\mathrm{mean}}$ and $v^{\mathrm{Fe\,XXI}}_{\mathrm{mean}}$	-0.20	0.54	-0.13	0.78	—
$v^{\mathrm{C\,II}}_{5\%red}$ and $v^{\mathrm{Fe\,XXI}}_{5\%\ \mathrm{blue}}$	-0.24	0.45	-0.19	0.69	—
Modeling parameters					
F_{nonth} and $v^{\mathrm{C\,II}}$	-0.58	0.0012	-0.73	$2.4 \cdot 10^{-4}$	$v^{\mathrm{C\,II}} = (359.0 \pm 77.0) - (35.9 \pm 7.9) \cdot log_{10}F_{\mathrm{nonth}}$ (5)
F_{nonth} and $v^{\mathrm{Fe\,XXI}}$	0.77	0.00012	0.84	$4.6 \cdot 10^{-5}$	$\mathrm{E}v^{\mathrm{Fe\,XXI}} = (3500.0 \pm 662.0) + (386.0 \pm 66.0) \cdot log_{10}F_{\mathrm{nonth}}$ (6)
$v^{\mathrm{C\,II}}$ and $v^{\mathrm{Fe\,XXI}}$	-0.78	$2.8 \cdot 10^{-5}$	-0.92	$4.3 \cdot 10^{-7}$	$v^{\mathrm{Fe\,XXI}} = (373.0 \pm 24.5) - (7.45 \pm 0.84) \cdot v^{\mathrm{C\,II}}$ (7)

Note: : the observed and modeling parameters include non-thermal energy flux, F_{nonth}; 25-50 keV photon flux, F_{ph}; C II mean Doppler shift, $v^{\mathrm{C\,II}}_{\mathrm{mean}}$; C II strongest redshifts, $v^{\mathrm{C\,II}}_{5\%red}$; Fe XXI mean Doppler shift, $v^{\mathrm{Fe\,XXI}}_{\mathrm{mean}}$; Fe XXI strongest blueshifts, $v^{\mathrm{Fe\,XXI}}_{5\%\ \mathrm{blue}}$ (v in km/s, F_{ph} in photons/cm^{2}arcsec^{2}s, F_{nonth} in erg/cm^{2}s).

*p-value for a hypothesis test whose null hypothesis is an absence of association (Kendall's τ is zero).

$^+$p-value for a hypothesis test whose null hypothesis is that the slope is zero.

Source: [196].

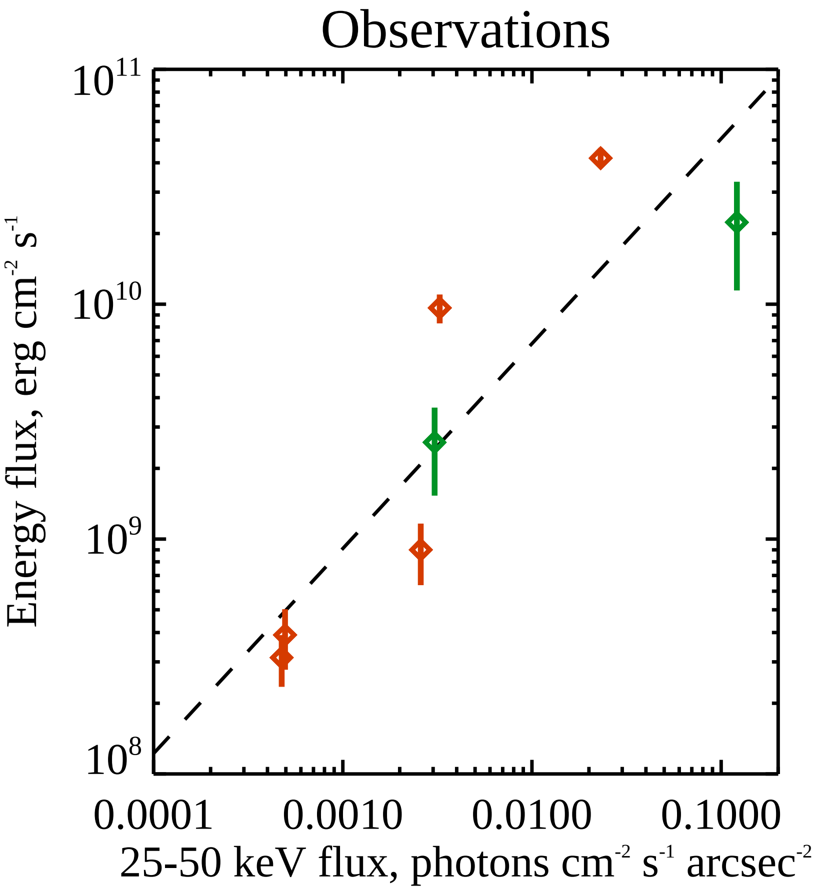

Figure 4.4 Dependence of the deposited electron energy flux estimated using the thick-target model fits to the X-ray spectra on the mean flux of 25-50 keV photons for the analyzed flare events. Different colors correspond to the closest low-energy cutoff values among 15 keV (green), 20 keV (red) and 25 keV (black). The inclined dashed line indicates the best linear log-log fit. The linear fit coefficients and corresponding correlation coefficient are presented in Table 4.3.

Source: [196]

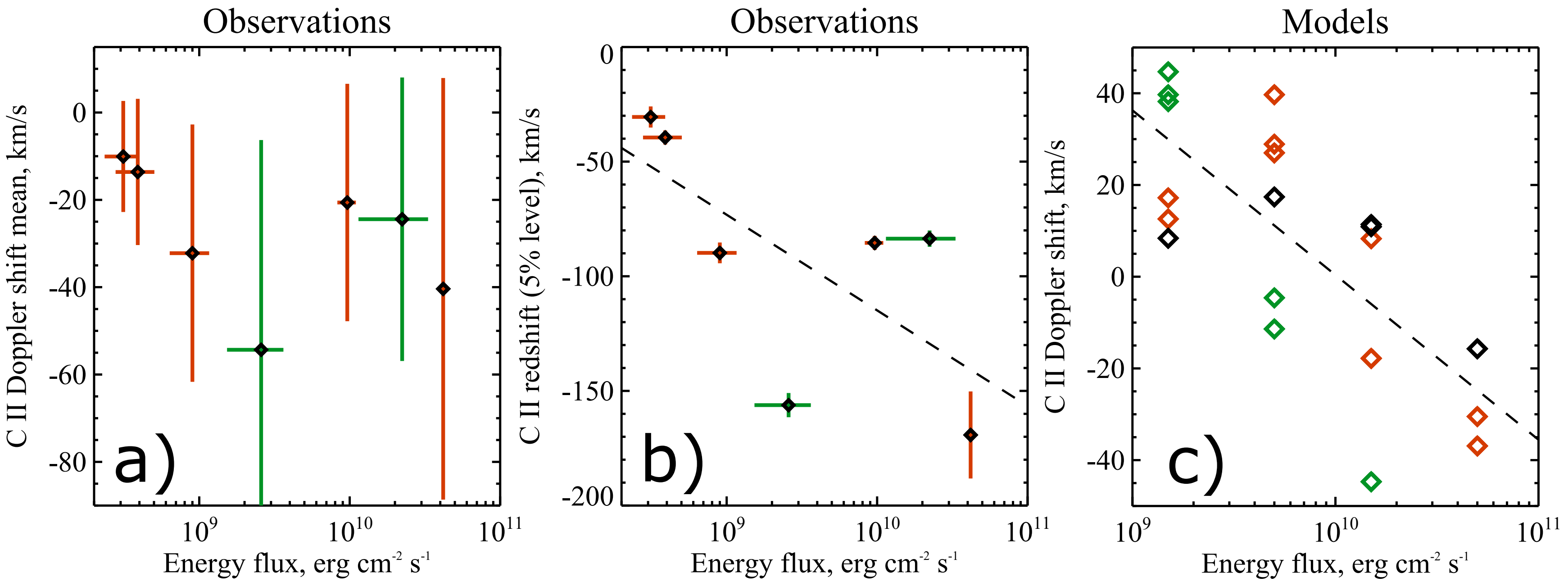

Figure 4.5 Dependence of the C II 1334.5 Å line Doppler shift estimates on the deposited energy flux from the observations (panels a and b, mean values and the strongest redshifts) and the RADYN models (panel c, strongest Doppler shifts over the run). The size of crosses in panels b) and c) corresponds to the errors estimated for each flare event. Different colors correspond to the closest low-energy cutoff values among 15 keV (green), 20 keV (red) and 25 keV (black). The inclined dashed lines show the best linear fits. The fitting and correlation coefficients are presented in Table 4.3.

Source: [196]

Figure 4.6 shows the observed relationship between (a) the Fe XXI,1354.1 Å line mean Doppler shift and the deposited energy flux, and (b) the Fe XXI line strongest blueshifts and the deposited energy flux. Panel (c) shows the Fe XXI Doppler shift and energy flux relationships for the RADYN models. Although the models demonstrate a very strong correlation (panel c, $\tau = 0.77$, CC $= 0.84$), the observed Fe XXI Doppler shift mean values do not show any significant dependence on the deposited energy flux. The Fe XXI strongest blueshifts show weak correlation (τ=0.33, CC=0.39) with the energy flux which, moreover, cannot be called statistically-significant. We still show the corresponding linear fit in Figure 4.6b, however, point out that low number of events does not allow us to confirm or decline presented trend. Also, one can see that many models demonstrate very strong Fe XXI Doppler shifts, in the range of 400-700 km/s, while there is only one observational result exceeding 200 km/s.

Figure 4.7 shows the observed relationship between (a) the C II 1334.5 Å line mean Doppler shift and the Fe XXI,1354.1 Å line mean Doppler shift, and (b) the C II line strongest redshifts and Fe XXI strongest blueshift. Panel (c) shows the C II Doppler shift and Fe XXI Doppler shift relationships for the corresponding RADYN models. Although the correlations for the models are strong demonstrating that higher velocities of chromospheric evaporation correspond to faster downflows in the colder atmospheric layers, we do not find such behavior for observations.

4.4 Discussion

In this work, we have performed a statistical analysis of the Doppler shifts of two UV lines, C II 1334.5 Å and Fe XXI 1354.1 Å, which characterize the lower transition region and coronal dynamics during solar flares, and compared the results with the corresponding radiative hydrodynamic RADYN models. To estimate the deposited energy flux, we assumed the thick-target flare model of bremsstrahlung radiation. Figure 4.4 illustrates the general correctness of this assumption. Such kind of

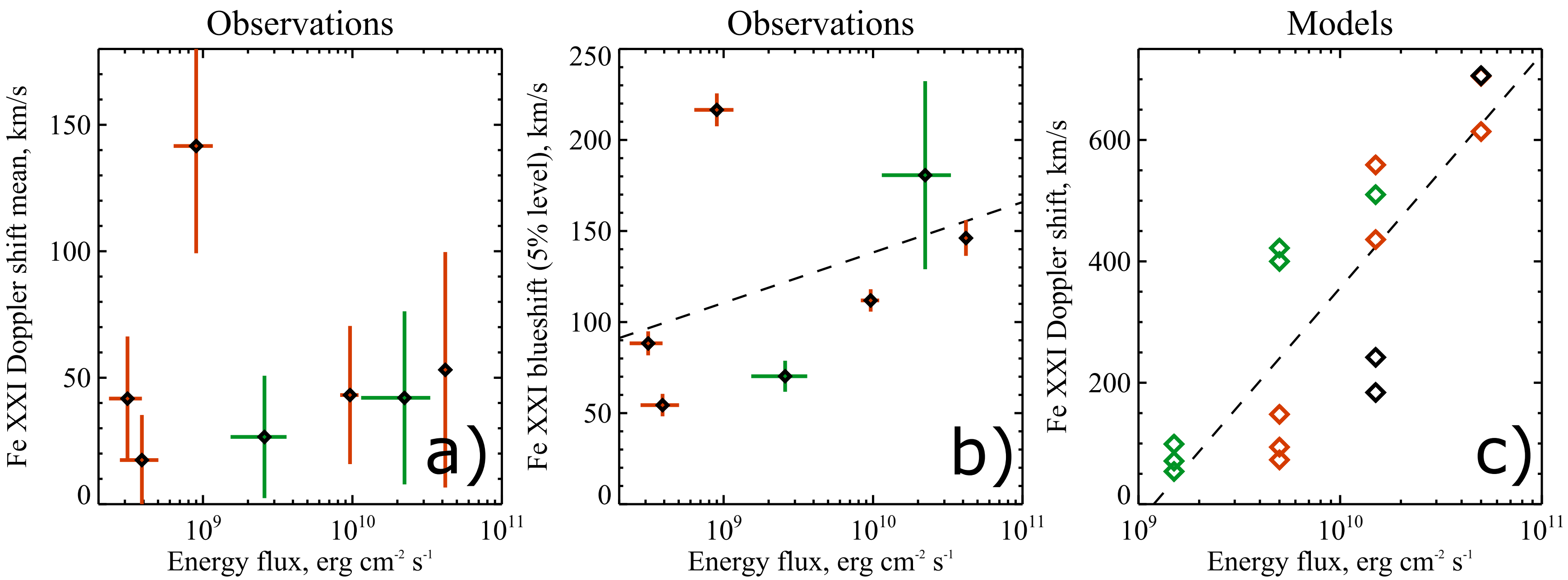

Figure 4.6 The same as in Figure 4.5 for the relationship between the energy flux and the Fe XXI 1354.1 Å line Doppler shift. *Source:* [196]

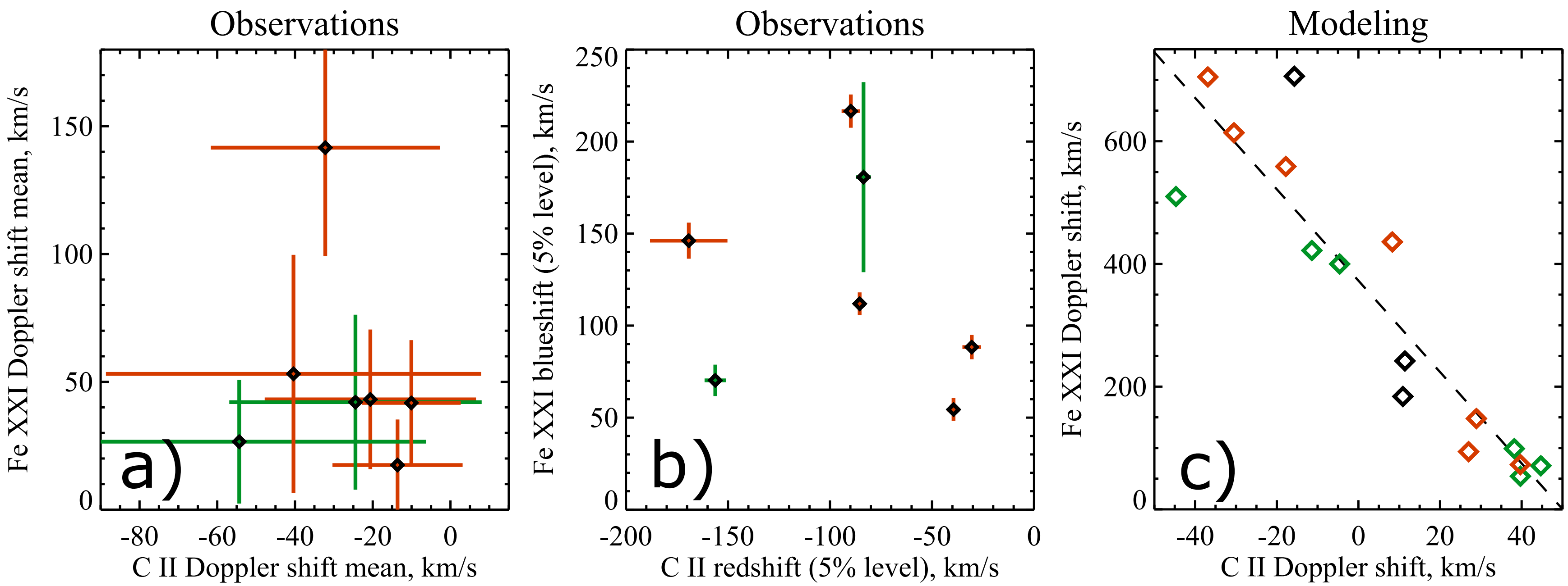

Figure 4.7 The same as in Figure 4.5 for the relationship between the C II 1334.5 Å and Fe XXI 1354.1 Å line Doppler shift estimates.

Source: [196]

relationships potentially allows us to filter out the flare events for which the thick-target model is inappropriate or the fitting procedure is performed incorrectly.

It is found from the RADYN flare hydrodynamic models of chromospheric evaporation that the relationships between the Doppler shifts of the UV lines and the energy flux (Figures 4.5c-4.7c) can be approximated by a linear-log regression (see the correlation coefficients and fitting parameters in Table 4.3), although the considered data set has a multi-parametric nature (low-energy cutoffs and slopes of the energetic electron spectra are not taken into account in the correlation analysis). Thus, one should expect to find similar trends for the observations to reasonable degree, given the assumptions of the model, the lack of geometric considerations, and the impact of spatio-temporal resolution on the observed profiles. However, such trends are not so clear for the considered observational data set. Figures 4.5a,b-4.7a,b show significantly weaker correlations. The only correlation with a tendency to be statistically-significant is found between the C II strongest redshift and the deposited energy flux, and is described by the empirical Eq. 3 (Table 4.3). In principle, this relation could be used as an indirect diagnostic tool of the deposited energy flux, allowing the estimation of the energy flux at least by an order of magnitude. We cannot make a comparison with the modeling Eq. 5 due to absence of the mean blueshifts in observational results.

In Section 4.1 we have discussed two regimes of chromospheric evaporation: the "explosive" regime characterized by supersonic velocities of evaporated plasma and chromospheric condensation downflow, and "gentle" regime with subsonic evaporation and upflows of colder layers. Using the empirical relations we can estimate the energy flux corresponding to transition between these regimes. For RADYN models, we use Eq. 5 and 6 in Table 4.3 assuming $v^{\mathrm{C\,II}}[\mathrm{km/s}] = 0$ and the coronal sound speed $v^{\mathrm{Fe\,XXI}}$ =100-200 km/s. Considering the uncertainties of fitting coefficients, we obtain that the transition energy flux is (2.2-10.1)$\cdot 10^9$ erg cm^{-2} s^{-1} for the models. We note that this flux is lower than the $\sim 10^{10}$ erg cm^{-2} s^{-1} transition flux obtained by Fisher et al. [67, 20 keV low-energy cutoff is assumed for the beam]. Unfortunately, it is impossible to derive reliable transition energy flux from the observations. The only way to get an estimate is to use the Eq. 5 (Table 4.3) for Fe XXI strongest blueshifts, because no positive mean Doppler shifts were observed for C II, and no correlation for the Fe XXI mean Doppler shift was found. Assuming that there are no supersonic flows (greater than 100-200 km/s) for the flares with gentle evaporation, we estimate the transition energy flux to be (2-8)$\cdot 10^9$ erg cm^{-2} s^{-1}. Notice again that high ambiguities of the observational relation and high p-value do not allow us to claim that the estimated transition energy flux is statistically-reliable. We also need to mention that the transition energy depends in general not only on the deposited energy fluxes, but also on the low-energy cutoff values, the power law of the non-thermal spectra, and the duration of heating [64, 175]. It seems that the low-energy cutoff dependence dominates over the spectral slope variations [211]. We see signatures of this effect in the models.

Our analysis revealed the difference between the simulated and observed Fe XXI Doppler velocities: the observed Doppler velocities rarely exceed 150 km/s, while the Doppler shifts calculated for the RADYN models indicate significantly higher upflow velocities, ranging from 200 km/s to 700 km/s. The Doppler shifts of the Fe XXI line detected in other works also rarely exceed 200 km/s. For example, Young et al. [239] reported the evaporation velocities of about 100-200 km/s for the SOL2014-03-29T17:35:00 flare. Brosius and Daw [30] reported Doppler shifts of 150 km/s for the Fe XXI line during the M7 flare of 2014 April 18. Polito et al. [168] detected 82 km/s blueshift for the C6.5 class flare of 2014 February 3. For two X1.6 class solar flares of 2014 September 10 and October 22, Li et al. [129] found the Fe XXI velocities up to 200 km/s. Zhang et al. [241] found the upflows of 35-120 km/s during the C4.2 circular-ribbon flare on 2015 October 16. Polito et al. [167] detected the evaporation flow velocities of 200 km/s for fully-resolved (single-gaussian) Fe XXI line profile. Why does this discrepancy happen? Graham and Cauzzi [76] pointed out that the Fe XXI line is very strongly blueshifted in the beginning of the flare, but its emission is weak. As evaporation develops, the line becomes stronger but less blueshifted. This effect is also seen in Figure 4.2b. The weak forbidden Fe XXI line, with several blends on it, might simply be non-detectable during the most blueshifted phase, when the maximum of the evaporation velocities takes place. The RADYN models confirm such line behavior in general: the intensity of the synthesized Fe XXI line continues to grow at the time of the Doppler shift peak for most of the models. We also note here that it is not possible to detect Fe XXI line blueshifts of $\gtrapprox$ 300 km/s because of the limited wavelength range of IRIS O I spectral channel. However, the Doppler shifts found in this work rarely exceed 200 km/s, and there is no strong influence of this effect on our results.

The RADYN models available from the F-CHROMA database website (`http://www.fchroma.org/`, accessed on 04/08/2019) have a standard time dependence of the energy input in a form of triangle 20 s duration with the peak at 10 s. To estimate the influence of the deposited energy flux profile shape on the Doppler shifts of the C II and Fe XXI lines without changing the heating phase duration and energetics (average and peak deposited energy fluxes), we performed four additional RADYN runs. Two of them were similar to the run "d5_1.0e12_t20s_25keV", with the only difference that the location of the peak of the heating function was at 5 s (1^{st} run) and at 15 s (2^{nd} run) from the start of the run. The 2^{nd} run was computationally demanding, and so we show here the first 18 s that we have computed (long enough to demonstrate any large scale differences). For two other runs, the total energy of 10^{10} erg cm^{-2} (lower than in any F-CHROMA run) was deposited by a population of accelerated electrons with 15 keV low-energy cutoff and spectral slope of 7. The heating was, again, triangular shape, lasted 20 s, and peaked at 5 s (3^{rd} run) and at 15 s (4^{th} run). We applied the same analysis for these runs as for the F-CHROMA runs, and calculated the peak Doppler shifts for C II and Fe XXI. For the 1^{st} and 2^{nd} runs, the C II peak Doppler shift was -21.6 km/s and -13.4 km/s, which is relatively close to the Doppler shift derived for "d5_1.0e12_t20s_25keV" run (-15.7 km/s). The corresponding Fe XXI peak Doppler shift for the 1^{st} run was 550 km/s (compare with 706 km/s for "d5_1.0e12_t20s_25keV" run). Unfortunately, the Fe XXI peak Doppler shift was not reached during the first 18 s of the 2^{nd} run, but the calculated Doppler velocities of the Fe XXI line were >330 km/s at 18 s and continued to grow. The 3^{rd} and 4^{th} runs showed consistent behavior. The peak Doppler shifts for these runs were 20.5 km/s and 21.2 km/s (for C II line) and 34 km/s and 35 km/s (for Fe XXI line) correspondingly. Thus, we can expect that the heating profile variations (with the total and peak deposited energy fluxes fixed) do not significantly affect the overall response and large scale trends of the atmospheric response, but do introduce differences.

Among the studied flares, we did not find any with positive mean Doppler shift of the C II line. The C II line is always mainly redshifted in observations. However, the RADYN models suggest that for the low energy fluxes found in several studied events, we should detect "gentle" chromospheric evaporation with blueshifts of the C II line. One of the possibilities to explain this discrepancy is that we significantly overestimate the area into which energy is deposited, thus underestimating the energy fluxes of the observed events. As an example, the deposited energy flux for the SOL2014-03-29T17:35:00 flare estimated by Kleint et al. [104] is more than 10 times higher than one obtained in this work. On the other hand, Sadykov et al. [198] previously found gentle chromospheric evaporation during the SOL2014-06-12T21:01:00 M1.0 where the C II line was also mainly redshifted. Despite negative values of the C II mean Doppler shifts, we found that for all observed events there are areas with blueshifted C II line during the impulsive phase. This finding is in agreement with the multi-thread nature of solar flares [76, 234, 178, 183] and requires further detailed investigation.

4.5 Summary and Conclusion

In summary,

1. We analyzed seven flares jointly observed by the RHESSI and IRIS satellites that allowed us to perform a statistical study of the chromospheric evaporation, and investigate relationships between the energy release properties and the atmospheric response. To compare observational findings with the results of the chromospheric evaporation process simulations, we calculated synthetic C II and Fe XXI line profiles for 20 different radiative hydrodynamic (RADYN) models and derived the corresponding Doppler shifts.

2. For the observations, the deposited energy fluxes (derived using the thick-target model assumption) correlate with the 25-50 keV photon fluxes averaged over the HXR sources. The linear correlation coefficient for their logarithmic values is very high (0.88, see Figure 4.4 and Table 4.3). Strong deviations from this dependence may indicate on inapplicability of the thick-target model for some flare events.

3. Despite differences in the slopes and low-energy cutoffs of the deposited energy electron spectra, RADYN models reveal linear dependence of the C II and Fe XXI peak Doppler shifts from the logarithm of the deposited energy flux, with high statistically-significant correlation coefficients (-0.73 for C II and 0.84 for Fe XXI).

4. The only observational relation having a tendency to be statistically-significant is found for the strongest C II Doppler shifts and deposited energy flux. The empirical relation Eq. 3 (Table 4.3) is the best candidate for the energy flux diagnostics from the UV spectroscopic data.

5. The C II and Fe XXI line Doppler shifts derived for the studied flares do not correlate with each other in observations but do strongly correlate in RADYN models (the correlation coefficients are -0.13/-0.19 for observational results and -0.92 for the results of the models).

6. The energy flux required for the transition from "gentle" to "explosive" evaporation regime is (2.2-10.1)$\cdot 10^9$ erg cm^{-2} s^{-1} from the RADYN models, and (2-8)$\cdot 10^9$ erg cm^{-2} s^{-1} from the observations. The observational estimate require verification on a larger statistics of events.

7. There are qualitative discrepancies between the observations and RADYN models:

   a) The observed Fe XXI Doppler shifts are weaker than ones derived from the models. The maximum observed Fe XXI Doppler shifts reach 220 km/s, while the models show the Doppler shifts of 400 km/s and higher. However, notice that the synthesized Fe XXI emission is integrated over the whole loop, and it is likely that Fe XXI is unobservable during the most blueshifted phase due to low plasma emission measure at high ($> 1\,MK$) temperatures at that moment.

b) The observed mean C II Doppler shifts are always negative (corresponding to redshifts) during the studied flares even for the events with relatively weak deposited energy fluxes (of about 10^9 erg cm^{-2} s^{-1}). Contrary, the models predict that the C II Doppler shift should change from negative to positive with the decrease of the energy flux. However, for all events there are areas with blueshifted C II line during the impulsive phase of flares, which is in agreement with the multi-thread nature of solar flares.

There are several assumptions made in this study. First, the IRIS raster scans cover only a part of the flare ribbons, and we assume that the distribution of chromospheric responses is the same in covered and uncovered parts of the ribbons. Second, we consider only certain descriptors of the UV line Doppler shifts but not their dynamical properties. Third, the synthetic spectral line profiles are calculated under assumption of statistical equilibrium for the C II line and ionization equilibrium optically-thin emission assumption for the Fe XXI line. Under these assumptions, our observational statistical study demonstrated for the first time how the Doppler shifts of UV lines during the chromospheric evaporation process depend on the deposited heat flux. Further joint X-ray and UV spectroscopic observations of flares as well as development of more sophisticated data analysis techniques are needed for better understanding of the flare energy release and transport.

CHAPTER 5

STATISTICAL PROPERTIES OF SOFT X-RAY EMISSION OF SOLAR FLARES

5.1 Introduction into the Problem

Although different mechanisms can be responsible for chromospheric evaporation during the solar flares, the general sequence of physical processes is qualitatively similar. After the flare starts, the energy release mechanism heats the dense chromospheric plasma until it reaches maximum temperature, T_{max}. During and after this process, the hot chromospheric plasma expands into the coronal loops. Once the energy release weakens, the evaporated plasma flow also weakens, and at some point the plasma starts condensing back into the chromosphere. At this time moment, the plasma reaches its maximum emission measure, $EM = \int n^2 dV$.

The X-ray Sensor [23, XRS] at the Geostationary Operational Environmental Satellite (GOES) series currently provides one of the longest continuous observations of solar activity. GOES measures the Soft X-ray (SXR) flux in two channels, 1-8 Å and 0.5-4 Å. The maximum emission in the 1-8 Å channel is traditionally used to define the flare class, which often serves as a measure of the flare strength. Thus it is important to understand what physical characteristics, such as the plasma temperature and emission measure, are represented by the GOES classes. Assuming a single-temperature plasma approximation, Thomas et al. [219], Garcia [72], and White et al. [237] developed a procedure to compute the temperature (T) and emission measure (EM) of the flare plasma based on the GOES SXR measurements. Studies of Feldman et al. [62], Garcia [71], Ryan et al. [187] demonstrated correlations of the GOES SXR flux maximum with the maximum temperature and emission measure during solar flares. Because the instrument response per unit emission measure [237, Figure 7] is a monotonically increasing function of temperature, increasing both T and EM can increase the SXR flux in both GOES channels. Since the maximum temperature, T_{max}, is expected to occur before the maximum of emission measure, EM_{max}, one can suggest that the maximum of the GOES SXR 1-8 Å flux is likely to occur between the T and EM maxima. The timeline of events is illustrated in Figure 5.1.

Figure 5.2 illustrate the SXR 1-8 Å flux, its derivative, temperature, and emission measure calculated for the standard flare model using the RADYN radiative hydrodynamic code [7]. The model results are in qualitative agreement with the timeline in Figure 5.1. The RADYN code solves time-dependent hydrodynamic, radiative transfer, and non-equilibrium atomic level population equations on an adaptive 1D vertical grid. Specifically, Figure 5.2 shows the results for the RADYN model "radyn_out.val3c_d3_1.0e12_t20s_15kev_fp" from the F-CHROMA solar flare model database (`http://www.fchroma.org/`, accessed on 04/08/2019). In this model, the energy flux is deposited by a beam of accelerated electrons (with a 15 keV low-energy cutoff and a power-law spectral index of 3) propagating downwards and delivering a total of 10^{12}erg cm^{-2} into the atmosphere in 20 seconds. The SXR emission is calculated for each grid point of the RADYN model assuming that the loop cross-section is $S = 10^{18}\,\mathrm{cm}^2$, and summed up over the grid points for each time snapshot. Using these SXR light curves and assuming a single-temperature plasma approximation, we calculate T and EM.

The motivation of this work is to understand the relationships between the plasma parameters (maximum values of T and EM and the corresponding times) and the properties of the SXR emission (GOES class, emission duration, characteristic times, etc). In particular, we define events as "T-controlled flares" if the SXR maximum – T maximum time interval is at least two times shorter than the EM maximum – SXR maximum interval, and as "EM-controlled flares" if the EM

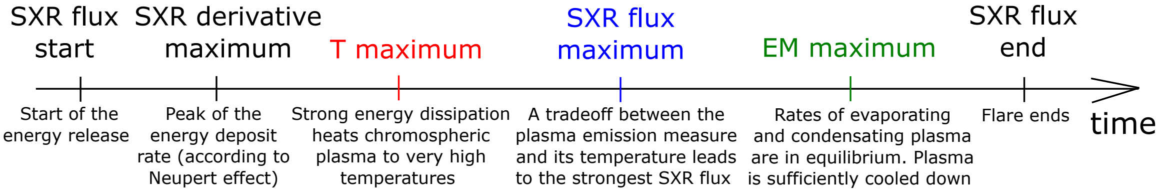

Figure 5.1 Time sequence of events during the chromospheric evaporation process in solar flares.

Source: [193].

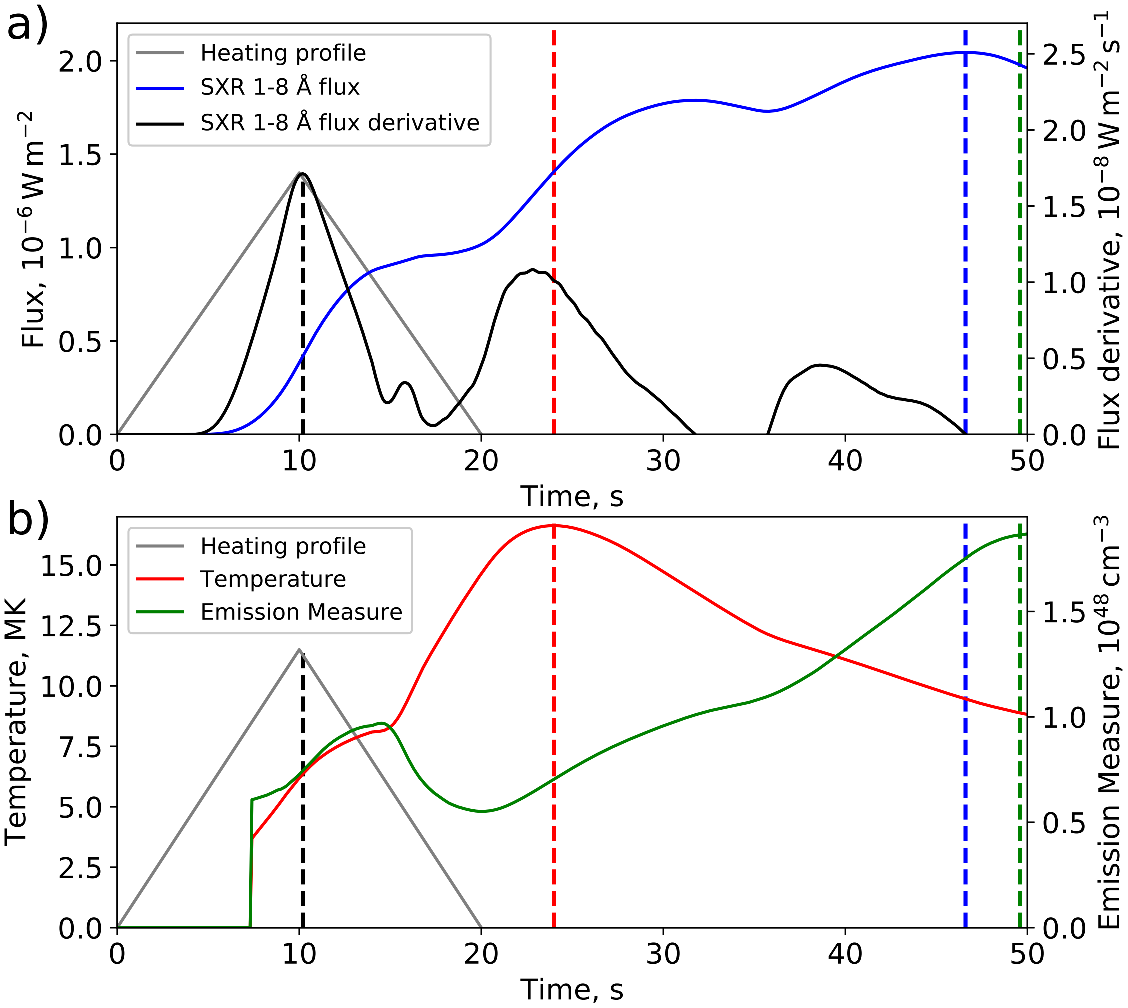

Figure 5.2 (a) SXR 1-8 Å flux and its derivative calculated for RADYN model "radyn_out.val3c_d3_1.0e12_t20s_15kev_fp" from the F-CHROMA solar flare model database (http://www.fchroma.org/, accessed on 04/08/2019); (b) temperature and emission measure calculated from the modeled SXR 0.5-4 Å and 1-8 Å fluxes. Loop cross-section of $S = 10^{18}\,\mathrm{cm}^2$ is assumed for these calculations. Gray triangle represents the deposited energy flux profile. Dashed vertical lines mark the maxima of presented characteristics.

Source: [193].

maximum – SXR maximum time interval is at least two times shorter than the SXR maximum – T maximum interval, and try to answer the following questions:

1. How often do flares obey the scenario of the chromospheric evaporation process illustrated in Figure 5.1?
2. Which of the plasma properties, T or EM, mainly influence the SXR maximum value and timing for the different GOES flare classes?
3. What is the physical difference between the T-controlled and EM-controlled flares of the same GOES class range?

The implemented algorithm to calculate T and EM and the event selection process are described in Section 5.2. Relationships among the flare characteristics are presented in Section 5.3, followed by a discussion and conclusions in Section 5.4.

5.2 Data Selection and Processing

To estimate behavior of T and EM during solar flares, we have applied the Temperature and Emission measure-Based Background Subtraction algorithm [22, 187, TEBBS], which allows the user to obtain T and EM values for flares detected by the GOES satellite. In this algorithm, the background level of the GOES X-ray emission is taken into account in order to obtain T and EM during the whole flare duration, including the rising phase. Our Python realization of the TEBBS algorithm for coronal element abundances is available at `https://github.com/vsadykov/TEBBS` (accessed on 04/08/2019). We note that the GOES data allow us to determine the flare temperature and emission measure only in a single-temperature approximation, because the data are obtained only in two SXR energy channels.

In this work, we analyze the GOES data obtained from January 2002 to December 2017. The full list of events for this time period is obtained from the Interactive Multi-Instrument Database of Solar Flares [191, IMIDSF, `https://helioportal.nas.nasa.gov`, accessed on 04/08/2019]. In the TEBBS algorithm, we add the Savitzky-Golay smoothing procedure with third-order polynomials and a 30-second running window function [199]. This allows us to perform analysis for relatively weak B-class flares and also compute smooth derivatives of the light curves.

For each event, we determine the maximum values and times of the temperature, emission measure, and background-subtracted SXR 1-8 Å flux and its derivative. We determine the flare end time as the moment when the background-subtracted flux drops by a factor of two from its maximum value. This definition is the same as in the GOES flare catalog but instead of the preflare SXR flux level we subtract the derived background. The resulting difference in the flare end times does not change our conclusions. Then, we calculate various parameters related to the flare temporal behavior: the duration, growth time (defined as the maximum time minus start time), relative growth time (defined as the growth time divided by the flare duration), and the time intervals among the maxima of T, EM, SXR, and SXR derivative. Following Reep and Toriumi [177] we calculate the FWHM of the GOES 1-8 Å light curve (defined as the difference between two time moments when the SXR reaches the half maximum value before and after its maximum) and its characteristic decay time, τ_{decay}, at the flare end defined as:

$$\tau_{decay} = -\frac{F_{SXR}(t)}{dF_{SXR}(t)/dt}|_{t=t_{end}} \tag{5.1}$$

In addition, when possible, we define the flare ribbon areas from the catalog by Kazachenko et al. [95] (for the events of the SDO epoch only). We exclude from our analysis the events, for which:

- The background-subtracted SXR maximum flux is lower than the flux of B1.0 class flare ($10^{-7}\,\mathrm{W\,m^{-2}}$) because of the low S/N ratio;
- The maximum temperature shows the presence of the super-hot plasma [39, >30 MK], indicating that the single-temperature model is not valid [210];

- The relative uncertainties of the maximum temperature or emission measure are greater than 100%;
- The maximum of the emission measure occurs when the flux in the GOES 0.5-4 Å channel is smaller than 1% of the flare maximum flux in this channel (i.e., almost at the level of the background);
- The gaps in the GOES data are longer than 5% of the flare duration;
- The TEBBS algorithm does not return any reliable background combination (for all combinations (1) the number of rising phase time bins is low, (2) the flare maximum temperature does not exceed 3 MK [187], or (3) the preflare T and EM values are higher than their maximum values during the flare);

We found that a total of 14955 out of 22728 flares satisfy these criteria. The flares, which do not satisfy the above criteria and are excluded from the consideration, are mainly weak B-class or C-class events. The final statistical sample includes 5915 B-class, 7774 C-class, 1159 M-class, and 107 X-class flare events. Hereafter, we consider the X-class flares in one group together with the M-class flares.

5.3 Results

5.3.1 Time Sequence of Events During Solar Flares

We compare the order of appearance of the maxima of T, EM, and SXR flux, as well as their derivatives, with the flare scenario illustrated in Figure 5.1. First, we found that 94.5% of B-class flares (5587 out of 5915), 97.3% of the C-class flares (7568 out of 7774), and 98.6% of M- and X-class flares (1248 out of 1266) follow the sequential appearance of the T, SXR, and EM maxima, i.e., the assumed chromospheric evaporation scenario. On average, 96.3% of all flares follow the sequence, and the fraction of such flares increases with the GOES class.

Second, we found that for 82.5% of all flare events (82.6% of B-class flares, 83.4% of C-class flares, and 76.7% of M- and X-class flares) the 1-8 Å SXR derivative maximum mainly occurs prior the T maximum. Interestingly, the fraction of such events does not increase with the GOES class, and even becomes lower for M- and X-class flares.

5.3.2 Physical Parameters Controlling the SXR Emission for Flares of Different Classes

In order to understand which of the two parameters, T or EM, determines the timing of the maximum of the SXR emission, we consider the time intervals between the SXR and T maxima and between the EM and SXR maxima. Two-dimensional diagrams of the SXR-T and EM-SXR intervals for different flare classes are presented in Figure 5.3. White horizontal and vertical dashed lines restrict the zones where events do not obey the sequential T, SXR, and EM maxima appearances. Inclined white dashed lines represent places in the histogram where one of the intervals is two times longer than another.

The relationships are very different for the different flare classes. Among the B-class flares (Figure 5.3a), 34.0% are T-controlled and 26.4% are EM-controlled. The situation is completely opposite for the M- and X-class flares (Figure 5.3c): the number of EM-controlled events is 82.8% and just 1.7% are T-controlled. The C-class flares (Figure 5.3b) fall between these two cases: 43.6% events are EM-controlled and 18.0% are T-controlled. We can see that the SXR maximum occurs very close to the EM maximum mostly for the M- and X-class flares and closer to the T maximum for the B-class flares. In this respect, the weak and strong flares behave differently.

Figures 5.4a and 5.4b show the dependence of the T and EM maximum values from the SXR maximum flux. It is essentially the same as previously presented by Ryan et al. [187]. As one can see, both the temperature and emission measure maxima are correlated with the SXR maximum, and the correlations for the EM are more prominent. For M- and X-class events (with the logarithm of the maximum flux of -5.0 or greater) the logarithm of the EM maximum is proportional to the logarithm of the SXR flux maximum.

Figure 5.4c presents the relationship between the flare SXR class as defined in the GOES flare catalog and the SXR maximum flux calculated after subtraction of

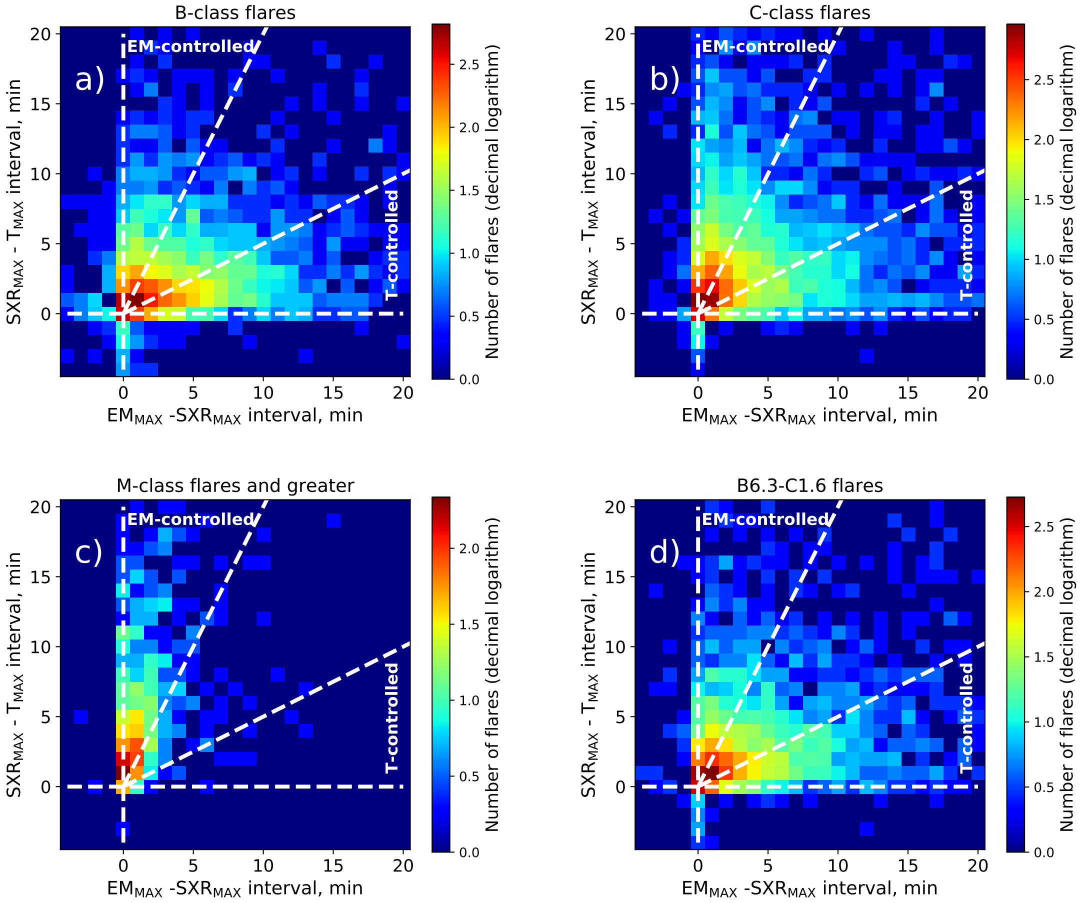

Figure 5.3 Two-dimensional relationships of the time intervals between the EM and SXR maxima (x-axis) and SXR and T maxima (y-axis) for a) B-class flares, b) C-class flares, and c) M- and X-class flares. White dashed lines show zones for the T-controlled events and the EM-controlled events. Panel (d) illustrates the same relationships for the flares of B6.3 - C1.6 classes.

Source: [193]

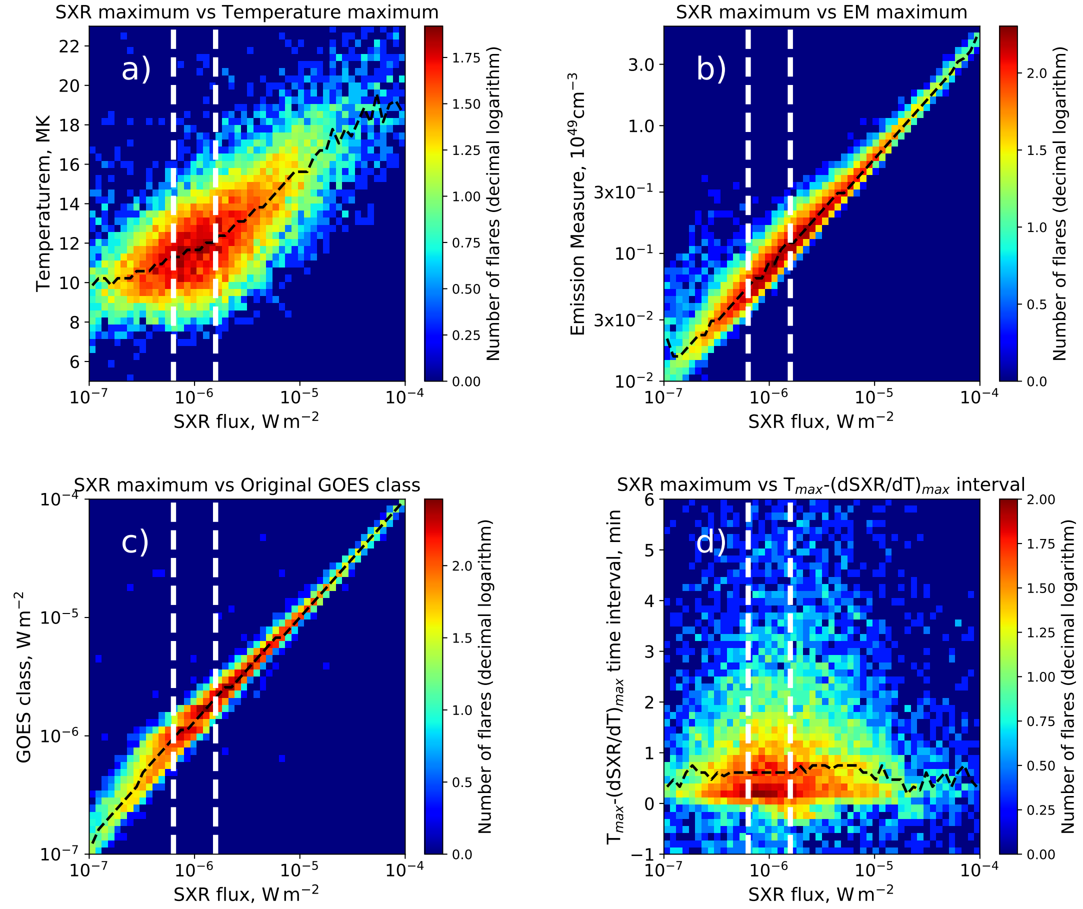

Figure 5.4 Two-dimensional relationships of (a) temperatures, (b) emission measures, (c) GOES classes, and (d) time intervals between the T and SXR derivative maxima of flare events, and their SXR maximum fluxes. Black dashed lines show median values for each SXR maximum flux. White vertical lines mark the B6.3 - C1.6 flare class range selected for the detailed study.

Source: [193]

the background. The background subtraction is especially important for the B-class and low C-class events, because, as is evident from the figure, the same SXR flux corresponds to a wide spread of the flare classes in the GOES catalog.

Figure 5.4d illustrates the relationship between the SXR maximum flux, and the time interval between the temperature and the SXR derivative maxima. As one can see, the temperature reaches the maximum in most cases after the derivative maximum. The median value of the time interval slightly varies with the SXR flux maximum, and for strong $\geq$M-class flares becomes smaller than for B-class and C-class flares (for the flares with SXR flux maxima of $< 10^{-5}\,\mathrm{W\,m^{-2}}$), although it does not exceed one minute for any flare class.

5.3.3 Difference between T-controlled and EM-controlled Events.

Figure 5.3 reveals a transition in behavior of the time intervals with an increase in the flare's SXR maximum flux. One should expect that in some range of the SXR maximum fluxes the number of the T- and EM-controlled events is almost the same. We have found that such situation happens when the logarithm of the SXR flux maximum (in $\mathrm{W\,m^{-2}}$) is between -6.20 and -5.80 (i.e., for the background-subtracted SXR classes of B6.3 - C1.6). Figure 5.3d illustrates the time interval relationship for this range. Among the selected flares, 1365 are EM-controlled, and 1176 are T-controlled. The B6.3 - C1.6 class range is indicated in Figure 5.4 by white vertical dashed lines.

Previously, we have concluded that the relationship between the SXR-T and EM-SXR time intervals depends on the SXR flux maximum. By selecting relatively narrow class ranges, we can study the influence of other physical parameters to the partition among the intervals. Table 5.1 summarizes the median values and corresponding median absolute deviations of physical parameters for the EM-controlled and T-controlled flares in several such class ranges. The median absolute deviation is a dispersion measure of a univariate data set, and is equal to a median of absolute deviations of the data points from the data set median. One can see the following trends from this table. Except for the ≥M1.0 class range (due to insufficient statistics), the T-controlled events are cooler on average than the EM-controlled events and have larger emission measures. Also, these events are typically longer in duration, but grow faster (have shorter relative growth times) and have greater FWHM and characteristic decay times.

Figure 5.5a-f presents histograms of various physical parameters for the T-controlled (red) and EM-controlled (gray) flare events of the B6.3 - C1.6 class range for the same characteristics as in Table 5.1. As one can see, although the distributions significantly overlap, they prominently differ from each other. The difference is especially visible for the relative growth times, where two peaks of the histogram are clearly separated. The histograms constructed for other class ranges (B1.0 - B2.5, B2.5 - B6.3, C1.6 - C4.0, and C4.0 - M1.0) are found to have similar behaviors.

5.4 Discussion and Conclusion

In this section, we summarize our answers to the questions posted in Section 5.1 and discuss possible explanations.

5.4.1 How Often do the Flares Obey the Scenario of the Chromospheric Evaporation Process Illustrated in Figure 5.1?

We found that the temperature (T), soft X-ray flux (SXR), and emission measure (EM) maxima appear sequentially during solar flares for most of analyzed events (96.3% on average). The fraction of such events increases with increasing SXR flux maximum. The observed sequence of the temperature, soft X-ray emission, and emission measure maxima fits into the standard picture of chromospheric evaporation,

Table 5.1 Median Values and Median Absolute Deviations of the SXR Characteristics of the T-controlled and EM-controlled Flares for Different GOES Class Ranges

GOES class	Regime	Number of events	Physical characteristics		Flare temporal characteristics, min				Number of events in Flare Ribbon Catalog
			T max, 10^6 K	EM max, 10^{48} cm^{-3}	Duration, min	Relative growth time, min	FWHM, min	Decay time, min	
B1.0 - B2.5	T-controlled	329	9.87±0.71	0.23±0.06	13.2±5.0	0.43±0.09	9.20±4.00	3.79±1.12	0
	EM-controlled	198	10.9±1.1	0.17±0.04	11.2±4.9	0.57±0.10	6.98±3.43	3.33±1.39	0
B2.5 - B6.3	T-controlled	946	10.6±0.9	0.43±0.09	15.2±6.3	0.44±0.09	10.6±4.2	6.44±2.38	19
	EM-controlled	639	11.1±0.9	0.36±0.07	11.8±5.1	0.60±0.09	7.65±3.65	5.06±2.43	18
B6.3 - C1.6	T-controlled	1176	11.2±0.9	0.89±0.22	20.4±10.2	0.42±0.09	14.2±6.6	9.20±4.64	228
	EM-controlled	1365	12.0±1.1	0.80±0.18	13.5±5.9	0.58±0.09	8.65±4.30	6.00±3.33	240
C1.6 - C4.0	T-controlled	660	12.0±1.1	1.80±0.38	23.1±10.9	0.42±0.10	16.3±7.6	6.49±2.98	112
	EM-controlled	1434	13.3±1.1	1.69±0.34	15.0±6.4	0.58±0.09	9.73±4.88	5.83±2.87	289
C4.0 - M1.0	T-controlled	155	13.3±1.2	3.77±0.73	32.6±14.7	0.40±0.13	24.2±11.8	11.2±4.35	23
	EM-controlled	1138	14.9±1.2	3.67±0.74	16.9±7.4	0.59±0.10	10.6±5.4	8.12±4.19	273
≥M1.0	T-controlled	21	16.0±1.1	8.37±1.38	31.5±16.0	0.50±0.18	23.6±15.3	8.90±5.23	4
	EM-controlled	1030	17.5±1.6	11.1±4.5	20.5±9.6	0.61±0.09	11.4±6.0	8.27±4.39	215

Note: The last column gives the number of events for which information about the flare ribbon areas is available [95].

Source: [193].

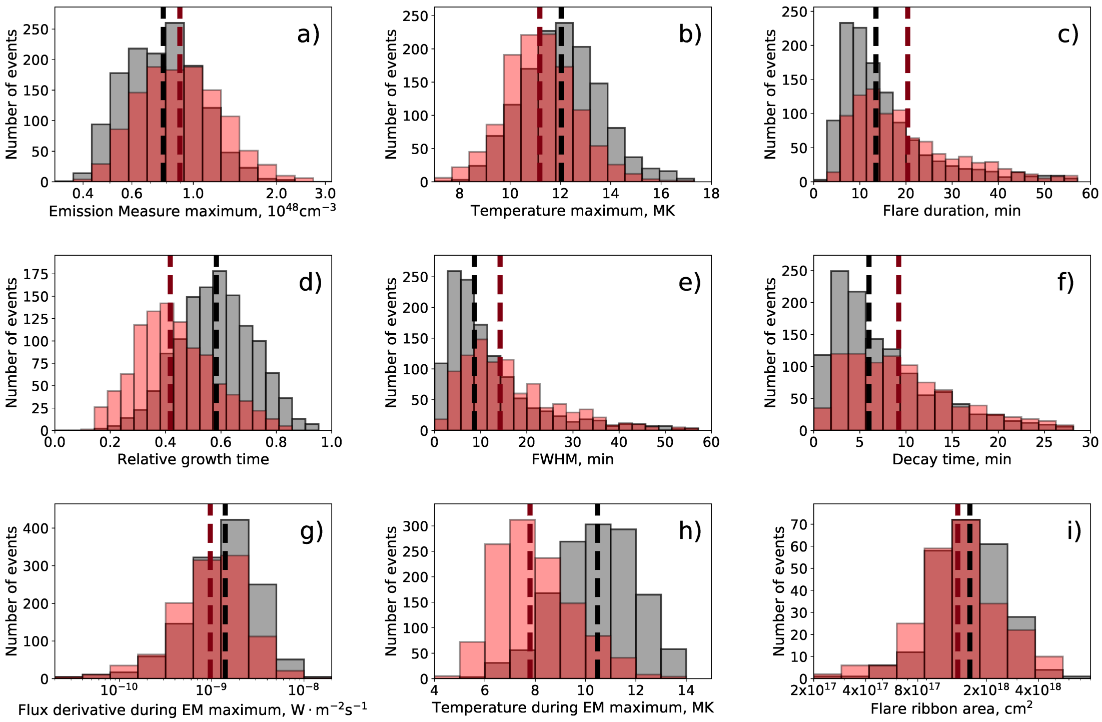

Figure 5.5 Histograms for the T-controlled (red) and the EM-controlled (gray) events of (a) EM maxima, (b) T maxima, (c) duration of the event, (d) event growth time (from SXR start to maximum time) normalized to the duration of the event, (e) FWHM, (f) characteristic decay time, (g) the SXR derivative during the EM maximum, (h) temperature during the EM maximum, and (i) ribbon areas of the events, for the flares of B6.3 - C1.6 GOES classes. Red dashed vertical line represents the median value for T-controlled events, black — for EM-controlled events. The median absolute deviations are presented in Table 5.1.

Source: [193]

supported by the radiative hydrodynamic simulations (Figure 5.1). However, what is the reason for the remaining 3.7% (552 out of 14955) of events not following the sequence? Most of these events are weak B-class flares. Possibly, the T and EM calculations for weak events are not sufficiently accurate because of the relatively strong background level during these events.

Another interesting fact is that, for most flares, the SXR derivative maximum occurs even before the temperature maximum. According to the Neupert effect [154], the derivative of the SXR flux are correlated with the time of the energy deposit of high-energy electrons. Therefore, for most of events the strongest energy deposit happens before the plasma reaches the highest temperature, because some time is required for the deposited energy to heat the plasma. This is in agreement with the considered RADYN simulation (Figures 5.1b and 5.1c). Note that the fraction of such events decreases with the flare class. We do not try to explain this in the present study.

5.4.2 Which of the Plasma Properties, T or EM, Mainly Influence the SXR Maximum Value and Timing for the Different GOES Flare Classes?

Figure 5.3 illustrates that the temperature, emission measure, and SXR 1-8 Å flux light curves behave differently for different class flares. For the weak B-class flare events, we see that the SXR maximum predominantly occurs closer to the T maximum than to the EM maximum. For the stronger M- and X-class flares, the SXR maximum occurs very close to the emission measure maximum. Also, Figure 5.4b illustrates that the logarithm of the SXR maximum is proportional to the logarithm of the EM maximum for strong flares. Thus, one can conclude that the GOES class of strong M- and X-class flares most often represents the emission measure of the evaporated plasma and not the plasma temperature.

In contrast, for the weak B-class flares we see that the SXR maximum is close to the T maximum. However, Figure 5.3a (illustrating the relations between the T and SXR maxima) does not show any direct relations between these two parameters for weak B-class flares. This means that for the weak events the corrected-for-background GOES class depends on both the temperature and emission measure.

5.4.3 What is the Physical Difference between the T-controlled and EM-controlled Flares of the Same GOES Class Range?

Our results indicate that for relatively narrow class ranges (see Table 5.1) the T-controlled events are colder, have larger maximum EMs, are longer in duration, have shorter relative growth times, and have longer FWHMs as well as longer decay times. One of the possibilities is that the high-temperature plasma in the T-controlled events evolves in longer magnetic loops than in the EM-controlled events.

Several previous studies point to this conclusion. For example, Bowen et al. [25] performed a statistical study of 17 flares of the ≈C8 class simultaneously observed by GOES, SDO/AIA, and SDO/EVE. The authors found that the flares with longer durations are usually cooler and evolve in larger volumes. As was mentioned before, the T-controlled events are on average longer and have lower temperatures than the EM-controlled flares and thus should evolve in larger volumes to maintain the observed EM level. Figure 5.5i illustrates the flare ribbon areas for events of the B6.3 - C1.6 class range from the flare ribbon catalog [95]. One can see that the ribbon areas on average are almost the same for the T-controlled and EM-controlled events. Thus, the larger volumes with the same ribbon areas will correspond to the longer loops. Several works based on the classical relations for coronal loop parameters [181] predicted longer decay times for the events evolving in longer loops [205, 11]. As seen in Table 5.1, the characteristic decay times are longer for the T-controlled events than for the EM-controlled events.

Reep and Toriumi [177] provided direct observational and modeling relations between the GOES SXR light curve parameters (FWHM and characteristic decay times) and the distances between the flare ribbons. One of the conclusions of this work is that the events with longer FWHM and decay times should have larger separation of flare ribbons, i.e., evolve in longer loops. Although the observational relations in Reep and Toriumi [177] are derived for the flares of M 5.0 GOES class or higher, the modeled SXR emission linearly scales with the assumed cross-section area, which makes it possible to extend the modeling relations to any GOES classes. The T-controlled events from our study have longer FWHMs and decay times and thus should evolve in longer loops according to the conclusion of Reep and Toriumi [177].

For further interpretation, we analyze the dynamics during the flare decay phase using the analytical equations for the spatially-averaged plasma parameters in magnetic loops implemented in Enthalpy-Based Thermal Evolution of Loops model [105, 35, 36, EBTEL]. Following Eq. 2 in Cargill et al. [35]:

$$\frac{L}{2(\gamma-1)}\frac{dp}{dt} = \frac{\gamma}{\gamma-1}p_0v_0 - F_0 + \frac{L}{2}Q - \frac{L}{2}n^2\Lambda(T) \tag{5.2}$$

Here p, n, T are the pressure, number density, and temperature averaged along the loop; γ is the adiabatic constant, L is the length of the loop, $F_0 = \kappa_0 T^{5/2}\frac{\partial T}{\partial s}|_{s=0}$ is the heat conduction flux at the loop footpoint, Q is the heating term, and $\Lambda(T)$ is the radiative loss function depending on the temperature. We consider the loop energetics during the EM maximum time for the four flare class ranges (B2.5 - B6.3, B6.3 - C1.6, C1.6 - C4.0, and C4.0 - M1.0), for which we have statistics for flares with defined ribbon areas (last column in Table 5.1). The B6.3 - C1.6 class properties presented in Figure 5.5g-i show that the T-controlled events have slightly lower SXR 1-8 Å derivative and lower temperatures during the EM maximum, and almost the same flare ribbon areas compared to the EM-controlled events. The median values of these parameters for the considered flare class ranges are summarized in Table 5.2.

Table 5.2 Median Values and Median Absolute Deviations of the SXR Flux Derivative and Temperature during EM Maximum, Flare Ribbon Area, and Loop Length of the T-controlled and EM-controlled Flares for Different GOES Class Ranges

GOES class	Regime	Flux derivative during EM maximum, 10^{-9} W m^{-2}s^{-1}	Temperature during EM maximum, MK	Flare ribbon area, 10^{18} cm^2	Loop lengths, 10^8 cm		
					$F_0 = 10^6$ erg cm^{-2}s^{-1}	$F_0 = 10^7$ erg cm^{-2}s^{-1}	$F_0 = 10^8$ erg cm^{-2}s^{-1}
B2.5 - B6.3	T-controlled	0.55±0.30	7.11±0.95	1.04±0.50	1.32±1.14	4.82±3.82	104.4±78.7
	EM-controlled	0.74±0.41	9.57±0.97	0.99±0.22	0.63±0.44	1.46±1.07	41.2±31.5
B6.3 - C1.6	T-controlled	0.97±0.58	7.79±1.02	1.36±0.42	6.18±5.42	12.9±10.7	189.3±154.2
	EM-controlled	1.40±0.81	10.48±1.13	1.60±0.50	2.34±2.03	5.44±4.50	85.4±71.5
C1.6 - C4.0	T-controlled	2.06±1.20	8.76±1.31	2.45±0.78	6.20±5.21	10.4±8.5	146.0±116.3
	EM-controlled	2.70±1.36	11.59±1.21	2.27±0.69	3.31±2.70	6.33±5.21	86.0±69.9
C4.0 - M1.0	T-controlled	3.26±1.91	9.89±1.48	4.01±1.58	24.8±18.4	36.0±27.9	411.4±359.6
	EM-controlled	5.01±2.48	13.08±1.03	3.57±1.02	6.70±5.53	10.2±8.3	98.3±82.1

Note: Loop lengths are is estimated from Eq. 5.6 for every event for each of three values of conduction flux, F_0, presented in the table.
Source: [191].

We assume that during the emission measure maximum, the inflow and outflow of plasma into the flare volume are balanced, $p_0v_0 = 0$, there is no heating along the loop at that time, i.e., $\frac{L}{2}Q = 0$, and there is no change of the flare volume, $\frac{dEM}{dt} = 0 \Rightarrow \frac{dn}{dt} = 0$. Following Rosner et al. [181], Aschwanden et al. [11], Aschwanden and Tsiklauri [12], we approximate the radiative loss function in the 2-40 MK temperature range as $\Lambda(T) \sim 10^{-17.73}T^{-2/3} = \Lambda T^{-2/3}$. The equation of state is taken to be $p = nk_BT$. The emission measure is $EM = n^2LS$, where S is the cross-sectional area of the loop. Then, from Eq. 5.2 we obtain:

$$\frac{dT}{dt} = \frac{2(\gamma-1)}{k_BL}\sqrt{LS/EM}(-F_0 - EM\frac{\Lambda}{2ST^{2/3}}) \tag{5.3}$$

Following White et al. [237], the GOES flux in 1-8 Å channel can be represented as $F_{1-8\mathring{A}} = C \times EM \times \phi(T)$, where $\phi(T)$ is the function corresponding to the coronal element abundances shown in lower panel of Figure 7 of White et al. [237]. Assuming linear behavior of $\phi(T)$ in the temperature range from 5 to 15 MK, we approximate $\phi(T) = AT + B$. Parameters C and A are estimated from the tabulated functions for T and EM calculation available in the SolarSoft package (the SXR flux per unit emission measure as a function of temperature). The results are averaged for the GOES10 — GOES15 satellites (the difference is negligible). The derived parameter values are $C = 0.7 \times 10^{-55}\,\mathrm{erg\,cm\,s^{-1}}$, $A = 2.22 \times 10^{-3}\,\mathrm{K^{-1}}$. The flux equation becomes $F_{1-8\mathring{A}} = C \times EM \times (AT + B)$. At the EM maximum $\frac{dEM}{dt} = 0$, hence:

$$\frac{dF_{1-8\mathring{A}}}{dt} = A \times C \times EM\frac{dT}{dt} \tag{5.4}$$

Replacing the temperature derivative from Eq. 5.3 we obtain:

$$\frac{dF_{1-8\mathring{A}}}{dt} = -\frac{1}{\sqrt{L}}\sqrt{EM \times S}\left(F_0 + EM\frac{\Lambda}{2ST^{2/3}}\right)\frac{2AC(\gamma-1)}{k_B} \tag{5.5}$$

$$L = EM \times S\left(\frac{dF_{1-8\mathring{A}}}{dt}\right)^{-2}\left(F_0 + EM\frac{\Lambda}{2ST^{2/3}}\right)^2\frac{4A^2C^2(\gamma-1)^2}{k_B^2} \tag{5.6}$$

There are two processes which can decrease the SXR flux: heat conduction at the loop footpoints and radiative losses along the loop. $F_0 = \kappa_0 T^{5/2} \frac{\partial T}{\partial s}|_{s=0}$, where $\kappa_0 \approx 10^{-6}\mathrm{erg\,s^{-1}\,cm^{-1}\,K^{-7/2}}$ [215], represents the conduction flux at the loop footpoints. If the temperature increases from $T \approx 10^4\,\mathrm{K}$ to $T \approx 10^6\,\mathrm{K}$ at the loop footpoints on scales of $\approx 1000\,\mathrm{km}$, then $\frac{\partial T}{\partial s} \approx 10^{-2}\,\mathrm{K\,cm^{-1}}$, and flux in the transition region is $10^7\,\mathrm{erg\,cm^{-2}s^{-1}}$. Notice that the radiative loss term is comparable with the conduction flux: for example, for the median characteristics of B6.3 - C1.6 class events $\frac{EM \times \Lambda}{2ST^{2/3}} \approx (2-3) \times 10^7\,\mathrm{erg\,cm^{-2}s^{-1}}$, where $\Lambda = 10^{-17.73}\,\mathrm{erg\,cm^3\,K\,s^{-1}}$, $T \approx (8-10) \times 10^6\,\mathrm{K}$, $EM = (8-9) \times 10^{47}\,\mathrm{cm^{-3}}$, $S \approx (0.7-0.8) \times 10^{18}\,\mathrm{cm^2}$ (half of the ribbon area).

Assuming $F_0 = 10^7\,\mathrm{erg\,cm^{-2}s^{-1}}$ and the flaring loop cross-sections $S = S_{ribbon}/2$, we estimate from Eq. 5.6 the lengths of the loops where the chromospheric evaporation was developed for every flare (for which information about the flare ribbon areas is available) in the B2.5 - B6.3, B6.3 - C1.6, C1.6 - C4.0, and C4.0 - M1.0 class ranges. The histograms for the selected class ranges are presented in Figure 5.6. The corresponding median values are presented in Table 5.2 (column for $F_0 = 10^7\,\mathrm{erg\,cm^{-2}s^{-1}}$). The median values of the loop lengths are 2 - 4 times longer for the T-controlled flares in all selected class ranges than those for the EM-controlled events. Variation of the conduction flux from $10^6\,\mathrm{erg\,cm^{-2}s^{-1}}$ to $10^8\,\mathrm{erg\,cm^{-2}s^{-1}}$ leads to the same conclusion about the loop lengths (see Table 5.2). However, high conduction fluxes ($\geq 10^8\,\mathrm{erg\,cm^{-2}s^{-1}}$) result in unrealistic median loop lengths of $\geq 10^{10}\,\mathrm{cm}$. The results allow us to conclude that the development of flares in coronal loops of different length can be one of the reasons for the difference between the T-controlled and EM-controlled events.

In the case of two or more temporarily-overlapping distinct events of approximately the same magnitude occurring at the solar disk, the presented analysis is not valid. To estimate the influence of this effect, we analyzed spatially-

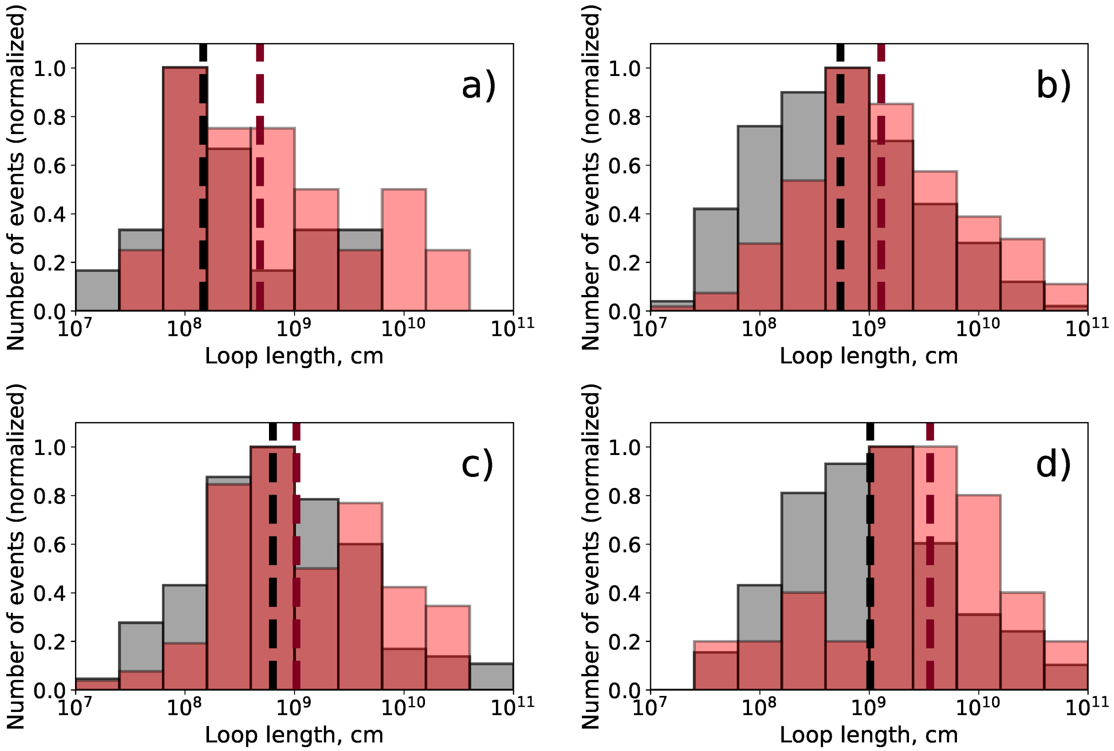

Figure 5.6 Histograms of the loop lengths calculated from Eq. 5.6 (for $F_0 = 10^7\,\mathrm{erg\,cm^{-2}s^{-1}}$) for T-controlled (red) and EM-controlled (gray) events of (a) B2.5 - B6.3, (b) B6.3 - C1.6, (c) C1.6 - C4.0, and (d) C4.0 - M1.0 GOES class ranges. Red dashed vertical line represents the median value for T-controlled events, black — for EM-controlled events. The median absolute deviations are presented in Table 5.2.

Source: [193]

resolved observations of flares obtained from the 131 Å data of the Atmospheric Imaging Assembly onboard Solar Dynamics Observatory [125, SDO/AIA] using image processing algorithms [138]. These data are collected in the Heliophysics Event Knowledgebase [88, HEK], which is incorporated in the IMIDSF [191]. We found that in 2010-2017 about 6.5% (530 out of 8115 events) of the GOES flares with the SDO/AIA 131 Å counterparts were overlapping with other flares of comparable EUV magnitude (at least a half of the EUV flux of the primary flare identified in the GOES catalog). However, the analysis of such overlapping events led us to qualitatively the same conclusions as for the entire data set (i.e., the existence of temporarily-overlapping flare events did not influence our conclusions).

Our conclusions are the following:

1. The soft X-ray radiation of most flares (96.3%) follows the sequential appearance of the temperature (T), radiation flux (SXR), and emission measure (EM) maxima in agreement with the chromospheric evaporation scenario. The fraction of such flares increases with the amplitude of the SXR maximum (GOES X-ray class). For 82.5% of such flares, the SXR derivative reaches its maximum before the T maximum.
2. The SXR maximum of weak B-class flares mainly occurs very close to the temperature maximum (34.0% of the events are the T-controlled). The situation is opposite for the M- and X-class flares, 82.8% of which are EM-controlled;
3. The transition between the two regimes occurs in the range of X-ray class B6.3 - C1.6. The number of the T-controlled (1176) and EM-controlled (1365) events is almost the same in this class range;
4. The following differences in the averaged physical parameters are found for the T-controlled and EM-controlled events (see Table 5.1). Compared to the EM-controlled events, the T-controlled events have:
    - larger maximum emission measure and lower maximum temperature;
    - shorter relative growth time and longer duration;
    - larger SXR FWHM and longer characteristic decay times;
5. The lengths of the flare loops estimated from the analysis of a single loop dynamics supports the conclusion that the T-controlled events can be developed in longer loops than the EM-controlled events.

This interpretation of the statistical results is based on several simplifications due to the limited information in the GOES data. It does not take into account the possible presence of heating in the gradual and decay phases of the flare [49, 48, 186] and the multi-thread nature of solar flares when the different coronal loops are heated at different times [233]. Also, we consider a single-temperature approximation of the flaring plasma, although there is evidence for its multi-thermal structure [232, 210]. Further studies with the use of complimentary observations by RHESSI [39], SDO/AIA [125, 188], SDO/EVE [145], SphinX/CORONAS-Photon [77, 102], etc. will increase understanding of the limitations of the single-temperature plasma approximation. Nevertheless, the statistical analysis of 14955 events performed in this study allows us to better understand the physical characteristics of flare SXR emission.

CHAPTER 6

BEHAVIOR OF SDO/HMI OBSERVABLES FOR SOLAR ATMOSPHERE HEATED BY PRECIPITATING HIGH-ENERGY ELECTRONS

6.1 Introduction

Observations of changes of line-of-sight (LOS) photospheric magnetic fields in active regions during solar flares are of high interest for both individual case studies, and for larger scale statistical studies [132, 40]. The LOS magnetic field maps obtained by the Helioseismic and Magnetic Imager onboard the Solar Dynamics Observatory [200, 44, SDO/HMI] currently represent one of the most widely-used data product in solar physics. Correct interpretation of these measurements is important for understanding the underlying physics and expansion of our knowledge about magnetic energy release in solar flares.

The HMI measurements take 45 s during which the Fe 6173 Å line formed deep in the solar photosphere [158, 152, 103, at the height range of 0-300 km] is scanned at six wavelength points (filtergrams) in two polarizations (right-circular, RCP, and left-circular, LCP). The HMI observables (line depth and width, continuum intensity, Doppler velocity, and LOS magnetic field) are calculated from the filtergrams using a line profile model. If the characteristic times of variations of the Fe I line profile are comparable with the time required for one observing sequence, then one should expect deviations of the HMI observables from the actual line parameters (and consequently, derived atmospheric parameters). Consideration of the non-instantaneous nature of the measurements is especially important for interpretation of “magnetic transients” — reversible sharp changes of magnetic field measured during the solar flares [244, 162]. Previous reports of such magnetic transients observed from SOHO/MDI and SDO/HMI concluded that such transients may represent real changes of magnetic field strength [113, 242, 82] as well as artifacts due to rapid changes of the line profile and data analysis algorithms [171, 141].

The CSHKP flare model [38, 218, 83, 108, 169, 212], often referred as the standard flare model, is a scenario in which the solar atmosphere is heated by precipitating high-energy electrons accelerated in the corona. Many results [209, 207, etc.] found that impulsive variations observed in SDO/HMI filtergrams are highly correlated with the Hard X-ray (HXR) signals, thus qualitatively supporting the standard model and demonstrating that deposited high-energy particles can disturb the photosphere. Radiative hydrodynamic simulations of the standard flare model developed in recent years allow us to investigate effects of the flare energy release on the HMI observables. Currently one of the most advanced codes for flare modeling is RADYN, a radiative hydrodynamic code [37, 2, 5, 6, 7]. A grid of RADYN models is available online from the F-CHROMA project (`http://www.fchroma.org/`), allowing us to investigate the response of the solar photosphere to impulsive beam heating.

We use the RADYN models to simulate the Fe I 6173 Å line Stokes profiles, and derive the corresponding SDO/HMI observables by applying to the synthetic data the data analysis algorithms implemented in the SDO/HMI JSOC pipeline. We analyze how strongly the synthetic observables deviate from the actual properties of the line profile and atmospheric conditions in the flare models. The modeling of the Fe 6173 Å spectral line and procedure of SDO/HMI LOS observable calculations are explained in Section 6.2. The results are presented in Section 6.3, followed by a short discussion in Section 6.4.

6.2 Modeling of SDO/HMI Observables

The F-CHROMA database is a collection of 1D radiative hydrodynamic (RADYN) models of solar flares driven by an electron beam of a power-law electron energy distribution (averaged energy fluxes from $1.5\times10^{9}\,\mathrm{erg\,cm^{-2}s^{-1}}$ to $5.0\times10^{10}\,\mathrm{erg\,cm^{-2}s^{-1}}$, low-energy cutoff values of 10 keV, 15 keV, 20 keV, or 25 keV, and spectral indexes ranging from 3 to 8) heating the atmosphere for 20 s. The RADYN code solves coupled, non-linear, equations of hydrodynamics, radiation transport, and non-equilibrium atomic level populations, using an adaptive 1D vertical grid. The elements that are important for the chromospheric energy balance are treated in non-Local Thermodynamic Equilibrium (NLTE), and other species are included in the radiative loss function in the LTE approximation. The atomic level population and radiation transport equations are solved for a 6-level-with-continuum hydrogen atom, a 9-level-with-continuum helium atom, and a 6-level-with-continuum Ca II atom. For a detailed description see Allred et al. [7] and references therein. In the F-CHROMA database, the 1D flare models are calculated with 300 height grid points and 201 frequency points of the radiation spectrum. The initial atmosphere is similar to the VAL3C model [229], but with a somewhat deeper transition region. The temporal profile of the deposited energy flux rate is a triangle; the electron beam heating lasts for 20 s with a peak at 10 s. In addition to the F-CHROMA models, we consider one high-energy RADYN model. This model, which was used in Kerr et al. [98], injected an electron beam of constant flux, $\mathrm{F} = 1.0\times10^{11}\,\mathrm{erg\,cm^{-2}s^{-1}}$, for a period of 10 s. The electron beam spectra had a 20 keV low-energy cutoff, and a power law index of $\delta = 4$. This high energy model (called “GSK19” hereafter) also used a different pre-flare atmosphere: a hotter and denser corona (3 MK vs 1 MK). See Kerr et al. [98] for further details of this simulation. In Figure 6.1 we show the atmospheric stratification for the pre-flare atmospheres, along with the temporal profiles of energy injection.

For 80 available F-CHROMA models and for the GSK19 model, we calculate the Stokes profiles for the Fe I 6173 Å line using the RH radiative transfer code [189, 190, 227, 164]. The latest massively-parallel version of the RH 1.5D code [164] has been adopted for the calculations. Snapshots of the RADYN flare atmospheres were used as input to RH. Since RH is a stationary code, the NLTE atomic level

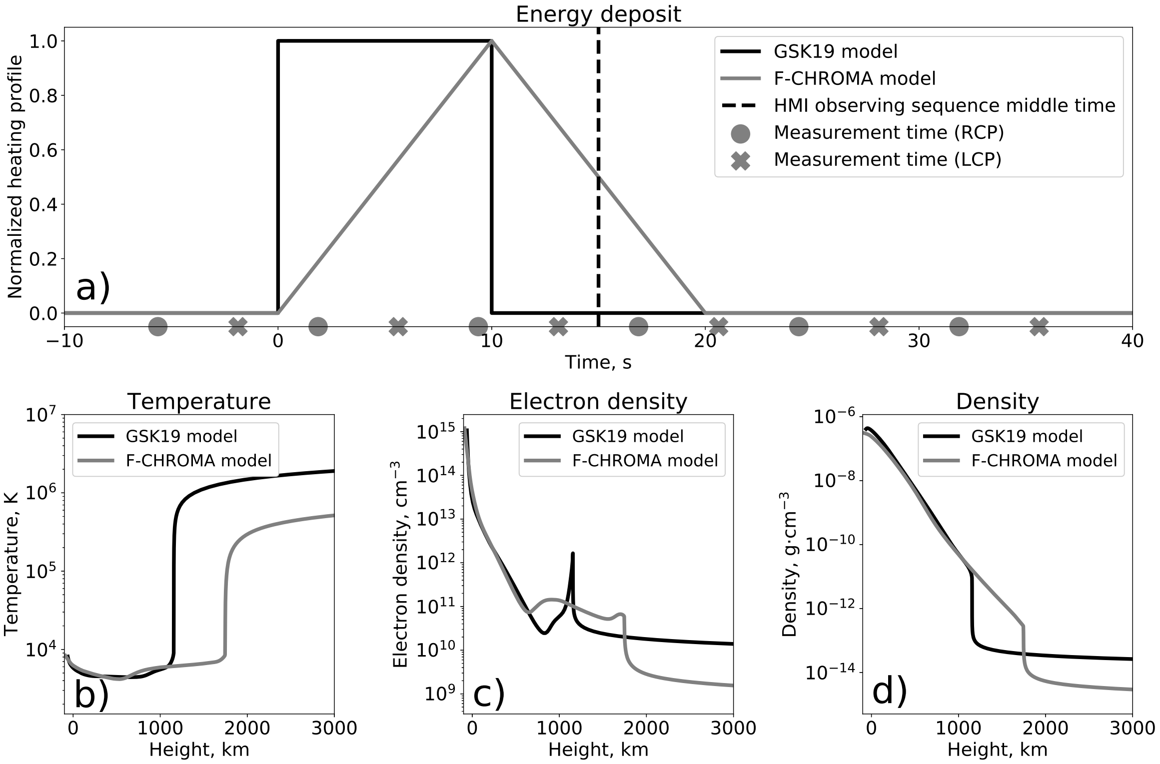

Figure 6.1 Illustration of (a) heating profiles, (b) initial temperatures, (c) initial electron number densities, and (d) initial densities for RADYN models from F-CHROMA database and for GSK19 model. Markers on the x-axis illustrate HMI LOS observing sequence and point out when RCP and LCP filtergrams are assumed to be taken. Dashed black vertical line shows the middle time of the illustrated observing sequence.

Source: [195]

populations were solved using statistical equilibrium, meaning that non-equilibrium and non-thermal effects are not included in our model. This is somewhat mitigated by using the non-equilibrium electron density from the RADYN snapshots. This procedure has been used by others [99, 182, 196]. To take into account magnetic field effects we make a simplistic assumption that the beam heating occurs in a vertical flux tube with a 100 G or 1000 G uniform vertical magnetic field. The vertical magnetic field does not affect the flare hydrodynamics in the models but affects the line properties. The Fe atom (described by 31 Fe I bound states, one singly-ionized Fe II state, and one two times-ionized Fe III state) was calculated in non-LTE statistical equilibrium simultaneously with H atom and Si atom. Other species were excluded from calculations because they did not affect the Fe I 6173 Å line profile. We included 2 km/s microturbulence in the line profile calculations. For each model, the calculations are performed with 1 s time step, and the resulting Stokes profiles are interpolated linearly for any time moment required for calculation of the observables. The right-circular polarization (RCP) and left-circular polarization (LCP) signals are derived from the Stokes I and V profiles. For each considered snapshot, we derive the line continuum as an averaged intensity at $\pm 0.20\,\mathring{A}$ from the line reference wavelength (λ_{ref} =6173.3390 Å), the line depth as the continuum intensity minus the average of the smallest intensities in the LCP and RCP signals. The line Doppler shift is calculated using the center-of-gravity approach $\triangle\lambda =< \lambda > -\lambda_{ref} = \int_{\lambda_{ref}-0.2\,\mathring{A}}^{\lambda_{ref}+0.2\,\mathring{A}}(I - I_c)d\lambda - \lambda_{ref}$. The examples of the atmospheric properties and the polarization profiles for the “val3c_d4_1.0e12_t20s_20keV” F-CHROMA RADYN model (which has the average deposited energy flux of $5.0 \times 10^{10}\,\mathrm{erg\,cm^{-2}\,s^{-1}}$, the power law index of the injected electron spectrum of 4, and the low-energy cutoff of 20 keV) are illustrated in Figure 6.2 for $t = 0\,\mathrm{s}$ and $t = 10\,\mathrm{s}$ snapshots. The 100 G uniform magnetic field is assumed. The neutral and ionized Fe number densities are computed using Chianti atomic database [119].

Each RADYN run lasts 50 s from the beginning of the beam impact. For the purposes of processing the synthetic results through the SDO/HMI pipeline, we assumed that the pre-flare state was unvarying. We replicated the pre-flare state for 42 s. We then replicated the final RADYN snapshot ($t = 50\,$s) for additional 42 seconds at the end of the simulation. The flare phases were then: pre-flare $t = -42 - 0\,$s, energy injection $t = 0 - 20\,$s, dynamic cooling phase $t = 20 - 50\,$s, fixed cooling phase $t = 50 - 92\,$s. We are aware that this final "fixed" cooling phase is rather unrealistic as the atmosphere would continue to radiate and conduct in a dynamic fashion since it had not reached equilibrium. However, for the purposes of this experiment it is a sufficient approximation. At a cadence of 1 s between $t = -21\,$s and $t = 71\,$s, we apply the HMI observing sequence algorithm as illustrated in Figure 6.1a. The filtergrams correspond to $\pm 34.4\, m\mathring{A}$, $\pm 103.2\, m\mathring{A}$, and $172.0 \pm\, m\mathring{A}$ relative to λ_{ref} [152]. The temporal order of scanned wavelength is assumed as in Table 3 of Schou et al. [202]. The SDO/HMI transmission profiles for each measurement are modeled with the Gaussian of $FWHM = 76\, m\mathring{A}$ [82]. Also, the measurements are integrated for 3.75 s centered at the time point of the filtergram. The examples of the synthesized SDO/HMI measurements for the RADYN model "val3c_d4_1.0e12_t20s_20keV" and the observing sequences centered at $t = 0\,$s and $t = 10\,$s time moments are also illustrated in Figure 6.2.

We calculate the line width, line depth, Doppler shift and vertical LOS magnetic field following the procedure described by Couvidat et al. [44, 46, 45]. First, we estimate the first and second Fourier components of the line profile separately for each polarization sequence as:

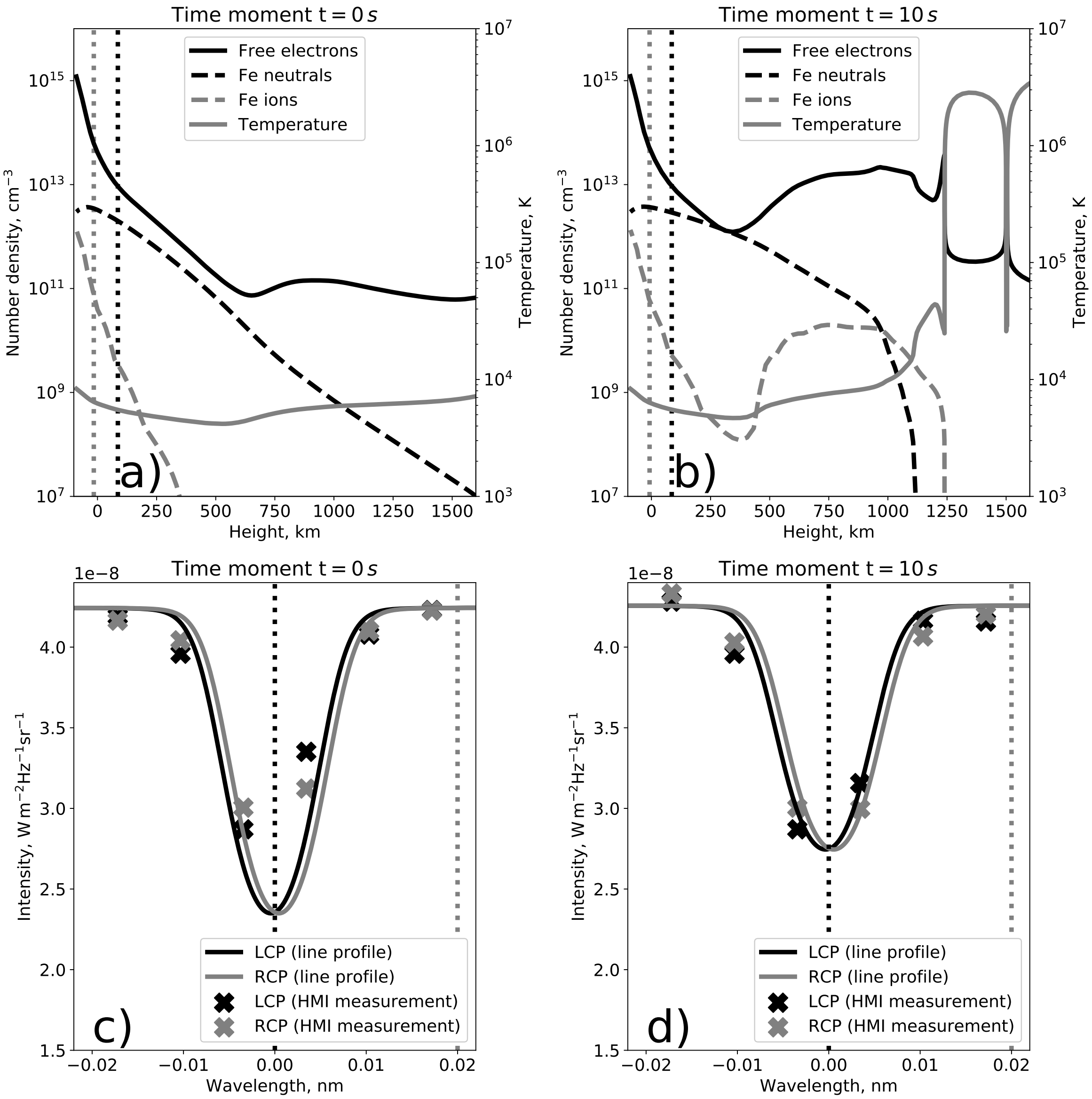

Figure 6.2 Illustration of the atmospheric properties (a,b) and Fe I 6173 Å line profiles (c,d) for $t = 0$ s and $t = 10$ s snapshots of the "val3c_d4_1.0e12_t20s_20keV" RADYN model. Corresponding SDO/HMI filtergram signals obtained for measurement series centered at $t = 0$ s and $t = 10$ s are also presented in panels (c) and (d). The dashed vertical lines in panels (a,b) correspond to $\tau = 1$ optical depths for the Fe I 6173 Å line center (black) and continuum (gray), the wavelengths are correspondingly marked in panels (c,d).

Source: [195]

$$a_k \approx \frac{2}{6}\sum_{j=0}^{5} I_j \mathrm{cos}(2k\pi\frac{2.5-j}{6}), k=1,2 \tag{6.1}$$

$$b_k \approx \frac{2}{6}\sum_{j=0}^{5} I_j \mathrm{sin}(2k\pi\frac{2.5-j}{6}), k=1,2 \tag{6.2}$$

Then, we estimate the line depth, line width, Doppler velocity and LOS magnetic field strength as:

$$v_1 = \frac{dv}{d\lambda}\frac{T}{2\pi}\mathrm{atan}\left(\frac{b_1}{a_1}\right) \tag{6.3}$$

$$\lambda_0 = \lambda_{ref} + v_1\frac{d\lambda}{dv} \tag{6.4}$$

$$v = \frac{v_1^{LCP} + v_1^{RCP}}{2} \tag{6.5}$$

$$B = (v_1^{LCP} - v_1^{RCP})K_m \tag{6.6}$$

$$I_d = \frac{T}{2\sigma\sqrt{\pi}}\sqrt{a_1^2+b_1^2}\mathrm{exp}\left(\frac{\pi^2\sigma^2}{T^2}\right) \tag{6.7}$$

$$I_c = \frac{1}{6}\sum_{j=0}^{5}\left[I_j + I_d\mathrm{exp}\left(-\frac{(\lambda_j-\lambda_0)^2}{\sigma^2}\right)\right] \tag{6.8}$$

Here $K_m = 0.231\,\mathrm{G\,m^{-1}}$, $\frac{dv}{d\lambda} = 48562.4\,\mathrm{ms^{-1}Å^{-1}}$, T =412.8 mÅ. We do not apply any velocity corrections from the lookup tables suggested in Couvidat et al. [45] as they lead to incorrect estimates of the vertical magnetic field in the unperturbed atmosphere. In the SDO/HMI algorithm, a significant error comes from incorrect determination of the Gaussian line widths because of the coarse sampling of the line profile. The correction implemented in the SDO/HMI pipeline is based on azimuthal average of the measured width derived at the solar disc center obtained during a period of low solar activity [45]. In our calculations, we assume that the exact line width is derived from the preflare state ($\sigma = 0.0623\,\mathring{A}$ at $t = 0\,\mathrm{s}$). In addition, we multiplied the line width used in the above equations, as well as the resulting line depth, by the correction coefficients, $K_2 = 6/5$ and $K_1 = 5/6$, respectively as suggested by Couvidat et al. [45].

6.3 Results

Figure 6.3 illustrates the Fe I line properties derived from the simulated line profiles, "instant" HMI observables (the results of instantaneous application of the HMI observing sequence to the current line profile), and the HMI observables obtained with the proper timing for the "val3c_d4_1.0e12_t20s_20keV" F-CHROMA RADYN flare model. Two setups with vertical uniform magnetic field of 100 G and 1000 G are considered. Panels (a) and (b) in Figure 6.3 show that perturbations of the continuum level do not exceed 6% during the flare. Deviations of the HMI line-depth observable (panels c and d in Figure 6.3) from the actual values are significant during the heating phase. For example, the actual line depth significantly decreases in the middle of the heating phase, but the corresponding value of the HMI observable centered at this time moment shows an increase. Nevertheless, the formation heights of the Fe I 6173 Å line core and continuum do not experience significant changes during the peak of the heating phase (see Figure 6.2 for details).

While the instant observables for the Doppler velocity and magnetic field agree with the properties of the line profile (which confirms that the HMI algorithm is correct in general), the HMI observables calculated for the time-dependent observing sequence are in strong disagreement with the actual line properties (panels e-h). The strongest deviations are found for the Doppler velocities: while the actual values are less than 0.1 km/s, the HMI observable gives up to 0.5 km/s. The magnetic field observable can deviate for about 40% for the 100 G background vertical field and about 6% for the 1000 G field. Such deviations result from strong changes of the Fe 6173 Å line depth and non-instantaneous nature of the HMI observing sequence.

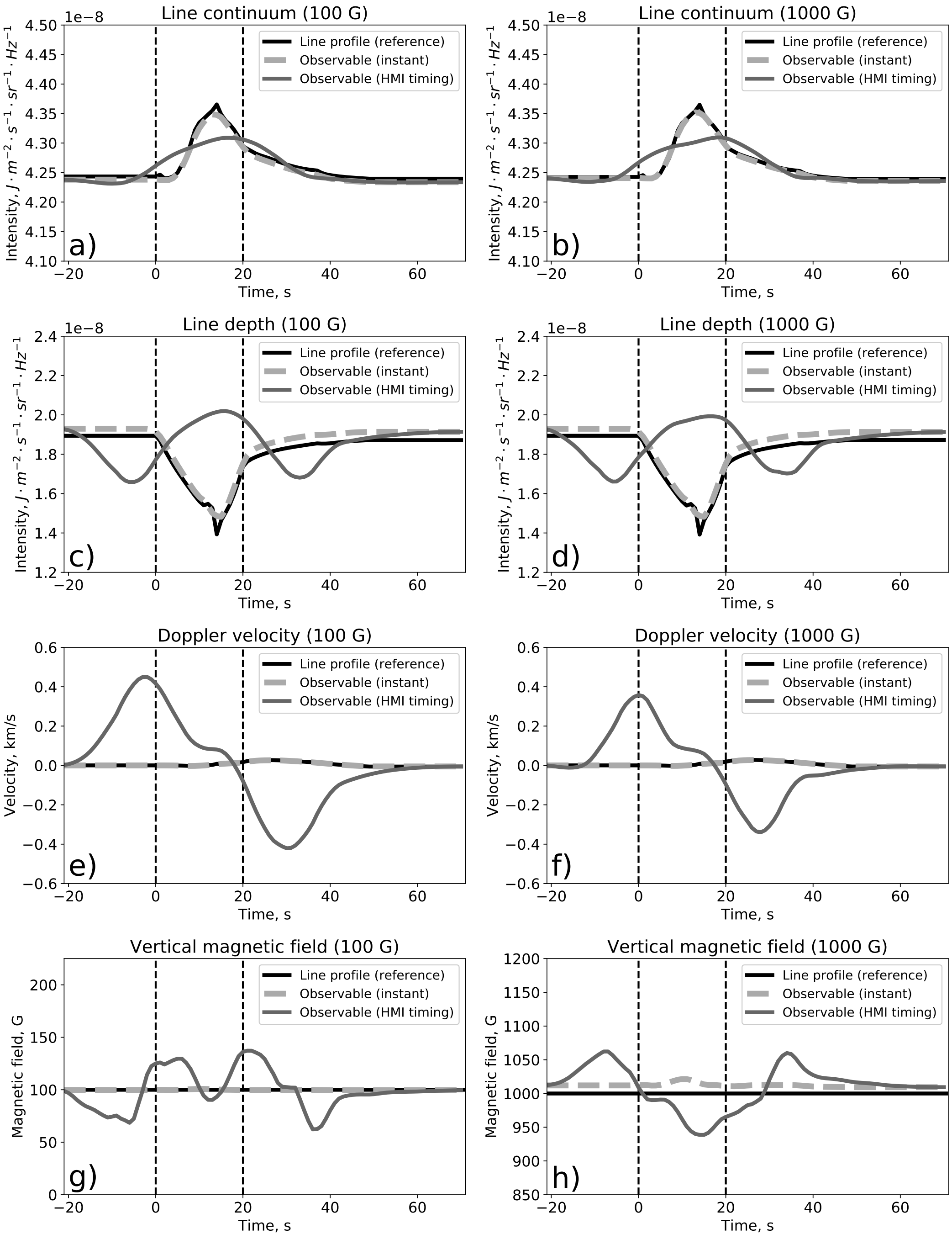

Figure 6.3 Fe I 6173 Å line parameters and corresponding SDO/HMI observables for RADYN model "val3c_d3_1.0e12_t20s_15keV" for the vertical uniform 100 G (panels a, c, e, g) and 1000 G (panels b, d, f, h) fields. Black curves correspond to the measures obtained from the exact line profiles. Gray dashed curves correspond to HMI algorithm applied to the line profile instantly. Dark gray curves correspond to the HMI algorithm applied with proper timing centered at the referred time. Dashed vertical black lines mark the heating phase of the run.

Source: [195]

Figure 6.4 illustrates the strongest deviations of the Doppler shift and magnetic field which we found for the RADYN models. For the illustration, the results are presented only for the high-energy electron beam spectra with the power law indexes of 3 (panels a-d) and low energy cutoffs of 20 keV (panels e-h). As one can see, the deviations depend on the deposited energy flux, and increase with the flux value. The strongest Doppler velocity deviations found for $F = 5.0 \times 10^{10}$ erg cm^{-2}s^{-1} are about 0.6 km/s, and the strongest deviations of the LOS magnetic field observable can reach 60% for 100 G field and 10% for 1000 G field. Incompleteness of the grid of the F-CHROMA RADYN flare models with high deposited energy fluxes ($F = 5.0 \times 10^{10}$ erg cm^{-2}s^{-1}) does not allow us to conclude the dependence of the strongest deviations of the observables on low-energy cutoffs and power law indexes.

Figure 6.5 illustrates the same Fe I line properties as in Figure 6.3 but for the GSK19 model. One can see that this high-energy model ($F = 1.0 \times 10^{11}$ erg cm^{-2}s^{-1}) results in even stronger Doppler velocity and magnetic field deviations than these for the F-CHROMA models, likely due to more impulsive nature of the energy deposit and resulting dynamics. The deviation of the LOS magnetic field observable from the superimposed uniform vertical field are especially strong for the 100 G case (panel g). In such case, depending on the observing sequence center time, the measured magnetic field can be almost two times stronger for the sequence centered at around $t = 19\,s$ or even four times weaker for $t = -11\,s$.

6.4 Discussion and Conclusion

In this work we analyzed how heating of the solar atmosphere by precipitating high-energy electron beams during the impulsive phase of solar flares can affect the observables of SDO/HMI (line-of-sight magnetic field, Doppler velocity, line depth and continuum). We highlight two main results of our study:

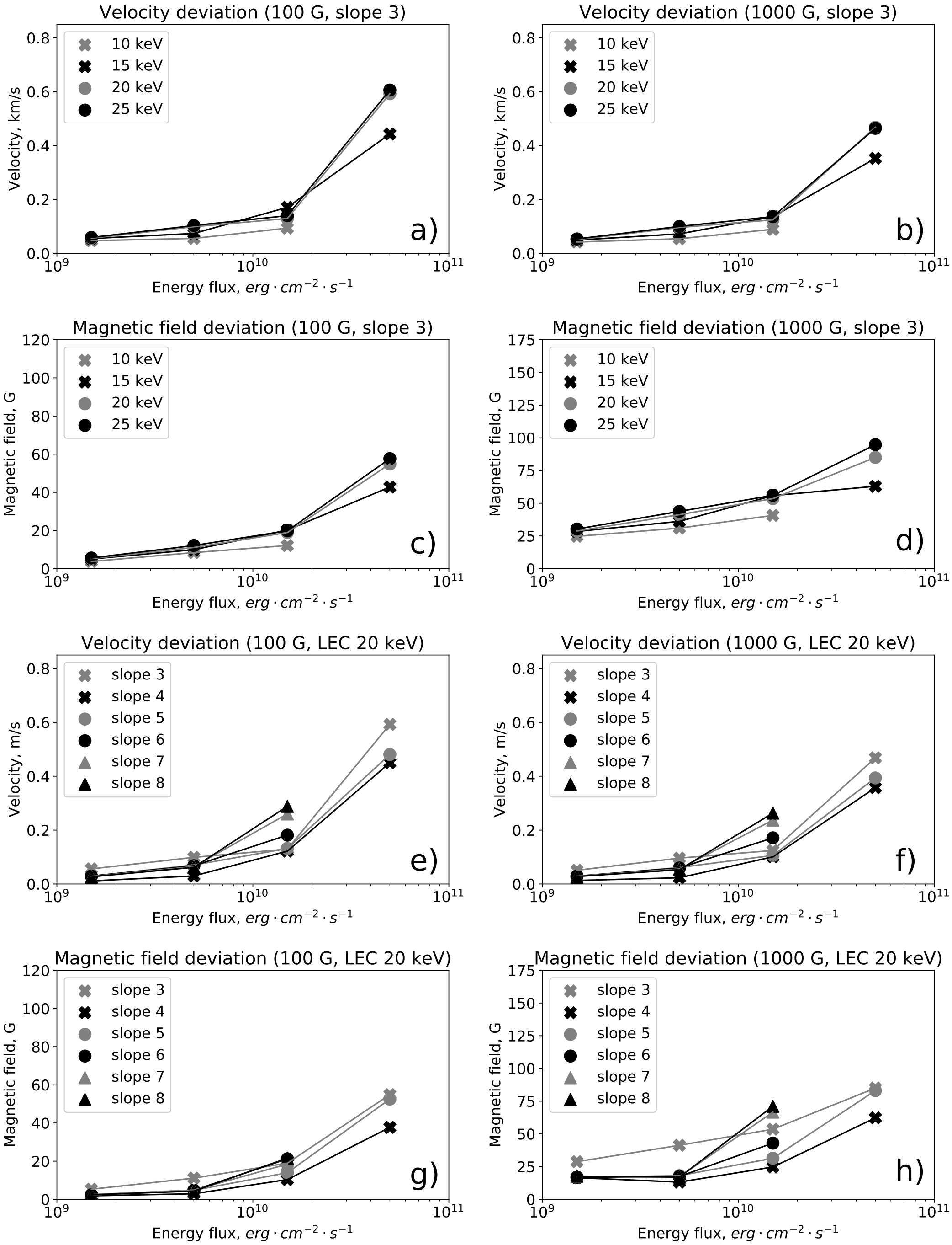

Figure 6.4 Illustration of the strongest deviations between Fe I 6173 Å line parameters and simulated HMI observables for various RADYN runs evolving in 100 G (panels a, c, e, g) and 1000 G (panels b, d, f, h) vertical uniform magnetic fields. Panels a-d correspond to the deposited electron beam spectra with the slope of 3, panels e-h — to the slope of 5. Different colors and markers correspond to the different low-energy cutoffs of the deposited electron beam spectra.
Source: [195]

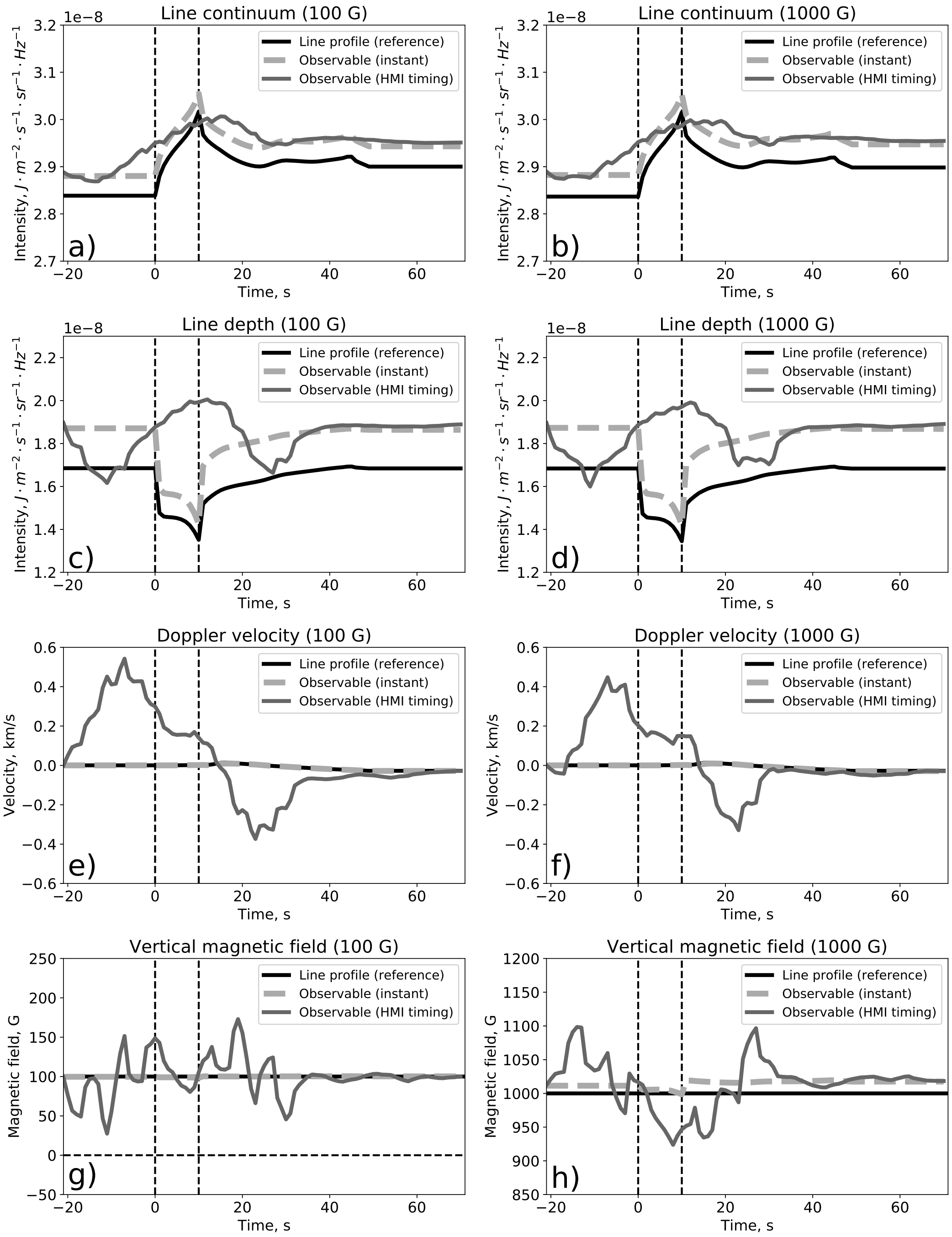

Figure 6.5 Same as Figure 6.3 but for GSK19 model.
Source: [195]

1. Because the HMI observables are obtained from individual filtergrams distributed in time, the Fe I 6173 Å line depth, Doppler velocity, and magnetic field strength measured by HMI during the flare impulsive phase can significantly deviate from the actual values. For beam heating events with the average deposited energy fluxes of $F = 5.0 \times 10^{10}$ erg/cm^{2}s, the deviations can be as strong as 0.6 km/s for the Doppler velocity, and about 60 G and 100 G for the vertical uniform 100 G and 1000 G magnetic field respectively.
2. The deviations increase with the increase of the energy flux. Electron beams with energy flux $F < 5.0 \times 10^{10}$ erg/cm^{2}s do not cause significant change in the Fe 6173 Å line profile and, thus, do not cause significant deviations of the HMI observables from the actual values. However, electron beams of $F \geq 5.0 \times 10^{10}$ erg/cm^{2}s cause stronger deviations of observables, and may even results in a very weak measured magnetic field (as observed for GSK19 model).

There are several qualitative conclusions about possible misinterpretation of the HMI magnetic field measurements during solar flares, which can be derived from this work. First, the magnetic field variations are reversible. However, this is the direct consequence of the fact that the field was imposed into the model externally, i.e. it was not a part of the hydrodynamic simulations. Second, the HMI magnetic field observable becomes about four times weaker than the actual embedded magnetic field (27 G) for the GSK19 model with the stronger electron energy flux, although such behavior was not observed for any of F-CHROMA models, which indicates a possibility to induce an artificial magnetic field sign reversal for the heating by a very high-energy electron beam ($F > 1.0 \times 10^{11}$ erg/cm^{2}s). Previously, the magnetic field reversals were studied by Harker and Pevtsov [82] who did not reproduce the magnetic field sign reversal (stokes V reversal) by considering forward modeling of the Fe I 6173 Å line Doppler shifts and concluded that the sign reversal can be reached only if the Fe I line profile goes to emission, which has not been observed. In our study, the modeled Fe I 6173 Å line profiles are always absorption profiles (i.e. the line depths derived from the exact line profile shapes is always positive). However, for the strong ($F = 1.0 \times 10^{11}$ erg/cm^{2}s) deposited energy fluxes the magnetic field observable reaches very low values because of the rapid changes of the line profile.

In the work by Švanda et al. [228], the authors highlighted the discrepancy between the Fe I 6173 Å line continuum observable from the SDO/HMI measurements (filtergrams), and the line continuum derived with the help of the inversion of Hinode Solar Optical Telescope spectropolarimetric data for the same spatial locations [115, 226, Hinode SOT]. The disagreement between the observed and modeled continua is found to be mostly within 10% from modeled values [228, Figure 5], with some points deviating for 20% or more. For our study, the disagreement for the continuum intensity can reach up to 7% for GSK19 model, which can qualitatively explain such results. However, Švanda et al. [228] also mentioned the presence of Fe I 6173 Å line profiles in emission which is not found in our simulations.

One of the significant restrictions of our study is that the initial atmospheric models were close to the quiet-Sun VAL3C atmospheres [229] except for the GSK19 models. However, it was shown in the simulations of Hong et al. [84] that Fe I 6173 Å line profile perturbations can be stronger for the initial atmospheric models corresponding to sunspot penumbra. So one can expect stronger deviations of the SDO/HMI observables from the actual values in such case. Also, the F-CHROMA and GSK19 models have a certain timing of the heating phase (triangular-shaped 20 s heating and 10 s uniform heating respectively) which is not necessarily the case for a particular solar flare. Nevertheless, we conclude that for correct interpretation of the SDO/HMI observables during solar flares it is necessary to model the line formation and variations of the line profile, taking into account the HMI observing sequence and data analysis procedure.

CHAPTER 7

RELATIONSHIPS BETWEEN CHARACTERISTICS OF THE LINE-OF-SIGHT MAGNETIC FIELD AND SOLAR FLARE FORECASTS

7.1 Introduction

Usually lasting from several minutes to several hours, solar flares can release more than 10^{32} erg of energy, and cause harmful effects to the terrestrial environment. The only possible source to accumulate such large amounts of energy is magnetic field of active regions. Emslie et al. [56] demonstrated for a sample of 38 flares that the free (non-potential) energy of magnetic field was sufficient to explain the flare energy release including Coronal Mass Ejections (CMEs), energetic particles, and hot plasma emission and dynamics. For understanding the flare physical mechanism and developing flare prediction methods it is important to find critical magnetic field characteristics that are linked to the flare initiation and strength.

There have been two types of such study. The first approach is to focus on global characteristics of active regions, and the second approach is to search for local critical properties of magnetic fields. For instance, in the first type studies, Mandage and McAteer [136] demonstrated a difference between the magnetic field power spectrum slopes of flaring and non-flaring active regions. Korsós et al. [109] found several promising preflare signatures using the SOHO/MDI-Debrecen Data sunspot catalog. Korsós et al. [111] introduced the weighted horizontal magnetic gradient, WG_M, which allowed them to predict the onset time for $\geq$M5.0 class flares, and conclude whether or not a flare is likely be followed by another event in the next 18 hours. The daily averages of WG_M together with a separation parameter S_{l-f} of magnetic polarities were used by Korsós and Erdélyi [110] to obtain some conditional probabilities of flare and CME characteristics. Many authors [19, 20, 156, 133] have used vector magnetograms from the Space-weather HMI

Active Region Patches (SHARP) and applied machine-learning techniques (Support Vector Machine, Random Forest, and Nearest-Neighbor classifiers) for flare and CME predictions. Also, a recent study of Raboonik et al. [172] used the Zerneke moments as characteristics of the active region magnetic field for flare prediction.

Many observational studies of the second type found that the magnetic field Polarity Inversion Line (PIL) in regions of strong field plays an important role in the flare activity [206, 81, 231, 61, 113, 91, 203, 116, 16, 204, 209, 225, 15, 243, etc.]. Kusano et al. [118] demonstrated from three-dimensional magnetohydrodynamic simulations that flare eruptions can be initiated by emergence of certain small magnetic structures near PIL, as evident from observations. Toriumi et al. [223, 224] pointed out an important role of highly-sheared magnetic field in the vicinity of PILs in the flare development process. Guennou et al. [79] found from simulations that the PIL parameters measuring the total non-potentiality of active regions present a significant ability to distinguish between eruptive and non-eruptive cases. From magnetograms one can extract several descriptors representing the local field in the PIL vicinity. Mason and Hoeksema [139] introduced the Gradient-Weighted PIL length as a characteristic for solar flare forecasts. Falconer et al. [60, 57, 58, 59] found that this characteristic is a good proxy for the free magnetic energy. Leka and Barnes [123, 122, 124] suggested to use a shear angle between the observed and reconstructed magnetic fields. Chernyshov et al. [42] used the PIL length, the area of strong magnetic field in the PIL vicinity, and the total flux in this area, as well as the rates of change of these characteristics.

In this project, we perform a critical analysis of various line-of-sight (LOS) magnetic field characteristics (derived for the entire active region and for the PIL vicinity), their relationship to the flaring activity, and importance for flare forecast. Such analysis based on the LOS magnetograms is important because these observations can be performed more easily and accurately than the full vector magnetic field measurements in near-real time by various space-based and ground-based observatories. In Section 7.2, we describe automatic procedures for identification of PIL, calculation of various magnetic field characteristics, association of the derived characteristics with flare events, and construction of "train" and "test" data sets. In Section 7.3, we estimate the effectiveness in the separation of flaring and non-flaring cases for different LOS characteristics. Section 7.4 describes the application of Support Vector Machine (SVM) classifier for prediction of M- and X-class flares. The results are summarizes in Section 7.5. The comparison with previous results, expert-based scores and following conclusion are presented in Section 7.6.

7.2 Data Preparation

7.2.1 Magnetogram Segmentation

For analysis we used the Line-of-Sight (LOS) magnetograms of Active Regions (AR), obtained by the Helioseismic and Magnetic Imager onboard the Solar Dynamics Observatory [200, SDO/HMI]. The active region data were represented in the form of $30^o \times 30^o$ data cubes with 1 h cadence, remapped onto the heliographic coordinates using the Postel's projection, and tracked with the solar differential rotation during the whole passage of active regions on the solar disk, employing the standard SDO software. To avoid projection effects, following Bobra and Couvidat [19] we consider ARs only when they are located within ±68deg from the disk center.

By definition, the Polarity Inversion Line (PIL) is the line where the LOS magnetic field changes its sign. For the automatic robust detection of the PIL of strong fields in active regions we use the algorithm initially introduced by Chernyshov et al. [42]. This algorithm is based on a magnetogram segmentation process formulated as an optimization task. The goal is to divide the magnetogram into regions with strong positive field ("positive" segments), strong negative field (“negative” segments), or weak field (“neutral” segments). We describe the algorithm in detail in Appendix A. An example of the segmentation and PIL detection for AR 11158 is illustrated in Figure 7.1.

To isolate the active region area, we use the following two algorithms. The first one is based on the segmentation result: we apply one morphological dilation (inclusion of neighboring pixels) to the positive/negative segments (see Appendix A), combine them, choose the largest segment containing the active region center, and determine the minimum bounding box around it. The second algorithm is implemented following the procedure of Stenflo and Kosovichev [216]. The magnetogram is smoothed, and for each strong magnetic field island the bounding box with a margin of fixed width ($18''$) on all sides is defined. Then, the intersecting bounding boxes are replaced by a larger bounding box. The solution represents the largest bounding box intersecting the center of the data cube (the center of AR). We have found that by applying both algorithms and selecting the smallest bounding box almost all ARs can be effectively separated from their neighbors. The bounding box extracted for AR 11158 is presented in Figure 7.1.

7.2.2 Derivation of PIL and AR Characteristics

After performing the segmentation and bounding procedures, we calculate the following descriptors (characteristics) using the derived PIL and the tracked and remapped magnetogram:

1. The PIL length defined as the number of pixels occupied by the PIL.
2. The PIL area obtained after 10 morphological dilations of the PIL.
3. The unsigned magnetic flux in the PIL area.
4. The unsigned horizontal gradient in the PIL area defined as the sum of $\nabla_h B_z = \sqrt{\left(\frac{\partial B_z}{\partial x}\right)^2 + \left(\frac{\partial B_z}{\partial y}\right)^2}$ over the PIL area pixels.

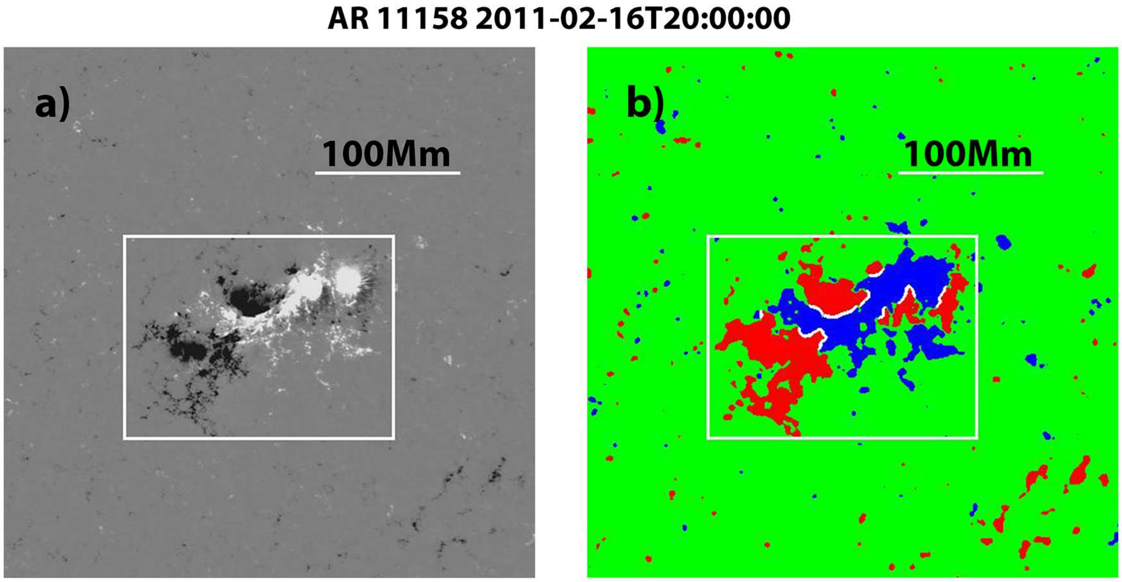

Figure 7.1 Illustration of the PIL automatic identification procedure: a) The magnetogram of AR 11158 obtained by the SDO/HMI at 2011-02-16 20:00:00 UT. b) The magnetogram segmentation and identification of PIL: red, green, and blue areas correspond to negative, neutral and positive segments. The PIL identified by the algorithm described in Appendix A is shown by white curves.
Source: [191].

5. The maximum gradient of the LOS magnetic field across the PIL.
6. The gradient-weighted PIL length [139] calculated as the sum of the PIL pixels multiplied by the unsigned horizontal gradient in each pixel.
7. The R-value [203] representing the unsigned magnetic flux weighted with the inverse distance from the PIL.

Also, we calculate the following characteristics of the entire AR ("global" characteristics):

8. The AR area defined as the total area of the positive and negative segments.
9. The unsigned magnetic flux in the AR area.
10. The maximum strength of magnetic field in AR.
11. The unsigned horizontal gradient in the AR area.

7.2.3 Definition of Positive and Negative Classes, and Construction of "Train" and "Test" Data Sets

The next important step is to associate the magnetic field characteristics derived for each AR with the flare events detected by the GOES satellite. Following Nishizuka et al. [156], we classify a set of magnetic field characteristics as a "positive" case if a ≥M1.0 flare occurred in the corresponding AR within 24 h after the last field measurement. This means that for each flare there can be 24 positive cases (sets of measured LOS magnetic field characteristics) or less. For the period from April, 2010 to June, 2016, 521 M-class and 31 X-class flares were associated with at least one positive case.

Ahmed et al. [3] introduced two ways to determine the negative cases, described by so-called "operational" and "segmented" associations of active region characteristics and flares. According to the operational association, the negative cases are defined to be exactly opposite to the positive cases, i.e., are assigned if there was no flare of $\geq$M1.0 X-ray class within 24 h after the magnetic field measurement. For the segmented association, the case is defined as negative if no flares occurred 48 h before and after the case time moment. In the following we will use the operational association for the "test" subset while keeping the segmented association for the "train" subset. The segmented association better separates the positive and negative cases (by neglecting negative cases occurring very close to the flare time), while the operational association is needed for real-time predictions. The same procedure was applied also for $\geq$X1.0 class flares.

For the operational-type real-time flare forecasts, the classifier is defined for future cases based on the previously observed classified cases. To simulate the real-time operational forecast, we constructed the "train" and "test" datasets to be sequential in time. We assign all the cases belonging to ARs with the NOAA numbers 11059-12158 to the "train" data set, and AR 12159-12559 to the "test" data set. The ratio of the "train" and "test" datasets is approximately 70% to 30% [19, 156]. We also assume that we have just one attempt to classify a "test" dataset for prediction of $\geq$M1.0 or $\geq$X1.0 flares, which means that the classifier tuning should be done on the "train" dataset only.

7.3 Effectiveness of Characteristics

In this Section, we analyze the effectiveness of the derived magnetic field characteristics to separate the positive and negative (flaring and non-flaring) cases. One of the simplest ways to illustrate the separation ability of magnetic field characteristics is to construct combined histograms for positive and negative cases. The examples of such histograms are presented in Figure 7.2. The upper two panels correspond to two PIL characteristics: the unsigned magnetic flux in the PIL area and the gradient-weighted PIL length; and the lower two panels correspond to two AR characteristics: the

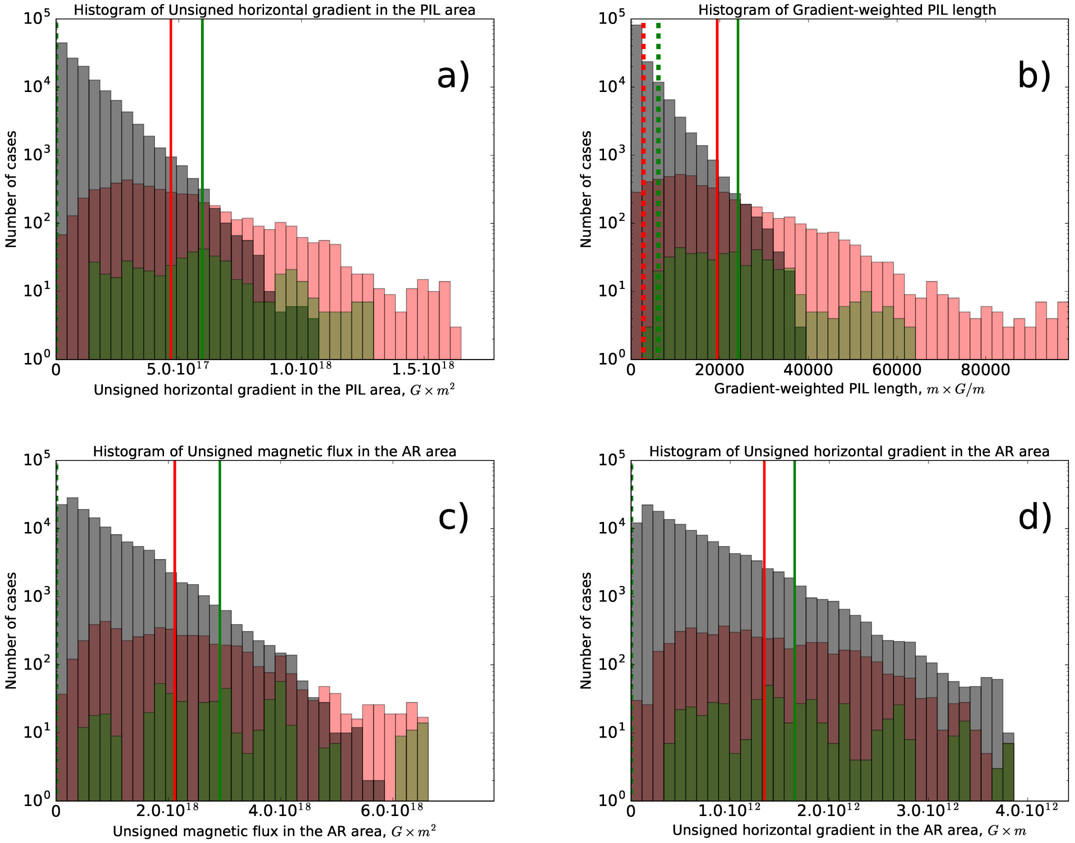

Figure 7.2 1D-histograms of a) unsigned magnetic flux in the PIL area; b) gradient-weighted PIL length; c) unsigned magnetic flux in the AR area; d) unsigned horizontal gradient in the AR area. The negative cases are shown in grey, the positive ≥M1.0 class cases are shown in red, and the positive ≥X1.0 class cases are shown in green. The darker areas represent the intersections of the histograms. The red and green solid lines represent the average values of the positive ≥M1.0 and ≥X1.0 cases, the corresponding dashed lines show the thresholds corresponding to 5% of positive cases. *Source:* [191].

unsigned magnetic flux in the AR area and the unsigned horizontal gradient in the AR area.

One can notice that for the PIL characteristics there are more flaring than non-flaring cases in the tails of the histograms (light color areas). We found such situation for all PIL characteristics that we computed. For the global AR characteristics, we found a slight dominance of positive cases in the distribution tail only for the unsigned magnetic flux, and did not observe it for other three characteristics.

There is one common feature in the histograms. The positive cases occur only if the characteristics reach some critical (threshold) value. For some LOS characteristics the existence of the critical values is more prominent in the normal-scaled histogram, but for others in the logarithmic-scaled histogram. This feature is used to simplify the classification (prediction) problem by reduction of the amounts of data considered for the classification. The red dashed (for ≥M1.0 flares) and green dashed (for ≥X1.0 flares) lines in Figure 7.2 represent the threshold values, above which 95% of positive cases are observed. Note that the threshold values are determined using the "train" data set. At the same time, the mean values of the positive cases are shown by solid lines of the same color. The threshold and mean values for the positive cases, as well as the mean value for the negative cases, are summarized in Table 7.1.

There are many ways to quantitatively determine which characteristics are most effective for a classification problem. The inclusion of characteristics that are not discriminative leads to a high computational cost without improvement of the result, and may even decrease the performance of the SVM [19]. Breiman [28] proposed to evaluate feature importance by using the Random Forest classification, which was also used by Nishizuka et al. [156]. Al-Ghraibah et al. [4] employed the univariate True Skill Statistics (TSS) score as a measure of feature importance. Ahmed et al. [3] used the Correlation-Based Feature-Selection (CFS) and Minimum Redundancy Maximum Relevance (MRMR) methods. Leka and Barnes [123] suggested the Mahalanobis

Table 7.1 Relationship between Magnetic Field Characteristics and Solar Flares of the GOES X-ray Classes Greater than M1.0 and X1.0

Characteristic	Average value (negative cases)	Average value (positive ≥M1.0 cases)	Average value (positive ≥X1.0 cases)	5% threshold (positive ≥M1.0 cases)	5% threshold (positive ≥X1.0 cases)
PIL length $[m]$	$(1.7\pm1.8)\cdot10^{7}$	$(6.8\pm4.0)\cdot10^{7}$	$(8.3\pm3.6)\cdot10^{7}$	$1.7\cdot10^{7}$	$3.2\cdot10^{7}$
PIL area $[m^2]$	$(7.3\pm5.5)\cdot10^{14}$	$(19.3\pm7.9)\cdot10^{14}$	$(21.8\pm7.6)\cdot10^{14}$	$7.9\cdot10^{14}$	$9.6\cdot10^{14}$
Unsigned magnetic flux in the PIL area $[G\cdot m^2]$	$(1.14\pm1.15)\cdot10^{17}$	$(4.68\pm2.98)\cdot10^{17}$	$(5.96\pm2.98)\cdot10^{17}$	$1.20\cdot10^{17}$	$1.57\cdot10^{17}$
Unsigned horizontal gradient in the PIL area $[G\cdot m]$	$(0.81\pm0.75)\cdot10^{11}$	$(2.93\pm1.67)\cdot10^{11}$	$(3.40\pm1.34)\cdot10^{11}$	$0.89\cdot10^{11}$	$1.47\cdot10^{11}$
Maximum gradient across the PIL $[G/m]$	$(3.8\pm2.3)\cdot10^{-4}$	$(9.0\pm4.4)\cdot10^{-4}$	$(10.3\pm3.4)\cdot10^{-4}$	$3.7\cdot10^{-4}$	$5.3\cdot10^{-4}$
Gradient-weighted PIL length $[m\cdot G/m]$	$(3.1\pm4.1)\cdot10^{3}$	$(19.4\pm16.4)\cdot10^{3}$	$(24.1\pm13.2)\cdot10^{3}$	$2.8\cdot10^{3}$	$6.2\cdot10^{3}$
R-value $[G\cdot m^2]$	$(2.4\pm3.2)\cdot10^{15}$	$(14.2\pm11.7)\cdot10^{15}$	$(19.1\pm10.7)\cdot10^{15}$	$2.0\cdot10^{15}$	$4.8\cdot10^{15}$
AR area $[m^2]$	$(4.8\pm4.0)\cdot10^{15}$	$(10.1\pm4.9)\cdot10^{15}$	$(11.9\pm4.7)\cdot10^{15}$	$3.2\cdot10^{15}$	$3.7\cdot10^{15}$
Unsigned magnetic flux in the AR area $[G\cdot m^2]$	$(7.7\pm7.1)\cdot10^{17}$	$(21.1\pm13.0)\cdot10^{17}$	$(29.2\pm13.0)\cdot10^{17}$	$5.6\cdot10^{17}$	$7.1\cdot10^{17}$
Maximum strength of magnetic field in the AR $[G]$	$(1.31\pm0.41)\cdot10^{3}$	$(1.66\pm0.48)\cdot10^{3}$	$(1.84\pm0.52)\cdot10^{3}$	$1.06\cdot10^{3}$	$1.20\cdot10^{3}$
Unsigned horizontal gradient in the AR area $[G\cdot m]$	$(6.1\pm5.4)\cdot10^{11}$	$(13.4\pm7.4)\cdot10^{11}$	$(16.5\pm8.2)\cdot10^{11}$	$3.9\cdot10^{11}$	$4.3\cdot10^{11}$

Note: Columns 2 and 3 show the average values of the parameters for the ≥M1.0 and ≥X1.0 class flares correspondingly. Columns 4 and 5 show the thresholds, above which 95% of all ≥M1.0 and ≥X1.0 class flares were observed.

Source: [191].

distance between classes and Hotelling's T^2-test to measure statistical differences between flaring and non-flaring cases. Bobra and Couvidat [19] calculated the Fisher Ranking score (or F-score) as a measure of a univariate effectiveness of the separation ability.

In this work, we calculated two simple univariate scores for the obtained magnetic field characteristics. Firstly, for each characteristic we derived the threshold separating 5% of the positive cases. As seen from Table 7.1, these threshold values (for both ≥M1.0 and ≥X1.0 flares) are comparable or even greater than the mean values for the negative cases for most characteristics. Thus, the fraction of negative cases which could be cut off by this threshold is used as a measure of effectiveness of characteristics in separating the "train" and "test" data sets. Secondly, we calculate the Fisher ranking score [19, F-score]:

$$F(i) = \frac{(\bar{x}_i^+ - \bar{x}_i)^2 + (\bar{x}_i^- - \bar{x}_i)^2}{\frac{1}{n^+ - 1}\sum_{k=1}^{n^+}(x_{k,i}^+ - \bar{x}_i^+)^2 + \frac{1}{n^- - 1}\sum_{k=1}^{n^-}(x_{k,i}^- - \bar{x}_i^-)^2},$$

where $\bar{x}_i$ is the mean value of characteristic i; $\bar{x}_i^+$ and $\bar{x}_i^-$ are the mean values of characteristic i for the positive and negative cases; and n^+ and n^- are the total numbers of the positive and negative cases. We calculated the F-score for all the characteristics for the train dataset. Sometimes, the F-score is higher if calculated for the logarithms of the parameters. Therefore, we also calculated the F-scores of decimal logarithms of each parameter and used it if the score was higher than the one for the normal-scaled characteristic.

The results for both estimates of effectiveness are combined and summarized in Tables 7.2 and 7.3 for the ≥M1.0 and ≥X1.0 class flares respectively. The cases for which the logarithmic scale was used in the F-score calculation are labeled as (log) in Tables 7.2 and 7.3. The SVM training and testing were also done in the logarithmic scale for such parameters. One can notice from Tables 7.2 and 7.3 that for every

Table 7.2 Importance of Magnetic Field Characteristics for the Forecast of $\geq$M1.0 Class Solar Flares

Characteristic	Fraction of negative cases below threshold, %	F-score
PIL length (log)	0.63	1.41
PIL area	0.60	1.46
Unsigned magnetic flux in the PIL area (log)	0.63	1.41
Unsigned horizontal gradient in the PIL area (log)	0.64	1.48
Maximum gradient across the PIL (log)	0.56	1.15
Gradient-weighted PIL length (log)	0.62	1.45
R-value (log)	0.61	1.35
AR area (log)	0.44	0.66
Unsigned magnetic flux in the AR area (log)	0.49	0.86
Maximum strength of magnetic field in the AR (log)	0.29	0.30
Unsigned horizontal gradient in the AR area	0.44	0.69

Source: [191].

Table 7.3 Importance of Magnetic Field Characteristics for the Forecast of ≥X1.0 Class Solar Flares

Characteristic	Fraction of negative cases below threshold, %	F-score
PIL length	0.84	2.68
PIL area	0.71	2.36
Unsigned magnetic flux in the PIL area	0.74	2.51
Unsigned horizontal gradient in the PIL area	0.83	2.81
Maximum gradient across the PIL	0.79	2.46
Gradient-weighted PIL length (log)	0.84	2.62
R-value (log)	0.84	2.47
Total AR area	0.51	1.32
Unsigned magnetic flux in the AR area (log)	0.60	1.91
Maximum strength of magnetic field in the AR (log)	0.41	0.68
Unsigned horizontal gradient in the AR area (log)	0.49	1.29

Source: [191].

considered univariate test the PIL characteristics have higher scores than the global AR parameters.

7.4 Methodology of Flare Prediction

Currently most operational flare forecasts are based on expert decision. However, many recent works [19, 213, 80, 8, 133, 172, 156] demonstrated that the Machine-Learning algorithms can be successfully applied for flare prediction. In this Section, we test if it is possible to forecast $\geq M\,1.0$ and $\geq X\,1.0$ flares, using Machine-Learning algorithms based solely on the LOS magnetic field characteristics. Our approach is to utilize the Support Vector Machine [43, SVM] classifier for flare forecasting using the Python module "Scikit-Learn" [163]. The description of SVM can be found in Bobra and Couvidat [19], and in Appendix B.1.

The computational cost of the SVM classifier scales with the number of cases in the "train" data set and the number of features (characteristics, descriptors) as $O(N^2 \times M)$ if $N >> M$. On one hand, a large number of training samples should positively affect the classifier performance. On the other hand, the SVM classifier has many parameters that should be optimized, and the computing time quadratically increases with the size of "train" dataset. Thus, any possibility to reduce the number of cases which need to be classified should be utilized. In the previous Section we have found that the flaring cases mostly occur if a specific characteristic exceeds a certain threshold. We have also obtained that the PIL descriptors are more effective in the separation of the positive and negative cases. Thus, we first performed the classification based on the PIL characteristics only. We automatically classified a case as negative if any of its PIL characteristics was below the corresponding threshold. It was found that this procedure allows us to reduce the amount of data for the SVM classification by 74.4% (leaving about 1/4 of all cases) for the $\geq$M1.0 class flares and by 91.2% for the $\geq$X1.0 class flares. Only about 11.6% of positive cases for the

$\geq$M1.0 and 14.0% for the $\geq$X1.0 class flares were misclassified as negative at this stage. To check the validity of this approach, we repeated the training procedure with the threshold values decreased by a factor of two that led to exclusion of 52.2% of cases (two times more cases need to be classified) for the $\geq$M1.0 class and 72.8% (three times more cases need to be classified) for the $\geq$X1.0 class cases. We have also checked how the inclusion of the global AR parameters (AR area, unsigned magnetic flux, maximum strength of magnetic field, and unsigned horizontal gradient) affect the forecasting result by repeating the training procedure with all 11 parameters.

For the SVM training, we normalize the "train" dataset: $Z = (X - \mu)/\sigma$, where X is a non-normalized data set, μ is the mean, and σ is the standard deviation [156]. We use the same μ and σ parameters to normalize the "test" data set. To find the optimal SVM kernel (among the Linear, RBF, Polynomial, and Sigmoid available in the Python Scikit-Learn package) and its parameters, we perform a cross-validation procedure on the "train" dataset: divide it into two subsets (one simulating the train data set, and another simulating the test data set) ten times, and then average the SVM results. As a measure of the SVM performance, we use the True Skill Statistics (TSS) metrics defined as:

$$TSS = \frac{TP}{TP + FN} - \frac{FP}{FP + TN},$$

where TP is the true positive prediction (number of positive cases predicted as positive), TN is the true negative prediction (number of negative cases predicted as negative), FP is the false positive prediction (number of negative cases predicted as positive), FN is the false negative prediction (number of positive cases predicted as negative). The TSS score is not sensitive to the class imbalance ratio (the relative number of positive and negative cases), and is zero for a pure negative prediction (when all cases are predicted as negative). The standard deviation of the TSS was estimated from the scores obtained during the cross-validation procedure with the optimal parameters.

7.5 Results

In Section 7.3 it was pointed out that the PIL characteristics separate flaring and non-flaring cases more effectively than the global (integrated) characteristics obtained for the whole ARs. The results in Tables 7.2 and 7.3 demonstrate that all PIL characteristics give approximately the same scores in both tests for both, the ≥M1.0 and ≥X1.0 flare predictions. Among the global AR characteristics, the highest score is obtained for the unsigned magnetic flux in the AR area, but still it does not exceed the scores for any PIL parameter.

The results of prediction tests based on the PIL parameters only are summarized in the second column of Table 7.4. For the ≥M1.0 class solar flares, we found that the best score of $TSS = 0.76 \pm 0.03$ can be obtained using the "sigmoid" SVM kernel (described in Appendix B.1) with parameters $C = 0.1$, $\gamma = 0.01$ and $r = 0.001$, and the negative/positive class weights of 1/20. Description of these parameters can be found in Appendix B.1. The score was derived from the following classification results: $TP = 1932$, $TN = 42382$, $FP = 6654$, $FN = 234$ (including all cases in the test dataset). For the ≥X1.0 class solar flares, we obtained $TSS = 0.84 \pm 0.07$ for the same "sigmoid" SVM kernel but with different parameters: $C = 0.0001$, $\gamma = 10.0$ and $r = 0.0001$, and the negative/positive classes weights of 1/100. This TSS was derived from the following classification results: $TP = 194$, $TN = 44991$, $FP = 6009$, $FN = 8$.

Interestingly, the flare forecasts performed using only the PIL characteristics have almost the same TSS scores as the forecasts based on the full set of characteristics (including both the PIL and global AR characteristics). The TSS scores for the full set of characteristics are summarized in the third column of Table 7.4. For prediction of

Table 7.4 Comparison of TSS Scores for Different Methods of Prediction of ≥M1.0 and ≥X1.0 Class Solar Flares

	Prediction of ≥M1.0 flares	Prediction of ≥X1.0 flares
PIL characteristics only	0.76±0.03	0.84±0.07
PIL + global characteristics	0.74±0.03	0.84±0.07
50% decreased cutoff values	0.76±0.03	0.85±0.04

Note: The standard deviations are estimated using a cross-validation procedure.

Source: [191].

≥M1.0 solar flares, the inclusion of global characteristics even decreased the TSS score from TSS =0.76 to TSS =0.74. For prediction of ≥X1.0 flares, we have obtained the same TSS =0.84 score.

The last column of Table 7.4 summarizes the results of the classification using the PIL parameters with the pre-classification threshold decreased by a factor of two. The 50% decrease of the threshold (which results in a smaller number of pre-classified samples) leads to an insignificant increase of TSS for the ≥X1.0 flare prediction (from TSS =0.84 to TSS =0.85) and gives the same TSS for the ≥M1.0 flare prediction. Thus, we can conclude that it is possible to pre-classify a significant number of cases (74.4% for the ≥M1.0 class flares and 91.2% for the ≥X1.0 class flares) by applying thresholds to the PIL parameters without a significant decrease of the prediction TSS score.

7.6 Discussion and Conclusion

In this study, we have developed a machine-learning procedure solely based on the line-of-sight (LOS) magnetic field observations that are available in near-real time from space-based and ground-based observatories. The procedure is based on analysis of characteristics of the magnetic field Polarity Inversion Line (PIL) which is automatically identified by performing the magnetogram segmentation formulated as an optimization task. The PIL characteristics were derived from the SDO/HMI magnetograms for each AR with 1 h cadence. We estimated the effectiveness of these characteristics for forecasting ≥M1.0 and ≥X1.0 solar flares, and trained the Support Vector Machine (SVM) to maximize the True Skill Statistics (TSS) metrics. Interestingly, the univariate effectiveness scores are similar for all PIL characteristics, probably, because the PIL characteristics (except, possibly, the Maximum gradient across PIL) correlate with each other (depend on the same PIL length or the PIL area that depends on the PIL length).

The obtained True Skill Statistics scores $TSS = 0.76$ for prediction of ≥M1.0 class flares, and $TSS = 0.84$ for prediction of ≥X1.0 class flares, can be compared with the scores mentioned in other works. For example, Anastasiadis et al. [8] reported $TSS \approx 0.5$ for the prediction of ≥C1.0 class flares, Shin et al. [213] received a maximum of $TSS = 0.371$ for ≥M1.0 class flares, Hada-Muranushi et al. [80] — the $TSS = 0.295$ for ≥M1.0 class flares, Liu et al. [133] — $TSS = 0.50$ for ≥M1.0 class flares. On the other hand, our TSS score for ≥M1.0 is lower than ones in the works of Bobra and Couvidat [19, TSS =0.817], Nishizuka et al. [156, TSS =0.88 for SVM classifier], Raboonik et al.[172, TSS =0.856]. Also, Nishizuka et al. [156] reported a higher TSS score for ≥X1.0 class flares ($TSS = 0.88$ for SVM classifier). Our results solely based on the line-of-sight magnetic field observations are lower than those obtained with the use of vector magnetograms, but still comparable.

The score for ≥M1.0 class flares received in our work is higher than the known expert predictions quoted by Nishizuka et al. [156]: $TSS = 0.50$ for the NICT Space Weather Forecasting Center and $TSS = 0.34$ for the Royal Observatory of Belgium [53]. It is also higher than the $TSS = 0.53$ of the National Oceanic and Atmospheric Administration (NOAA) Space Weather Prediction Center (SWPC) deduced from Table 4 of Crown [47]. For the ≥X1.0 flares, again, our result is higher than the expert prediction with $TSS = 0.21$ [156, the NICT Space Weather Forecasting Center] and with $TSS = 0.49$ [47, Table 4]. We can conclude that the accurately-tuned machine-learning technique, even if it is solely based on the LOS magnetic field measurements, can compete with the expert-based predictions.

It is necessary to discuss the influence of the data set construction on the prediction results. First, the way of the division of the data set into the “train” and “test” subsets can change the prediction scores. For example, the shuffled division (when the “train” and “test” subsets are not consequent in time, but all cases from one AR are kept in one subset) reduces the scores from $TSS = 0.76$ to $TSS = 0.70$ for

≥M1.0 class flares, and from $TSS = 0.84$ to $TSS = 0.63$ for ≥X1.0 class flares. The strong difference in the TSS score for ≥X1.0 class flares is caused by a low number of X-class flares in the data set. In this work, we relied on the NOAA AR detection and considered every case with the detectable PIL, which already makes the data set to be subjective to the PIL detection method. Nishizuka et al. [156] used their own method to detect ARs, which definitely leads to another data set with larger number of cases. Bobra and Couvidat [19] reduced the actual data set by cutting out some randomly-selected portion of negative cases. Thus, to guarantee the accurate comparison of different prediction methods, one should unify the starting data set and its division into the "train" and "test" subsets. Such attempts were done previously [16], and hopefully will be continue in the future.

The important role of PIL in the flare development process was pointed out in many observations, simulations and forecasts of solar flares. Generally, the PILs are characterized by highly-sheared magnetic fields, strong field gradients and complicated topology of neighboring magnetic field structures. These properties result in a substantial amount of free magnetic energy that can be released in flares. It is not surprising that many flares are developed locally in the PIL vicinity. Our study statistically confirms the importance of the PIL characteristics for flare forecasting. In particular, it demonstrated that the PIL characteristics obtained just from the line-of-sight magnetic field component can be used to obtain flare predictions compatible with expert-based forecasts and comparable to the predictions that are based on full vector magnetic field observations. However, our results are accompanied by a significant number of false positive predictions. Generally, a more accurate comparison of machine-learning-based and expert-based predictions is required. Despite the promising results, we should always keep in mind that the prediction is metrics-dependent. In this work, we maximize the True Skill Statistics in a single parameter setup. Maximizing other metrics can result in other optimal SVM parameters and prediction scores [19]. Further work is needed to develop algorithms for quantitative prediction of the flare class and physical properties (eruptive or non-eruptive nature, geo-effectiveness etc).

CHAPTER 8

ENHANCEMENT OF BINARY AND PROBABILISTIC SWPC NOAA FLARE FORECAST BY USING MACHINE LEARNING

8.1 Introduction

Solar flares are important agents of the solar-terrestrial interactions and drivers of the space weather. Often accompanied by fast coronal mass ejections (CME), solar energetic particles (SEP), and high-energy radiation, strong solar flares can lead to harmful consequences to the terrestrial environment. The prediction of solar flares and accompanying events, as well as understanding their physical triggers, remains one of the most important problems in heliophysics for many decades. The Helioseismic and Magnetic Imager onboard Solar Dynamics Observatory [200, SDO/HMI] obtained tremendous amounts of magnetic field observations starting from 2010, which significantly increased number of forecasting attempts, including employment of the state-of-art deep learning techniques [86, 155].

Regions of the strong-field Polarity Inversion Lines (PIL) in active regions are of a special interest. The evolution and structure of the magnetic field in the vicinity of the PIL plays a crucial role in the development of the flare process [91, 118, 223, 204, 15, 209]. Parameters related to the PIL are previously demonstrated to correlate with the flaring and CME productivity of active regions [139, 222, 120], and are very often considered as proxies for the “free energy” budget of the active regions [81, 60, 203, 57]. Sadykov and Kosovichev [191] summarized seven commonly-used PIL properties together with four active region properties calculated from line-of-sight (LOS) magnetic field measurements, and tested the possibility to build the solar flare forecast for active regions based on LOS data.

Other commonly-used properties of the active regions are Space weather HMI Active Region Patches [21, SHARPs]. SHARPs represent 18 descriptors calculated on routine basis for each identified active region (magnetic field patch) with 12 min cadence, and form the largest database of active region descriptors in solar physics. Bobra and Couvidat [19], Bobra and Ilonidis [20] used the Support Vector Machines (SVM) to predict the solar flares and coronal mass ejections based on SHARP descriptors. Liu et al. [133] tested the Random Forest classification algorithm for prediction of the solar flares of different classes.

In addition to the properties of the magnetic field, the descriptors of the flaring prehistory can significantly enhance the flare forecasts [58, 156]. The flares are historically defined as enhancements of the 1-8 Å Soft X-ray (SXR) flux measured by the X-ray Sensor- onboard Geostationary Operational Environmental Satellite [23, GOES/XRS]. Inclusion of both the number of strong flares happened during the previous day and the properties of the preceding SXR 1-8 Å flux should be tested for the forecast.

In general, since the amounts and quality of the observational data and descriptors are continuously rising, there are more and more attempts appearing to predict the solar flares and flare-related events using the machine learning techniques [170, 3, 59, 4, 8, 165] on various temporal and spatial scales. However, because the structures of the utilized data sets are not the same among the studies, it is almost impossible to compare them with each other [16]. The question of the unification of the data sets are especially important for comparison of the results from the developed prediction attempt with the forecasts of any operational facility [53, 151, 47].

The main goal of the current study is an accurate comparison of the prediction of M-class and X-class flares using machine learning algorithms with the forecast issued by SWPC NOAA [47], investigation of properties of the operational forecast probabilities, and demonstration of the possibility to enhance the forecast. Because of this, we use the same spatial (whole-Sun descriptors) and temporal (one-day forecast) scales as for SWPC probabilities, which will allows us not only to have more direct comparison with SWPC NOAA in terms of both binary and probabilistic forecasts, but also to check if the SWPC NOAA probabilities contain any additional information with respect to PIL, SHARP, and SXR descriptors derived in this work by including them as one of the descriptors in the classification algorithm.

The study has the following structure. Section 8.2 summarizes the data preparation and feature extraction steps for the study. Section 8.3 describes the feature selection and machine learning procedures. The results of the binary and probabilistic forecasts are presented in Section 8.4. The discussion of the results is initiated in Section 8.5 and is followed by a brief summary of the main findings and conclusions in Section 8.6.

8.2 Data Description and Preparation

8.2.1 SWPC NOAA Operational Forecasts

Operational space weather forecasts are currently prepared jointly by United States Department of Commerce, SWPC NOAA, and the United States Air Force. The forecasts are issued on daily basis, at 22:00 UT, for the next day according to the universal time. The forecasts are available via ftp (`ftp://ftp.swpc.noaa.gov/pub/warehouse/`, accessed on 04/08/2019) under RSGA folder for each year. The forecast of solar flares is presented in terms of probabilities (ranging from 1 to 100) of M-class and X-class flares to occur next day, day after next day, and two days after next day, in the section “III” of the document. Currently operational flare forecasts are performed by SWPC NOAA by forecasters using a modified three-component Zurich class [144] and magnetic class [214] for each active region and historical look-up tables of flare probability as a function of active region class, flaring history, growth/decay of sunspots. The calculated probability is corrected by forecasters based on their experience. The usage of this subjective forecast was proven to be more reasonable in terms of Brier Skill Score [47, BSS] than non-corrected probabilities.

For the presented study we utilize only the next-day probabilities of the M-class and X-class flares. The data are collected for each day of May, 2010 — December, 2017. The probabilities for the days when the reports were not issued were interpolated from the neighboring days. Figure 8.1 presents Pearson's correlation coefficient of the SWPC NOAA next-day probability of an M-class or X-class flare and presence/absence of such flare during the day, as well as SXR 1-8 Å daily-averaged flux, with respect to different time lags between the data sets. As one can see, the next-day flare probabilities are highly correlated with the current flare activity, even stronger than with the next-day flare activity. This confirms one more time that the flare prehistory is one of the key parameters influencing the forecast. However, the correlation coefficients with the next-day SXR activity are still high, indicating that the SWPC NOAA flare probabilities definitely represent valuable descriptors for the flare forecasts.

8.2.2 Magnetic Field Descriptors

SWPC NOAA operational forecasts of next-day M-class or X-class flare is essentially one number (probability) issued on a daily basis for the whole Sun, and it somehow describes the state of the Sun at that day. Our idea is to build a set of magnetic field and SXR descriptors also characterizing the entire Sun for the whole day (i.e., each descriptor is one number per day). This will allow us not only to preserve the same spatial and temporal scales of forecast at SWPC NOAA, but also to include the SWPC NOAA probabilities as one of the descriptors for the learning procedure, and evaluate if the inclusion of these probabilities results in higher prediction scores.

In this work we use two types of magnetic field descriptors previously mentioned in the literature. The first are the PIL and AR descriptors from Sadykov and Kosovichev [191] which are computed for each NOAA active region with 1 hr cadence for 2010-2015. We extend the computations of the descriptors for active regions of 2016-2017 for

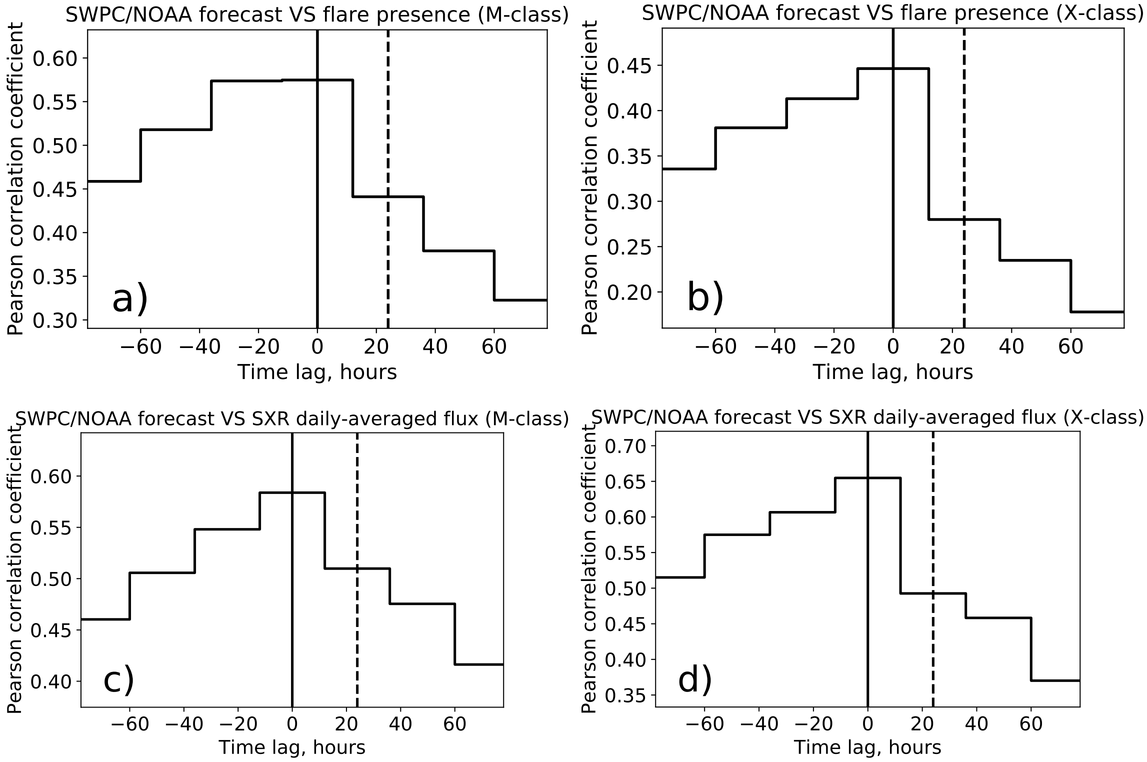

Figure 8.1 Pearson's correlation coefficient for the next-day SWPC NOAA operational forecast and flare presence (a,b) or SXR 1-8 Å daily average flux (c,d) as a function of the time lag between these quantities. Panels (a) and (c) correspond to M-class flares, panels (b) and (d) — to X-class flares. Dashed vertical line corresponds to 1 day time lag (i.e., correlation between next-day forecast and next-day activity), solid vertical line — to the time lag for which the maximum correlation is found.

Source: [192]

this study. Another set of the magnetic field descriptors is SHARPs [21], which are calculated for every magnetic field patch with 12 min cadence. In this work, we will use only SHARPs for patches related to NOAA active regions.

We emphasize here that there are many ways to construct the daily descriptors of the entire Sun from the high-cadence descriptors of solar active regions. We follow a simplistic approach. In the previous study, Sadykov and Kosovichev [191] found that the stronger values of PIL descriptors correspond to higher flare activity. This is also true for absolute values of most of the SHARP descriptors in this study. Thus, one expects that the region with the strongest values of the descriptors at the current day is the most likely to flare. Following that logic, we make two steps: 1) calculate the mean and the absolute maximum daily values of each descriptor of each active region separately; 2) for each day for each descriptor, select the absolute maxima among the previously-calculated mean and maximum values for the active regions presented at the Sun. Thus, any considered PIL/AR and SHARP descriptor produces two daily descriptors of the Sun. Such way of obtaining descriptors results in 22 PIL descriptors and 36 SHARP descriptors for the whole Sun for the entire day.

8.2.3 Flare Statistics and SXR Descriptors

Statistics of solar flares is recovered from the Helioportal [194, `https://helioportal.nas.nasa.gov/`, accessed on 04/08/2019], and cross-checked for completeness with the original NOAA GOES flare catalog (`ftp://ftp.swpc.noaa.gov/pub/warehouse/`, accessed on 04/08/2019). For each day, we get the number of M-class and X-class flares occurred on the Sun. We use these numbers as the descriptors for the presented study, as well as for the label/class assignment. We also obtain several descriptors related to the GOES/SXR 1-8 Å flux and flare statistics. We use the mean and maximum flux values for the day, two days, and three days before the forecast. Also, we count the total number of M-class and X-class flares 1-3 days before the forecast time. This results in additional 12 descriptors for each day. We will call them SXR descriptors further in the text.

8.2.4 Data Set Cleaning and Labeling

One should be careful while processing the magnetic field descriptors: once the flare-producing active region moves closer to the limb, very strong projection effects corrupt the derived PIL and SHARP properties. Thus, it is better to neglect the cases when the flare-productive active regions were located very close to the limb. For our study, we use the following criteria. If the Sun is flaring the day after the considered day, and all the flares were produced only from the active regions located farther than 68^o from the disk center at the current day, then we discard that day from the consideration. This weak selection criteria allows us to keep as many days in the data set as possible. Remember that we keep the day also if there is at least one flare next day produced by region within 68^o from the disk center, or if the Sun is flare-silent for that day.

For each of the remaining days we have 70 descriptors and one SWPC NOAA flare probability. We label each day according to the fact if the flare of M-class or X-class (depending what class we are focusing at) happens next day ("1") or not ("0"). It was found previously [191] that sometimes the descriptors are better-performing if used in linear scale, and sometimes in logarithmic scale. We test each of the descriptors and keep the scale which results in higher F-score for this descriptor:

$$F(i) = \frac{(\bar{x}_i^+ - \bar{x}_i)^2 + (\bar{x}_i^- - \bar{x}_i)^2}{\frac{1}{n^+ - 1}\sum_{k=1}^{n^+}(x_{k,i}^+ - \bar{x}_i^+)^2 + \frac{1}{n^- - 1}\sum_{k=1}^{n^-}(x_{k,i}^- - \bar{x}_i^-)^2} \tag{8.1}$$

Here $\bar{x}_i$ is the mean value of characteristic i; $\bar{x}_i^+$ and $\bar{x}_i^-$ are the mean values of characteristic i for the flaring and non-flaring cases; and n^+ and n^- are the total numbers of the flaring and non-flaring cases. We also normalize each descriptor by subtracting its mean across the data set and by normalizing to its standard deviation.

For each study, we consider both the classification solely based on one group of features by their origin (PIL, SHARP, SXR) and the combination of all these features, with or without the SWPC NOAA flare probabilities.

Although we tried to keep as many days of 2010-2017 as possible, the number of data points is not too large (2698 days for M-class flares, and 2776 days for X-class flares). Because of this, we do not create a fully-separated test data set for this study. Instead, we perform the cross-validation, and derive the validation prediction score together with its generalization error obtained through 10 train-validation pairs of the data sets constructed with 10-times "shuffle and divide" approach. Notice again that all obtained scores are the validation scores rather than the scores from performance on the test data. Also, because the class-imbalance ratio for X-class flares is very high, we will just briefly mention the results related for X-class flares in this study, without going into details. The methodology for the X-class flares is essentially the same as for M-class flares but the results are much more ambiguous due to low occurrence rate of X-class flares.

8.3 Methodology of the Forecast

After the data preparation step, we have the labeled normalized data set subdivided 10 times to the train-validation pairs, fully-prepared for the classification problem. In this study, we test the machine learning classification algorithms available in the Scikit-Learn package for Python [163]. The description of the classification algorithms, together with their hyperparameters for this study, is provided in Appendix B. Here we just list their abbreviations: Support Vector Machines (SVM) with Linear, Radial Basis Function (RBF), and Sigmoid kernels; Logistic Regression (LR); k-Nearest Neighbors (kNN); Adaptive Boosting (AdaBoost) with the Decision Tree classifier as a basis; and Multi-Layer Perceptron with two hidden layers of 200 neurons each (MLP1), of five hidden layers of 200 neurons each (MLP2), and of five hidden layers having 200, 100, 50, 25, and 10 neurons correspondingly (MLP3). In addition to the classification problem, we evaluate a probabilistic forecast for the Support Vector Machines [166], which is also a part of the Scikit-Learn package and described in Appendix B.

Any classification problem has a result of four numbers: TP (True Positive; number of cases where the flaring day predicted as flaring), TN (True Negative; number of cases where the non-flaring day predicted as non-flaring), FP (False Positive; number of cases where the non-flaring day predicted as flaring), and FN (False Negative; number of cases where the flaring day predicted as non-flaring). The ultimate goal of any classification problem is to minimize FP and FN. Because there are two numbers of minimize, the particular minimization strategy depends on the desired purposes of the prediction (e.g., robust detection of "all-clear" cases and maximum-accuracy classification are different tasks). In this work, we will use three measures which are commonly considered in the works of the flare prediction, namely Accuracy, True Skill Score (TSS), and Heidke Skill Score (HSS):

$$Accuracy = \frac{TP + TN}{TP + TN + FP + FN} \tag{8.2}$$

$$TSS = \frac{TP}{TP + FN} - \frac{FP}{FP + TN} \tag{8.3}$$

$$HSS = \frac{2 \times (TP \times TN - FN \times FP)}{(TP + FN) \times (FN + TN) + (TP + FP) \times (TN + FP)} \tag{8.4}$$

As a measure of the success of the probabilistic forecast, we use the Brier Score and the Brier Skill Score [143, BS and BSS] with respect to the flare climatology (when the probability of the flare to happen is the same for each day and equal to the flaring day occurrence rate), defined as:

$$BS = \frac{1}{n} \sum_{i=1}^{n} (P_i - Q_i)^2 \tag{8.5}$$

$$BSS = 1 - \frac{BS}{BS_{clim}} \tag{8.6}$$

Here BS_{clim} is the Brier Score for climatological forecast. BS is indicating how strongly the probabilities deviate from the precise prediction of 0% or 100%: lower BS indicated better forecast. BSS indicates how strongly the probabilistic forecast outperforms the event occurrence rate: higher BSS indicates better forecast.

The next important step is the selection of descriptors which will be utilized in the forecast. Usage of all descriptors may not improve the forecast or even can decrease the forecast score [19]. Also, the usage of highly-correlated descriptors is meaningless because addition of such descriptors does not introduce new information into the classification problem. In this case, selection of descriptors based on any univariate measures (such as F-score) is not suitable because this measure do not count for correlations. Our advantage is in the relatively small size of the data set (less than 3000 data points). For each classification algorithm, metrics to maximize, feature type (PIL, SHARP, SXR, all of them), inclusion of exclusion SWPC NOAA probabilities, we performed the following algorithm to select the descriptors/features:

1. Make the initial ranking of descriptors according to their F-scores on the entire data set;
2. Select two descriptors with the highest F-score if the SWPC probabilities are not used, or the SWPC flare probability and the descriptor with the highest F-score if opposite;
3. Find the classifier hyperparameters maximizing the mean of the metrics (score) across the train-validation data sets;
4. Introduce the descriptor with the next highest F-score and temporarily add it to the previously-considered descriptors. If the F-score of the descriptor is below the threshold (1/4 of the maximum F-score among features for M-class flares, and 1/10 for X-class flares), stop the procedure;
5. Find again the classifier hyperparameters which maximize the mean of the metrics (score) across the train-validation data sets;
6. If the score is higher (lower for BS) than previously-obtained with certain threshold (0.002 for TSS and HSS, 0.001 for accuracy and BS), keep the descriptor for the classification. Discard it otherwise. Return to step 4.

Although such algorithm may not guarantee the optimal basket of features, it allows us to collect only the features which introduce significant additional information to the forecast (i.e., improve the forecast), and discard highly-correlated features. An example of work of the feature selection algorithm is presented in Table 8.1. Notice that here prediction of M-class flares was considered, all features were used except the SWPC NOAA probabilities, the classifier was the SVM with the Radial Basis Function (RBF) kernel. As one can see, different metrics require different number and type of features. We found that typically 5-15 features maximize the targeted score.

SWPC NOAA flare forecasts represent the probability of the flare to happen next day. To convert the probabilistic forecast into binary, we need to set up a probability threshold above which we predict the flare to happen. We did this also using the train-validation data sets for each metrics separately, by varying probability threshold and maximizing the metrics on the train data set, and applying the same threshold on validation data set. The scores are finally averaged over the validation data sets to evaluate the binary "operational" forecast. We will call them "expert scores" hereafter in the text.

8.4 Results

8.4.1 Binary Forecast

The results for the binary forecasts of M-class flares for different classifiers and different groups of features are presented in Tables 8.2-8.4. The top left corner of the tables indicates the metrics which we maximize, the top bar indicates the algorithms used to obtain the prediction, the left column indicates the groups of features. Here "+/- ES" refers to if the SWPC NOAA probabilities were included or excluded as descriptors for the forecast. The cross-section of "Expert Scores (ES)" row and "ES thresholding" column refers to the average score obtained by thresholding

Table 8.1 List of Parameters Maximizing the Target Score (Accuracy, TSS, HSS, or BS) for the SVM RBF Classifier Trained on all Features except the SWPC NOAA Probabilities

Score / Skill score	Descriptor type		
	PIL	SHARP	SXR
Accuracy	Gradient-weighted length (mean)	Absolute value of the net current helicity (mean)	3 day peak SXR flux
	Gradient-weighted length (max)		1 day history of M and X class flares
	PIL area (mean)		
TSS	Gradient-weighted length (mean)	Absolute value of the net current helicity (max)	1 day mean SXR flux
	Gradient-weighted length (max)		2 day mean SXR flux
	PIL area (mean)		1 day peak SXR flux
	Maximum gradient across PIL (mean)		2 day peak SXR flux
	Maximum gradient across PIL (max)		
HSS	Gradient-weighted length (mean)	Total unsigned current helicity (max)	1 day mean SXR flux
	Gradient-weighted length (max)	Sum of the modulus of the net current per polarity (max)	2 day mean SXR flux
	PIL area (mean)	Proxy for total photospheric magnetic free energy density (max)	1 day peak SXR flux
	PIL area (max)		
	Unsigned magnetic flux in PIL area (mean)		
	AR area (mean)		
	Unsigned horizontal gradient in AR area (max)		
BS/BSS	Gradient-weighted length (mean)	Absolute value of the net current helicity (max)	1 day mean SXR flux
	Gradient-weighted length (max)		1 day peak SXR flux
	PIL area (mean)		2 day peak SXR flux
	Unsigned horizontal gradient in PIL area (max)		

Note: The descriptors are grouped by their origin (PIL, SHARP, SXR) in columns for convenience.
Source: [192].

Table 8.2 Summary of Accuracy Scores Obtained for Prediction of M-class Flares Using Different Machine Learning Classifiers (Columns) and Different Types of Descriptors (Rows)

Accuracy, M flares	ES threshold	SVM Linear	SVM RBF	SVM Sigmoid	LR	kNN	AdaBoost	MLP1	MLP2	MLP3
Expert scores (ES)	0.891±0.002	-	-	-	-	-	-	-	-	-
PIL + ES	-	0.886±0.007	0.899±0.007	0.896±0.006	0.898±0.005	0.901±0.006	0.897±0.007	0.900±0.005	0.900±0.007	0.897±0.006
SHARP + ES	-	0.886±0.007	0.898±0.007	0.894±0.010	0.899±0.006	0.897±0.006	0.896±0.007	0.900±0.007	0.899±0.004	0.899±0.006
SXR + ES	-	0.893±0.006	0.897±0.006	0.897±0.005	0.898±0.006	0.897±0.007	0.898±0.006	0.897±0.006	0.896±0.005	0.898±0.007
ALL + ES	-	0.899±0.006	0.901±0.008	0.900±0.006	0.904±0.006	0.903±0.007	0.901±0.006	0.902±0.007	0.901±0.006	0.897±0.006
PIL - ES	-	0.888±0.008	0.899±0.005	0.901±0.008	0.901±0.007	0.901±0.007	0.898±0.007	0.902±0.006	0.902±0.005	0.898±0.005
SHARP - ES	-	0.886±0.007	0.894±0.008	0.891±0.008	0.896±0.006	0.895±0.009	0.892±0.008	0.894±0.006	0.895±0.009	0.892±0.007
SXR - ES	-	0.891±0.007	0.895±0.007	0.897±0.006	0.898±0.006	0.895±0.007	0.896±0.007	0.899±0.007	0.898±0.007	0.894±0.005
ALL - ES	-	0.897±0.006	0.903±0.006	0.900±0.007	0.904±0.006	0.903±0.007	0.901±0.007	0.902±0.008	0.903±0.005	0.902±0.007

Note: The score represent the average over the scores obtained for train-validation subsets, with corresponding standard deviation. Top left score represents the accuracy of the M-class flare forecast obtained using SWPC NOAA probabilities. The probability threshold for binary forecast was obtained by maximizing accuracy on train data set and applied to validation data set for each train-validation data set pair, and averaging the result.

Source: [192].

Table 8.3 Summary of True Skill Statistics (TSS) Scores Obtained for Prediction of M-class Flares Using Different Machine Learning Classifiers (Columns) and Different Types of Descriptors (Rows)

TSS, M flares	ES threshold	SVM Linear	SVM RBF	SVM Sigmoid	LR	kNN	AdaBoost	MLP1	MLP2	MLP3
Expert scores (ES)	0.56±0.02	-	-	-	-	-	-	-	-	-
PIL + ES	-	0.60±0.04	0.60±0.03	0.60±0.04	0.59±0.03	0.57±0.03	0.59±0.03	0.62±0.03	0.61±0.04	0.60±0.04
SHARP + ES	-	0.56±0.02	0.59±0.03	0.58±0.03	0.58±0.03	0.56±0.03	0.56±0.03	0.59±0.02	0.59±0.02	0.58±0.03
SXR + ES	-	0.57±0.04	0.57±0.04	0.57±0.04	0.57±0.04	0.52±0.04	0.56±0.04	0.57±0.04	0.57±0.02	0.57±0.04
ALL + ES	-	0.61±0.04	0.63±0.03	0.62±0.04	0.62±0.03	0.60±0.02	0.61±0.04	0.62±0.03	0.63±0.03	0.62±0.04
PIL - ES	-	0.59±0.03	0.59±0.04	0.59±0.02	0.59±0.02	0.55±0.04	0.57±0.03	0.61±0.02	0.59±0.02	0.61±0.02
SHARP - ES	-	0.57±0.04	0.58±0.03	0.59±0.03	0.58±0.03	0.55±0.04	0.57±0.03	0.58±0.03	0.59±0.03	0.60±0.03
SXR - ES	-	0.56±0.04	0.57±0.04	0.57±0.04	0.57±0.03	0.51±0.04	0.57±0.04	0.58±0.04	0.57±0.04	0.58±0.04
ALL - ES	-	0.62±0.03	0.63±0.03	0.63±0.03	0.63±0.02	0.60±0.03	0.62±0.03	0.64±0.03	0.63±0.02	0.64±0.03

Source: [192].

Table 8.4 Summary of Heidke Skill Scores (HSS) Obtained for Prediction of M-class Flares Using Different Machine Learning Classifiers (Columns) and Different Types of Descriptors (Rows)

HSS, M flares	ES threshold	SVM Linear	SVM RBF	SVM Sigmoid	LR	kNN	AdaBoost	MLP1	MLP2	MLP3
Expert scores (ES)	0.41±0.01	-	-	-	-	-	-	-	-	-
PIL + ES	-	0.44±0.03	0.45±0.04	0.44±0.03	0.45±0.03	0.43±0.04	0.43±0.03	0.46±0.04	0.46±0.03	0.45±0.04
SHARP + ES	-	0.40±0.03	0.43±0.03	0.41±0.04	0.41±0.03	0.40±0.04	0.41±0.03	0.42±0.04	0.42±0.04	0.42±0.03
SXR + ES	-	0.42±0.02	0.42±0.02	0.41±0.02	0.43±0.02	0.39±0.02	0.41±0.04	0.42±0.03	0.43±0.02	0.43±0.02
ALL + ES	-	0.47±0.03	0.48±0.03	0.47±0.04	0.48±0.03	0.46±0.03	0.45±0.02	0.48±0.03	0.48±0.02	0.47±0.02
PIL - ES	-	0.43±0.04	0.43±0.04	0.43±0.04	0.44±0.04	0.44±0.03	0.42±0.04	0.44±0.04	0.44±0.04	0.44±0.04
SHARP - ES	-	0.42±0.04	0.44±0.04	0.43±0.04	0.42±0.04	0.38±0.06	0.41±0.04	0.41±0.05	0.43±0.04	0.43±0.04
SXR - ES	-	0.41±0.03	0.41±0.03	0.41±0.02	0.42±0.02	0.39±0.03	0.40±0.03	0.43±0.02	0.42±0.02	0.42±0.02
ALL - ES	-	0.48±0.04	0.49±0.04	0.48±0.04	0.48±0.03	0.46±0.03	0.46±0.04	0.48±0.03	0.48±0.03	0.48±0.02

Source: [192].

SWPC/NOAA probabilities (described in the end of Section 8.3), and represents the score which we are aimed to improve.

As one can see, all methods perform approximately at the same level for any group of descriptors. For example, the Support Vector Machine (SVM) classifier (which determines separatrix for the data points in the descriptor space and, thus, is relatively easy to interpret), performs at the same level or better than other considered machine-learning algorithms. The fact that Linear SVM and Logistic Regression algorithms also perform very good may indicate that the data are relatively simple in nature, and again could be separated by hyperplane in the descriptor space.

Another interesting finding is that almost any classifier trained on just one group of descriptors (PIL, SHARP, or SXR) performs at the same level or better than the operational probabilities converted to the binary forecast. The most interesting are the cases when the classifier is trained solely on the SXR features, with no inclusion of expert probabilities (i.e., “SXR — ES”). As one can see, training on SXR descriptors gives scores comparable to expert scores. This again confirms the importance of the flare activity prehistory for the forecasts.

If the classifier is trained in all available features excluding SWPC NOAA operational probabilities (i.e., “ALL-ES” rows) then the achieved scores are higher with the significance than ones obtained solely from the SWPC NOAA probabilities. For the accuracy, the maximum “ALL-ES” score is obtained for LR and is 0.904 ± 0.006, while the expert score is 0.891 ± 0.002. The maximum obtained TSS (for MLP3) is 0.64 ± 0.03, while the expert score is 0.56 ± 0.02. The maximum obtained HSS (for RBF SVM) is 0.49 ± 0.04, while the expert score is 0.41 ± 0.01. As one can see, the scores obtained with machine learning algorithms enhance the expert scores, and the enhancement is significant in terms of generalization errors of these scores. This also demonstrates that the enhancement is possible only if considering jointly magnetic field features and SXR descriptors.

One more important point to mention is that the “ALL+ES” and “ALL-ES” rows have approximately the same scores, which indicates that SWPC NOAA flare probabilities do not introduce new information in addition to the derived descriptors. The information is already included in the properties of the magnetic field and the flare prehistory.

Table 8.5 illustrates the classification results for TSS metrics for the X-class flares. The qualitative results for the prediction of X-class flares are essentially the same as for the M-class flares. However, the poor occurrence rate of such strong flares makes their prediction almost meaningless in the framework of this study, as visible from huge uncertainties and spread of the results.

8.4.2 Probabilistic Forecast

The SWPC/NOAA operational forecast is probabilistic in nature. Attempts to apply thresholding the probability and convert the forecast to binary one will be accompanied by loss of essential information. One can try to construct the probabilistic prediction using the machine learning algorithms, and compare the issued probabilities directly. Attempts to build the probabilistic forecasts have previously been developed [217]. Also the probabilistic forecast of solar flares using the McIntosh classification of sunspots was tested by McCloskey et al. [143].

Our decision was to evaluate the event probabilities using the technique introduced by Platt [166] for SVMs (see Appendix B, SVM Section), and compare them with SWPC NOAA probabilities in terms of the Brier Score. Also, for both forecasts, we evaluate their Brier Skill Scores (BSS) with respect to the flare climatology. We use only SVM with two different kernels (RBF and Sigmoid) to evaluate probabilities, and consider all features (PIL, SHARP, and SXR) jointly, with or without SWPC NOAA probabilities.

Table 8.5 Summary of True Skill Statistics (TSS) Scores Obtained for Prediction of X-class Flares Using Different Machine Learning Classifiers (Columns) and Different Types of Descriptors (Rows)

TSS, X flares	ES threshold	SVM Linear	SVM RBF	SVM Sigmoid	LR	kNN	AdaBoost	MLP1	MLP2	MLP3
Expert scores (ES)	0.57±0.08	-	-	-	-	-	-	-	-	-
PIL + ES	-	0.61±0.13	0.60±0.15	0.68±0.13	0.65±0.15	0.58±0.09	0.68±0.11	0.68±0.15	0.65±0.13	0.64±0.13
SHARP + ES	-	0.51±0.23	0.56±0.17	0.61±0.18	0.65±0.15	0.37±0.17	0.56±0.16	0.67±0.15	0.60±0.19	0.60±0.16
SXR + ES	-	0.72±0.07	0.73±0.07	0.74±0.10	0.75±0.08	0.71±0.21	0.78±0.06	0.79±0.07	0.78±0.07	0.77±0.09
ALL + ES	-	0.74±0.07	0.73±0.07	0.77±0.07	0.75±0.08	0.71±0.21	0.78±0.06	0.80±0.09	0.78±0.07	0.77±0.09
PIL - ES	-	0.66±0.09	0.66±0.08	0.67±0.04	0.68±0.11	0.41±0.13	0.68±0.12	0.70±0.08	0.68±0.09	0.70±0.08
SHARP - ES	-	0.40±0.22	0.40±0.21	0.47±0.15	0.45±0.18	0.41±0.19	0.42±0.17	0.48±0.19	0.44±0.21	0.45±0.19
SXR - ES	-	0.77±0.07	0.75±0.08	0.76±0.07	0.76±0.08	0.58±0.15	0.78±0.06	0.80±0.06	0.78±0.07	0.79±0.04
ALL - ES	-	0.77±0.07	0.78±0.08	0.76±0.07	0.77±0.07	0.72±0.15	0.78±0.06	0.82±0.06	0.79±0.07	0.79±0.04

Source: [192].

The results are presented in Table 8.6 for both M-class and X-class flares. As one can see, the probabilities issued by SVM classifier have lower BS than the SWPC NOAA probabilities. The BSS demonstrates that the SWPC NOAA probabilities are slightly better than the climatological forecast for M-class flares (i.e., constant probability equal to the event occurrence rate), but forecasts based on SVM have significantly higher BSS. Also, one can find that for X-class flares, the climatology is even better than the forecasts issued by SWPC NOAA, and the SVM methods give no improvement with respect to it. As was found for the binary forecast, the inclusion of SWPC NOAA probabilities does not improve the score.

Figure 8.2 illustrates the probabilities of the M-class flare to happen for every day in 2016-2017 if we train RBF SVM on 2010-2015 data. The features summarized in Table 8.1 for BS/BSS are used for the training. One can see that, in “operational” sense, machine learning based probabilities are also better than the SWPC NOAA probabilities.

8.5 Discussion

In this work, we made an attempt to compare the probabilistic operational forecast with the predictions based on various machine learning methods. Our results indicate the the performance of various machine learning classification algorithms is comparable to each other. The same result was previously demonstrated by Domijan et al. [54] using the features from Solar Monitor Active Region Tracker (SMART) and different machine learning algorithms (LR, SVM, Random Forest, MLP). Such conclusions indicate that, most probably, the classification scores are limited by the structure of our data set and derived descriptors rather than by the impurity of the algorithms, i.e., it is essentially impossible to improve the classification without improving descriptors.

Table 8.6 Summary of Brier Scores (BS) and Bries Skill Scores (BSS, with respect to Event Climatology) Obtained for Prediction of M-class and X-class Flares using SVM Classifiers with RBF and Sigmoid Kernels

BS/BSS, M flares	Expert scores (ES)	SVM RBF	SVM Sigmoid
Expert scores (ES)	0.092±0.004 / 0.09±0.04	-	-
ALL + ES	-	0.073±0.004 / 0.28±0.04	0.073±0.004 / 0.28±0.04
ALL - ES	-	0.072±0.004 / 0.29±0.04	0.072±0.004 / 0.29±0.04
BS, X flares	Expert Scores (ES)	SVM RBF	SVM Sigmoid
Expert scores (ES)	0.011±0.001 / -0.63±0.18	-	-
ALL + ES	-	0.007±0.001 / 0.01±0.20	0.007±0.001 / 0.04±0.18
ALL - ES	-	0.007±0.001 / 0.01±0.19	0.007±0.001 / 0.03±0.19

Note: The probabilities for the SVM classification results are obtained using method by Platt [166] and implemented in Python Scikit-learn package [163]. The score represents the average over the scores obtained for train-validation subsets, with corresponding standard deviation. Top left scores for each flare class represents the Brier scores of the probabilistic SWPC NOAA forecast averaged over the validation data sets, showed with corresponding standard deviations. One can see that the forecast improvements for the X-class flares cannot be considered to be statistically significant with respect to climatology.

Source: [192].

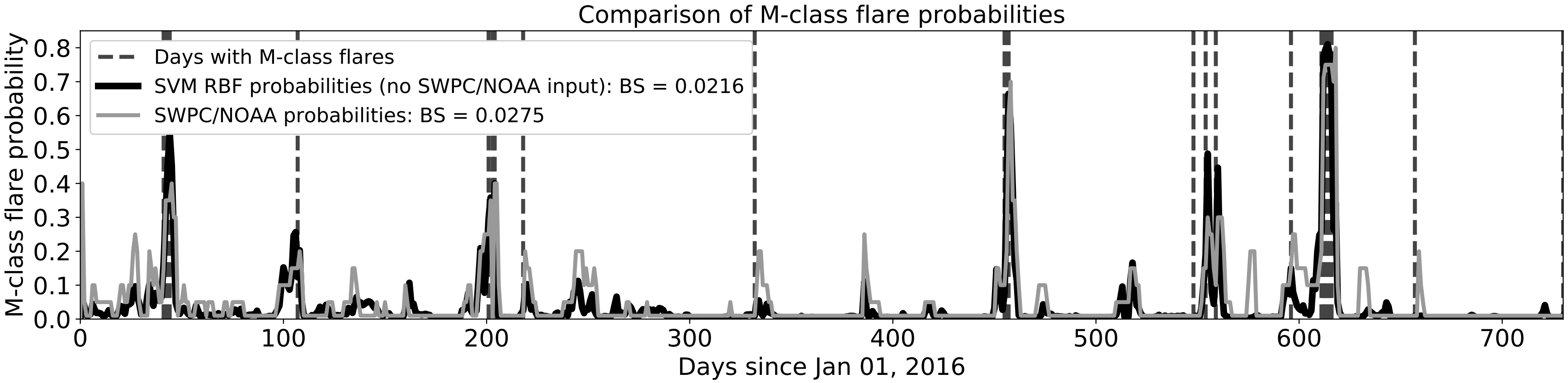

Figure 8.2 Comparison of next-day M-class flare probabilities issued for 2016-2017 on daily basis by SWPC NOAA (gray) and probabilities of flaring for SVM with RBF kernel trained on 2010-2015 data (black). Dashed gray vertical lines mark days with the M-class flares.

Source: [192]

An interesting moment regarding the binary forecast is that the scores are not so high as ones evaluated for hourly forecasts of M-class flares for active regions or magnetic field patches [19, 156, 191]. In these works, the TSS scores were ≥ 0.76, peaking at ≈ 0.90. However, the features for our work were derived from the same descriptors as used in these works. Most probably, such discrepancy in scores is caused by the structure of the data sets and different separation to the train/validation/test data subsets. Our descriptors are constructed on daily basis rather than hourly, for the whole Sun rather than for the active regions. This results, for example, in completely different class-imbalance ratio (about 1/7 flaring to non-flaring cases rather than about 1/50 in these studies). This confirms that the comparison of the scores among the prediction algorithm and the operational facility should not be done unless the prediction of the algorithm is issued in the same format (i.e., preserving the spatial and temporal scale of operational facility). The same is true for comparison of the predictions made by different algorithms. In this aspect, the development of the benchmark data sets for algorithm testing is especially necessary [137].

When one separates data points from consequent time moments to different (train and validation) data sets, one has to make sure that high prediction scores are not the results of the strong correlation between these data points. To check for this issue, we try to subdivide the data set to train and validation not randomly but by 5-day and 15-day chunks, and obtain scores for M-class flares for RBF SVM classifier using all features except SWPC NOAA probabilities. The results show a slight decrease of the score which is, however, strongly within the cross-validation error. Although there are some correlations between the train and validation data sets, they do not seem to influence the obtained results.

One more parameter which we have used in our feature selection procedure is the threshold for the score improvement starting from which we keep the feature for the classifier. Decrease of this threshold may lead to inclusion of more features in classification but less robustness to occasional fluctuations of the scores. To check the issue, we have decreased the threshold twice for M-class flares for RBF SVM classifier using all features except SWPC NOAA probabilities. We found that the scores remain the same, strongly within cross-validation error.

One can mention that the BS for M-class flares for the "operational" separation of the train and test data sets presented in Figure 8.2 is significantly lower (≈0.022) than one obtained for cross-validation and presented in Table 8.6 (≈0.072). We have found that this issue is common: accuracy, TSS, and HSS become higher if the classifier is trained on 2010-2015 and tested on 2016-2017. This illustrates one more time that the subdivision of the data set into the train and test can affect the score and should be done similarly for the prediction algorithms aimed to be compared.

8.6 Summary and Conclusion

In this work we investigated whether it is possible to enhance daily whole-Sun operational SWPC NOAA flare forecast by utilizing descriptors of the photospheric magnetic field and soft X-ray flux and employing various machine learning classification algorithms. Let us summarize the main findings of the study:

1. SWPC NOAA operational forecasts (next-day probabilities of M-class and X-class flares) are strongly correlated with the current flare activity rather than with the next-day flare activity;
2. Typically just 5 to 15 descriptors are enough to achieve maximum score for any considered pool of descriptors, any metrics, and any classifier;
3. Almost all analyzed classifiers perform approximately at the same level for every metrics, including SVM classifiers;
4. Binary (yes/no) forecasts of M-class and X-class flares based on each pool of descriptors (PIL, SHARP, SXR) separately have a potential of the same or better performance than the SWPC NOAA operational forecasts;
5. It is possible to enhance binary forecast of M-class and X-class flares by considering joint magnetic (PIL, SHARP) and SXR characteristics. The

accuracy increases from 0.891 ± 0.002 to 0.904 ± 0.006, TSS increases from 0.56 ± 0.02 to 0.64 ± 0.03, the HSS increases from 0.41 ± 0.01 to 0.49 ± 0.04;

6. Inclusion of the SWPC NOAA operational forecasts as features usually does not improve the forecast;
7. Probabilistic forecast of M-class flares based on the SVM improves to the SWPC NOAA operational forecasts in terms of Brier Score, and has a significant Brier Skill Score (0.29 ± 0.04) with respect to the flare climatology.

Although this study demonstrated a possibility to enhance the operational forecast, its results should be taken with caution. The proper test data set was not established for this study, and all scores represent validation scores. Also, the study was limited to the time period of the solar cycle 24 and corresponding flare activity and statistics. Nevertheless, we made an attempt to establish more direct comparison between SWPC NOAA forecast and our predictions in terms of temporal and spatial resolutions of descriptors, as well as qualitatively analyzed its informational value.

Of course, there are many possibilities to improve this study. First, one can construct more complex magnetic field descriptors of the whole Sun, and test other parameters characterizing the magnetic field in active regions [124, 111, 110, 136, 161, 172, 106, 107]. Also, one can discover more complicated non-linear relations between the observational data and solar flares using deep learning algorithms [86, 94, 155, 160]. Although deep learning is more complicated for interpretation and knowledge extraction, it demonstrated a strong potential for prediction problems. Finally, the questions of prediction of the flare occurrence time and its soft X-ray emission properties, although discussed in literature [24, 213], still remain an undiscovered field.

CHAPTER 9

SUMMARY AND CONCLUDING REMARKS

9.1 Summary of the Presented Studies

In this section we highlight the main results of the presented studies, one paragraph per one dissertation chapter.

In Chapter 2 we present a detailed analysis of spatially-resolved multi-wavelength observations of chromospheric evaporation during an M 1.0-class solar flare (SOL2014-06-12T21:12) using data from the NASA's IRIS (Interface Region Imaging Spectrograph) and HMI/SDO (Helioseismic and Magnetic Imager onboard Solar Dynamics Observatory), and high-resolution observations from VIS/NST (Visible Imaging Spectrometer at New Solar Telescope). The results show that the averaged over the flare region Fe XXI blueshift of the hot ($10^7 K$) evaporating plasma is delayed relative to the C II redshift of the relatively cold ($10^4 K$) chromospheric plasma by about 1 min. The spatial distribution of the delays is not uniform across the region and can be as long as 2 min in several zones. Using vector magnetograms from HMI we reconstruct the magnetic field topology and the quasi-separatrix layer (QSL), and find that the blueshift delay regions as well as the Hα flare ribbons are connected to the region of magnetic polarity inversion line (PIL) and an expanding flux rope via a system of low-lying loop arcades with height $\lesssim 4.5\,\mathrm{Mm}$. As a result, the chromospheric evaporation may be driven by the energy release in the vicinity of PIL, and has the observed properties due to a local magnetic field topology.

Inspired by the case study, we have developed an Interactive Multi-Instrument Database of Solar Flares (`https://solarflare.njit.edu/`, `https://helioportal.nas.nasa.gov/`), a tool for efficient data search, integration of different flare lists and representation of observational data. We present this tool in Chapter 3.

The web accessible database is fully functional and allows the user to search for uniquely-identified flare events based on their physical descriptors and availability of observations by a particular set of instruments. Currently, the data from three primary flare lists (GOES, RHESSI and HEK) and a variety of other event catalogs (Hinode, Fermi GBM, Konus-Wind, OVSA flare catalogs, CACTus CME catalog, Filament eruption catalog) and observing logs (IRIS and Nobeyama coverage) are integrated, and an additional set of physical descriptors (temperature and emission measure) is provided along with an observing summary, data links, and multi-wavelength light curves for each flare event since January, 2002. We envision that this new tool will allow researchers to significantly speed up the search of events of interest for statistical and case studies.

In Chapter 4 we present a statistical study of chromospheric evaporation in solar flares using simultaneous observations by the RHESSI X-ray telescope and the IRIS UV spectrograph. The selection of the events was done using the IMIDSF mentioned in the previous paragraph. The results are compared with radiation hydrodynamic flare models from the F-CHROMA RADYN database. For each event, we study spatially-resolved Doppler shifts of spectral lines formed in the transition region (C II 1334.5 Å) and hot coronal plasma (Fe XXI 1354.1 Å) to investigate the dynamics of the solar atmosphere during the flare impulsive phase. We estimate the energy fluxes deposited by high-energy electrons using X-ray imaging spectroscopy and assuming the standard thick-target model. Using the RADYN flare models, the RH 1.5D radiative transfer code and the Chianti atomic line database, we calculate C II and Fe XXI line profiles and compare with the observations. While the RADYN models predict a correlation between the Doppler shifts and deposited energy flux for both lines, this was only observed in the C II data. Several quantitative discrepancies are found between the observations and models: the Fe XXI Doppler shifts are substantially stronger in the models than in the data; the C II mean blueshifts are absent in the observations but predicted by the models. The transition energy between "gentle" and "explosive" evaporation regimes estimated from the observations ($2 - 8 \times 10^9$ erg cm^{-2} s^{-1}) and derived from the models ($2.2 - 10.1 \times 10^9$ erg cm^{-2} s^{-1}) are comparable with each other. The results illustrate relationships among the processes of chromospheric evaporation, response of the colder layers, and the flare energy flux deposited by high-energy electrons, although demonstrating discrepancy between analyzed observations and RADYN models.

In Chapter 5 we analyze properties of Soft X-Ray (SXR) emission, plasma temperature (T), and emission measure (EM), derived from GOES observations of flares in 2002-2017. The temperature and emission measures are obtained using the TEBBS algorithm [187], which delivers reliable results together with uncertainties even for weak B-class flare events. The calculations of T, EM, and corresponding timing properties is a part of the data enrichment procedure for the IMIDSF database. More than 96% of flares demonstrate a sequential appearance of T, SXR, and EM maxima, in agreement with the expected behavior of the chromospheric evaporation process. The relative number of such flares increases with increasing the SXR flux maximum. The SXR maximum is closer in time to the T maximum for B-class flares than for $\geq$C-class flares, while it is very close to the EM maximum for M- and X-class flares. We define flares as "T-controlled" if the time interval between the SXR and T maxima is at least two times shorter than the interval between the EM and SXR maxima, and as "EM-controlled" if the time interval between the EM and SXR maxima is at least two times shorter than the interval between the SXR and T maxima. For any considered flare class range, the T-controlled events compared to EM-controlled events have: a) higher EM but lower T; b) longer durations and shorter relative growth times; c) longer FWHM and characteristic decay times. Interpretation of these statistical results based on analysis of a single loop dynamics suggests that for flares of the same class range, the T-controlled events can be developed in longer loops than the EM-controlled events.

Chapter 6 presents the modeling of the line-of-sight (LOS) observables of the Helioseismic and Magnetic Imager (HMI) onboard the Solar Dynamics Observatory (SDO) for models of the solar atmosphere heated by precipitating high-energy electrons during solar flares. The radiative hydrodynamic (RADYN) flare models are obtained from the F-CHROMA database. The Stokes profiles for the Fe 6173 Å line observed by SDO/HMI are calculated using the radiative transfer code RH assuming statistical equilibrium and 100 G or 1000 G uniform vertical magnetic fields. The SDO/HMI data processing pipeline algorithm is applied to derive the observables (continuum intensity, line depth, Doppler velocity, LOS magnetic field). Our results reveal that for the flare models with the average deposited energy fluxes of 5.0×10^{10} $\mathrm{erg\,cm^{-2}\,s^{-1}}$ the deviations of the observables from the actual spectroscopic line parameters can reach 0.6 km/s for Doppler velocities, and about 100 G for the LOS magnetic field. Such deviations decrease significantly for the weaker flare models with the average deposited energy flux of $< 5.0 \times 10^{10}$ $\mathrm{erg\,cm^{-2}\,s^{-1}}$. Although changes of the LOS magnetic field observable for F-CHROMA RADYN models are not accompanied by magnetic field sign reversals, an additional investigation using a higher-energy RADYN model ($F = 1.0 \times 10^{11}$ erg/cm^{2}s) from Kerr et al. [98] reveals stronger deviations for the observables and the possibility to detect significantly weaker LOS magnetic field. The results highlight that the sharp magnetic transients observed during the solar flares by SDO/HMI may appear due to rapid heating of the atmosphere by accelerated electrons of high energy fluxes ($F \geq 5.0 \times 10^{10}$ erg/cm^{2}s), and should be interpreted with caution.

In Chapter 7 we analyze the relationship between the flare X-ray peak flux, and characteristics of the Polarity Inversion Line (PIL) and Active Regions (AR), derived from line-of-sight (LOS) magnetograms. The statistics of M-class and X-class flares used for the study is obtained from IMIDSF database. The PIL detection algorithm based on a magnetogram segmentation procedure is applied for each AR with 1 hour cadence. The PIL and AR characteristics are associated with the AR flare history and divided into flaring and non-flaring cases. Effectiveness of the derived characteristics for flare forecasting is determined by the number of non-flaring cases separated from flaring cases by a certain threshold, and by their Fisher ranking score. The Support Vector Machine (SVM) classifier trained only on the PIL characteristics is used for the flare prediction. We have obtained the following results: (1) the PIL characteristics are more effective than global characteristics of ARs, (2) the highest True Skill Statistics (TSS) values of 0.76 ± 0.03 for $\geq$M1.0 flares and 0.84 ± 0.07 for $\geq$X1.0 flares are obtained using the "Sigmoid" SVM kernel, (3) the TSS scores obtained using only the LOS magnetograms are slightly lower than the scores obtained using vector magnetograms, but significantly better than current expert-based predictions, (4) for prediction of $\geq$M1.0 class flares 74.4% of all cases, and 91.2% for $\geq$X1.0 class, can be pre-classified as negative with no significant effect on the results, (5) the inclusion of global AR characteristics does not improve the forecast. The study confirms the unique role of the PIL region characteristics in the flare initiation process, and demonstrate possibilities of flare forecasting using only the line-of-sight magnetograms.

Finally, in Chapter 8 we extend the previous study and investigate the possibility to enhance daily operational flare forecast performed at NOAA Space Weather Prediction Center (SWPC NOAA) by employing daily whole-Sun descriptors obtained from routine observations of the photospheric magnetic fields by SDO/HMI and soft X-ray (SXR) observations by XRS/GOES. The magnetic field descriptors are constructed from properties of the Polarity Inversion Lines of Active Regions [191, PIL] and the Space weather HMI Active Region Patches [21, SHARP]. The SXR descriptors include the flare history of the Sun, and properties of its SXR 1-8 Å emission. For each day in 2010-2017, we define vector of 70 PIL, SHARP, and SXR descriptors, and optionally include SWPC NOAA next-day flare probability as an additional descriptor. We subdivide the data set into 10 train-validation subsets and compare performance of various machine learning classification algorithms in terms of their accuracy, TSS, HSS, and BSS scores. Our results indicate that 1) Support vector classifiers perform at the same level or better than other considered classifiers; 2) binary (yes/no) forecasts of the M-class and X-class flares based on each groups of descriptors (PIL, SHARP, SXR) separately have the same or better performance than the SWPC NOAA operational forecasts; 3) it is possible to enhance the binary forecast of M-class and X-class flares by considering jointly PIL, SHARP, and SXR characteristics; 4) additional inclusion of the SWPC NOAA probabilities as descriptors does not improve the forecast; 5) Brier Skill Score (BSS) of probabilistic forecast of M-class flares based on the Support Vector Machine results ($BSS = 0.29 \pm 0.04$) is higher than for the SWPC NOAA operational forecasts ($BSS = 0.09 \pm 0.04$) and indicates the enhancement of the probabilistic forecast with respect to the flare climatology.

9.2 Concluding Remarks: the Multidisciplinary Nature of Solar Physics

The Sun is definitely the most observed star in our Universe. We continuously increase our knowledge about the origin and development of the solar activity, inner structure of the Sun and solar dynamo, influence of the solar activity on the terrestrial environment and formation of the Space Weather. The most critical component for such progress in understanding of the Sun is tremendous amounts of observational data acquired by the space-based and ground-based facilities. For example, the Atmospheric and Imaging Assembly telescope onboard the Solar Dynamics Observatory makes 4K-resolution images of the Sun faster than each two seconds, which results in around 1 TB of scientific data per day. I do not think that there is a person who looked through all SDO/AIA images.

At the same time, the fast development of realistic 3D simulations also results in large data volumes. As an example, let us consider the widely-used Bifrost simulation results of the enhanced network of the Sun [78]. One of the publicly-available results of these simulations cover the region of the solar atmosphere of the size 24 Mm×24 Mm×17 Mm for less than 30 min with 10 s temporal resolution, which already results in 1.5 TB of scientific data. These are also the data volumes which are very hard to handle manually.

Growing amounts of data from ground and space observing instruments and realistic 3D simulations, together with the demand on the reliable operational forecasts of solar activity and space weather, require implementation of new approaches for analysis of multidimensional data sets. A cross-disciplinary synergy based on machine learning and data mining becomes a necessity rather than a desired research direction. The machine learning techniques are already applied for prediction of solar and heliospheric events on certain timescales (strong solar flares, coronal mass ejections, solar energetic particles), reconstruction of coronal mass ejections, deconvolution of the solar observational images, similarity search among multidimensional spectroscopic data sets. Moreover, applications of such techniques not only deliver the results but allow us to understand better the physics behind the studied processes. Thus, the number of works containing “machine learning” term in the title or abstract increases continuously, and this trend will continue to exist.

In conclusion, it is very probable that the future solar and heliospheric physicists will have a fundamental knowledge from and understand both physics and data science disciplines. And it is a very proper time to anticipate that direction and prepare the next generation of solar scientists for the bright future full of discoveries in our interdisciplinary area.

APPENDIX A

MAGNETOGRAM SEGMENTATION AND PIL DETECTION ALGORITHM

Suppose B is a magnetic field strength map (magnetogram), Z_i is a class of pixel i of the magnetogram (i.e., "positive", "negative" or "neutral"), N is the total number of pixels in the magnetogram, $\varepsilon(i)$ is a neighborhood (e.g., the closest 8 pixels) of pixel i. The magnetogram segmentation can be formulated as the following optimization procedure to maximize function $p(Z, B)$ for a given B by finding optimal classification Z_{max} [42]:

$$p(Z_{max}, B) = \max_{Z}\, p(Z, B) \propto \prod_{i=1}^{N} \phi_i(Z_i, B_i) \prod_{j \in \varepsilon(i)} \phi(Z_i, Z_j)$$

Here $\phi_i(Z_i, B_i)$ and $\phi(Z_i, Z_j)$ are the scoring functions for each pixel depending on the magnetic field strength and assumed classes of pixels. The choice of the scoring function defines segmentation characteristics and, in fact, should do the following: separate the segments of positive and negative magnetic field polarity, and avoid very small segments with weak field probably coming from noise in the data. We use the scoring functions suggested by Chernyshov et al. [42]:

$$\phi_i(Z_i, B_i) = e^{-C_1\sqrt{|B_0 - B_i|}}, \text{ for } Z_i \text{ “positive”}$$

$$\phi_i(Z_i, B_i) = e^{-C_1\sqrt{|B_0 + B_i|}}, \text{ for } Z_i \text{ “negative”}$$

$$\phi_i(Z_i, B_i) = e^{-C_2|B_i|}, \text{ for } Z_i \text{ “neutral”}$$

$$\phi(Z_i, Z_j) = e^{C_{pair}[Z_i \neq Z_j]},$$

where parameters $C_1 = 1.0$, $C_2 = 1.0$, $C_{pair} = 20$, $B_0 = 1000\,\mathrm{G}$ are chosen to obtain a stable segmentation of magnetic polarities in strong field regions. Here $[Z_i \neq Z_j]$ is equal 1 if $Z_i \neq Z_j$, and zero otherwise. Following Chernyshov et al. [42], the function $p(Z, B)$ is interpreted as conditional probability density function $p(Z|B)$, and is approximated by the factorized probability density function $q(Z) = \prod_{i=1}^{n} q_i(Z_i)$. To measure how strongly the factorized distribution deviates from the actual, one can use the Kullback-Leibler (KL) divergence Bishop [18]. In order to find the best approximating factorized distribution, $q(Z)$, one can minimize the KL divergence:

$$\underset{q(Z)}{min}\ KL(q||p) = -\int q(Z)\log\frac{p(Z|B)}{q(Z)}dZ$$

Here we keep the original notation for KL-divergence $KL(q||p)$ between distributions q and p introduced in Bishop [18]. The optimal $q(Z)$ is given by solution of the equation [42]:

$$q_i(Z_i) = \frac{1}{C}\exp(\log(\phi_i(Z_i)) - C_{pair}\sum_{t\in\varepsilon(i)}\sum_{j\neq i} q_j(Z_j))$$

This solution can be found iteratively [42]:

$$q_i^{new}(Z_i) = \frac{1}{C}\exp(\log(\phi_i(Z_i)) - C_{pair}\sum_{t\in\varepsilon(i)}\sum_{j\neq i} q_j^{old}(Z_j))$$

Using this equation, one can calculate the factorized distribution multiplier q_i for each pixel i and its assumed class Z_i (“positive”, “negative”, or “neutral”). Because the factorized distribution represents the product of multipliers for each pixel, one can simply maximize $q_i(Z_i)$ for each pixel i separately and obtain Z_{max}.

For identification of PIL in active regions, we smooth the original HMI magnetogram using the Gaussian filter with width σ =1.5″, and apply the segmentation algorithm. Then, we apply a morphological dilation procedure separately for positive and negative segments (i.e., expand each segment to include neighboring pixels), and find the PIL as an intersection of the dilated positive and negative segments. Finally, we filter all small islands of the PIL with the number of pixels less than 3% of the total number of pixels occupied by PIL. This approach is quite robust, and allows us to automatically identify the PIL and calculate magnetic field properties.

APPENDIX B

DESCRIPTION OF CLASSIFIERS

B.1 Support Vector Machine (SVM) and Probabilistic Forecast

The SVM classifier [43] is aimed to find a separatrix manifold in the descriptor space, which optimally separates the classes by maximizing the following functional:

$$\underset{\omega,\epsilon}{min}\ L = \frac{1}{2}||\omega||^2 + C\sum_{i=1}^{m} W_i\epsilon_i, \tag{B.1}$$

$$y_i(\langle\omega, x_i\rangle + b) \geq 1 - \epsilon_i, \quad \epsilon_i \geq 0, \tag{B.2}$$

where ω is a vector normal to the separating manifold; i is case number in the “train” dataset, varying from 0 to m; C is a soft margin parameter; W_i is the weight of the group which the case i belongs to, ϵ_i is a measure of misclassification of case i; y_i is a constant equal to 1 for positive cases, and -1 for negative cases. After some transformations, the functional to minimize depends only on scalar products of descriptor vectors, $\langle x_i, x_j\rangle$. To work with cases which are not linearly-separated, one can replace the scalar product with the kernel function, $\langle x_i, x_j\rangle \to k(x_i, x_j)$. In this work, we have tested several kernels available in the Python Scikit-Learn package:

$$k(x_i, x_j) = \langle x_i, x_j\rangle \ \ (Linear), \tag{B.3}$$

$$k(x_i, x_j) = exp(-\gamma\, |x_i - x_j|^2)\ (RBF), \tag{B.4}$$

$$k(x_i, x_j) = \tanh(\gamma\, \langle x_i, x_j\rangle + r)\ (Sigmoid). \tag{B.5}$$

Notice here that γ and r, as well as previously-mentioned C and W_i, are SVM hyperparameters which should be selected and optimized during the cross-validation procedure. The decision about how to classify the upcoming data point is made by thresholding of evaluated decision function:

$$f(x) = \sum_i y_i \alpha_i k(x_i) + b, \tag{B.6}$$

where α_i and b are computed at the training stage. The idea of Platt [166] was to use the unthresholded output, $f(x)$, to build probabilistic forecast. The parametric model (the sigmoid function) is used to fit the posterior probabilities directly, i.e.,

$$P(y = 1|f(x)) = \frac{1}{1 + exp(Af + B)}, \tag{B.7}$$

where A and B are fit using a maximum likelihood estimation from a training set. Although the method of mapping of classifier decision function to probabilities is not unique, we use the described implementation in our research.

B.2 Logistic Regression (LR)

The LR is essentially the smooth regularized mapping of the descriptor space to their binary outputs using the logistic function:

$$P(x) = \frac{1}{1 + exp(-\beta_0 + < \beta_1 x >)}, \tag{B.8}$$

where β_0 is a scalar parameter, and β_1 is a vector parameter with the dimension equal to number of descriptors, both are subject to optimize across the train data sets with involvement of regularization. The regularization parameters are determined during the cross-validation procedure in our study.

B.3 k-Nearest Neighbors (kNN)

The kNN algorithm is an algorithm where the class of each point from the test data set is determined based on the classes of points from the train data set which are closest to that point (i.e., its “neighbors”). It is possible to vary several hyperparameters for the kNN classifier: 1) number of neighbors influencing the decision; 2) the weights of the neighbors on the decision depending on their class; 3) the weights of the neighbors on the decision depending on their distance from the point; 4) the measure of the distance between points (Euclidean or Manhattan). In our study, these hyperparameters were maximized across the train-validation data set pairs.

B.4 Adaptive Boosting (AdaBoost) based on Decision Trees

AdaBoost is a meta-algorithm rather than an algorithm: it proposes an idea to handle an ensemble of weak classifiers and adapt their voting weights during the training process [70]. If one has T classifiers, then their combined output may be written as:

$$F_T(x) = \sum_{t=1}^{T} f_t(x) \tag{B.9}$$

After each training loop, one can minimize the sum training error E_t by adapting coefficients with which the classifiers contribute to the decision:

$$E_t = \sum_i E\left[F_{t-1}(x_i) + \alpha_t h(x_i)\right], \tag{B.10}$$

$$f_t(x) = \alpha_t h(x) \tag{B.11}$$

Here F_{t-1} is the boosted classifier built in the previous stage, and $E(F)$ is some function to minimize, $h(x)$ is the output of each single classifier participating in boosting. For our case, each single classifier is the decision tree classifier with the maximum depth of one, and the only hyperparameter to optimize is the number of decision tree classifiers.

B.5 Multi-Layer Perceptron (MLP)

In this work, MLP is referred to a class of the feed-forward neural networks. MLP consists of several neuron layers, and each neuron is connected to the each neuron at the next layer only. The number of neurons at the first layer is equal to the number of inputs (descriptors), and there is just one neuron in the output layer. The layers between them are called “hidden”. The neurons from the preceding layer i contribute to the neurons at the next layer j according to some weights, and fire according to the selected activation function (hyperbolic tangent function in our case), i.e.,:

$$x_j = \sum_i y_i w_{i,j} \tag{B.12}$$

$$y_j = tanh(x_j) \tag{B.13}$$

In this work, we use MLPs with two hidden layer of 200 neurons each, with five hidden layers with 200 neurons each, and with five hidden layers with 200, 100, 50, 25, and 10 neurons, correspondingly. To find the optimal weights $w_{i,j}$, we use a method for stochastic optimization called “Adam” [101] available as an option for MLP training in Scikit-learn. To prevent the MLP from overfitting the data, for each train-validation pair separately, we evaluate the validation score at each epoch (each complete pass through the available training data points) and stop training once the validation score stops to increase.

BIBLIOGRAPHY

[1] W. P. Abbett. *A Theoretical Investigation of Optical Emission in Solar Flares*. PhD thesis, Michigan State University, East Lansing, MI, 1998.

[2] W. P. Abbett and S. L. Hawley. Dynamic Models of Optical Emission in Impulsive Solar Flares. *The Astrophysical Journal*, 521:906–919, August 1999.

[3] O. W. Ahmed, R. Qahwaji, T. Colak, P. A. Higgins, P. T. Gallagher, and D. S. Bloomfield. Solar Flare Prediction Using Advanced Feature Extraction, Machine Learning, and Feature Selection. *Solar Physics*, 283:157–175, March 2013.

[4] A. Al-Ghraibah, L. E. Boucheron, and R. T. J. McAteer. An Automated Classification Approach to Ranking Photospheric Proxies of Magnetic Energy Build-up. *Astronomy & Astrophysics*, 579:A64, July 2015.

[5] J. C. Allred, S. L. Hawley, W. P. Abbett, and M. Carlsson. Radiative Hydrodynamic Models of the Optical and Ultraviolet Emission from Solar Flares. *The Astrophysical Journal*, 630:573–586, September 2005.

[6] J. C. Allred, S. L. Hawley, W. P. Abbett, and M. Carlsson. Radiative Hydrodynamic Models of Optical and Ultraviolet Emission from M Dwarf Flares. *The Astrophysical Journal*, 644:484–496, June 2006.

[7] J. C. Allred, A. F. Kowalski, and M. Carlsson. A Unified Computational Model for Solar and Stellar Flares. *The Astrophysical Journal*, 809:104, August 2015.

[8] A. Anastasiadis, A. Papaioannou, I. Sandberg, M. Georgoulis, K. Tziotziou, A. Kouloumvakos, and P. Jiggens. Predicting Flares and Solar Energetic Particle Events: The FORSPEF Tool. *Solar Physics*, 292:134, September 2017.

[9] S. K. Antiochos and P. A. Sturrock. Evaporative Cooling of Flare Plasma. *The Astrophysical Journal*, 220:1137–1143, March 1978.

[10] R. L. Aptekar, D. D. Frederiks, S. V. Golenetskii, V. N. Ilynskii, E. P. Mazets, V. N. Panov, Z. J. Sokolova, M. M. Terekhov, L. O. Sheshin, T. L. Cline, and D. E. Stilwell. Konus-W Gamma-Ray Burst Experiment for the GGS Wind Spacecraft. *Space Science Reviews*, 71:265–272, February 1995.

[11] M. J. Aschwanden, R. A. Stern, and M. Güdel. Scaling Laws of Solar and Stellar Flares. *The Astrophysical Journal*, 672:659–673, January 2008.

[12] M. J. Aschwanden and D. Tsiklauri. The Hydrodynamic Evolution of Impulsively Heated Coronal Loops: Explicit Analytical Approximations. *The Astrophysical Journal Supplement Series*, 185:171–185, November 2009.

[13] G. Aulanier, M. Janvier, and B. Schmieder. The Standard Flare Model in Three Dimensions. I. Strong-to-weak Shear Transition in Post-Flare Loops. *Astronomy & Astrophysics*, 543:A110, Jul 2012.

[14] G. Aulanier, E. Pariat, P. Démoulin, and C. R. DeVore. Slip-Running Reconnection in Quasi-Separatrix Layers. *Solar Physics*, 238:347–376, Nov 2006.

[15] Y. Bamba, S. Inoue, K. Kusano, and D. Shiota. Triggering Process of the X1.0 Three-ribbon Flare in the Great Active Region NOAA 12192. *The Astrophysical Journal*, 838:134, April 2017.

[16] G. Barnes, K. D. Leka, C. J. Schrijver, T. Colak, R. Qahwaji, O. W. Ashamari, Y. Yuan, J. Zhang, R. T. J. McAteer, D. S. Bloomfield, P. A. Higgins, P. T. Gallagher, D. A. Falconer, M. K. Georgoulis, M. S. Wheatland, C. Balch, T. Dunn, and E. L. Wagner. A Comparison of Flare Forecasting Methods. I. Results from the “All-Clear” Workshop. *The Astrophysical Journal*, 829:89, October 2016.

[17] M. Battaglia, L. Kleint, S. Krucker, and D. Graham. How Important Are Electron Beams in Driving Chromospheric Evaporation in the 2014 March 29 Flare? *The Astrophysical Journal*, 813:113, November 2015.

[18] C. M. Bishop. *Pattern Recognition and Machine Learning (Information Science and Statistics)*. Berlin, Heidelberg: Springer-Verlag, 2006.

[19] M. G. Bobra and S. Couvidat. Solar Flare Prediction Using SDO/HMI Vector Magnetic Field Data with a Machine-learning Algorithm. *The Astrophysical Journal*, 798:135, January 2015.

[20] M. G. Bobra and S. Ilonidis. Predicting Coronal Mass Ejections Using Machine Learning Methods. *The Astrophysical Journal*, 821:127, April 2016.

[21] M. G. Bobra, X. Sun, J. T. Hoeksema, M. Turmon, Y. Liu, K. Hayashi, G. Barnes, and K. D. Leka. The Helioseismic and Magnetic Imager (HMI) Vector Magnetic Field Pipeline: SHARPs - Space-Weather HMI Active Region Patches. *Solar Physics*, 289:3549–3578, September 2014.

[22] P. L. Bornmann. Limits to Derived Flare Properties Using Estimates for the Background Fluxes - Examples from GOES. *The Astrophysical Journal*, 356:733–742, June 1990.

[23] P. L. Bornmann, D. Speich, J. Hirman, L. Matheson, R. Grubb, H. Garcia, and R. Viereck. GOES X-ray Sensor and Its Use in Predicting Solar-Terrestrial Disturbances. In E. R. Washwell, editor, *GOES-8 and Beyond*, volume 2812 of *GOES-8 and Beyond*, pages 291–298, October 1996.

[24] L. E. Boucheron, A. Al-Ghraibah, and R. T. J. McAteer. Prediction of Solar Flare Size and Time-to-Flare Using Support Vector Machine Regression. *The Astrophysical Journal*, 812:51, October 2015.

[25] T. A. Bowen, P. Testa, and K. K. Reeves. Multi-wavelength Observations of Solar Flares with a Constrained Peak X-Ray Flux. *The Astrophysical Journal*, 770:126, June 2013.

[26] S. J. Bradshaw. A Numerical Tool for the Calculation of Non-equilibrium Ionisation States in the Solar Corona and Other Astrophysical Plasma Environments. *Astronomy & Astrophysics*, 502:409–418, Jul 2009.

[27] S. Brannon and D. Longcope. Modeling Properties of Chromospheric Evaporation Driven by Thermal Conduction Fronts from Reconnection Shocks. *The Astrophysical Journal*, 792:50, September 2014.

[28] L. Breiman. Random forests. *Machine Learning*, 45(1):5–32, October 2001.

[29] J. W. Brosius. Chromospheric Evaporation in Solar Flare Loop Strands Observed with the Extreme-ultraviolet Imaging Spectrometer on Board Hinode. *The Astrophysical Journal*, 762:133, January 2013.

[30] J. W. Brosius and A. N. Daw. Quasi-periodic Fluctuations and Chromospheric Evaporation in a Solar Flare Ribbon Observed by IRIS. *The Astrophysical Journal*, 810:45, September 2015.

[31] J. W. Brosius and G. D. Holman. Observations of the Thermal and Dynamic Evolution of a Solar Microflare. *The Astrophysical Journal*, 692:492–501, Feb 2009.

[32] J. W. Brosius and A. R. Inglis. Explosive Chromospheric Evaporation and Warm Rain in a C3.1 Flare Observed by IRIS, Hinode/EIS, and RHESSI. *The Astrophysical Journal*, 848:39, October 2017.

[33] J. W. Brosius and K. J. H. Phillips. Extreme-Ultraviolet and X-Ray Spectroscopy of a Solar Flare Loop Observed at High Time Resolution: A Case Study in Chromospheric Evaporation. *The Astrophysical Journal*, 613:580–591, September 2004.

[34] J. C. Brown. The Deduction of Energy Spectra of Non-Thermal Electrons in Flares from the Observed Dynamic Spectra of Hard X-Ray Bursts. *Solar Physics*, 18:489–502, July 1971.

[35] P. J. Cargill, S. J. Bradshaw, and J. A. Klimchuk. Enthalpy-based Thermal Evolution of Loops. II. Improvements to the Model. *The Astrophysical Journal*, 752:161, June 2012.

[36] P. J. Cargill, S. J. Bradshaw, and J. A. Klimchuk. Enthalpy-based Thermal Evolution of Loops. III. Comparison of Zero- dimensional Models. *The Astrophysical Journal*, 758:5, October 2012.

[37] M. Carlsson and R. F. Stein. Formation of Solar Calcium H and K Bright Grains. *The Astrophysical Journal*, 481:500–514, May 1997.

[38] H. Carmichael. A Process for Flares. *NASA Special Publication*, 50:451, 1964.

[39] A. Caspi, S. Krucker, and R. P. Lin. Statistical Properties of Super-hot Solar Flares. *The Astrophysical Journal*, 781:43, January 2014.

[40] J. S. Castellanos Durán, L. Kleint, and B. Calvo-Mozo. A Statistical Study of Photospheric Magnetic Field Changes During 75 Solar Flares. *The Astrophysical Journal*, 852:25, January 2018.

[41] R. Chandra, B. Schmieder, C. H. Mandrini, P. Démoulin, E. Pariat, T. Török, and W. Uddin. Homologous Flares and Magnetic Field Topology in Active Region NOAA 10501 on 20 November 2003. *Solar Physics*, 269:83–104, Mar 2011.

[42] V. Chernyshov, D. Laptev, and D Vetrov. Short-term solar flare forecast. In *in The 21st Int. Conf. Computer Graphics and Vision*, 2011.

[43] C. Cortes and V. Vapnik. Support-vector networks. *Machine Learning*, 20(3):273–297, Sep 1995.

[44] S. Couvidat, S. P. Rajaguru, R. Wachter, K. Sankarasubramanian, J. Schou, and P. H. Scherrer. Line-of-Sight Observables Algorithms for the Helioseismic and Magnetic Imager (HMI) Instrument Tested with Interferometric Bidimensional Spectrometer (IBIS) Observations. *Solar Physics*, 278:217–240, May 2012.

[45] S. Couvidat, J. Schou, J. T. Hoeksema, R. S. Bogart, R. I. Bush, T. L. Duvall, Y. Liu, A. A. Norton, and P. H. Scherrer. Observables Processing for the Helioseismic and Magnetic Imager Instrument on the Solar Dynamics Observatory. *Solar Physics*, 291:1887–1938, August 2016.

[46] S. Couvidat, J. Schou, R. A. Shine, R. I. Bush, J. W. Miles, P. H. Scherrer, and R. L. Rairden. Wavelength Dependence of the Helioseismic and Magnetic Imager (HMI) Instrument onboard the Solar Dynamics Observatory (SDO). *Solar Physics*, 275:285–325, January 2012.

[47] M. D. Crown. Validation of the NOAA Space Weather Prediction Center's solar flare forecasting look-up table and forecaster-issued probabilities. *Space Weather*, 10:S06006, June 2012.

[48] A. Czaykowska, D. Alexander, and B. De Pontieu. Chromospheric Heating in the Late Phase of Two-Ribbon Flares. *The Astrophysical Journal*, 552:849–857, May 2001.

[49] A. Czaykowska, B. De Pontieu, D. Alexander, and G. Rank. Evidence for Chromospheric Evaporation in the Late Gradual Flare Phase from SOHO/CDS Observations. *The Astrophysical Journal*, 521:L75–L78, August 1999.

[50] B. De Pontieu, A. M. Title, J. R. Lemen, G. D. Kushner, D. J. Akin, B. Allard, T. Berger, P. Boerner, M. Cheung, C. Chou, J. F. Drake, D. W. Duncan, S. Freeland, G. F. Heyman, C. Hoffman, N. E. Hurlburt, R. W. Lindgren, D. Mathur, R. Rehse, D. Sabolish, R. Seguin, C. J. Schrijver, T. D. Tarbell, J.-P. Wülser, C. J. Wolfson, C. Yanari, J. Mudge, N. Nguyen-Phuc, R. Timmons, R. van Bezooijen, I. Weingrod, R. Brookner, G. Butcher, B. Dougherty, J. Eder, V. Knagenhjelm, S. Larsen, D. Mansir, L. Phan, P. Boyle, P. N. Cheimets, E. E. DeLuca, L. Golub, R. Gates, E. Hertz, S. McKillop, S. Park, T. Perry, W. A. Podgorski, K. Reeves, S. Saar, P. Testa, H. Tian, M. Weber, C. Dunn, S. Eccles, S. A. Jaeggli, C. C. Kankelborg, K. Mashburn, N. Pust, L. Springer, R. Carvalho, L. Kleint, J. Marmie, E. Mazmanian, T. M. D. Pereira, S. Sawyer, J. Strong, S. P. Worden, M. Carlsson, V. H. Hansteen, J. Leenaarts, M. Wiesmann, J. Aloise, K.-C. Chu, R. I. Bush, P. H. Scherrer, P. Brekke, J. Martinez-Sykora, B. W. Lites, S. W. McIntosh, H. Uitenbroek, T. J. Okamoto, M. A. Gummin, G. Auker, P. Jerram, P. Pool, and N. Waltham. The Interface Region Imaging Spectrograph (IRIS). *Solar Physics*, 289:2733–2779, July 2014.

[51] P. Demoulin, L. G. Bagala, C. H. Mandrini, J. C. Henoux, and M. G. Rovira. Quasi-Separatrix Layers in Solar Flares. II. Observed Magnetic Configurations. *Astronomy & Astrophysics*, 325:305–317, Sep 1997.

[52] P. Demoulin, J. C. Henoux, E. R. Priest, and C. H. Mand rini. Quasi-Separatrix Layers in Solar Flares. I. Method. *Astronomy & Astrophysics*, 308:643–655, Apr 1996.

[53] A. Devos, C. Verbeeck, and E. Robbrecht. Verification of Space Weather Forecasting at the Regional Warning Center in Belgium. *Journal of Space Weather and Space Climate*, 4:A29, October 2014.

[54] K. Domijan, D. S. Bloomfield, and F. Pitie. Solar Flare Forecasting from Magnetic Feature Properties Generated by Solar Monitor Active Region Tracker. *arXiv e-prints*, page arXiv:1812.02652, December 2018.

[55] G. A. Doschek, H. P. Warren, and P. R. Young. Chromospheric Evaporation in an M1.8 Flare Observed by the Extreme-ultraviolet Imaging Spectrometer on Hinode. *The Astrophysical Journal*, 767:55, April 2013.

[56] A. G. Emslie, B. R. Dennis, A. Y. Shih, P. C. Chamberlin, R. A. Mewaldt, C. S. Moore, G. H. Share, A. Vourlidas, and B. T. Welsch. Global Energetics of Thirty-eight Large Solar Eruptive Events. *The Astrophysical Journal*, 759:71, November 2012.

[57] D. Falconer, A. F. Barghouty, I. Khazanov, and R. Moore. A Tool for Empirical Forecasting of Major Flares, Coronal Mass Ejections, and Solar Particle Events from a Proxy of Active-Region Free Magnetic Energy. *Space Weather*, 9:S04003, April 2011.

[58] D. A. Falconer, R. L. Moore, A. F. Barghouty, and I. Khazanov. Prior Flaring as a Complement to Free Magnetic Energy for Forecasting Solar Eruptions. *The Astrophysical Journal*, 757:32, September 2012.

[59] D. A. Falconer, R. L. Moore, A. F. Barghouty, and I. Khazanov. MAG4 versus Alternative Techniques for Forecasting Active Region Flare Productivity. *Space Weather*, 12:306–317, May 2014.

[60] D. A. Falconer, R. L. Moore, and G. A. Gary. A Measure from Line-of-Sight Magnetograms for Prediction of Coronal Mass Ejections. *Journal of Geophysical Research (Space Physics)*, 108:1380, October 2003.

[61] D. A. Falconer, R. L. Moore, J. G. Porter, G. A. Gary, and T. Shimizu. Neutral-Line Magnetic Shear and Enhanced Coronal Heating in Solar Active Regions. *The Astrophysical Journal*, 482:519–534, Jun 1997.

[62] U. Feldman, G. A. Doschek, W. E. Behring, and K. J. H. Phillips. Electron Temperature, Emission Measure, and X-Ray Flux in A2 to X2 X-Ray Class Solar Flares. *The Astrophysical Journal*, 460:1034, April 1996.

[63] S. Felix, R. Bolzern, and M. Battaglia. A Compressed Sensing-based Image Reconstruction Algorithm for Solar Flare X-Ray Observations. *ArXiv e-prints*, September 2017.

[64] G. H. Fisher. Dynamics of Flare-driven Chromospheric Condensations. *The Astrophysical Journal*, 346:1019–1029, November 1989.

[65] G. H. Fisher, R. C. Canfield, and A. N. McClymont. Flare Loop Radiative Hydrodynamics - Part Seven - Dynamics of the Thick Target Heated Chromosphere. *The Astrophysical Journal*, 289:434, February 1985.

[66] G. H. Fisher, R. C. Canfield, and A. N. McClymont. Flare Loop Radiative Hydrodynamics - Part Six - Chromospheric Evaporation due to Heating by Nonthermal Electrons. *The Astrophysical Journal*, 289:425, February 1985.

[67] G. H. Fisher, R. C. Canfield, and A. N. McClymont. Flare Loop Radiative Hydrodynamics. V - Response to Thick-target Heating. *The Astrophysical Journal*, 289:414–441, February 1985.

[68] L. Fletcher, B. R. Dennis, H. S. Hudson, S. Krucker, K. Phillips, A. Veronig, M. Battaglia, L. Bone, A. Caspi, Q. Chen, P. Gallagher, P. T. Grigis, H. Ji, W. Liu, R. O. Milligan, and M. Temmer. An Observational Overview of Solar Flares. *Space Science Reviews*, 159:19–106, Sep 2011.

[69] S. Freeland and R. Bentley. *SolarSoft.* Encyclopedia of Astronomy and Astrophysics, November 2000.

[70] Y. Freund and R. E. Schapire. A decision-theoretic generalization of on-line learning and an application to boosting. *Journal of Computer and System Sciences*, 55(1):119 – 139, 1997.

[71] H. A. Garcia. The Empirical Relationship of Peak Emission Measure and Temperature to Peak Flare X-ray flux during Solar Cycle 21. *Advances in Space Research*, 8:157–160, January 1988.

[72] H. A. Garcia. Temperature and Emission Measure from Goes Soft X-Ray Measurements. *Solar Physics*, 154:275–308, October 1994.

[73] D. E. Gary and G. J. Hurford. Multifrequency Observations of a Solar Microwave Burst with Two-Dimensional Spatial Resolution. *The Astrophysical Journal*, 361:290–299, September 1990.

[74] P. Gömöry, A. M. Veronig, Y. Su, M. Temmer, and J. K. Thalmann. Chromospheric Evaporation Flows and Density Changes Deduced from Hinode/EIS during an M1.6 flare. *Astronomy & Astrophysics*, 588:A6, April 2016.

[75] P. R. Goode and W. Cao. The 1.6 m Off-Axis New Solar Telescope (NST) in Big Bear. In T. R. Rimmele, A. Tritschler, F. Wöger, M. Collados Vera, H. Socas-Navarro, R. Schlichenmaier, M. Carlsson, T. Berger, A. Cadavid, P. R. Gilbert, P. R. Goode, and M. Knölker, editors, *Second ATST-EAST Meeting: Magnetic Fields from the Photosphere to the Corona.*, volume 463 of *Astronomical Society of the Pacific Conference Series*, page 357, Dec 2012.

[76] D. R. Graham and G. Cauzzi. Temporal Evolution of Multiple Evaporating Ribbon Sources in a Solar Flare. *The Astrophysical Journal Letters*, 807:L22, July 2015.

[77] M. Gryciuk, M. Siarkowski, J. Sylwester, S. Gburek, P. Podgorski, A. Kepa, B. Sylwester, and T. Mrozek. Flare Characteristics from X-ray Light Curves. *Solar Physics*, 292:77, June 2017.

[78] B. V. Gudiksen, M. Carlsson, V. H. Hansteen, W. Hayek, J. Leenaarts, and J. Martínez-Sykora. The Stellar Atmosphere Simulation Code Bifrost. Code Description and Validation. *Astronomy & Astrophysics*, 531:A154, Jul 2011.

[79] C. Guennou, E. Pariat, J. E. Leake, and N. Vilmer. Testing Predictors of Eruptivity using Parametric Flux Emergence Simulations. *Journal of Space Weather and Space Climate*, 7:A17, Aug 2017.

[80] Y. Hada-Muranushi, T. Muranushi, A. Asai, D. Okanohara, R. Raymond, G. Watanabe, S. Nemoto, and K. Shibata. A Deep-Learning Approach for Operation of an Automated Realtime Flare Forecast. *arXiv e-prints*, page arXiv:1606.01587, Jun 2016.

[81] M. J. Hagyard, P. Venkatakrishnan, and Jr. Smith, J. B. Nonpotential Magnetic Fields at Sites of Gamma-Ray Flares. *The Astrophysical Journal Supplement Series*, 73:159, June 1990.

[82] B. J. Harker and A. A. Pevtsov. Case Study of a Magnetic Transient in NOAA 11429 Observed by SDO/HMI during the M7.9 Flare on 2012 March 13. *The Astrophysical Journal*, 778:175, December 2013.

[83] T. Hirayama. Theoretical Model of Flares and Prominences. I: Evaporating Flare Model. *Solar Physics*, 34:323–338, February 1974.

[84] J. Hong, M. D. Ding, Y. Li, and M. Carlsson. Non-LTE Calculations of the Fe I 6173 Å Line in a Flaring Atmosphere. *The Astrophysical Journal*, 857:L2, April 2018.

[85] N. Huang, Y. Xu, V. Sadykov, J. Jing, and H. Wang. Spectral diagnosis of mg ii and hα lines during the initial stage of an m6.5 flare. *The Astrophysical Journal, under review*, 2019.

[86] X. Huang, H. Wang, L. Xu, J. Liu, R. Li, and X. Dai. Deep Learning Based Solar Flare Forecasting Model. I. Results for Line-of-sight Magnetograms. *The Astrophysical Journal*, 856:7, March 2018.

[87] G. J. Hurford, R. B. Read, and H. Zirin. A frequency-agile interferometer for solar microwave spectroscopy. *Solar Physics*, 94(2):413–426, 1984.

[88] N. Hurlburt, M. Cheung, C. Schrijver, L. Chang, S. Freeland, S. Green, C. Heck, A. Jaffey, A. Kobashi, D. Schiff, J. Serafin, R. Seguin, G. Slater, A. Somani, and R. Timmons. Heliophysics Event Knowledgebase for the Solar Dynamics Observatory (SDO) and Beyond. *Solar Physics*, 275:67–78, January 2012.

[89] M. Janvier, G. Aulanier, V. Bommier, B. Schmieder, P. Démoulin, and E. Pariat. Electric Currents in Flare Ribbons: Observations and Three-dimensional Standard Model. *The Astrophysical Journal*, 788:60, Jun 2014.

[90] M. Janvier, G. Aulanier, E. Pariat, and P. Démoulin. The Standard Flare Model in Three Dimensions. III. Slip-running Reconnection Properties. *Astronomy & Astrophysics*, 555:A77, Jul 2013.

[91] J. Jing, H. Song, V. Abramenko, C. Tan, and H. Wang. The Statistical Relationship between the Photospheric Magnetic Parameters and the Flare Productivity of Active Regions. *The Astrophysical Journal*, 644:1273–1277, June 2006.

[92] C. D. Johnston, A. W. Hood, P. J. Cargill, and I. De Moortel. A New Approach for Modelling Chromospheric Evaporation in Response to Enhanced Coronal Heating. I. The Method. *Astronomy & Astrophysics*, 597:A81, January 2017.

[93] C. D. Johnston, A. W. Hood, P. J. Cargill, and I. De Moortel. A New Approach for Modelling Chromospheric Evaporation in Response to Enhanced Coronal Heating. II. Non-uniform Heating. *Astronomy & Astrophysics*, 605:A8, August 2017.

[94] E. Jonas, M. Bobra, V. Shankar, J. Todd Hoeksema, and B. Recht. Flare Prediction Using Photospheric and Coronal Image Data. *Solar Physics*, 293:48, March 2018.

[95] M. D. Kazachenko, B. J. Lynch, B. T. Welsch, and X. Sun. A Database of Flare Ribbon Properties from the Solar Dynamics Observatory. I. Reconnection Flux. *The Astrophysical Journal*, 845:49, August 2017.

[96] M. B. Kennedy, R. O. Milligan, J. C. Allred, M. Mathioudakis, and F. P. Keenan. Radiative Hydrodynamic Modelling and Observations of the X-class Solar Flare on 2011 March 9. *Astronomy & Astrophysics*, 578:A72, June 2015.

[97] G. S. Kerr, J. C. Allred, J. Leenaarts, E. Butler, and A. Kowalski. Simulating the Mg II NUV Spectra & C II Resonance Lines During Solar Flares. In *AAS/Solar Physics Division Abstracts #48*, page 1.02, August 2017.

[98] G. S. Kerr, M. Carlsson, J. C. Allred, P. R. Young, and A. N. Daw. SI IV Resonance Line Emission during Solar Flares: Non-LTE, Nonequilibrium, Radiation Transfer Simulations. *The Astrophysical Journal*, 871:23, Jan 2019.

[99] G. S. Kerr, L. Fletcher, A. J. B. Russell, and J. C. Allred. Simulations of the Mg II k and Ca II 8542 lines from an AlfvÉn Wave-heated Flare Chromosphere. *The Astrophysical Journal*, 827:101, August 2016.

[100] G. S. Kerr, P. J. A. Simões, J. Qiu, and L. Fletcher. IRIS Observations of the Mg ii h and k Lines During a Solar Flare. *Astronomy & Astrophysics*, 582:A50, October 2015.

[101] D. P. Kingma and J. Ba. Adam: A Method for Stochastic Optimization. *arXiv e-prints*, page arXiv:1412.6980, December 2014.

[102] A. S. Kirichenko and S. A. Bogachev. Plasma Heating in Solar Microflares: Statistics and Analysis. *The Astrophysical Journal*, 840:45, May 2017.

[103] I. N. Kitiashvili, S. Couvidat, and A. Lagg. Using Realistic MHD Simulations for Modeling and Interpretation of Quiet-Sun Observations with the Solar Dynamics Observatory Helioseismic and Magnetic Imager. *The Astrophysical Journal*, 808:59, Jul 2015.

[104] L. Kleint, P. Heinzel, P. Judge, and S. Krucker. Continuum Enhancements in the Ultraviolet, the Visible and the Infrared during the X1 Flare on 2014 March 29. *The Astrophysical Journal*, 816:88, January 2016.

[105] J. A. Klimchuk, S. Patsourakos, and P. J. Cargill. Highly Efficient Modeling of Dynamic Coronal Loops. *The Astrophysical Journal*, 682:1351–1362, August 2008.

[106] I. Kontogiannis, M. K. Georgoulis, S.-H. Park, and J. A. Guerra. Non-neutralized Electric Currents in Solar Active Regions and Flare Productivity. *Solar Physics*, 292:159, November 2017.

[107] I. Kontogiannis, M. K. Georgoulis, S.-H. Park, and J. A. Guerra. Testing and Improving a Set of Morphological Predictors of Flaring Activity. *Solar Physics*, 293:96, June 2018.

[108] R. A. Kopp and G. W. Pneuman. Magnetic Reconnection in the Corona and the Loop Prominence Phenomenon. *Solar Physics*, 50:85–98, October 1976.

[109] M. B. Korsós, T. Baranyi, and A. Ludmány. Pre-flare Dynamics of Sunspot Groups. *The Astrophysical Journal*, 789:107, Jul 2014.

[110] M. B. Korsós and R. Erdélyi. On the State of a Solar Active Region Before Flares and CMEs. *The Astrophysical Journal*, 823:153, June 2016.

[111] M. B. Korsós, A. Ludmány, R. Erdélyi, and T. Baranyi. On Flare Predictability Based on Sunspot Group Evolution. *The Astrophysical Journal*, 802:L21, April 2015.

[112] A. G. Kosovichev. Simulating Thermal and Gasdynamic Processes in Solar-Flare Pulse Phases. *Bulletin Crimean Astrophysical Observatory*, 75:6, 1986.

[113] A. G. Kosovichev and V. V. Zharkova. Magnetic Energy Release and Transients in the Solar Flare of 2000 July 14. *The Astrophysical Journal*, 550:L105–L108, March 2001.

[114] N. D. Kostiuk and S. B. Pikelner. Gasdynamics of a Flare Region Heated by a Stream of High-Velocity Electrons. *Soviet Astronomy*, 18:590–599, April 1975.

[115] T. Kosugi, K. Matsuzaki, T. Sakao, T. Shimizu, Y. Sone, S. Tachikawa, T. Hashimoto, K. Minesugi, A. Ohnishi, T. Yamada, S. Tsuneta, H. Hara, K. Ichimoto, Y. Suematsu, M. Shimojo, T. Watanabe, S. Shimada, J. M. Davis, L. D. Hill, J. K. Owens, A. M. Title, J. L. Culhane, L. K. Harra, G. A. Doschek, and L. Golub. The Hinode (Solar-B) Mission: An Overview. *Solar Physics*, 243:3–17, Jun 2007.

[116] P. Kumar, V. Yurchyshyn, H. Wang, and K.-S. Cho. Formation and Eruption of a Small Flux Rope in the Chromosphere Observed by NST, IRIS, and SDO. *The Astrophysical Journal*, 809:83, Aug 2015.

[117] D. Kuridze, M. Mathioudakis, P. J. A. Simões, L. Rouppe van der Voort, M. Carlsson, S. Jafarzadeh, J. C. Allred, A. F. Kowalski, M. Kennedy, L. Fletcher, D. Graham, and F. P. Keenan. Hα Line Profile Asymmetries and the Chromospheric Flare Velocity Field. *The Astrophysical Journal*, 813:125, November 2015.

[118] K. Kusano, Y. Bamba, T. T. Yamamoto, Y. Iida, S. Toriumi, and A. Asai. Magnetic Field Structures Triggering Solar Flares and Coronal Mass Ejections. *The Astrophysical Journal*, 760:31, November 2012.

[119] E. Landi, P. R. Young, K. P. Dere, G. Del Zanna, and H. E. Mason. CHIANTI —An Atomic Database for Emission Lines. XIII. Soft X-Ray Improvements and Other Changes. *The Astrophysical Journal*, 763:86, February 2013.

[120] E.-J. Lee, S.-H. Park, and Y.-J. Moon. Flare Productivity of Major Flaring Solar Active Regions: A Time-series Study of Photospheric Magnetic Properties. *ArXiv e-prints*, October 2018.

[121] K.-S. Lee, S. Imada, K. Watanabe, Y. Bamba, and D. H. Brooks. IRIS, Hinode, SDO, and RHESSI Observations of a White Light Flare Produced Directly by Nonthermal Electrons. *The Astrophysical Journal*, 836:150, February 2017.

[122] K. D. Leka and G. Barnes. Photospheric Magnetic Field Properties of Flaring versus Flare-quiet Active Regions. I. Data, General Approach, and Sample Results. *The Astrophysical Journal*, 595:1277–1295, Oct 2003.

[123] K. D. Leka and G. Barnes. Photospheric Magnetic Field Properties of Flaring versus Flare-quiet Active Regions. II. Discriminant Analysis. *The Astrophysical Journal*, 595:1296–1306, Oct 2003.

[124] K. D. Leka and G. Barnes. Photospheric Magnetic Field Properties of Flaring versus Flare-quiet Active Regions. IV. A Statistically Significant Sample. *The Astrophysical Journal*, 656:1173–1186, February 2007.

[125] J. R. Lemen, A. M. Title, D. J. Akin, P. F. Boerner, C. Chou, J. F. Drake, D. W. Duncan, C. G. Edwards, F. M. Friedlaender, G. F. Heyman, N. E. Hurlburt, N. L. Katz, G. D. Kushner, M. Levay, R. W. Lindgren, D. P. Mathur, E. L. McFeaters, S. Mitchell, R. A. Rehse, C. J. Schrijver, L. A. Springer, R. A. Stern, T. D. Tarbell, J.-P. Wuelser, C. J. Wolfson, C. Yanari, J. A. Bookbinder, P. N. Cheimets, D. Caldwell, E. E. Deluca, R. Gates, L. Golub, S. Park, W. A. Podgorski, R. I. Bush, P. H. Scherrer, M. A. Gummin, P. Smith, G. Auker, P. Jerram, P. Pool, R. Soufli, D. L. Windt, S. Beardsley, M. Clapp, J. Lang, and N. Waltham. The Atmospheric Imaging Assembly (AIA) on the Solar Dynamics Observatory (SDO). *Solar Physics*, 275:17–40, January 2012.

[126] D. Li, Z. J. Ning, Y. Huang, and Q. M. Zhang. Explosive Chromospheric Evaporation Driven by Nonthermal Electrons around One Footpoint of a Solar Flare Loop. *The Astrophysical Journal Letters*, 841:L9, May 2017.

[127] D. Li, Z. J. Ning, and Q. M. Zhang. Observational Evidence of Electron-driven Evaporation in Two Solar Flares. *The Astrophysical Journal*, 813:59, November 2015.

[128] T. Li and J. Zhang. Quasi-periodic Slipping Magnetic Reconnection During an X-class Solar Flare Observed by the Solar Dynamics Observatory and Interface Region Imaging Spectrograph. *The Astrophysical Journal*, 804:L8, May 2015.

[129] Y. Li, M. D. Ding, J. Qiu, and J. X. Cheng. Chromospheric Evaporation in an X1.0 Flare on 2014 March 29 Observed with IRIS and EIS. *The Astrophysical Journal*, 811:7, September 2015.

[130] Y. Li, M. Kelly, M. D. Ding, J. Qiu, X. S. Zhu, and W. Q. Gan. Spectroscopic Observations of Magnetic Reconnection and Chromospheric Evaporation in an X-shaped Solar Flare. *ArXiv e-prints*, August 2017.

[131] R. P. Lin, B. R. Dennis, G. J. Hurford, D. M. Smith, A. Zehnder, P. R. Harvey, D. W. Curtis, D. Pankow, P. Turin, M. Bester, A. Csillaghy, M. Lewis, N. Madden, H. F. van Beek, M. Appleby, T. Raudorf, J. McTiernan, R. Ramaty, E. Schmahl, R. Schwartz, S. Krucker, R. Abiad, T. Quinn, P. Berg, M. Hashii, R. Sterling, R. Jackson, R. Pratt, R. D. Campbell, D. Malone, D. Landis, C. P. Barrington-Leigh, S. Slassi-Sennou, C. Cork, D. Clark, D. Amato, L. Orwig, R. Boyle, I. S. Banks, K. Shirey, A. K. Tolbert, D. Zarro, F. Snow, K. Thomsen, R. Henneck, A. McHedlishvili, P. Ming, M. Fivian, J. Jordan, R. Wanner, J. Crubb, J. Preble, M. Matranga, A. Benz, H. Hudson, R. C. Canfield, G. D. Holman, C. Crannell, T. Kosugi, A. G. Emslie, N. Vilmer, J. C. Brown, C. Johns-Krull, M. Aschwanden, T. Metcalf, and A. Conway. The Reuven Ramaty High-Energy Solar Spectroscopic Imager (RHESSI). *Solar Physics*, 210:3–32, November 2002.

[132] C. Liu, W. Cao, J. Chae, K. Ahn, D. Prasad Choudhary, J. Lee, R. Liu, N. Deng, J. Wang, and H. Wang. Evolution of Photospheric Vector Magnetic Field Associated with Moving Flare Ribbons As Seen By GST. *ArXiv e-prints*, October 2018.

[133] C. Liu, N. Deng, J. T. L. Wang, and H. Wang. Predicting Solar Flares Using SDO/HMI Vector Magnetic Data Products and the Random Forest Algorithm. *The Astrophysical Journal*, 843:104, July 2017.

[134] W. Liu, V. Petrosian, and J. T. Mariska. Combined Modeling of Acceleration, Transport, and Hydrodynamic Response in Solar Flares. I. The Numerical Model. *The Astrophysical Journal*, 702:1553–1566, September 2009.

[135] M. A. Livshits, O. G. Badalian, A. G. Kosovichev, and M. M. Katsova. The Optical Continuum of Solar and Stellar Flares. *Solar Physics*, 73:269–288, Oct 1981.

[136] R. S. Mandage and R. T. J. McAteer. On the Non-Kolmogorov Nature of Flare-productive Solar Active Regions. *The Astrophysical Journal*, 833:237, December 2016.

[137] P. C. Martens and R. A. Angryk. Data Handling and Assimilation for Solar Event Prediction. *ArXiv e-prints*, December 2017.

[138] P. C. H. Martens, G. D. R. Attrill, A. R. Davey, A. Engell, S. Farid, P. C. Grigis, J. Kasper, K. Korreck, S. H. Saar, A. Savcheva, Y. Su, P. Testa, M. Wills-Davey, P. N. Bernasconi, N.-E. Raouafi, V. A. Delouille, J. F. Hochedez, J. W. Cirtain, C. E. Deforest, R. A. Angryk, I. de Moortel, T. Wiegelmann, M. K. Georgoulis, R. T. J. McAteer, and R. P. Timmons. Computer Vision for the Solar Dynamics Observatory (SDO). *Solar Physics*, 275:79–113, January 2012.

[139] J. P. Mason and J. T. Hoeksema. Testing Automated Solar Flare Forecasting with 13 Years of Michelson Doppler Imager Magnetograms. *The Astrophysical Journal*, 723:634–640, November 2010.

[140] S. Masson, E. Pariat, G. Aulanier, and C. J. Schrijver. The Nature of Flare Ribbons in Coronal Null-Point Topology. *The Astrophysical Journal*, 700:559–578, Jul 2009.

[141] R. A. Maurya, P. Vemareddy, and A. Ambastha. Velocity and Magnetic Transients Driven by the X2.2 White-light Flare of 2011 February 15 in NOAA 11158. *The Astrophysical Journal*, 747:134, March 2012.

[142] P. I. McCauley, Y. N. Su, N. Schanche, K. E. Evans, C. Su, S. McKillop, and K. K. Reeves. Prominence and Filament Eruptions Observed by the Solar Dynamics Observatory: Statistical Properties, Kinematics, and Online Catalog. *Solar Physics*, 290:1703–1740, June 2015.

[143] A. E. McCloskey, P. T. Gallagher, and D. S. Bloomfield. Flare Forecasting Using the Evolution of McIntosh Sunspot Classifications. *ArXiv e-prints*, May 2018.

[144] P. S. McIntosh. The Classification of Sunspot Groups. *Solar Physics*, 125:251–267, September 1990.

[145] J. M. McTiernan, A. Caspi, and H. P. Warren. The Multi-Instrument (EVE-RHESSI) DEM for Solar Flares, and Implications for Non-Thermal Emission. *ArXiv e-prints*, May 2018.

[146] C. Meegan, G. Lichti, P. N. Bhat, E. Bissaldi, M. S. Briggs, V. Connaughton, R. Diehl, G. Fishman, J. Greiner, A. S. Hoover, A. J. van der Horst, A. von Kienlin, R. M. Kippen, C. Kouveliotou, S. McBreen, W. S. Paciesas, R. Preece, H. Steinle, M. S. Wallace, R. B. Wilson, and C. Wilson-Hodge. The Fermi Gamma-ray Burst Monitor. *The Astrophysical Journal*, 702:791–804, September 2009.

[147] R. O. Milligan. Extreme Ultra-Violet Spectroscopy of the Lower Solar Atmosphere During Solar Flares (Invited Review). *Solar Physics*, 290:3399–3423, December 2015.

[148] R. O. Milligan and B. R. Dennis. Velocity Characteristics of Evaporated Plasma Using Hinode/EUV Imaging Spectrometer. *The Astrophysical Journal*, 699:968–975, July 2009.

[149] R. O. Milligan, P. T. Gallagher, M. Mathioudakis, and F. P. Keenan. Observational Evidence of Gentle Chromospheric Evaporation during the Impulsive Phase of a Solar Flare. *The Astrophysical Journal Letters*, 642:L169–L171, May 2006.

[150] R. O. Milligan and J. Ireland. On the Effectiveness of Multi-Instrument Solar Flare Observations During Solar Cycle 24. *ArXiv e-prints*, March 2017.

[151] S. A. Murray, S. Bingham, M. Sharpe, and D. R. Jackson. Flare Forecasting at the Met Office Space Weather Operations Centre. *Space Weather*, 15:577–588, April 2017.

[152] Löptien B. Gizon L. Birch A.C. Cameron R. Couvidat S. Danilovic S. Fleck B. Stein R. Nagashima, K. Interpreting the Helioseismic and Magnetic Imager (HMI) Multi-Height Velocity Measurements. *Solar Physics*, 289:3457–3481, Sep 2014.

[153] H. Nakajima, M. Nishio, S. Enome, K. Shibasaki, T. Takano, Y. Hanaoka, C. Torii, H. Sekiguchi, T. Bushimata, S. Kawashima, N. Shinohara, Y. Irimajiri, H. Koshiishi, T. Kosugi, Y. Shiomi, M. Sawa, and K. Kai. The Nobeyama Radioheliograph. *IEEE Proceedings*, 82:705–713, May 1994.

[154] W. M. Neupert. Comparison of Solar X-Ray Line Emission with Microwave Emission during Flares. *The Astrophysical Journal*, 153:L59, July 1968.

[155] N. Nishizuka, K. Sugiura, Y. Kubo, M. Den, and M. Ishii. Deep Flare Net (DeFN) model for solar flare prediction. *ArXiv e-prints*, May 2018.

[156] N. Nishizuka, K. Sugiura, Y. Kubo, M. Den, S. Watari, and M. Ishii. Solar Flare Prediction Model with Three Machine-learning Algorithms using Ultraviolet Brightening and Vector Magnetograms. *The Astrophysical Journal*, 835:156, February 2017.

[157] G.M. Nita, D.E. Gary, and J. Lee. Statistical study of two years of solar flare radio spectra obtained with the owens valley solar array. *Astrophysical Journal*, 605(1 I):528–545, 2004.

[158] A. A. Norton, J. Pietarila Graham, R. K. Ulrich, J. Schou, S. Tomczyk, Y. Liu, B. W. Lites, A. López Ariste, R. I. Bush, H. Socas-Navarro, and P. H. Scherrer. Spectral Line Selection for HMI: A Comparison of Fe I 6173 Å and Ni I 6768 Å. *Solar Physics*, 239:69–91, Dec 2006.

[159] V. D. Pal'shin, Y. E. Charikov, R. L. Aptekar, S. V. Golenetskii, A. A. Kokomov, D. S. Svinkin, Z. Y. Sokolova, M. V. Ulanov, D. D. Frederiks, and A. E. Tsvetkova. Konus- Wind and Helicon- Coronas-F observations of solar flares. *Geomagnetism and Aeronomy*, 54:943–948, December 2014.

[160] E. Park, Y.-J. Moon, S. Shin, K. Yi, D. Lim, H. Lee, and G. Shin. Application of the Deep Convolutional Neural Network to the Forecast of Solar Flare Occurrence Using Full-disk Solar Magnetograms. *The Astrophysical Journal*, 869:91, December 2018.

[161] S.-H. Park, J. A. Guerra, P. T. Gallagher, M. K. Georgoulis, and D. S. Bloomfield. Photospheric Shear Flows in Solar Active Regions and Their Relation to Flare Occurrence. *ArXiv e-prints*, July 2018.

[162] A. Patterson. Flares in Hale 17760 - Magnetic transients in the 1981 July 27 flare. *The Astrophysical Journal*, 280:884–886, May 1984.

[163] F. Pedregosa, G. Varoquaux, A. Gramfort, V. Michel, B. Thirion, O. Grisel, M. Blondel, P. Prettenhofer, R. Weiss, V. Dubourg, J. Vanderplas, A. Passos, D. Cournapeau, M. Brucher, M. Perrot, and E. Duchesnay. Scikit-learn: Machine learning in Python. *Journal of Machine Learning Research*, 12:2825–2830, 2011.

[164] T. M. D. Pereira and H. Uitenbroek. RH 1.5D: a Massively Parallel Code for Multi-Level Radiative Transfer with Partial Frequency Redistribution and Zeeman Polarisation. *Astronomy & Astrophysics*, 574:A3, February 2015.

[165] M. Piana, C. Campi, F. Benvenuto, S. Guastavano, and A. M. Massone. Flare Forecasting and Feature Ranking using SDO/HMI Data. *arXiv e-prints*, page arXiv:1812.07258, December 2018.

[166] J. Platt. Probabilities for sv machines. In *Advances in Large Margin Classifiers*, pages 61–74, 01 1999.

[167] V. Polito, J. W. Reep, K. K. Reeves, P. J. A. Simões, J. Dudík, G. Del Zanna, H. E. Mason, and L. Golub. Simultaneous IRIS and Hinode/EIS Observations and Modelling of the 2014 October 27 X2.0 Class Flare. *The Astrophysical Journal*, 816:89, January 2016.

[168] V. Polito, K. K. Reeves, G. Del Zanna, L. Golub, and H. E. Mason. Joint High Temperature Observation of a Small C6.5 Solar Flare With Iris/Eis/Aia. *The Astrophysical Journal*, 803:84, April 2015.

[169] E. R. Priest and T. G. Forbes. The Magnetic Nature of Solar Flares. *Astronomy & Astrophysics Reviews*, 10:313–377, 2002.

[170] R. Qahwaji and T. Colak. Automatic Short-Term Solar Flare Prediction Using Machine Learning and Sunspot Associations. *Solar Physics*, 241:195–211, March 2007.

[171] J. Qiu and D. E. Gary. Flare-related Magnetic Anomaly with a Sign Reversal. *The Astrophysical Journal*, 599:615–625, December 2003.

[172] A. Raboonik, H. Safari, N. Alipour, and M. S. Wheatland. Prediction of Solar Flares Using Unique Signatures of Magnetic Field Images. *The Astrophysical Journal*, 834:11, January 2017.

[173] C. L. Raftery, P. T. Gallagher, R. O. Milligan, and J. A. Klimchuk. Multi-Wavelength Observations and Modelling of a Canonical Solar Flare. *Astronomy & Astrophysics*, 494:1127–1136, February 2009.

[174] B. Rathore and M. Carlsson. The Formation of IRIS Diagnostics. V. A Quintessential Model Atom of C II and General Formation Properties of the C II Lines at 133.5 nm. *The Astrophysical Journal*, 811:80, October 2015.

[175] J. W. Reep, S. J. Bradshaw, and D. Alexander. Optimal Electron Energies for Driving Chromospheric Evaporation in Solar Flares. *The Astrophysical Journal*, 808:177, August 2015.

[176] J. W. Reep, S. J. Bradshaw, and G. D. Holman. X-Ray Source Heights in a Solar Flare: Thick-target versus Thermal Conduction Front Heating. *The Astrophysical Journal*, 818:44, Feb 2016.

[177] J. W Reep and S. Toriumi. The Direct Relation between the Duration of Magnetic Reconnection and the Evolution of GOES Light Curves in Solar Flares. *ArXiv e-prints*, November 2017.

[178] J. W. Reep, H. P. Warren, N. A. Crump, and P. J. A. Simões. Transition Region and Chromospheric Signatures of Impulsive Heating Events. II. Modeling. *The Astrophysical Journal*, 827:145, August 2016.

[179] E. Robbrecht and D. Berghmans. Automated Recognition of Coronal Mass Ejections (CMEs) in Near-Real-Time Data. *Astronomy & Astrophysics*, 425:1097–1106, October 2004.

[180] E. Robbrecht, D. Berghmans, and R. A. M. Van der Linden. Automated LASCO CME Catalog for Solar Cycle 23: Are CMEs Scale Invariant? *The Astrophysical Journal*, 691:1222–1234, February 2009.

[181] R. Rosner, W. H. Tucker, and G. S. Vaiana. Dynamics of the Quiescent Solar Corona. *The Astrophysical Journal*, 220:643–645, March 1978.

[182] F. Rubio da Costa and L. Kleint. A Parameter Study for Modeling Mg II h and k Emission during Solar Flares. *The Astrophysical Journal*, 842:82, Jun 2017.

[183] F. Rubio da Costa, L. Kleint, V. Petrosian, W. Liu, and J. C. Allred. Data-driven Radiative Hydrodynamic Modeling of the 2014 March 29 X1.0 Solar Flare. *The Astrophysical Journal*, 827:38, August 2016.

[184] F. Rubio da Costa, L. Kleint, V. Petrosian, A. Sainz Dalda, and W. Liu. Solar Flare Chromospheric Line Emission: Comparison Between IBIS High-resolution Observations and Radiative Hydrodynamic Simulations. *The Astrophysical Journal*, 804:56, May 2015.

[185] F. Rubio da Costa, W. Liu, V. Petrosian, and M. Carlsson. Combined Modeling of Acceleration, Transport, and Hydrodynamic Response in Solar Flares. II. Inclusion of Radiative Transfer with RADYN. *The Astrophysical Journal*, 813:133, November 2015.

[186] D. F. Ryan, P. C. Chamberlin, R. O. Milligan, and P. T. Gallagher. Decay-phase Cooling and Inferred Heating of M- and X-class Solar Flares. *The Astrophysical Journal*, 778:68, November 2013.

[187] D. F. Ryan, R. O. Milligan, P. T. Gallagher, B. R. Dennis, A. K. Tolbert, R. A. Schwartz, and C. A. Young. The Thermal Properties of Solar Flares over Three Solar Cycles Using GOES X-Ray Observations. *The Astrophysical Journal Supplement Series*, 202:11, October 2012.

[188] D. F. Ryan, A. M. O'Flannagain, M. J. Aschwanden, and P. T. Gallagher. The Compatibility of Flare Temperatures Observed with AIA, GOES, and RHESSI. *Solar Physics*, 289:2547–2563, July 2014.

[189] G. B. Rybicki and D. G. Hummer. An Accelerated Lambda Iteration Method for Multilevel Radiative Transfer. I - Non-overlapping Lines with Background Continuum. *Astronomy & Astrophysics*, 245:171–181, May 1991.

[190] G. B. Rybicki and D. G. Hummer. An Accelerated Lambda Iteration Method for Multilevel Radiative Transfer. II - Overlapping Transitions with Full Continuum. *Astronomy & Astrophysics*, 262:209–215, August 1992.

[191] V. M. Sadykov and A. G. Kosovichev. Relationships between Characteristics of the Line-of-sight Magnetic Field and Solar Flare Forecasts. *The Astrophysical Journal*, 849:148, November 2017.

[192] V. M. Sadykov, A. G. Kosovichev, and I. N. Kitiashvili. Enhancement of Binary and Probabilistic SWPC NOAA Flare Forecast by Using Machine Learning Algorithms. *In preparation*, 2019.

[193] V. M. Sadykov, A. G. Kosovichev, I. N. Kitiashvili, and A. Frolov. Statistical Study of Properties of the Soft X-ray Emission during Solar Flares. *ArXiv e-prints*, page arXiv:1810.05610, October 2018.

[194] V. M. Sadykov, A. G. Kosovichev, V. Oria, and G. M. Nita. An Interactive Multi-instrument Database of Solar Flares. *The Astrophysical Journal Supplement Series*, 231:6, July 2017.

[195] V. M. Sadykov, A. G. Kosovichev, I. N. Sharykin, and G. S. Kerr. Behavior of SDO/HMI observables for solar atmosphere heated by precipitating high-energy electrons. *In preparation*, 2019.

[196] V. M. Sadykov, A. G. Kosovichev, I. N. Sharykin, and G. S. Kerr. Statistical Study of Chromospheric Evaporation in Impulsive Phase of Solar Flares. *The Astrophysical Journal*, 871:2, Jan 2019.

[197] V. M. Sadykov, A. G. Kosovichev, I. N. Sharykin, I. V. Zimovets, and S. Vargas Dominguez. Relationship Between Chromospheric Evaporation and Magnetic Field Topology in an M-Class Solar Flare. *The Astrophysical Journal*, 828:4, September 2016.

[198] V. M. Sadykov, S. Vargas Dominguez, A. G. Kosovichev, I. N. Sharykin, A. B. Struminsky, and I. Zimovets. Properties of Chromospheric Evaporation and Plasma Dynamics of a Solar Flare from Iris. *The Astrophysical Journal*, 805:167, June 2015.

[199] A. Savitzky and M. J. E. Golay. Smoothing and differentiation of data by simplified least squares procedures. *Analytical Chemistry*, 36(8):1627, 1964.

[200] P. H. Scherrer, J. Schou, R. I. Bush, A. G. Kosovichev, R. S. Bogart, J. T. Hoeksema, Y. Liu, T. L. Duvall, J. Zhao, A. M. Title, C. J. Schrijver, T. D. Tarbell, and S. Tomczyk. The Helioseismic and Magnetic Imager (HMI) Investigation for the Solar Dynamics Observatory (SDO). *Solar Physics*, 275:207–227, January 2012.

[201] B. Schmieder, G. Aulanier, P. Demoulin, L. van Driel-Gesztelyi, T. Roudier, N. Nitta, and G. Cauzzi. Magnetic Reconnection Driven by Emergence of Sheared Magnetic Field. *Astronomy & Astrophysics*, 325:1213–1225, Sep 1997.

[202] J. Schou, P. H. Scherrer, R. I. Bush, R. Wachter, S. Couvidat, M. C. Rabello-Soares, R. S. Bogart, J. T. Hoeksema, Y. Liu, T. L. Duvall, D. J. Akin, B. A. Allard, J. W. Miles, R. Rairden, R. A. Shine, T. D. Tarbell, A. M. Title, C. J. Wolfson, D. F. Elmore, A. A. Norton, and S. Tomczyk. Design and Ground Calibration of the Helioseismic and Magnetic Imager (HMI) Instrument on the Solar Dynamics Observatory (SDO). *Solar Physics*, 275:229–259, January 2012.

[203] C. J. Schrijver. A Characteristic Magnetic Field Pattern Associated with All Major Solar Flares and Its Use in Flare Forecasting. *The Astrophysical Journal*, 655:L117–L120, February 2007.

[204] C. J. Schrijver. The Nonpotentiality of Coronae of Solar Active Regions, the Dynamics of the Surface Magnetic Field, and the Potential for Large Flares. *The Astrophysical Journal*, 820:103, April 2016.

[205] S. Serio, F. Reale, J. Jakimiec, B. Sylwester, and J. Sylwester. Dynamics of flaring loops. I - Thermodynamic decay scaling laws. *Astronomy & Astrophysics*, 241:197–202, January 1991.

[206] A. B. Severny. Solar Flares. *Annual Review of Astronomy and Astrophysics*, 2:363, Jan 1964.

[207] I. N. Sharykin and A. G. Kosovichev. Onset of Photospheric Impacts and Helioseismic Waves in X9.3 Solar Flare of 2017 September 6. *The Astrophysical Journal*, 864:86, September 2018.

[208] I. N. Sharykin, A. G. Kosovichev, V. M. Sadykov, I. V. Zimovets, and I. I. Myshyakov. Investigation of Relationship between High-energy X-Ray Sources and Photospheric and Helioseismic Impacts of X1.8 Solar Flare of 2012 October 23. *The Astrophysical Journal*, 843:67, Jul 2017.

[209] I. N. Sharykin, V. M. Sadykov, A. G. Kosovichev, S. Vargas-Dominguez, and I. V. Zimovets. Flare Energy Release in the Lower Solar Atmosphere near the Magnetic Field Polarity Inversion Line. *The Astrophysical Journal*, 840:84, May 2017.

[210] I. N. Sharykin, A. B. Struminskii, and I. V. Zimovets. Plasma Heating to Super-hot Temperatures (>30 MK) in the August 9, 2011 Solar Flare. *Astronomy Letters*, 41:53–66, January 2015.

[211] I. N. Sharykin, A. B. Struminsky, I. V. Zimovets, and W.-Q. Gan. Solar Flares with Similar Soft but Different Hard X-ray Emissions: Case and Statistical Studies. *Research in Astronomy and Astrophysics*, 16:5, January 2016.

[212] K. Shibata and T. Magara. Solar Flares: Magnetohydrodynamic Processes. *Living Reviews in Solar Physics*, 8, December 2011.

[213] S. Shin, J.-Y. Lee, Y.-J. Moon, H. Chu, and J. Park. Development of Daily Maximum Flare-Flux Forecast Models for Strong Solar Flares. *Solar Physics*, 291:897–909, March 2016.

[214] S. F. Smith and R. Howard. Magnetic Classification of Active Regions. In Karl Otto Kiepenheuer, editor, *Structure and Development of Solar Active Regions*, volume 35 of *IAU Symposium*, page 33, January 1968.

[215] L. Spitzer and R. Härm. Transport phenomena in a completely ionized gas. *Phys. Rev.*, 89:977–981, Mar 1953.

[216] J. O. Stenflo and A. G. Kosovichev. Bipolar Magnetic Regions on the Sun: Global Analysis of the SOHO/MDI Data Set. *The Astrophysical Journal*, 745:129, Feb 2012.

[217] G. Steward, V. Lobzin, I. H. Cairns, B. Li, and D. Neudegg. Automatic Recognition of Complex Magnetic Regions on the Sun in SDO Magnetogram Images and Prediction of Flares: Techniques and Results for the Revised Flare Prediction Program Flarecast. *Space Weather*, 15:1151–1164, September 2017.

[218] P. A. Sturrock. A Model of Solar Flares. In K. O. Kiepenheuer, editor, *Structure and Development of Solar Active Regions*, volume 35 of *IAU Symposium*, page 471, 1968.

[219] R. J. Thomas, R. Starr, and C. J. Crannell. Expressions to Determine Temperatures and Emission Measures for Solar X-Ray Events from Goes Measurements. *Solar Physics*, 95:323–329, February 1985.

[220] H. Tian, G. Li, K. K. Reeves, J. C. Raymond, F. Guo, W. Liu, B. Chen, and N. A. Murphy. Imaging and Spectroscopic Observations of Magnetic Reconnection and Chromospheric Evaporation in a Solar Flare. *The Astrophysical Journal Letters*, 797:L14, December 2014.

[221] H. Tian, P. R. Young, K. K. Reeves, B. Chen, W. Liu, and S. McKillop. Temporal Evolution of Chromospheric Evaporation: Case Studies of the M1.1 Flare on 2014 September 6 and X1.6 Flare on 2014 September 10. *The Astrophysical Journal*, 811:139, Oct 2015.

[222] S. K. Tiwari, D. A. Falconer, R. L. Moore, P. Venkatakrishnan, A. R. Winebarger, and I. G. Khazanov. Near-Sun Speed of CMEs and the Magnetic Nonpotentiality of Their Source Active Regions. *Geophysical Research Letters*, 42:5702–5710, July 2015.

[223] S. Toriumi, Y. Iida, Y. Bamba, K. Kusano, S. Imada, and S. Inoue. The Magnetic Systems Triggering the M6.6 Class Solar Flare in NOAA Active Region 11158. *The Astrophysical Journal*, 773:128, August 2013.

[224] S. Toriumi, Y. Iida, K. Kusano, Y. Bamba, and S. Imada. Formation of a Flare-Productive Active Region: Observation and Numerical Simulation of NOAA AR 11158. *Solar Physics*, 289:3351–3369, Sep 2014.

[225] S. Toriumi, C. J. Schrijver, L. K. Harra, H. Hudson, and K. Nagashima. Magnetic Properties of Solar Active Regions That Govern Large Solar Flares and Eruptions. *The Astrophysical Journal*, 834:56, Jan 2017.

[226] S. Tsuneta, K. Ichimoto, Y. Katsukawa, S. Nagata, M. Otsubo, T. Shimizu, Y. Suematsu, M. Nakagiri, M. Noguchi, T. Tarbell, A. Title, R. Shine, W. Rosenberg, C. Hoffmann, B. Jurcevich, G. Kushner, M. Levay, B. Lites, D. Elmore, T. Matsushita, N. Kawaguchi, H. Saito, I. Mikami, L. D. Hill, and J. K. Owens. The Solar Optical Telescope for the Hinode Mission: An Overview. *Solar Physics*, 249:167–196, Jun 2008.

[227] H. Uitenbroek. Multilevel Radiative Transfer with Partial Frequency Redistribution. *The Astrophysical Journal*, 557:389–398, August 2001.

[228] M. Švanda, J. Jurčák, J. Kašparová, and L. Kleint. Understanding the HMI Pseudocontinuum in White-light Solar Flares. *The Astrophysical Journal*, 860:144, June 2018.

[229] J. E. Vernazza, E. H. Avrett, and R. Loeser. Structure of the Solar Chromosphere. III. Models of the EUV Brightness Components of the Quiet Sun. *The Astrophysical Journal Supplement Series*, 45:635–725, April 1981.

[230] O. Vilhu, P. Muhli, R. Mewe, and P. Hakala. The Coronal FeXXI Lambda 1354.094 Line in AB Doradus. *Astronomy & Astrophysics*, 375:492–497, Aug 2001.

[231] H. Wang, Jr. Ewell, M. W., H. Zirin, and G. Ai. Vector Magnetic Field Changes Associated with X-Class Flares. *The Astrophysical Journal*, 424:436, Mar 1994.

[232] A. Warmuth and G. Mann. Constraints on Energy Release in Solar Flares from RHESSI and GOES X-ray Observations. I. Physical Parameters and Scalings. *Astronomy & Astrophysics*, 588:A115, April 2016.

[233] H. P. Warren. Multithread Hydrodynamic Modeling of a Solar Flare. *The Astrophysical Journal*, 637:522–530, January 2006.

[234] H. P. Warren, J. W. Reep, N. A. Crump, and P. J. A. Simões. Transition Region and Chromospheric Signatures of Impulsive Heating Events. I. Observations. *The Astrophysical Journal*, 829:35, September 2016.

[235] K. Watanabe, S. Masuda, and T. Segawa. Hinode Flare Catalogue. *Solar Physics*, 279:317–322, July 2012.

[236] M. S. Wheatland, P. A. Sturrock, and G. Roumeliotis. An Optimization Approach to Reconstructing Force-free Fields. *The Astrophysical Journal*, 540:1150–1155, Sep 2000.

[237] S. M. White, R. J. Thomas, and R. A. Schwartz. Updated Expressions for Determining Temperatures and Emission Measures from Goes Soft X-Ray Measurements. *Solar Physics*, 227:231–248, April 2005.

[238] T. N. Woods, F. G. Eparvier, R. Hock, A. R. Jones, D. Woodraska, D. Judge, L. Didkovsky, J. Lean, J. Mariska, H. Warren, D. McMullin, P. Chamberlin, G. Berthiaume, S. Bailey, T. Fuller-Rowell, J. Sojka, W. K. Tobiska, and R. Viereck. Extreme Ultraviolet Variability Experiment (EVE) on the Solar Dynamics Observatory (SDO): Overview of Science Objectives, Instrument Design, Data Products, and Model Developments. *Solar Physics*, 275:115–143, January 2012.

[239] P. R. Young, H. Tian, and S. Jaeggli. The 2014 March 29 X-flare: Subarcsecond Resolution Observations of Fe XXI λ1354.1. *The Astrophysical Journal*, 799:218, February 2015.

[240] D. M. Zarro and J. R. Lemen. Conduction-Driven Chromospheric Evaporation in a Solar Flare. *The Astrophysical Journal*, 329:456–463, June 1988.

[241] Q. M. Zhang, D. Li, Z. J. Ning, Y. N. Su, H. S. Ji, and Y. Guo. Explosive Chromospheric Evaporation in a Circular-ribbon Flare. *The Astrophysical Journal*, 827:27, August 2016.

[242] V. V. Zharkova and A. G. Kosovichev. Fast Magnetic Field Variations Associated with Solar Flares. In A. Wilson, editor, *From Solar Min to Max: Half a Solar Cycle with SOHO*, volume 508, pages 159–162, June 2002.

[243] I. V. Zimovets, R. Wang, Y. D. Liu, C. Wang, S. A. Kuznetsov, I. N. Sharykin, A. B. Struminsky, and V. M. Nakariakov. Magnetic Structure of Solar Flare Regions Producing Hard X-ray Pulsations. *Journal of Atmospheric and Solar-Terrestrial Physics*, 174:17–27, Sep 2018.

[244] H. Zirin and K. Tanaka. Magnetic Transients in Flares. *The Astrophysical Journal*, 250:791–795, November 1981.